2010

Focusing aberration corrections for ultrasonic inspections of disk forgings when using a surface compensating mirror and segmented annular phased array

Jon Hiram Friedl

Iowa State University

Focusing aberration corrections for ultrasonic inspections of disk forgings when using a surface compensating mirror and segmented annular phased array

by

Jon Hiram Friedl, Jr.

A dissertation submitted to the graduate faculty

in partial fulfillment of the requirements for the degree of

DOCTOR OF PHILOSOPHY

Major: Engineering Mechanics

Program of Study Committee:
R. Bruce Thompson, Major Professor
Ronald A. Roberts
Timothy A. Gray
Lester W. Schmerr, Jr.
Ralph E. Napolitano
Rohit K. Trivedi

Iowa State University

Ames, Iowa

2010

TABLE OF CONTENTS

LIST OF TABLES

LIST OF FIGURES

ACKNOWLEDGEMENTS

Several individuals have contributed to my being able to earn this doctorate. If not for them, this dissertation would not exist. I'd like to thank Kate Kappel for drawing my attention to Dr. Jane Johnson's speech at the 25th Annual ISU Martial Arts Banquet in February of 2000 regarding similarities between Grandmaster Yong Chin Pak, our mutual martial arts instructor, and Professor R. Bruce Thompson. Dr. Jane Johnson has my heartfelt appreciation for making the aforementioned banquet speech as well as the engaging conversation we had shortly thereafter, during which she recommended Professor Thompson to me as a potential engineering Ph.D. advisor. And so, as they say, the rest is history.

I also wish to thank my parents, Dorothy and Jon, Sr. Well, Dad, I now have that 40 hours per week job you've always wanted for me! Mom, I'm so glad you could spend a few years in Iowa while I attended graduate school. It's been great getting to know both of you as adults these last few years.

Others I'd like to acknowledge include my sisters, Nita and Jackie, as well as my nieces, Jessica and Sara. Whether they knew it or not, each of these women in my family have provided much of the drive I've needed to complete this graduate program. In addition, Jackie's husband Eric, in our family of strong women, has been more helpful than he knows.

Other family members I'd like to thank include my uncle Harry (Bud) Wendzik, Jr. as well as, posthumously, my grandparents Pearl Friedl and Harry Wendzik, Sr. Uncle Bud taught me to have a sense of humor, which I still try to exercise regularly. Grandma Friedl always saw me as a scholar, with whom I enjoyed many interesting conversations. Grandpa Harry always inspired a wonderful sense of inventiveness in myself as well as demonstrating, towards my maternal grandmother, how it is possible to truly care for another person for a lifetime.

One last family member I'd like to thank is my daughter Shelley, adopted at birth by her mother's family, whom I've since gotten to know well. At first by her mere existence, she has motivated me to many of my life's goals in the hope that I might better contribute to her life. She's in her early 20's now, and is a lovely, intelligent, independent, and generally wonderful young woman.

I'd also like to thank the faculty and staff at the Center for Nondestructive Evaluation (CNDE) at Iowa State University. I have very much appreciated all the help and support you've provided these many years while I worked to complete this doctorate.

Finally, I know that the reason I've been able to accomplish what I have is because of the many people who have, one way or another, supported and encouraged me over the years. Thank you, all.

ABSTRACT

Phased array transducers are playing an increasing role in ultrasonic nondestructive evaluation inspection applications, and one area of their use is in the inspection of critical jet engine components such as titanium alloy turbine disk forgings. Inspection of these forging disks is performed during stages of their manufacturing, particularly at an intermediate stage when the forging disk has a deliberate "sonic shape." A forging's sonic shape, from which the final disk shape will be machined, is conducive to ultrasonic testing inspections due to its simple entry surfaces. These entry surfaces are primarily planar or conical surfaces.

In prior work, forgings from General Electric Aircraft Engines, Pratt & Whitney, and Honeywell Engines and Systems were ultrasonically inspected through their planar interfaces, accomplished with a 10 MHz, segmented annular, compound spherical, phased array transducer designed to perform inspections through planar interfaces. Proof-of-concept research used this array along with surface compensating ultrasonic mirrors to inspect through the conical entry surfaces in these forgings. While successful, it was believed that the results of these inspections fell below what would be possible due to non-ideal focusing conditions and other focusing aberrations.

To correct for focusing aberrations when inspecting through forging material planar and curved interfaces, three progressively more sophisticated ray-tracing algorithms were developed to generate delay time sets for phasing transducer array elements, including an initial 2D method from prior work, a refined 2D method designed to more accurately account for refraction at interfaces, and a 3D method designed for circumferentially phasing the segmented annular array.

Ultrasonic inspections using these methods were performed on two sets of forging material specimens, with either planar or curved interfaces, thicknesses ranging from 0.2 inches to 2.7 inches, and each containing a 1/128-inch-diameter flat bottom hole (#1/2 FBH) reflector. FBH responses from planar interface specimens allowed comparison of the initial and refined 2D inspection methods. The refined 2D inspection method used on the planar and curved interface specimens evaluated the performance of the surface compensating mirror. The refined 2D and 3D inspection methods were compared using the curved interface specimens.

CHAPTER 1. GENERAL INTRODUCTION

Introduction

This dissertation studies an improved method for detecting flaws in critical rotating components of gas turbine engines. Increasing flaw sensitivity in aerospace titanium alloys such as Ti-6Al-4V is sought to improve flight safety, since the impact of not detecting a flaw can have severe consequences. Such was the case in the Sioux City crash of a United Airlines DC-10 in 1989, the result of the rupture of a Ti-6Al-4V rotating disk. Later investigation found the source of the failure to be a fatigue crack originating from an internal region made brittle by a high content of interstitial nitrogen, also known as a hard alpha region. In addition to fatigue cracks, voids can also be associated with the hard alpha defect. The preferred method for detecting such internal defects is ultrasound. Increased sensitivity can be applied to critical rotating parts at either the billet stage, forging stage, or both. Inspection of billets provides the opportunity to identify defective material before large value has been added in the manufacturing process. However, inspection of forging disks allows for higher sensitivity due to shorter material paths than those required for billet inspections. In general, inspection sensitivity is calibrated to flat-bottom-hole (FBH) defects machined into material similar to that being inspected. The current flaw detection capability for production inspection of forgings is a FBH sensitivity of 1/64-inch diameter, also known as a #1 FBH. A #1 FBH sensitivity is specifically taken to mean that within each inspection zone, the peak noise seen in the ultrasonic inspection of all locations within the forging material, including the noisiest volumes of the forging microstructure, should be at least 3 decibels (dB) below the peak response from a #1 FBH located in that zone. This corresponds to a minimum signal-to-noise ratio (SNR) of approximately 1.4. It is assumed that the application of a four-fold increase in sensitivity, i.e., inspection at a FBH sensitivity of 1/128-inch diameter (#1/2 FBH), will also increase the sensitivity to hard alpha defects.

Ultrasonic inspections of critical rotating parts are typically performed under immersion with fixed focus, single element transducers. Calibration standards with 1/64-inch diameter FBHs at several material paths are used to achieve a #1 FBH inspection sensitivity, while a depth amplitude correction adjusts gain as required to maintain #1 FBH sensitivity throughout the inspection depth. Once noise becomes too great, a second scan is performed with the beam focus at a deeper region of the material by moving the location of the transducer closer to the material surface or by using a different transducer with different focusing characteristics. In this way, several depth zones can be inspected ultrasonically wherein the beam focus is maintained as a tight beam throughout the depth of the part. Hence, the ultrasonic noise is managed by the application of a small beam diameter that samples few grains at a given time in the inspection volume.

Ultrasonic phased arrays, a technology relatively new to aerospace that has been developed over several decades in other acoustic areas of endeavor, including medical, offers an alternative to fixed focus transducers in immersion inspections of rotating forging disks. A properly designed ultrasonic phased array

positioned at a constant distance from a material surface can be used in place of a set of fixed focus, single element transducers at variable distances from the surface. This substitution is possible due to the phased array's ability to electronically vary its focus. The focus can be varied so swiftly that multiple depth zones can be inspected nearly simultaneously, allowing for a significant reduction in overall inspection time when compared to the multiple scans required by fixed focus, single element transducers. Additionally, ultrasonic phased arrays can achieve wider apertures, and hence smaller focal spot sizes, relative to the current state-of-the-art fabrication technology of conventional, single element UT probes.

Significantly, Howard and Gilmore demonstrated the relationship that the ultrasonic SNR from a point defect in a noisy microstructure varies inversely to the volume of the ultrasonic pulse [1] by examining SNR from FBHs in noisy titanium microstructures using different degrees of focus, center frequency and bandwidth. The volume of the ultrasonic pulse can be viewed roughly as the product of the spatial extent of the pulse in the direction of propagation and the ultrasonic beam area. In turn, the spatial extent of the pulse in the direction of propagation can be seen to be the product of the wavelength and the number of wavelengths in the pulse for a given center frequency and bandwidth. Following this experimental work, Margetan predicted the result of Howard and Gilmore theoretically by using an independent scattering approximation for a point scatterer in a random microstructure [2]. Margetan shows that the SNR varies in inverse proportion to the square of the pulse volume, which will be referred to in this dissertation as the *pulse volume model*.

The pulse volume model can assist in the design of forging inspections to meet specific detection sensitivity targets. Once an embedded reference reflector such as a FBH is located in the highest noise region in a forging, where SNR for any defects tend to be smallest, SNR is measured for several choices of the pulse volume to establish the linear dependency between the inverse of SNR and the square root of the pulse volume. From that dependency, one can then determine the largest pulse volume that can be tolerated to keep SNR sufficiently large.

In prior work which led to the topic of this dissertation, an annular phased array transducer was designed and fabricated to perform #1/2 FBH sensitivity inspections through planar interfaces of titanium alloy forgings [3] (See Figure 1.1). The pulse volume model was the engineering tool used to define the design of the annular phased array. Suppliers were unable to fabricate fixed focus, single element probes of sufficient aperture using current state-of-the-art transducer fabrication technology. Since forging disks have both planar and conical entry surfaces, proof-of-concept research was conducted, using this array along with surface compensating mirrors, to see if that array could be used to successfully inspect through the conical entry surfaces of these forgings. While the concept was successfully verified experimentally, quantitative evaluation of the results of these inspections indicated that the performance fell below what would be possible. It is postulated that this was due to non-ideal focusing conditions and other focusing aberrations.

Figure 1.1: 10 MHz, segmented, annular, compound spherical, phased array transducer.

It is the hypothesis of this dissertation that the non-ideal focusing that limited the performance realized in the above, proof-of-concept, experiments can be improved through the development of more sophisticated focusing algorithms that take advantage of the great flexibility of phased array technology. The major emphasis has thus been on the development of such algorithms which minimize focusing aberrations during ultrasonic inspections through planar and curved entry surfaces, as compensated by surface mirrors.

It is the goal of this dissertation to minimize focusing aberrations during ultrasonic inspections through planar entry surfaces, and curved entry surfaces using surface compensating mirrors, of titanium alloy forging disks when employing the previously designed phased array transducer.

Dissertation Organization

This dissertation has been organized in the following manner. Chapter 1 provides a general introduction into the nondestructive evaluation of forging disks during ultrasonic immersion inspections as well as the basic principles behind phased array technology. Chapter 2 is an introduction to ultrasonic phased array inspection through planar and curved interfaces of forging disks, including the initial delay time generation method, a description of surface compensating mirrors used during inspections through curved interfaces, and sources of focusing aberrations. Chapter 3 presents several delay time generation methods, each more sophisticated than the next, that were developed to reduce or eliminate sources of focusing aberrations found during forging disk inspections. Chapter 4 shows the results of experimentally attempting each proposed method. Chapter 5 concludes the dissertation with general conclusions and suggests ideas for future research.

Basic Principles of Phased Arrays

Transducers used in conventional ultrasonic testing (UT) and nondestructive inspection (NDI) applications can be manufactured as a single monolithic transducer or arranged as an array of individual transducer elements. Conventional UT probes produce ultrasonic beams via fixed focus, single element transducers. As a mature area of interest, research and applications when using conventional UT probes are extensive and will not be specifically addressed here.

An ultrasonic phased array system uses a multi-element probe for the transmission and reception of ultrasonic beams. Individual elements of a phased array may be arranged in a variety of configurations (See Figure 1.2). One-dimensional or "linear" arrays are the simplest and most common configuration, with all elements arranged in a line. The characteristics of ultrasonic beams generated by linear arrays have been well documented [4, 5]. Elements may also be arranged in a two-dimensional rectangular matrix. Annular arrays have elements arranged in concentric circles with either whole rings (1-D annular array) or as rings segmented into sections (2-D segmented annular matrix). As needed, specific applications have led to the design of additional configurations, including phased arrays with cylindrically-shaped, spherically-shaped, and other types of curved transducer faces.

Ultrasonic waves are mechanical vibrations generated in an elastic medium by a piezoelectric crystal excited by an electrical voltage. Each active element in a phased array probe generates wavelets that combine to form a resultant wave front. This resultant ultrasonic beam can be electronically steered. focused, or both by applying a time delay to each element (See Figure 1.3). A set of delays for all elements is known as a *delay law* or *focal law*. By changing the timing of pulse generation across the array of elements in a phased array transducer, features such as beam angle, focal depth, shape, and emission point can be electronically controlled. Analogous concepts apply upon detection of ultrasonic waves by the phased array.
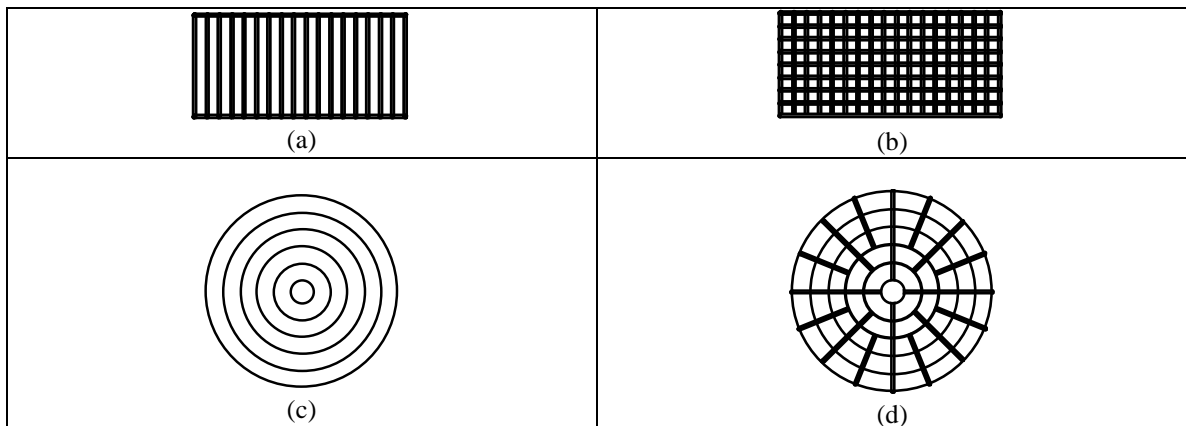
Figure 1.2: Typical geometries of phased array probes: (a) 1-D linear, (b) 2-D rectangular matrix, (c) 1-D annular, and (d) 2-D segmented annular matrix.
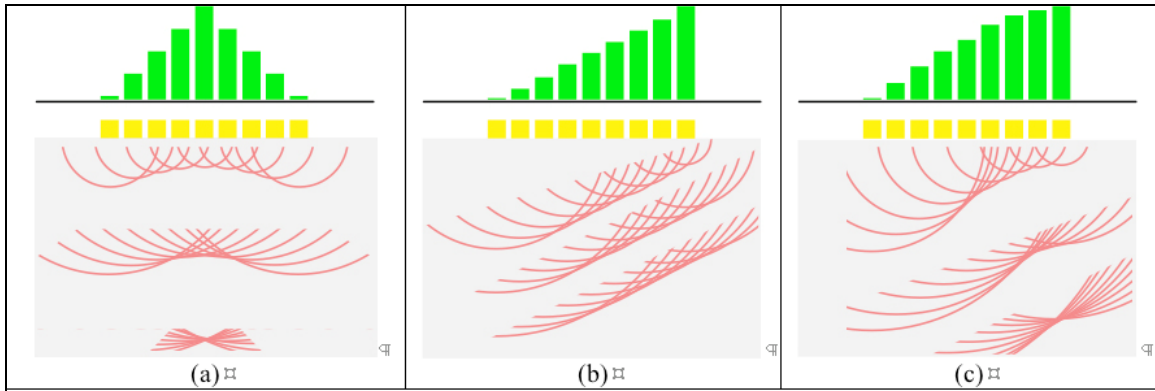
Figure 1.3: Illustration of wavelets (red) generated with sets of delay times (green) for individual elements (yellow) of a 1-D linear phased array where the resultant beam is (a) focused, (b) steered, and (c) focused and steered.

A linear array can generate a synchronous beam (e.g., electronic scanning with a set of delay times multiplexed over a group of active elements), a focused beam, perform beam steering, or simultaneously perform beam steering and focusing. A two-dimensional rectangular grid can perform beam steering and/or beam focusing in two planes. A 1-D annular array cannot perform beam steering, but can generate a high quality, axially focused beam at varying depths. A 2-D segmented annular matrix is capable of simultaneous beam steering and focusing, the quality of which depends on the degree of individual ring segmentation, through a wide range of focal depths.

The number of elements in an ultrasonic phased array generally ranges from 16 to 512. Both the maximum number of elements and delay generators in phased array instrumentation are expected to increase as further advances are made in computer processing speed, computer memory (dynamic as well as hard drive memory), and transducer array fabrication capabilities. Phased array instrumentation available to energize and phase the 10 MHz, 110-element, 36-ring, segmented annular array, with a compound spherical transducer face, used in this work had a hardware limitation of 128 elements and 32 delay time generators.

Acquisition and Presentation of Ultrasonic Data

The raw ultrasonic data obtained with a phased array, such as that presented in this dissertation, takes the form of non-rectified waveforms, also known as A-scan data (See Figure 1.4). Such data are captured at each scan-index position in the inspection. Parameters are then deduced from each A-scan, e.g., the maximum or absolute maximum amplitudes within a time gate, and stored. The set of such data, captured over the course of an inspection scan, are then presented as color or black-and-white images along with their palettes (See Figure 1.5), plotted as a function of scan coordinates. Possible color scheme palettes include grayscale and rainbow, among others, as well as user-defined color schemes. Such plots are known as C-scans. C-scan images of captured data collected will be presented using a rectified grayscale palette.
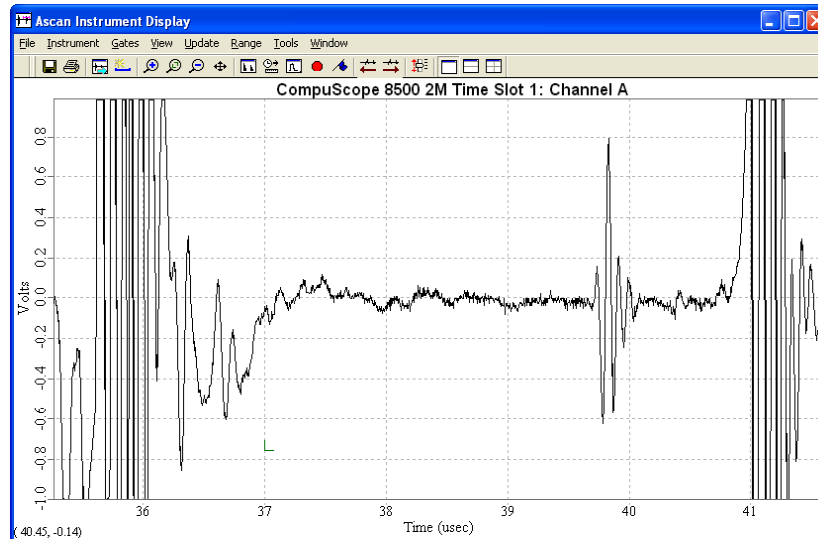
Figure 1.4: Typical non-rectified A-scan waveform data.
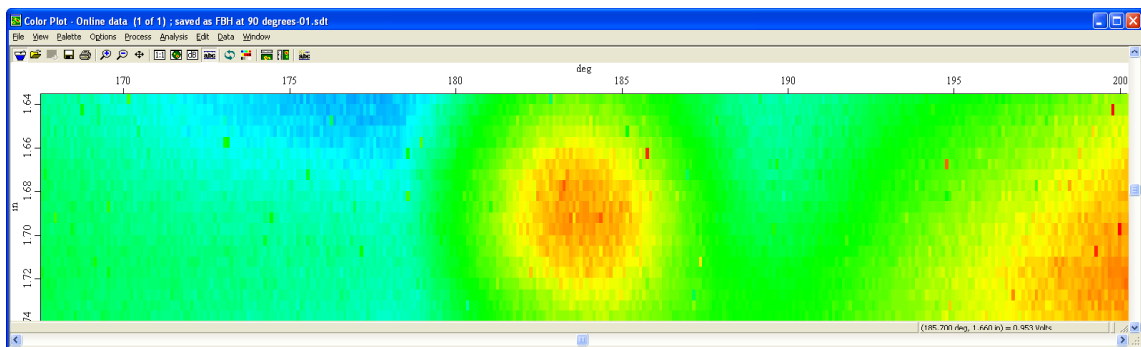
(a)
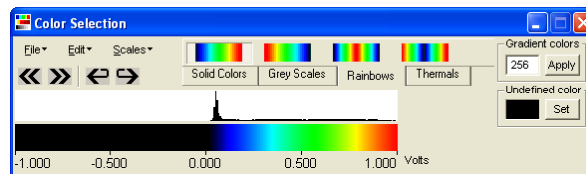
(b)

Figure 1.5: Overall amplitude C-scan results presented as (a) rectified image with (b) color palette.

CHAPTER 2. INTRODUCTION

Introduction

During prior zoned inspections of curved entry forging surfaces using compensating mirrors, the transducer array designed specifically for zoned forging inspections was phased with the same time delays as those used during planar entry forging surface inspections. Thus, in this previous proof-of-concept work, it was assumed that the compensating mirrors perfectly corrected for the focusing effects at the part surface, and focusing aberrations due to non-ideal mirror performance were mostly ignored. As mentioned in the introductory chapter, this dissertation presents studies on corrections for focusing aberrations, including those due to non-ideal mirror performance, when using surface compensating mirrors to ultrasonically inspect through the curved entry surfaces of titanium alloy forgings. This chapter identifies and describes the causes of focusing aberrations. Corrections for these observations will be proposed in the next chapter.

This chapter begins with a description of the initial method by which delay times, necessary in phasing the designed transducer array, were generated for zoned forging inspections through planar entry surfaces without compensating mirrors during proof-of-concept research by the FAA-ETC team. Surface compensating mirrors, as employed in the zoned forging inspections, will also be described, emphasizing reasons that the application of these mirrors only approximately compensated for forging surface curvatures. These descriptions will be followed by the identification and description of all the focusing aberration sources found in zoned forging inspections.

Phased Array Inspection Setups

Two immersion inspection setups were required for the phased array system when gathering data for this dissertation. The first setup was a X-Y raster scan for gathering reference data from the planar interface calibration specimens while another setup, a rotational-radial turntable scan incorporating surface compensating mirrors, was used to inspect the curved interface calibration specimens (See Figure 2.1). The ultrasonic mirror was placed in the water path between the transducer and part, oriented at 45° angle relative to the centerline of the transducer's ultrasonic beam through the use of a transducer-mirror assembly (See Figure 2.2). In both inspections, A-scan waveform data was captured for the volume of the calibration sets containing #1/2 FBH reference reflectors.

The element layout of the phased array transducer, photographed in Figures 1.1 and 2.2, are provided in Appendix A of this dissertation. The spherically shaped transducer face partially focuses, i.e., pre-focuses, the emitted ultrasonic beam prior to phasing, thus providing the overall focusing range for the phased array while continuing to meet #1/2 FBH inspection sensitivity [6].
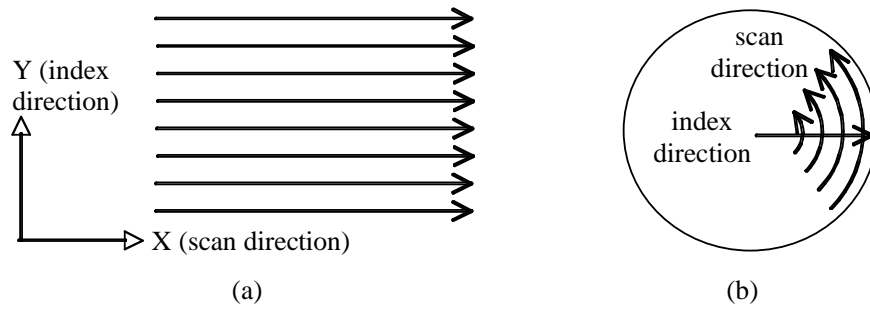
Figure 2.1: Schematics of immersion inspection setups, including (a) X-Y raster scan and (b) rotational-radial turntable scan.
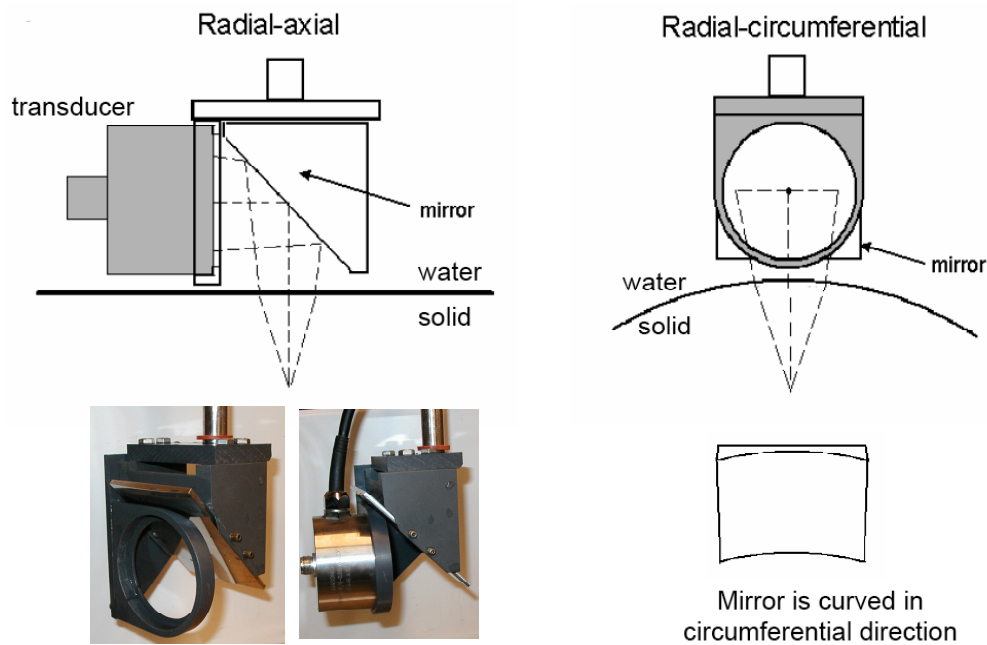
Figure 2.2: Mirror and transducer holder for rotational-radial inspections.

Calibration Specimens

Two sets of coupons machined from titanium alloy disk forgings were inspected to evaluate the methods presented in this dissertation. Each set of calibration specimens contains a #1/2 FBH reference reflector at a known depth. The set of 13 planar interface calibration blocks are shown in Figure 2.3, while Figure 2.4 shows the complete set of 19 curved interface calibration specimens. The sets of planar and curved interface coupons were machined from Pratt & Whitney (PW) and Honeywell Engines, Systems & Services (HW) Ti-6Al-4V forging disks, respectively. The first 13 coupons from each set have matching metal path hole depths for #1/2 FBH reference reflectors. Table 2.1 tabulates the metal path hole depth for blocks 2 through 13, the subset of blocks inspected for this dissertation, for both sets of forging coupon calibration specimens.
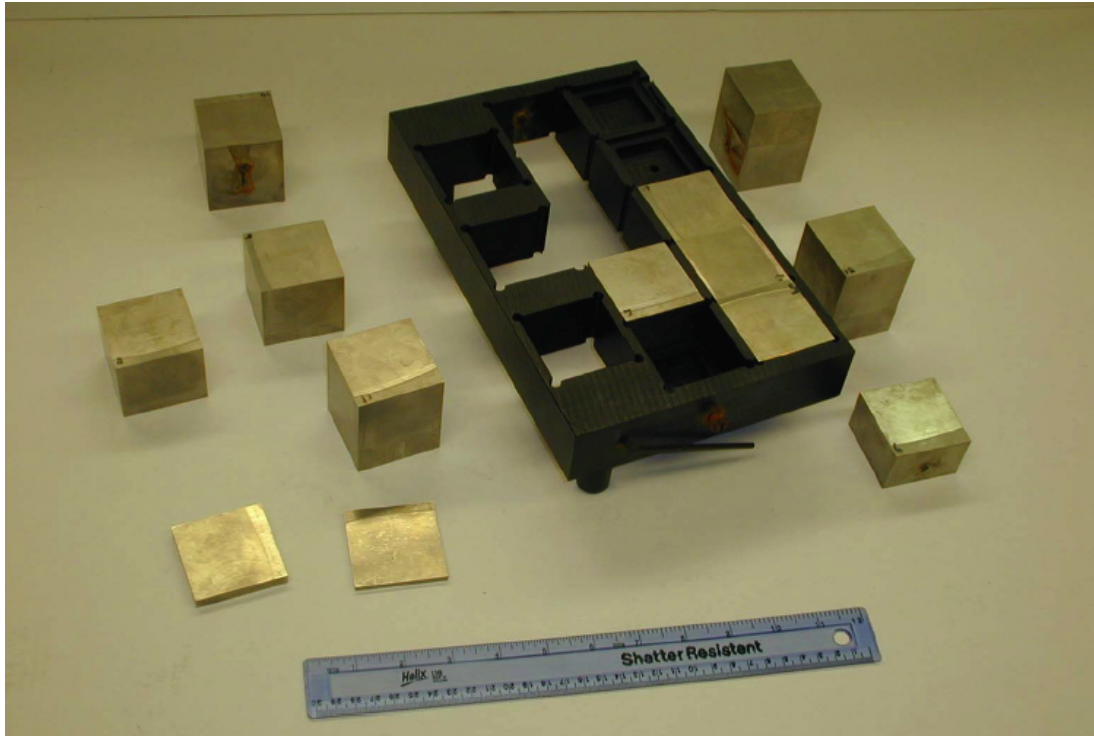
Figure 2.3: Set of planar interface calibration blocks.

Figure 2.4: Set of curved interface calibration specimens.

Table 2.1: Metal path depths of #1/2 FBHs for both sets of forging coupons.

Specimen #	Metal Path Hole Depth (inches)
2	0.200
3	0.450
4	0.700
5	0.900
6	1.150
7	1.350
8	1.600
9	1.800
10	2.050
11	2.250
12	2.500
13	2.700

To perform an immersion inspection of the curved interface calibration set with the rotational-radial scan described, each curved entry surface forging coupons required suspension at an angle and rotation on a turntable so as to pass beneath the transducer/mirror apparatus at a constant water path distance (See Figure 2.5). This was accomplished by reassembling the forging disk from which the curved entry surface coupons were cut, such that the disk functioned as a holder for the forging coupons reinserted
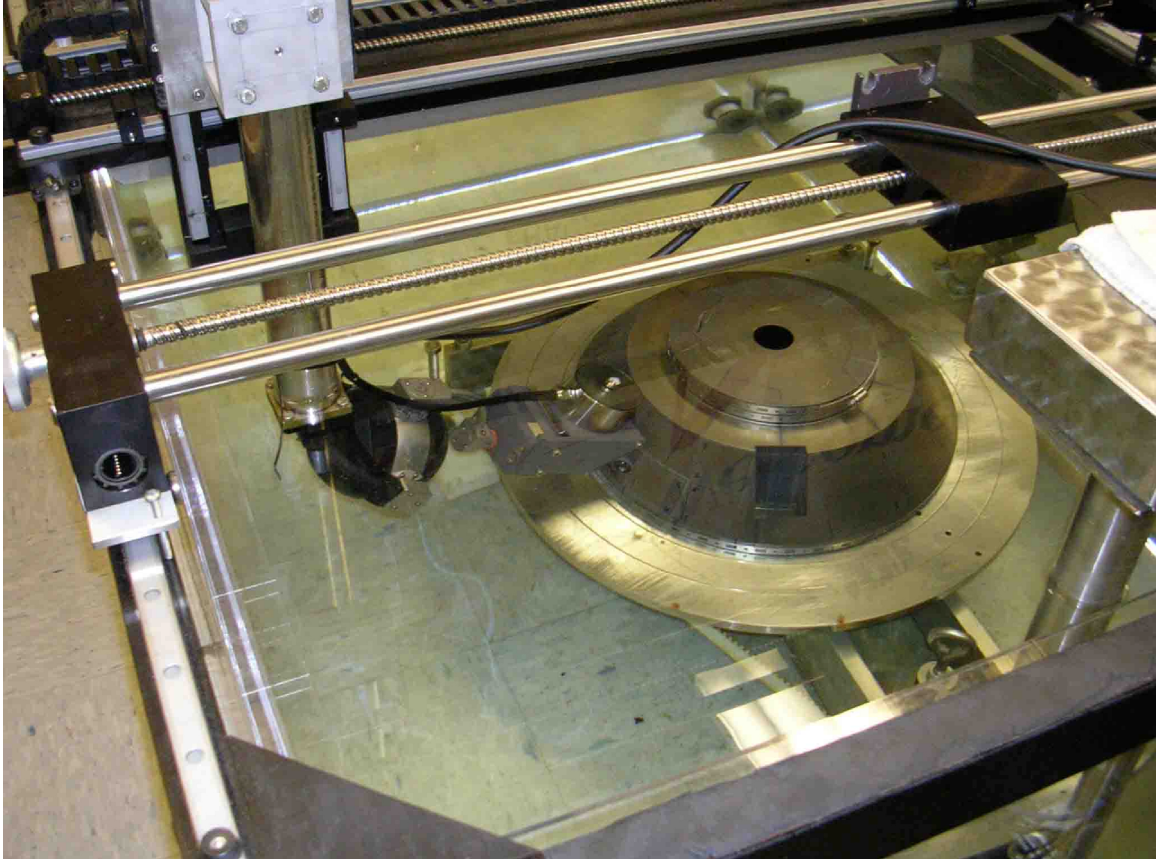
Figure 2.5: Rotational-radial immersion inspections of curved interface specimens in disk holder.

into their original positions (See Figure 2.6). Wire electron-discharge-machining (EDM) was the machining method used to cut the original HW forging disk, a precise machining method that can section metal parts with only small amounts of material loss. Figure 2.7 shows a schematic of the wire EDM cuts used to section the HW forging disk. Upon examination of the orientations of the coupons reinserted into the disk holder, each coupon were found to be very near their original position. It was noted, however, that each coupon was slightly recessed beneath the original forging disk surface. This elevation change was compensated for during positioning of the transducer-mirror assembly before inspections of each coupon.

Figure 2.6: Complete HW forging disk after wire EDM, including forging coupon set, excess forging material shards, and reassembled disk as holder.
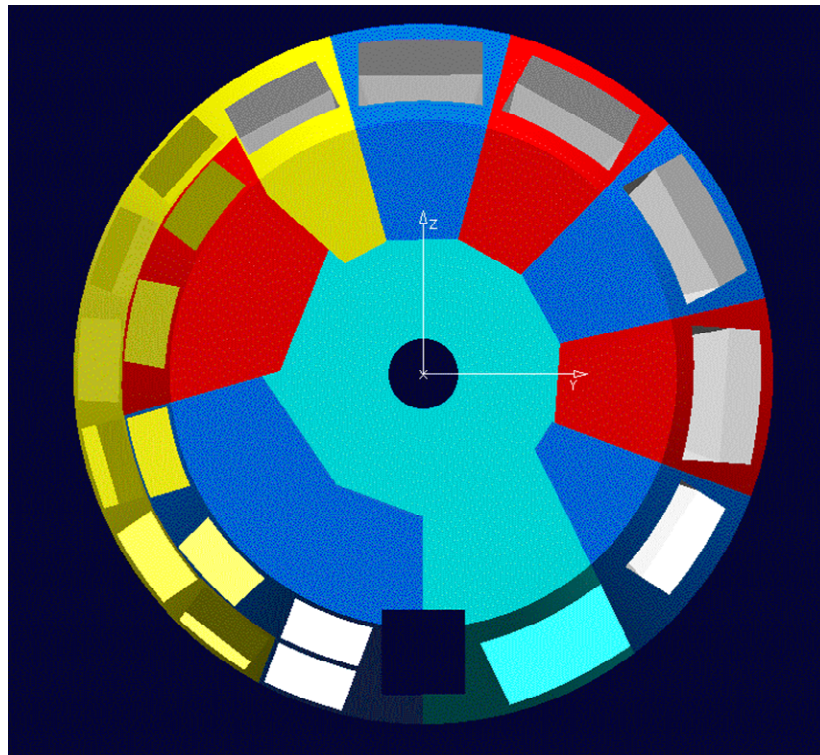
Figure 2.7: Schematic of wire EDM sectioning cuts made in Honeywell forging disk.

Surface Compensating Mirrors

In prior work, the phased array used here was designed for #1/2 FBH sensitivity inspections of disk forgings through the planar entry surface of sonic shapes up to a maximum metal depth of 2.70 inches when using a water path distance of 3.00 inches. Maintaining an F6 beam focus at this water path distance and maximum metal depth required the maximum aperture of the transducer. Proof-of-concept experiments was conducted, using this array along with a set of surface compensating mirrors, to see if that array could be used to successfully inspect through the conical entry surfaces of these sonic shaped disk forgings. An curved mirror placed between the transducer and the part under inspection pre-distorts the ultrasonic beam before the beam enters the part. After passing though a curved entry surface interface, this pre-distorted ultrasonic beam is again distorted by refraction. If the surface compensating mirror is properly designed, this final distortion returns the ultrasonic beam back into approximately the same shape the beam had during inspections beneath planar entry surfaces without surface compensating mirrors.

A cylindrical, concave mirror was employed during the rotational-radial inspections reported upon in this dissertation to compensate for the curved interface surfaces of forging coupons. The mirror design involved a procedure wherein rays were traced from a desired focal depth point source in the solid to the transducer face after refracting through the curved interface and reflecting off the mirror surface. The ray-tracing procedure was iterated to provide a cylindrically shaped surface compensating mirror radius of curvature that would produce equal wave front curvatures along orthogonal directions, identified as vertical and out-of-plane directions in Figure 2.8, from the center of the face of the transducer. Equal wave front curvatures were desired since the transducer focal laws were designed to produce a spherically focused beam.
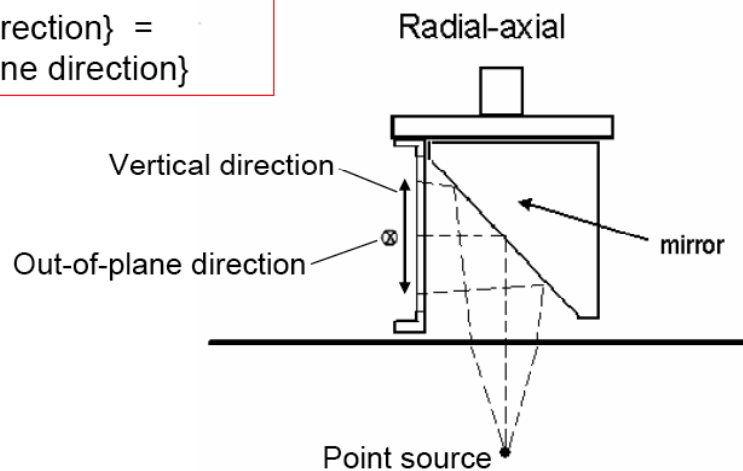
Figure 2.8: Schematics of surface compensating mirror configuration and design.

The mirror design procedure used as input parameters a water path distance of 3.50 inches with a depth of focus in the forging material of 2.50 inches. This water path distance, increased from 3.00 inches, was selected to accommodate the transducer-mirror holder assembly (See Figure 2.2). A concave surface compensating mirror with a 26.55-inch cylindrical radius of curvature was determined to be required for a 3.50-inch water path distance and a 2.50-inch deep focus in the HW forging disk, using the average convex surface radius of 8.60 inches as an input into the mirror design. In prior proof-of-concept experiments, a different forging required a concave mirror radius of 27.5 inches to compensate for its convex surface. A single concave mirror of radius 27.0 inches was fabricated to compensate for both the 26.55- and 27.5-inch radii of curvature forging surfaces. The mirror was fabricated from stainless steel, and had a surface area of 3.0 inches by 4.5 inches. As will be discussed subsequently, several factors were neglected in this mirror design such as diffraction and variations in disk curvature.

Initial Delay Time Generation Method

For prior proof-of-concept experiments, an initial 2-D delay time generation method was developed to phase, i.e., electronically focus, the transducer array along a direction normal to the probe face to inspect the aforementioned planar interface forging specimens containing #1/2 FBHs at various depths. This initial delay time method generated sets of focal laws designed to electronically focus the transducer array at the depth of these FBHs. Several parameters were selected or determined before generating these focal laws, including flaw depth in the part, water path distance, longitudinal sound velocity in the part, and transducer aperture diameter. These all served as inputs to the focal law calculation. Prior determination of these initial focal laws used flaw depths as tabulated in Table 2.1 and selected a 3.00-inch water path distance between the transducer face and the planar water-forging interface of the part.

The longitudinal sound velocity of the planar interface forging coupons inspected in prior work using the initial delay time generation method were measured experimentally. These longitudinal velocity measurements were performed using a conventional UT immersion transducer with a planar focus, 10 MHz center frequency, and a 0.5-inch-diameter aperture (Panametrics Model V311, S/N 157470), energized in pulse-echo mode with a UTEX Model UT-340 pulser-receiver unit set to a 300 V driving voltage, 10 ns pulse width, and 30 dB gain. Time-of-flight (TOF) measurements were performed on each coupon over a 1.4-inch by 1.4-inch scan area with a 0.020-inch resolution. TOF differences between the first back wall (BW) echo to the second BW echo, and also from the first and third BW echoes, were averaged over the scan area, then averaged together. The height of each planar coupon was precisely measured with a dial caliper. The longitudinal sound velocity was calculated by dividing twice the coupon thickness by the average roundtrip TOF for each planar interface calibration specimen, as tabulated in Table 2.2.

The transducer parameter *F*, defined as the ratio of focal length to aperture diameter, is a common optics term referred to as *F-number*, *F/number* or *focal ratio* [7]. This quantity determines, for a given

Table 2.2: Longitudinal sound velocities of planar interface forging coupons.

Block #	Block Height (in.)	$BW_2 – BW_1$ (μs)	$BW_3 – BW_1$ (μs)	Average TOF (μs)	Longitudinal Velocity (m/s)
2	0.280	2.297	4.590	2.296	6200
3	0.530	4.358	8.698	4.354	6180
4	0.780	6.395	12.793	6.396	6200
5	0.980	8.042	16.109	8.048	6190
6	1.230	10.112	20.210	10.109	6181
7	1.430	11.754	23.493	11.750	6182
8	1.680	13.787	27.596	13.793	6188
9	1.880	15.458	30.917	15.458	6178
10	2.130	17.512	35.008	17.508	6180
11	2.330	19.129	38.286	19.136	6185
12	2.580	21.203	42.422	21.207	6180
13	2.780	22.842	45.722	22.852	6180

wavelength, how tightly a beam will focus. As shown in Equation (2.1), the transducer aperture diameter, D, must be directly proportional to focal length, f, in order to keep the *F-number*, and hence the focal spot size, constant. For a spherical radiator, the beam diameter in the focal plane is commonly defined to be twice the distance from the central beam axis to the location where the pressure amplitude is reduced by 6 decibels (dB) as given in Equation (2.2), where W_f is the focal plane beam diameter, λ the wavelength of the ultrasonic beam, and D the transducer aperture diameter [8]. Equation (2.2) shows how the 6 dB beam diameter, W_f, depends on f, D, and λ (wavelength). This shows that the transducer diameter, D, must be inversely proportional to the desired beam diameter in the focal plane (See Equation 2.2) to maintain a constant beam diameter at a fixed wavelength.

$$F = \frac{f}{D} \tag{2.1}$$

$$W_f\left(-6dB\right) = 1.028\lambda\left(\frac{f}{D}\right) = 1.028\lambda F \tag{2.2}$$

To meet a #1/2 FBH sensitivity, prior work based on the pulse volume model for SNR determined that the inspection must be performed with beam diameters no larger than 45 mils (0.045 inches) within the inspection zone when using a 10 MHz center frequency transducer with a 60% bandwidth [6]. When a transducer focuses at a particular depth, there is a range of depth, i.e., inspection zone, in which the beam diameter meets the inspection criteria. Based on the focal properties of the transducer(s), multiple zones covering the entire depth of the part can be defined for forging inspections. A transducer with a focal ratio of F6 was determined to meet this inspection sensitivity, because a F6 transducer has the ability to generate a beam with a minimum beam diameter of 36 mils at its focal plane and does not exceed a beam diameter of 45 mils within the inspection zone [3].

When the focused beam produced by a transducer in water enters a solid, refraction causes the rays to converge more rapidly. Hence the distance from the water-solid interface to the focal point is less

than it would have been had the beam continued to propagate in water. Put in other terms, the focal length in water is always greater than the distance to a focal point in a solid. Equation (2.3) quantifies this relationship, a result that depends on small angles of the converging rays such that $\sin\theta \approx \theta$ as will be derived in more detail below. For example, focusing on a flaw at a 0.20-inch metal path depth in titanium when using a 3-inch water path distance corresponds to a focal distance of 3.83 inches in water.

$$\text{corresponding focal distance in water} = \text{waterpath} + \frac{v_{part}}{v_{water}}\left(\text{metal path to focus}\right) \qquad (2.3)$$

Converting metal path distances into a corresponding distance in water before calculating delay times is the unique feature of the initial delay time generation method when compared with the delay time generation methods presented in the next chapter of this dissertation. Focused, single-element immersion probes are traditionally labeled by their manufacturers with focal lengths in terms of inches in water. Ease of use led to an engineering rule often used in UT wherein the part/water velocity ratio is approximated as a factor of 4, allowing a water path and metal path focal distance to be converted into a corresponding focal length in water, and vice versa. For example, a single-element, spherically-focused, immersion UT transducer with a nominal focal length of 5 inches in water will focus at approximately 1 inch deep in a metal part, i.e., equivalent to approximately 4 inches in water, if the transducer is at normal incidence to the metal interface at a water path distance of 1 inch.

Converting a metal path distance into a corresponding distance in water is based on Snell's Law of Refraction (See Equation 2.4) [9, 10] when applying the small angle approximation, as illustrated in Figure 2.9. Both scenarios show incident rays being traced through one medium before passing through an interface, after which the rays focus to a point in a second medium. Also, the incident ray intersects with the interface at an incident angle θ_i at a distance x from the beam center. In the scenario on the left, the upper medium has a slower material velocity than the lower medium. Below the interface, the ray refracts with angle θ_1 before propagating to the beam focal point at a depth of y_1. In the scenario on the right, the lower medium is identical to the upper medium. Therefore, the refracted angle θ_2 is identical to the incident angle θ_i (See Equations 2.5 and 2.6). The ray reaches the beam focal point at a depth of y_2.

Snell's Law of Refraction is given by

$$\frac{\sin\theta_{\text{upper}}}{v_{\text{upper}}} = \frac{\sin\theta_{\text{lower}}}{v_{\text{lower}}} \qquad (2.4)$$

where v is the ultrasonic wave speed. In the right scenario of Figure 2.9,

$$v_{\text{upper}} = v_{\text{lower}} \qquad (2.5)$$
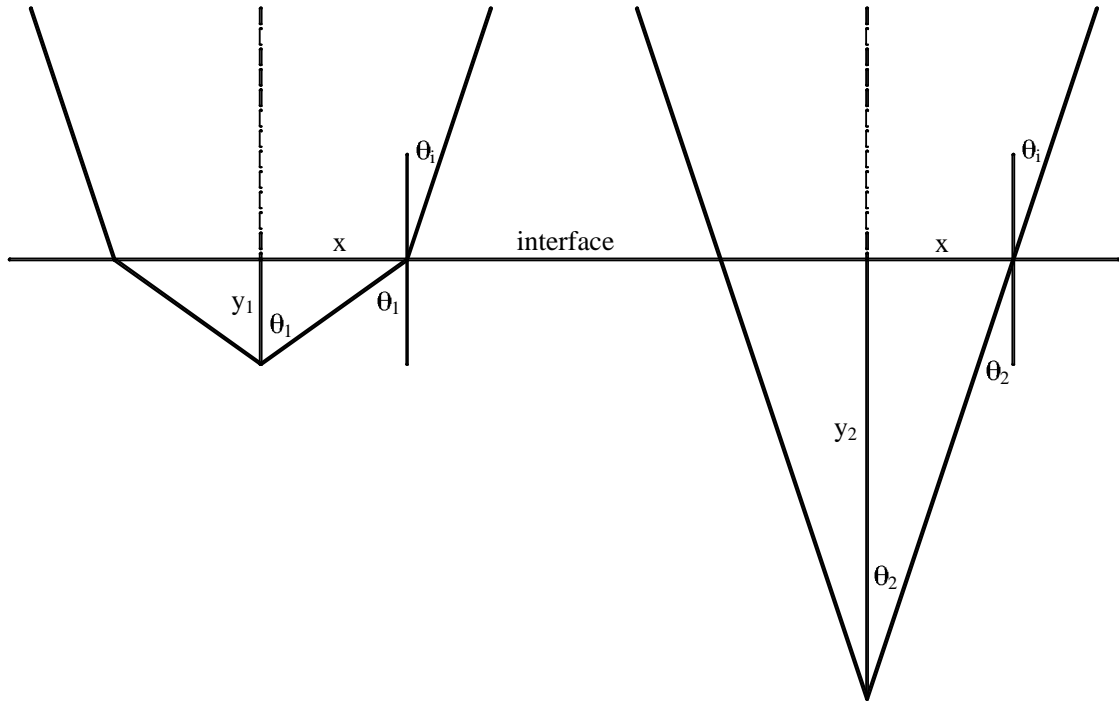
Figure 2.9: Schematic of initial 2D delay time generation method using small angle approximation.

$$\sin\theta_i = \sin\theta_2 \quad \Rightarrow \quad \theta_i = \theta_2 \tag{2.6}$$

In the left scenario of Figure 2.9, Snell's Law yields Equation 2.7. Substitution of Equation 2.6 into Equation 2.7 to eliminate θ_2 relates the geometry of the two scenarios of Figure 2.9 (See Equation 2.8). The depths of focus beneath the interface can be related through the variable x, the distance along the interface from beam center to the ray intersection point (See Equation 2.9). Using the small angle approximation (See Equation 2.10), the tangent terms of Equation 2.9 can be substituted with the sine terms of Equation 2.8. This results in Equation 2.11, whereby a metal path distance y_1 multiplied by the part/water velocity ratio results in a corresponding distance in water, y_2, as previously presented in the second term of Equation 2.3.

$$\frac{\sin\theta_i}{v_{\text{upper}}} = \frac{\sin\theta_1}{v_{\text{lower}}} \tag{2.7}$$

$$\frac{\sin\theta_2}{v_{\text{upper}}} = \frac{\sin\theta_1}{v_{\text{lower}}} \quad \text{or} \quad \frac{\sin\theta_1}{\sin\theta_2} = \frac{v_{\text{lower}}}{v_{\text{upper}}} \tag{2.8}$$

$$\tan\theta_1 = \frac{x}{y_1} \quad \text{and} \quad \tan\theta_2 = \frac{x}{y_2} \quad \Rightarrow \quad y_2 = \frac{\tan\theta_1}{\tan\theta_2} y_1 \tag{2.9}$$

$$\text{small angle approximation}: \quad \cos\theta = 1; \quad \sin\theta = \theta; \quad \tan\theta = \sin\theta = \theta \tag{2.10}$$

$$y_2 = \frac{v_{\text{lower}}}{v_{\text{upper}}} y_1 \tag{2.11}$$

It can also be shown that, within the small angle approximation, the 6 dB diameter for a beam focused in a metal part is the same as it would have been had the 6 dB diameter been measured at the focal plane in water. This can be proved by simple trigonometry or intuitively understood from Equation (2.2). When the beam enters the solid, the *F-number* effectively decreases because refraction causes the rays to converge more rapidly. However, the wavelength increases and, to first order, λF remains constant.

The forging coupon with the deepest flaw at 2.70 inches (see Table 2.1) has the maximum required focal distance, corresponding to 14.23 inches in water. For a F6 transducer, these minimum and maximum focal distances imply transducer aperture diameters of 0.639 inches (16.2 mm) and 2.37 inches (60.2 mm), respectively. As seen in Table A.1 from Appendix A of this dissertation, aperture radii of 8.1 mm and 30.1 mm would be achieved when using 6 and 34 rings, respectively, of the designed 110 element, 36 ring phased array transducer, thereby meeting the stated beam focus requirements.

The transducer array aperture consists of discrete rings. Ideally, each ring functions in a binary state, either energized or not. If any portion of a ring is required in the transducer aperture, then that entire ring must be energized as, given the current capabilities of phased array instrumentation, no individual ring may be partially energized. Apertures for a F6 transducer tabulated in Table 2.3 were calculated through the use of Equations (2.1) and (2.3), a 3.00-inch water path distance, a sound velocity in water of 1487.4 *m/s* based on a water bath temperature of 73.3°*F* [11], and measured longitudinal sound velocities for the planar interface forging coupons in Table 2.2.

The initial 2D delay time generation method is a ray-tracing procedure developed to obtain the delay times desired to phase each ring within the transducer aperture when focusing at the depth of the various #1/2 FBH reference reflectors located below the planar interface of forging coupons. Delay times for phasing a single ring of the transducer array were generated by calculating the differences between the distance from the transmitting/receiving ring to the desired point of focus, i.e., d_{ring} as shown in Figure 2.10, and the ray centerline reference distance, $z_1 + z_2 + z_3$, in units of time. The distance z_1 is the height of

Table 2.3: Transducer apertures for forging coupons when using 3.00-inch water path distance and F6 beam focus.

Block #	v_{block}/v_{water} (unitless)	Metal Path (inches)	Focal Distance (inches)	Radius (inches)	Radius (mm)	Rings in Aperture
2	4.165	0.200	3.833	0.319	8.113	6
3	4.158	0.450	4.871	0.406	10.310	10
4	4.165	0.700	5.916	0.493	12.521	14
5	4.159	0.900	6.743	0.562	14.273	17
6	4.156	1.150	7.779	0.648	16.466	20
7	4.156	1.350	8.611	0.718	18.226	22
8	4.160	1.600	9.656	0.805	20.439	24
9	4.154	1.800	10.477	0.873	22.177	26
10	4.155	2.050	11.518	0.960	24.379	28
11	4.159	2.250	12.358	1.030	26.157	30
12	4.155	2.500	13.388	1.116	28.337	32
13	4.155	2.700	14.219	1.185	30.096	34

the transmitting/receiving ring relative to the central element, as tabulated in Table A.1 of Appendix A. The distance $z_1 + z_2$ is the water path distance desired for the inspection. The distance z_3 is the metal distance to the focal point in the part as a corresponding distance in water.

Although not shown in Figure 2.10, the face of the transducer array is a compound spherically shaped surface providing partial mechanical focusing of the transducer array (See Figure 2.11). The innermost aperture of 12 rings, the middle aperture region of rings 13 through 26, and outermost aperture region of rings 27 through 36 have, respectively, radii of curvature of 5.389, 11.174, and 16.481 inches. This compound spherical surface partially focuses the ultrasonic beam before electronic phasing of the array is applied, effectively reducing the overall range of delay time values in a given focal law.

Delay time sets from the initial 2D delay time generation method for even-numbered planar forging coupons, the subset of planar interface forging coupons required for prior proof-of-concept experiments, are plotted in Figure 2.12 and tabulated in Table 2.4. Currently available phased array instrumentation has the limitation of a 2 ns time delay resolution and hence the delays were rounded here.

The sets of delay times plotted in Figure 2.12 have several features common to the sets of delay times to be presented in the next chapter of this dissertation due to being generated for the same physical geometry of phased array transducer element layout. The layout of the transducer rings, as documented in Appendix A of this dissertation, includes the elevation of each ring. Note that each curve has at least one value equal to zero, and that none of the delay times are negative in value. The compound spherically
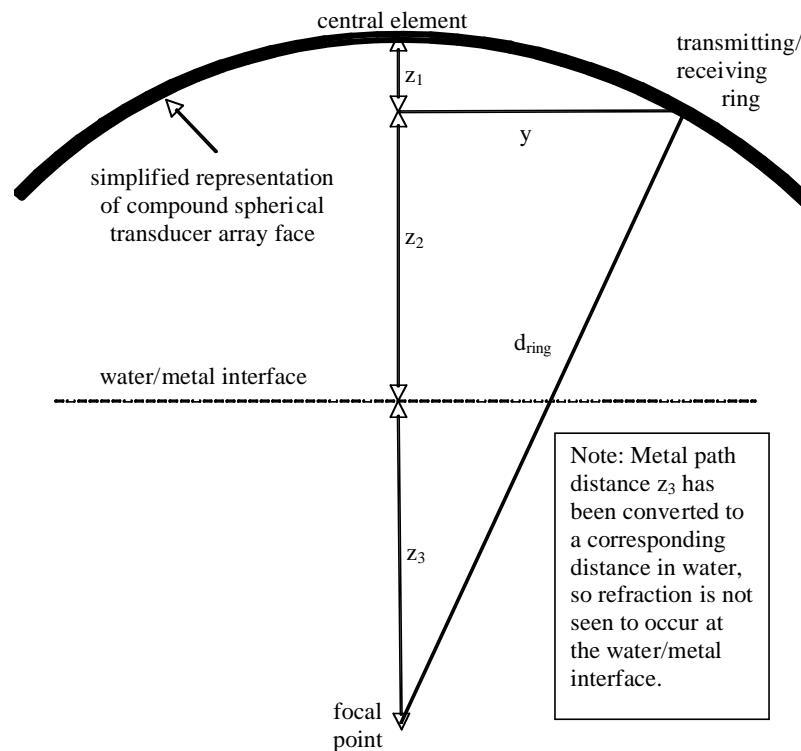
Figure 2.10: Schematic of determining delay times using the initial 2D delay time generation method.

focused face of the array partially focuses, geometrically, the transducer array to minimize the amount of electronic phasing required to focus the array as needed. For example, the focal law for block 2 shows that the geometrical focus of the transducer array must be electronically shortened because the first 12 rings have a geometrical focus length which focuses beyond the depth of the FBH when using a 3-inch water path distance. Also, the focal law for block 12 shows three sections, each related to the three spherical curvatures of the face of the transducer array.
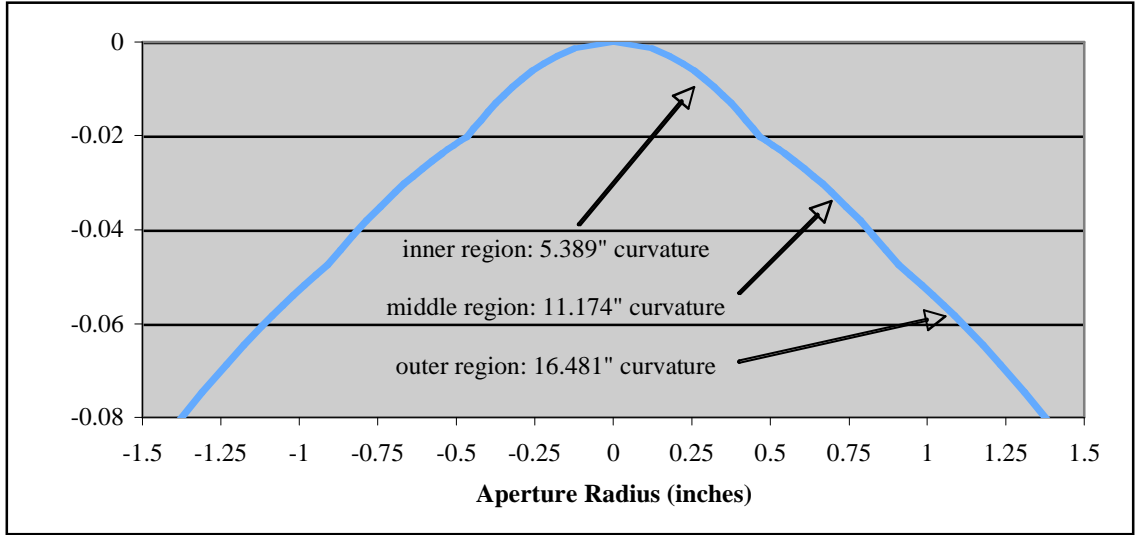
Figure 2.11: Compound spherical face of transducer array.
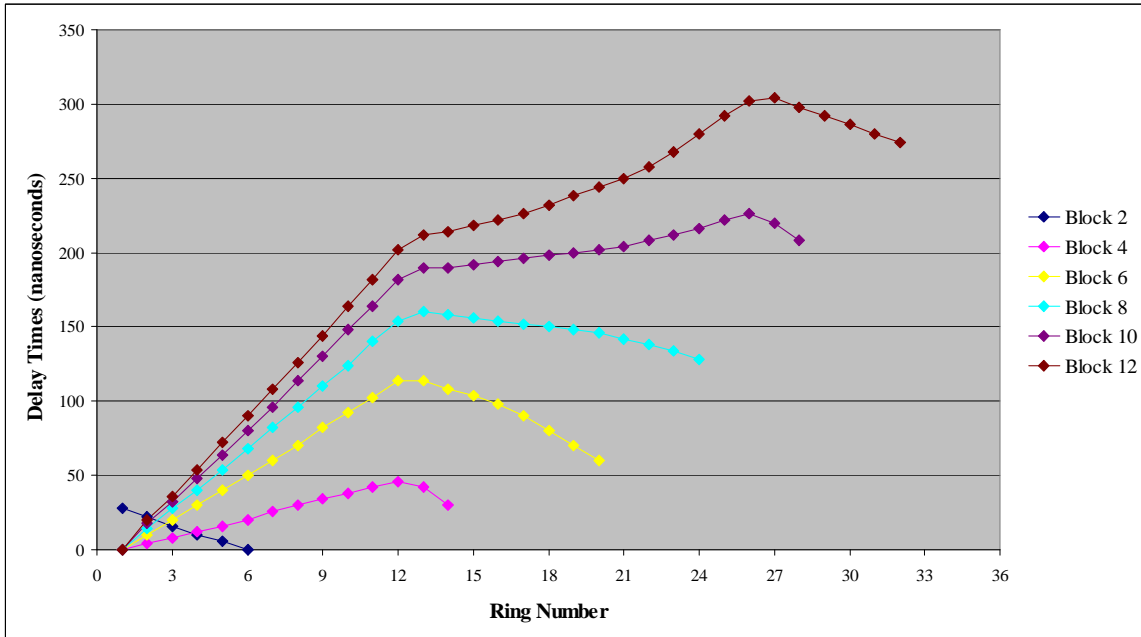
Figure 2.12: Delay times for even-numbered planar interface forging specimens at a 3.0-inch water path distance and F/6 beam focus using the initial 2D delay time generation method.

Table 2.4: Delay times for even-numbered planar interface forging specimens at a 3.0-inch water path distance and F/6 beam focus using the initial 2D delay time generation method.

Ring #	Block 2	Block 4	Block 6	Block 8	Block 10	Block 12
1	28	0	0	0	0	0
2	22	4	10	14	18	20
3	16	8	20	28	32	36
4	10	12	30	40	48	54
5	6	16	40	54	64	72
6	0	20	50	68	80	90
7		26	60	82	96	108
8		30	70	96	114	126
9		34	82	110	130	144
10		38	92	124	148	164
11		42	102	140	164	182
12		46	114	154	182	202
13		42	114	160	190	212
14		30	108	158	190	214
15			104	156	192	218
16			98	154	194	222
17			90	152	196	226
18			80	150	198	232
19			70	148	200	238
20			60	146	202	244
21				142	204	250
22				138	208	258
23				134	212	268
24				128	216	280
25					222	292
26					226	302
27					220	304
28					208	298
29						292
30						286
31						280
32						274

Sources of Focusing Aberrations

Focusing aberrations are sources of errors that occur when propagating rays do not truly converge to a single point in space called a focus. Although conceptually a point in space, the focus, physically, has a spatial extent. In UT, this focus is called the beam spot. The finite spot size has two causes: diffraction (as described in Equation 2.2) and aberrations. Aberrations are often analyzed by a ray theory that neglects diffraction. Aberrations are the consequence of rays intended to focus at one point actually arriving at different points following transmission through a system, resulting in focusing that is less than ideal. In optics, the design of an optical system is mainly concerned with the calculation of the various aberrations, and their suppression below a tolerable level [12]. Focusing aberrations can only be minimized or compensated for, but never completely eliminated.

When other significant aberrations are absent, the smallest possible spot size is limited by diffraction from the aperture creating the focus. Several criteria are used to define the smallest point size possible due to diffraction, such as 3 dB amplitude drops, 6 dB amplitude drops, and distance to diffraction pattern first minimum for a circular aperture. In this dissertation, the beam spot size (See Equation 2.2) is based on the far-field diffraction pattern of a planar piston transducer as defined by a 6 dB amplitude drop from the beam axis [13]. Larger apertures create smaller diffraction effects because they generate smaller spot sizes. Aberrations tend to get worse as aperture diameters increase as, in terms of geometrical optics, the appearance of the aberrations is associated with the occurrence of large angles of incidence and large angles of inclination between rays and the optical axis [14]. For these large angles, the small angle approximation, which is the central idea of focusing through an interface, begins to break down.

Focusing aberrations reduce the efficiency with which ultrasonic beams focus, leading to losses in inspection sensitivity. There are two classifications of focusing aberrations: chromatic and monochromatic. In UT, chromatic aberrations occur when a broadband ultrasonic beam disperses near a focal point due to the frequency dependent nature of sound speeds in an elastic medium. Having different refractive indexes, i.e., sound velocities, for different wavelengths of sound results in some frequencies traveling at a faster speed in an elastic medium than other frequencies. Dispersion of a broadband ultrasonic beam frequency may result in elongated spot sizes. Monochromatic aberrations refer to aberrations that occur without dispersion, i.e., at a single wavelength. In the language of optics, primary aberrations are called spherical, coma, astigmatism, field curvature, and distortion [14]. Additional monochromatic aberrations are piston, tilt and defocusing [15]. In the materials of interest in this dissertation, there is very little velocity dispersion and so the aberrations are primarily monochromatic.

There are several physical sources of focusing aberrations in the described ultrasonic phased array inspection of curved interface forging coupons using the designed transducer array with compensating mirrors. The ultrasonic beam is 1) transmitted by the transducer array, 2) travels through water to the cylindrically curved mirror, 3) reflects from the mirror, 4) travels through water to the curved forging interface, 5) refracts through the interface of the forging, 6) travels in the part, and 7) converges to a focal spot at a given depth in the forging material. For inspections of the planar interface forging coupons without a compensating mirror, beam travel segments (2) and (3) are eliminated. If a reflector exists at the focal spot, an ultrasonic beam response will travel a reverse path back to the transducer array where the beam is received as a reflector signal. Several sources of focusing aberrations exist along these beam path segments. In some cases, these aberrations may be minimized with the proper modification of delay times used to energize the transducer array. Known aberrations will be identified for the described beam path. The ability of each delay time generation method to minimize or otherwise reduce these known aberrations will be discussed for each method.

Following the described beam path, two known sources of aberrations exist due to the surface compensating, cylindrically focused mirror. When the ultrasonic beam reflects from the mirror, some

amount of defocusing aberration exists due to the mirrors not being ideally fabricated to precise design specifications, i.e., the mirrors could not physically be fabricated with zero tolerance to the requested radius of curvature. This aberration is assumed to have already been minimized through the use of high machining tolerances during mirror fabrication. Also, the mirrors were designed for optimal surface compensation at a focal depth of 2.50 inches in titanium alloy when used at a 3.50-inch water path distance. Defocusing again exists because the mirrors will be used in inspections of the curved forging coupons over a wide range of focal depths when using a 3.8-inch water path distance. This additional aberration source is not yet assumed to be minimized.

Sources of aberrations exist at the forging surface interface. The first source, common to all of the delay time generation methods is due to the level of machining tolerances used when finishing the coupon surfaces. Again, the machining tolerances are assumed to be sufficient so as to minimize this source of aberration from both the planar and curved interfaces of both forging coupon sets. Another aberration exists due to the conical shape of the curved interface coupons. The mirror is designed to compensate for cylindrical surfaces. Curved interfaces found in sonic-shaped forgings, with the exception of cylindrically shaped inner and outer forging diameters, are conically shaped. The mirrors were designed to compensate for the average radius of curvature of a conical forging surface. This aberration will be attempted to be minimized through cylindrical phasing of the array, to be discussed in the next chapter of this dissertation. A final source of aberration at the water/part interface occurs when refraction is not exactly calculated when determining delay time sets. This type of aberration is found in the initial delay time generation method due to the use of the small angle approximation previously described, and has been minimized in the other methods yet to be described in this dissertation by exactly calculating for refraction at the interface.

Other sources of aberrations are systematic to the phased array inspection system. Some amount of defocusing aberration may exist due to the shape of the transducer face being less than ideal. For example, slight fabrication errors may have occurred, resulting in a misshaping of the transducer face or variation in the layout of individual elements. The design criteria of the transducer array was crucial in minimizing this source of aberration. More reductions to defocusing aberrations occurred when refraction at the water/part interface was calculated exactly in some of the delay time generation methods presented in this dissertation.

Other systematic sources of aberrations in the inspection system include piston and tilt. While not true aberrations, as they do not model curvature in the wave front, piston and tilt influence focusing ability during inspections. Piston refers to the mean value of a wave front or phase profile across an aperture. Tilt refers to a deviation in the direction a wave propagates, quantifying the average slope of a wave front or phase profile across an aperture. Piston and tilt exist to some degree within the ultrasonic phased array forging inspection system as, respectively, transducer array delay time errors and misalignment of system components.

A source of aberration exists due to the arrangement of elements in the array. Specifically, the transducer face of the array may not be precisely manufactured to the requested design specifications. If some array elements are incorrectly located, particularly in a direction normal to the transducer face, then an aberration may exist as well as phase canceling of the ultrasonic beam due to other transducer elements. If a matching surface had been fabricated for the transducer face, then each element's elevation relative to all other elements in the array could have been experimentally measured [16]. As no matching surface for the designed transducer array was fabricated, these measurements were not performed. The phased array was assumed to be manufactured with sufficient tolerances so as to minimized aberrations, based on a transducer variability study performed on transducer arrays of the type used in this dissertation [17].

Summary

This chapter introduces the ultrasonic phased array inspection of forging material coupons, either in the form of planar or curved interface calibration specimens containing FBH ultrasonic signal reflectors. Immersion inspection setups were described, as well as the coupons being inspected. The use of surface compensating mirrors incorporated in the immersion inspection system to pre-distort an ultrasonic beam before propagation through the curved water-forging interface of forging coupons was introduced.

An initial two-dimensional delay time generation method was presented as the first of three delay time generation methods to be discussed in this dissertation. A unique feature of this first method involves calculating delay time sets only after converting metal path focal distances into corresponding distances in water, accomplished by application of the small angle approximation to Snell's law of refraction. A set of delay times or focal laws generated using this initial method for prior proof-of-concept experiments was presented and discussed

Potential sources of focusing aberration within the ultrasonic phased array inspection system when using the designed phased array transducer were identified along the path of the ultrasonic beam during inspections beneath planar interface forging coupons and beneath curved interface forging coupons when using surface compensating mirrors. One source of focusing error exists in the initial delay time generation method itself due to the use of the small angle approximation to account for refraction at the planar water-forging interface. The second of three delay time generation methods, presented in the next chapter as the refined 2D delay time generation method, will precisely account for refraction at the forging interface in an attempt to minimize this source of focusing error. Additional focusing aberration sources identified in this chapter could be minimized through the use of circumferential phasing of the transducer array, establishing the need for a 3D delay time generation method. This third delay time generation method, also presented in the next chapter, incorporates the geometry of reflecting from surface compensating mirrors and refracting through conically-curved water-forging interfaces in its ray-tracing algorithm.

CHAPTER 3. METHODS

Introduction

In previous chapters, an immersion UT forging inspection technique using a designed phased array transducer with and without surface compensating mirrors was described. This included an initial delay time generation method employing a simple ray-tracing algorithm to calculate time delay sets to electronically focus the beam launched by the transducer array at different depths. Sources of focusing aberrations were identified in the inspection system, one source due to the use of the small angle approximation in the initial delay time generation method. Other sources of focusing aberrations were also identified that were not addressed by that initial delay time generation method that had been developed in prior proof-of-concept experiments performed by the ETC-FAA team.

In this chapter, two additional delay time generation methods will be proposed in an attempt to reduce the previously described sources of focusing aberrations. In total, three ray-tracing algorithms for generation of delay time sets will be presented. These methods will be called the initial 2D, refined 2D, and 3D delay time generation methods. The first method, referred to as the initial 2D method and already described in Chapter 2 of this dissertation, will provide delay time sets for inspecting beneath planar interface forging coupons. This ray-tracing algorithm approximates the effect of refraction at the water-forging interface by using the small angle approximation, a source of focusing error to be minimized in the second ray-tracing algorithm by exactly calculating for refraction at the forging interface.

This second method, referred to as the refined 2D delay time generation method, contains a precise numerical calculation of refraction at the water-forging interface, thereby removing a source of focusing aberration found to the initial 2D method. This second method was developed to generate delay times for inspecting planar interface calibration blocks. The FBH response data acquired with these delay times will be compared to FBH data collected using delay times generated when using the initial 2D method. This comparison, presented in the next chapter of this dissertation, will provide experimental evidence as to whether or not using the small angle approximation in compensating for refraction at the water-forging interface leads to a significant focusing aberration effect. The delay time sets generated with the refined 2D method will also be used to inspect FBHs at similar depths within curved interface calibration blocks while using a surface compensating mirror.

The third ray-tracing algorithm presented is the 3D delay time generation method. This algorithm will generate delay times that vary around the circumference of a ring, i.e. produce circumferential phasing, in the segmented annular phased array transducer (See Figures D.4 through D.15 in Appendix D). As described in the previous chapter, several sources of focusing aberrations can be addressed though the use of circumferential phasing of the array, where different delay times can be used when phasing each element

of a segmented ring. The 3D method will attempt to minimize these sources of focusing errors, as it contains a precise numerical calculation of refraction at the water-forging interface, incorporates explicitly the use of a cylindrically curved surface compensating mirror, and accounts for the conically shaped water-forging interface of the curved interface forging coupons.

This chapter begins with a discussion of the determination of the additional input parameters required for the three methods. These include measurements of the longitudinal velocity of the curved interface forging coupons and determination of the apertures required for the transducer array to maintain an F/6 beam focus at a new water path distance, increased to accommodate the mirror holder being placed between transducer and curved interface forging specimens. This new water path distance, increased from 3.0 inches to 3.8 inches, was used for all forging inspections presented in the next chapter of this dissertation. This minimizes dissimilarity between inspections using the three delay time generation methods, i.e., all will be placed on an equal footing. After the presentation of these input parameters, delay time sets generated using the initial 2D delay time generation method at the increase water path distance will be presented, followed by detailed descriptions of both the refined 2D and 3D delay time generation methods.

General Input Parameters

The longitudinal sound velocity values for the curved interface calibration specimens were measured in a fashion similar to that described in Chapter 2 when measuring the longitudinal sound velocity in the planar interface calibration blocks. Velocity measurements of the 19 curved entry surface forging coupons containing #1/2 FBH reference reflectors (See Figure 2.4) were measured using a planar focus immersion transducer (10 MHz, 0.5-inch-diameter aperture, Panametrics Model V311, S/N 204899), energized in pulse-echo mode with a pulser-receiver unit (UTEX Model UT-340 set at 300 V, 10 ns and 30 dB). Time of flight (TOF) measurements was performed to determine the longitudinal sound velocity of each forging coupon. The maximum height of each curved forging coupon was precisely measured with a caliper. Unlike the planar interface forging coupon measurements, due the curved interface and tapered geometry of the curved interface forging coupons, only a single scan location at the maximum thickness of the coupon was used when performing this measurement. TOF differences between the first BW echo to the second BW echo, and also the first and third BW echoes, were again averaged to ensure accuracy of the measurement. The longitudinal sound velocity for each curved interface forging coupon was calculated by dividing twice the maximum coupon thickness by this average TOF. Again, material attenuation effects were ignored. Table 3.1 tabulates the measured maximum thickness, TOF, and longitudinal sound velocity calculated to 3 or 4 significant figures. Comparison of the longitudinal velocity values measured from the planar interface coupons (See Table 2.2) and those measured from the curved interface forging coupons (See Table 3.1) show a relatively small difference of 0.6% between blocks 2 through 13 for similar heights.

Table 3.1: Longitudinal sound velocity measurements of curved interface forging coupons.

Block #	Block Height (in.)	BW$_2$ – BW$_1$ (µs)	BW$_3$ – BW$_1$ (µs)	Time of Flight (µs)	Longitudinal Velocity (m/s)
1	0.345	2.82	5.65	2.82	6210
2	0.470	3.84	7.67	3.84	6220
3	0.720	5.89	11.75	5.88	6220
4	0.970	7.92	15.83	7.92	6220
5	1.170	9.57	19.11	9.56	6220
6	1.420	11.59	23.23	11.60	6217
7	1.620	13.25	26.57	13.27	6203
8	1.870	15.28	30.58	15.29	6215
9	2.070	16.95	33.90	16.95	6204
10	2.320	18.97	37.95	18.97	6212
11	2.520	20.60	41.22	20.61	6213
12	2.770	22.67	45.42	22.69	6202
13	2.970	24.29	48.62	24.30	6209
14	3.220	26.31	52.77	26.35	6208
15	3.420	27.97	56.09	28.01	6203
16	3.670	30.04	60.03	30.03	6209
17	3.870	31.67	63.30	31.66	6210
18	4.120	33.76	67.63	33.79	6195
19	4.320	35.43	70.75	35.40	6199

The water path distance was increased to 3.80-inches to allow for a direct FBH data comparison between ray-tracing algorithms. Aperture values when using the array at this increased water path distance with a F/6 beam focus are tabulated for coupons 2 through 13 in Tables 3.2 and 3.3 for both forging coupon sets. *F* and *r* refer to focal distance in water and aperture radius, respectively (See Equations 2.1 and 2.3). Given the use of a surface compensating mirror when inspecting through curved interfaces, curvature was ignored in Table 3.3 when calculating apertures. The longitudinal sound velocity in water was assumed to be 1487.4 *m/s*, based on a water bath temperature of 73.3°*F* [11]. The aperture for a given focal length, converted to rings using Table A.1, are similar enough that, given the discrete nature of the array rings and the precision of the metal path distance, the required inspection apertures are identical in both tables.

Table 3.2: Apertures for planar interface forging coupons at a 3.8-inch water path distance.

Block #	v_{block}/v_{water} (unitless)	Focal Length in Ti-alloy (inches)	F (inches)	r (inches)	r (mm)	Rings in Aperture
2	4.165	0.200	4.63	0.386	9.81	9
3	4.158	0.450	5.67	0.473	12.0	13
4	4.165	0.700	6.72	0.560	14.2	17
5	4.159	0.900	7.54	0.629	16.0	19
6	4.156	1.150	8.579	0.7150	18.16	22
7	4.156	1.350	9.411	0.7842	19.92	23
8	4.160	1.600	10.46	0.8713	22.13	25
9	4.154	1.800	11.28	0.9398	23.87	27
10	4.155	2.050	12.32	1.026	26.07	30
11	4.159	2.250	13.16	1.096	27.85	32
12	4.155	2.500	14.19	1.182	30.03	34
13	4.155	2.700	15.02	1.252	31.79	35

Table 3.3: Apertures for curved interface forging coupons at a 3.80-inch water path distance.

Block #	v_{block}/v_{water} (unitless)	Focal Length in Ti-alloy (inches)	H (inches)	r (inches)	r (mm)	Rings in Aperture
2	4.1765	0.200	4.64	0.386	9.81	9
3	4.1739	0.450	5.68	0.473	12.0	13
4	4.1778	0.700	6.73	0.560	14.2	17
5	4.1723	0.900	7.56	0.630	16.0	19
6	4.1735	1.150	8.600	0.7166	18.20	22
7	4.1638	1.350	9.421	0.7851	19.94	23
8	4.1720	1.600	10.48	0.8729	22.17	25
9	4.1645	1.800	11.30	0.9414	23.91	27
10	4.1699	2.050	12.35	1.029	26.14	30
11	4.1706	2.250	13.18	1.099	27.91	32
12	4.1631	2.500	14.21	1.184	30.07	34
13	4.1679	2.700	15.05	1.254	31.86	35

Initial 2D Ray-tracing Algorithm

The ray-tracing algorithm for the initial 2D delay time generation method was described in detail in Chapter 2. When employed using a 3.8-inch water path distance, the longitudinal sound velocity values of the planar interface calibration blocks tabulated in Table 2.1, and the aperture values tabulated in Table 3.2, the delay times presented in Table 3.4 are generated for planar interface calibration blocks 2 through 13. Figure 3.1 shows a plot of these delay times. The results of FBH data collected from each of the planar interface calibration blocks 2-13 when using this delay time sets will be presented in Chapter 4.
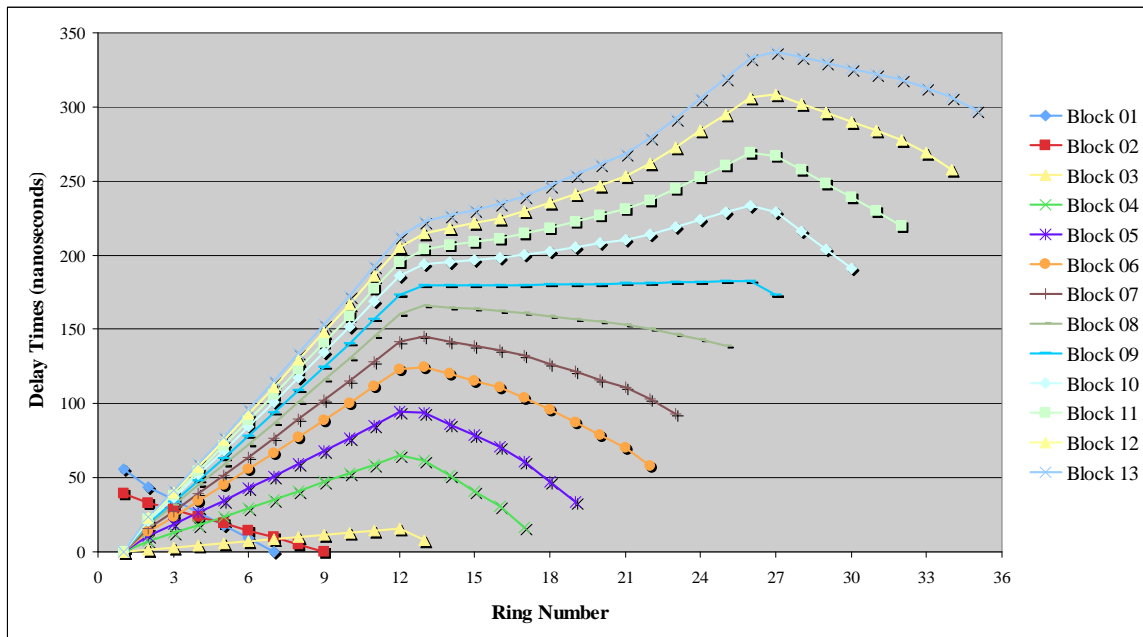
Figure 3.1: Delay times for focusing on FBHs in planar interface forging coupons at a 3.8-inch water path distance when using the initial 2D ray-tracing algorithm.

Table 3.4: Delay times for focusing on FBHs in planar interface forging coupons at a 3.8-inch water path distance when using the initial 2D ray-tracing algorithm.

Block \\ Ring	1	2	3	4	5	6	7	8	9	10	11	12	13
1	56	39	0	0	0	0	0	0	0	0	0	0	0
2	44	33	2	7	10	14	16	18	19	21	22	23	24
3	35	28	3	13	18	24	28	31	34	36	38	40	41
4	27	24	4	18	26	34	39	45	48	52	55	57	59
5	18	19	6	24	34	45	52	59	63	68	71	75	78
6	9	15	7	29	43	56	64	73	78	84	88	93	96
7	0	10	9	35	51	67	76	87	94	101	106	111	115
8		5	10	41	59	78	89	101	109	117	123	130	134
9		0	12	47	68	89	102	116	125	134	141	148	153
10			13	53	77	100	115	130	141	152	159	167	173
11			15	59	86	111	128	145	157	169	177	186	193
12			16	65	94	123	141	160	173	186	196	205	212
13			8	61	93	125	145	166	179	194	204	215	223
14				51	86	120	142	165	180	196	207	218	227
15				41	79	115	139	164	180	197	209	222	231
16				31	71	111	136	163	180	198	211	225	235
17				16	61	104	132	161	180	200	214	229	240
18					47	96	127	159	180	203	219	235	247
19					34	87	122	157	180	205	223	241	254
20						79	116	155	181	208	227	247	261
21						70	111	153	181	211	231	253	269
22						58	103	150	181	214	237	262	279
23							93	147	181	219	245	273	292
24								143	182	224	253	284	306
25								139	182	229	261	295	319
26									183	234	269	306	333
27									173	229	267	308	337
28										216	258	302	333
29										204	248	296	330
30										191	239	290	326
31											229	284	322
32											220	278	318
33												269	313
34												257	306
35													298

The set of delay times plotted in Figure 3.1 may be compared to delay times generated using this ray-tracing method for even-numbered planar interface forging coupons at a 3.00-inch water path distance (See Figure 2.12). Comparison between the two figures reveals similar delay time set curvatures associated with the compound spherical focus of the transducer array face while increasing water path distance led to a general increase in delay time values.

As shown in Figure 3.1 and Table 3.4, focusing on the FBH in block 3 requires the least amount of array phasing, a maximum of 16 nanoseconds for ring 12, when compared to the other delay time sets. This minimal amount of phasing is a result of the physical focus of the transducer array being nearly sufficient to focus the ultrasonic beam at 0.45 inches in titanium alloy at a water path distance of 3.80 inches.

Refined 2D Ray-tracing Algorithm

This delay time generation method is a refinement over the initial 2D delay time generation method in that it accounts for refraction at the water-forging interface for planar interface forging coupons without using the small angle approximation. Refraction is precisely calculated, through the numerical solution of a quartic equation, at the water-metal interface when employing Snell's Law of Refraction.

Several parameters are required as inputs in this ray-tracing algorithm. The water bath temperature in which the transducer and part would be immersed was assumed to be at a room temperature of $73.3°F$, resulting in a known longitudinal sound velocity in water of 1487.4 *m/s* [11]. The longitudinal velocity of sound for each set of forging coupons was also required (See Tables 2.2 and 3.1). A water path distance of 3.8 inches was selected. The F6 beam focus inspection requirement was maintained by using the apertures tabulated for focusing at the FBH depths of forging coupons 2 through 13 (See Tables 3.2 and 3.3).

In this ray-tracing algorithm, the transducer array face was assumed to be level with the planar part interface, i.e., at a constant TOF with the part interface for all segmented elements within each individual ring of the transducer array. Also, the desired focal spot in the forging material was taken to be the origin for the coordinate system used in this ray-tracing algorithm.

A schematic of the refined 2D delay time generation method is provided in Figure 3.2. The water path distance, *z*, from the center of the transducer array to the specimen's planar entry surface is shown in the schematic along with the focal depth in the material to be inspected, *f*, based on the FBH metal path distances in the forging coupon sets. The position of each ring relative to the focal spot coordinate origin, to be determined from the documented geometry of the transducer, is also shown.

To exactly take into account the refraction at the water-forging interface, the distance along the interface between where the beam focus centerline crosses the interface to the point at which the ray from a specific transducer ring refracts through the interface must be determined. In Figure 3.2, the distance between these two points is labeled *R*.

Consider two right triangles shown in Figure 3.2: a triangle having sides of lengths d, $x_0 - R$, and $y_0 - f$ above the interface and a triangle having sides of lengths a, f, and R located below the water-forging interface. When summed together after being converted to units of time, a and d will provide a delay time for a specific ring of the transducer array. Using Pythagorean's Theorem, the lengths a and d are shown to be functions of the unknown distance R (See Equations 3.1 and 3.2). Each triangle has a vertex angle labeled as either θ_0 or θ_1, and sine functions for both θ_0 or θ_1 can be determined in terms of defined parameters (See Equations 3.3 and 3.4, respectively).

Substitution of Equations 3.3 and 3.4 into Snell's Law of Refraction (See Equation 3.5) yields a 4th-order homogenous equation wherein R is the unknown value. The real and positive root of this quartic equation (See Equations 3.6 through 3.10) is determined numerically by resolving it into quadratic factors through the use of reverse interpolation [18].
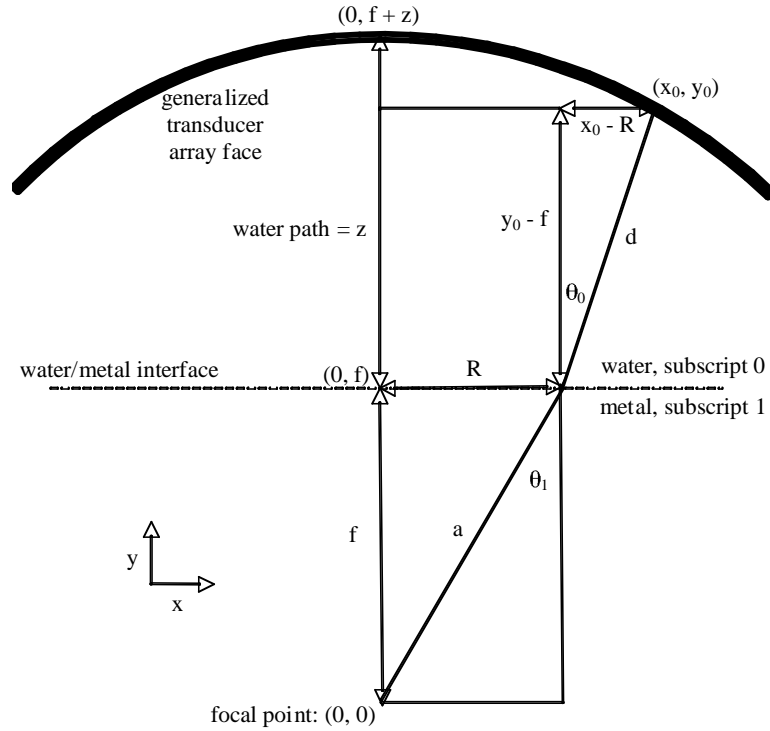
Figure 3.2: Schematic of the refined 2D ray-tracing algorithm.

$$a = \sqrt{f^2 + R^2} \tag{3.1}$$

$$d = \sqrt{(x_0 - R)^2 + (y_0 - f)^2} \tag{3.2}$$

$$\sin \theta_0 = \frac{x_0 - R}{d} = \frac{x_0 - R}{\sqrt{(x_0 - R)^2 + (y_0 - f)^2}} \tag{3.3}$$

$$\sin \theta_1 = \frac{R}{a} = \frac{R}{\sqrt{f^2 + R^2}} \tag{3.4}$$

$$\frac{\sin \theta_0}{v_0} = \frac{\sin \theta_1}{v_1} \tag{3.5}$$

$$R^4 + a_3 R^3 + a_2 R^2 + a_1 R + a_0 = 0 \tag{3.6}$$

$$a_3 = -2x_0 \tag{3.7}$$

$$a_2 = f^2 + x_0^2 + \frac{y_0^2 - 2fy_0}{1 - \left(\dfrac{v_1}{v_0}\right)^2} \tag{3.8}$$

$$a_1 = \frac{2x_0 f^2}{\left(\dfrac{v_0}{v_1}\right)^2 - 1} \tag{3.9}$$

$$a_0 = \frac{f^2 x_0^2}{1 - \left(\dfrac{v_0}{v_1}\right)^2} \qquad (3.10)$$

Once the distance R is obtained, substitution back into Equations (3.1) and (3.2) yields the distances a and d, respectively. Using the water and forging material longitudinal sound velocities, the distances a and d are then converted to TOF with units of time.

Summation and reference to the beam centerline TOF value results in the generation of the delay time required for a specific ring of the transducer array. This algorithm was repeated for each ring of the required aperture to generate a delay time set for focusing on a FBH located at a specific depth in a forging coupon, thereby providing sets of delay time for each planar interface forging coupon (See Table 3.5 and Figure 3.3). Using the measured longitudinal sound velocities of the curved interface forging coupons as input parameters, this algorithm also generated delay times for the curved interface forging coupons (See Table 3.6 and Figure 3.4) wherein a surface compensating mirror was assumed to be incorporated into the inspection. The results of FBH response data collected from each of the planar and curved interface forging coupons 2 through 13 will be presented in Chapter 4 of this dissertation.

The refined 2D ray-tracing algorithm was applied to both the planar and curved interface forging coupons, where the only difference between the values tabulated and plotted was due to the specific forging material longitudinal sound velocities used in the focal law calculations. Figure 3.5 shows a plot of the difference between the delay time values calculated for coupons from each set containing identical surface-to-FBH metal path distances. The sets of delay times are nearly identical. Recall that the delay time resolution for current phased array instrumentation is limited to 2 nanoseconds. Forging coupons with FBH depths shallower than 2 inches, e.g., blocks 1 through 9, do not exceed the 2 ns delay time resolution limit. In the delay time set differences for blocks 10 through 13 with FBH depths greater than 2 inches, only the outermost 4 rings, 4 rings, 2 rings, and 6 rings, respectively, of the apertures exceed the delay time resolution limit.

When gathering data using this algorithm to be presented in Chapter 4 of this dissertation, the same sets of delay times will be used for both planar and curved interface forging coupons as both sets of delay times are nearly identical within the resolution of the phased array instrumentation. The delay time sets for the planar interface forging coupons were selected as the delay times sets (See Table 3.4) to be used in acquisition of FBH inspection data when using the refined 2D delay time generation method.

A direct comparison of the delay time sets generated with the initial and refined 2D delay time generation methods may provide insight as to whether or not the approximation of refraction at the water-forging interface leads to a significant focusing aberration effect. Figure 3.6 plots the difference between delay time values calculated using the initial and refined 2D delay time generation methods.

The differences between delay time sets from the initial and refined 2D delay time generation methods plotted in Figure 3.6 show that exactly accounting for refraction at the water-metal interface should significantly reduce a source of focusing aberration. Beginning with the planar interface forging coupon block 2, the differences across the set of delay times for this forging coupon exceeds the minimum delay time resolution hardware limit of 2 nanoseconds. While the small time delay differences for coupons 2 through 4 are at the hardware resolution limit and might reasonably be considered negligible, the larger delay time differences for blocks 5 through 13 are in excess of 6 nanoseconds, indicating that a significant

Table 3.5: Delay times for focusing on FBHs in planar interface forging coupons at a 3.8-inch water path distance when using the refined 2D ray-tracing algorithm.

Ring \ Block	1	2	3	4	5	6	7	8	9	10	11	12	13
1	55	38	0	0	0	0	0	0	0	0	0	0	0
2	43	32	2	7	11	14	16	18	20	21	22	23	24
3	35	27	3	13	19	24	28	32	34	37	38	40	42
4	26	23	5	18	27	35	40	45	49	52	55	58	60
5	18	18	6	24	35	45	52	59	63	68	72	75	78
6	9	14	8	30	43	56	64	73	79	85	89	93	96
7	0	9	10	36	52	67	77	87	94	101	106	112	115
8		5	11	42	60	78	90	102	110	118	124	130	134
9		0	13	48	69	90	103	116	125	135	142	149	154
10			15	55	78	101	116	131	141	152	160	168	173
11			17	61	87	113	129	146	158	170	178	187	193
12			19	68	96	125	143	162	174	187	196	206	213
13			11	64	96	127	147	167	181	195	205	216	223
14				55	89	122	144	166	181	197	207	219	227
15				45	82	118	141	165	181	198	210	222	231
16				35	75	113	139	164	181	200	212	226	235
17				22	65	107	135	163	182	202	216	231	241
18					52	100	130	162	182	205	220	237	248
19					40	92	126	160	183	208	225	243	256
20						84	121	159	184	211	229	249	263
21						77	116	158	184	214	234	255	271
22						66	110	156	186	218	240	264	281
23							102	153	187	224	249	276	295
24								151	189	230	258	288	309
25								149	191	236	267	300	324
26									193	242	276	312	338
27									186	239	276	315	343
28										228	268	310	340
29										217	260	305	338
30										206	252	300	335
31											244	296	332
32											236	291	330
33												284	327
34												276	322
35													318

focusing error has been identified. Exactly calculating for refraction at the water-forging interface in the refined 2D ray-tracing algorithm should significantly reduce a focusing aberration. FBH signal response data acquired using these two delay time sets, to be presented and compared in the following chapter, will provide experimental evidence as to whether or not a significant focusing aberration has been reduced.

Table 3.6: Delay times for focusing on FBHs in curved interface forging coupons at a 3.8-inch water path distance when using the refined 2D ray-tracing algorithm.

| Block Ring	1	2	3	4	5	6	7	8	9	10	11	12	13
1	55	37	0	0	0	0	0	0	0	0	0	0	0
2	44	31	2	7	11	14	16	18	20	21	22	23	24
3	35	27	3	13	19	24	28	32	34	37	39	40	42
4	26	22	5	19	27	35	40	45	49	52	55	58	60
5	18	18	7	24	35	46	52	59	64	69	72	75	78
6	9	14	8	30	43	56	65	73	79	85	89	93	97
7	0	9	10	36	52	68	77	88	94	101	106	112	115
8		5	12	42	61	79	90	102	110	118	124	130	135
9		0	14	49	70	90	103	117	126	135	142	149	154
10			16	55	79	102	116	132	142	153	160	168	174
11			18	62	88	113	130	147	158	170	178	187	193
12			20	68	97	125	143	162	174	188	197	206	213
13			12	65	96	127	147	168	181	196	206	216	224
14				55	89	123	144	167	181	197	208	219	228
15				46	82	119	142	166	182	199	210	223	232
16				36	75	114	139	165	182	200	213	226	236
17				22	66	108	135	164	182	203	216	231	242
18					53	101	131	163	183	206	221	237	249
19					41	93	126	161	184	209	225	243	256
20						86	122	160	185	212	230	250	264
21						78	117	159	185	215	235	256	271
22						68	111	157	187	219	241	265	282
23							103	155	188	225	250	277	296
24								153	190	231	259	289	311
25								151	192	237	268	301	325
26									195	244	278	313	340
27									187	241	277	316	345
28										230	269	311	342
29										219	262	307	340
30										209	254	302	337
31											246	297	335
32											239	293	332
33												287	329
34												278	325
35													321
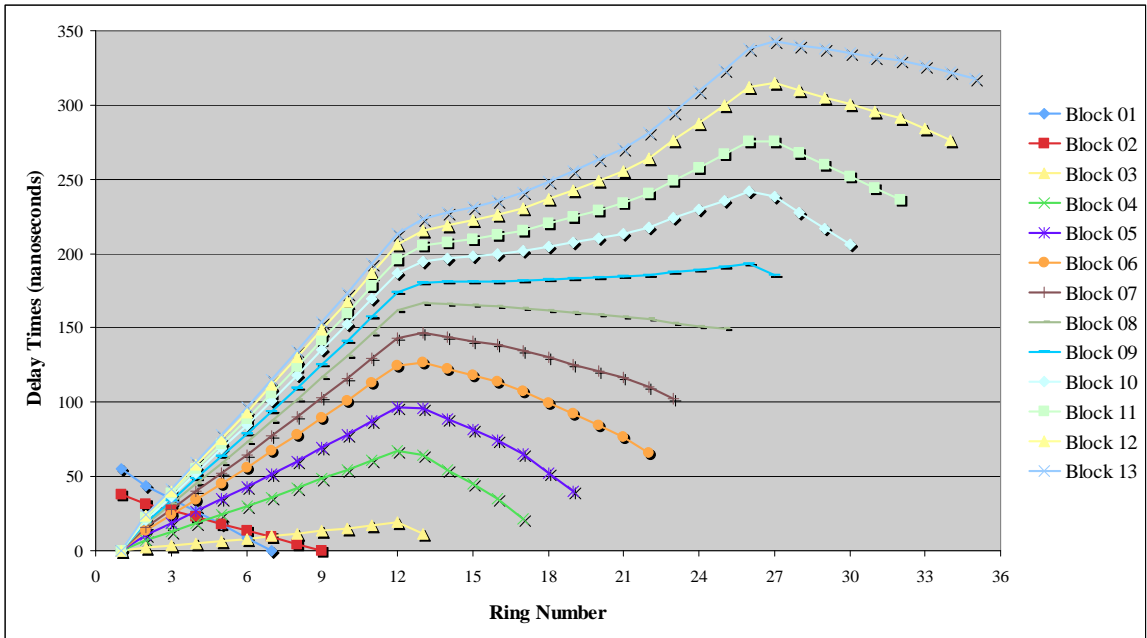
Figure 3.3: Delay times for focusing on FBHs in planar interface forging coupons at a 3.8-inch water path distance when using the refined 2D ray-tracing algorithm.
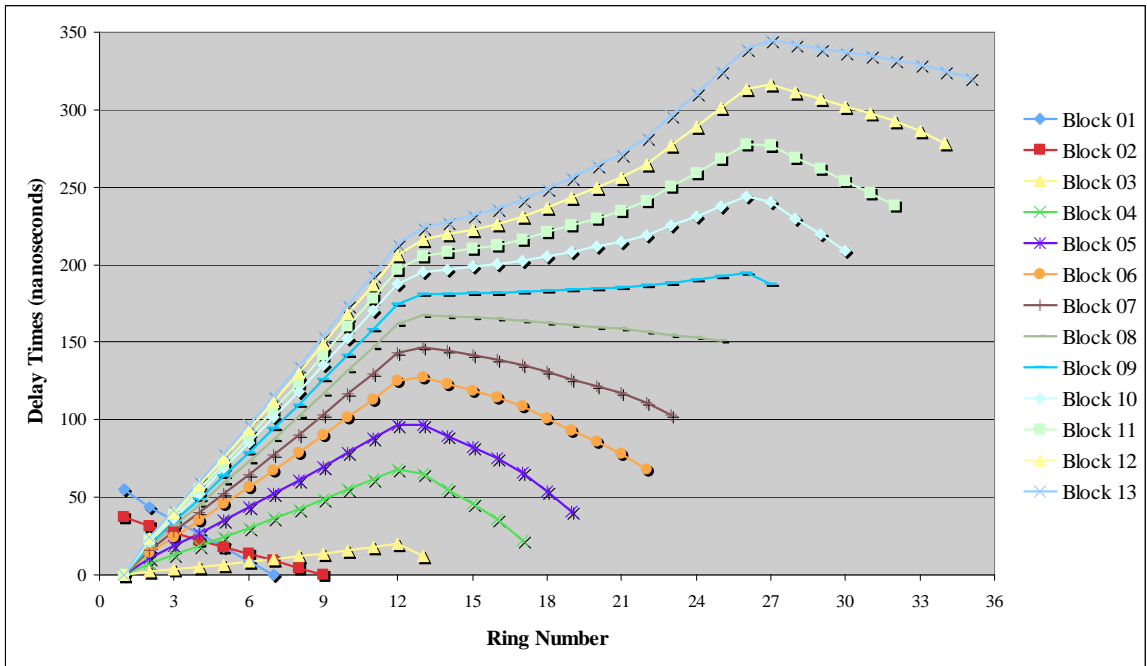
Figure 3.4: Delay times for focusing on FBHs in curved interface forging coupons at a 3.8-inch water path distance when using the refined 2D ray-tracing algorithm.
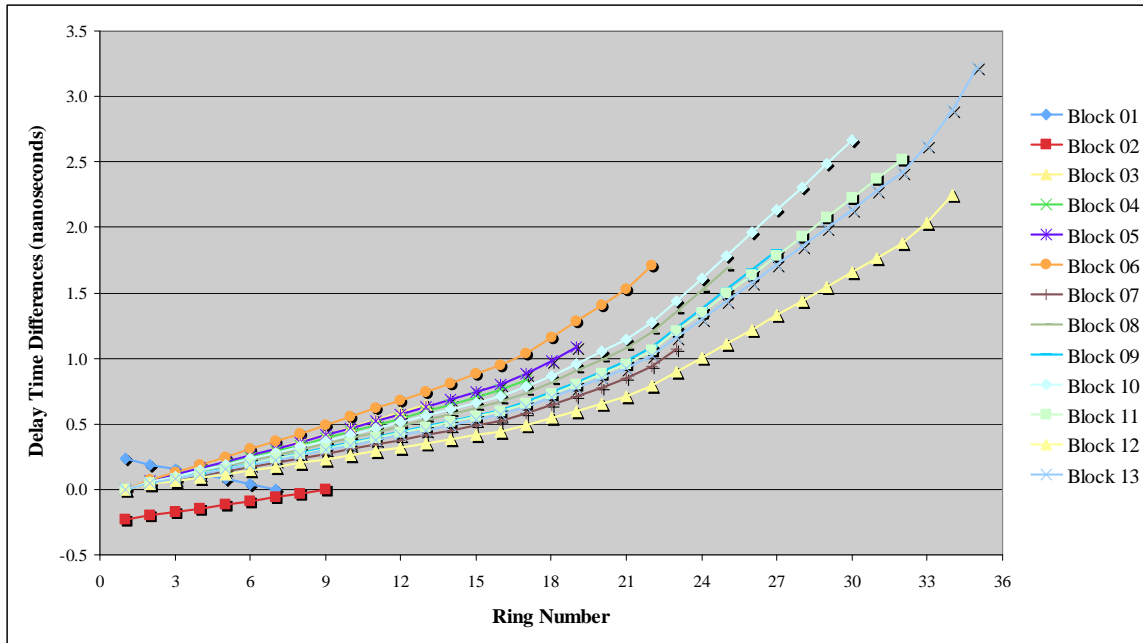
Figure 3.5: Differences between delay time sets from the refined 2D ray-tracing algorithm when focusing on FBHs at similar depths in both the planar and curved interface forging coupons.
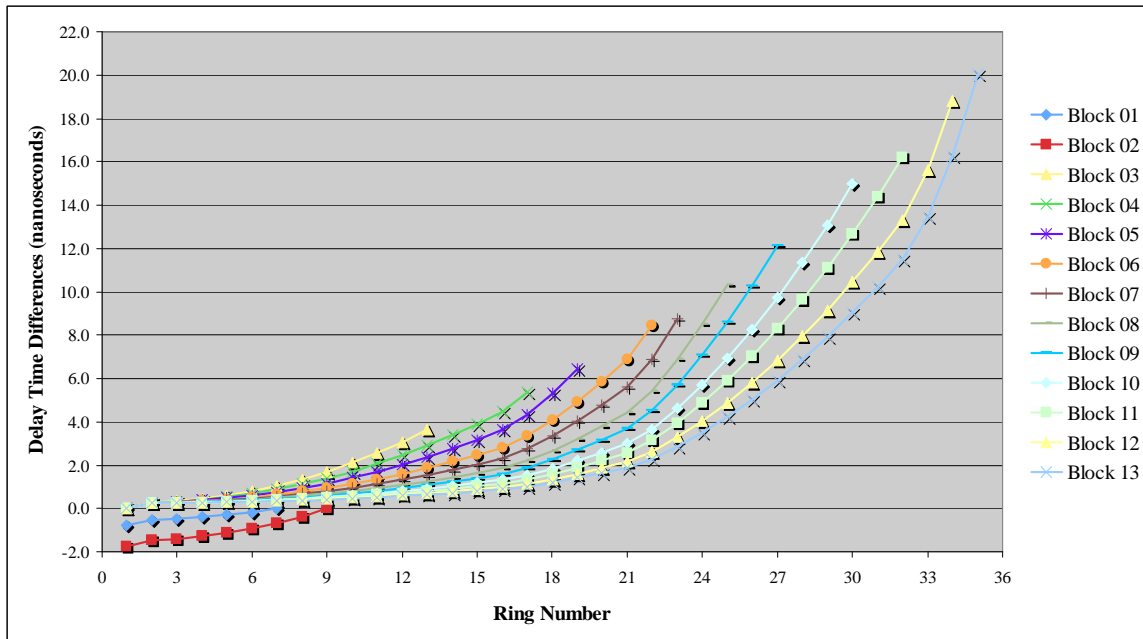
Figure 3.6: Differences between delay time sets when focusing on FBHs in the planar interface forging coupons when using the initial and refined 2D ray-tracing algorithms.

3D Ray-tracing Algorithm

The 3D ray-tracing algorithm for generating delay times, as with the refined 2D delay time generation method, will precisely account for refraction at the water-forging interface. However, this final method additionally incorporates both the curvature of the forging surface as well as the ultrasonic beam reflection from a surface compensating mirror. Although some simplifications will occur in the ray-tracing due to symmetry and the relative orientation of the cylindrically shaped mirror and the conically shaped forging surfaces, this ray-tracing algorithm performs 3-dimensional (3D) calculations. This distinguishes it from both of the previously described 2D ray-tracing algorithms, leading to the generation of delay times sets which will vary around the circumference of an array ring, i.e. producing circumferential phasing, in the segmented annular transducer array.

In the following chapter, inspection data of FBH responses in curved entry forging coupons when using mirrors and circumferential phasing provided by the 3D delay time generation method will be presented. This inspection data will be compared to FBH responses when using the refined 2D generation method to inspect both planar and curved interface forging coupon without and with mirrors, respectively, when not using circumferential phasing.

What follows is an outline of the ray-tracing algorithm used to calculate circumferential phasing of the array as applied to inspections of curved entry forging coupons.

Ray-tracing connects the desired point of focus in the forging material to points on the face of the transducer. Using the transit time from the point of focus at the FBH to the center of the transducer array as a reference value, a 3-D spatial surface is formed by points on all rays from the focal point having the same travel time as this centerline reference. During ray-tracing, a cylindrical mirror is introduced between the array face and the entry surface. The result of tracing rays from the focal point, refracting through the curved forging-water interface, reflecting off the cylindrical mirror, and terminating at an overall transit time provided by the reference centerline will result in a Fermat surface somewhat similar to the shape of the transducer face (See Figure 3.7). The difference between this Fermat surface and the known shape of the transducer face will result in the specific delay times required for circumferential phasing.

The Fermat surfaces generated using this ray-tracing algorithm were the basis for phase diagrams, which in turn produced the delay time sets necessary to circumferentially phase and focus the transducer array. Fermat surfaces will be presented graphically as phase diagrams, i.e., a set of delays times for each transducer element in the transducer array, from which circumferential phasing of the array is determined.

Figure 3.8 depicts the relative orientations of the designed transducer array, the cylindrically shaped mirror, and the conically shaped forging surface beneath which is a #1/2 FBH at a known metal path distance. As with all the presented delay time generators, the overall water path distance from the center of the transducer array along the centerline of the ultrasonic beam to the forging material interface has been selected to be 3.80 inches. The forging material specimens, each containing a FBH at a known
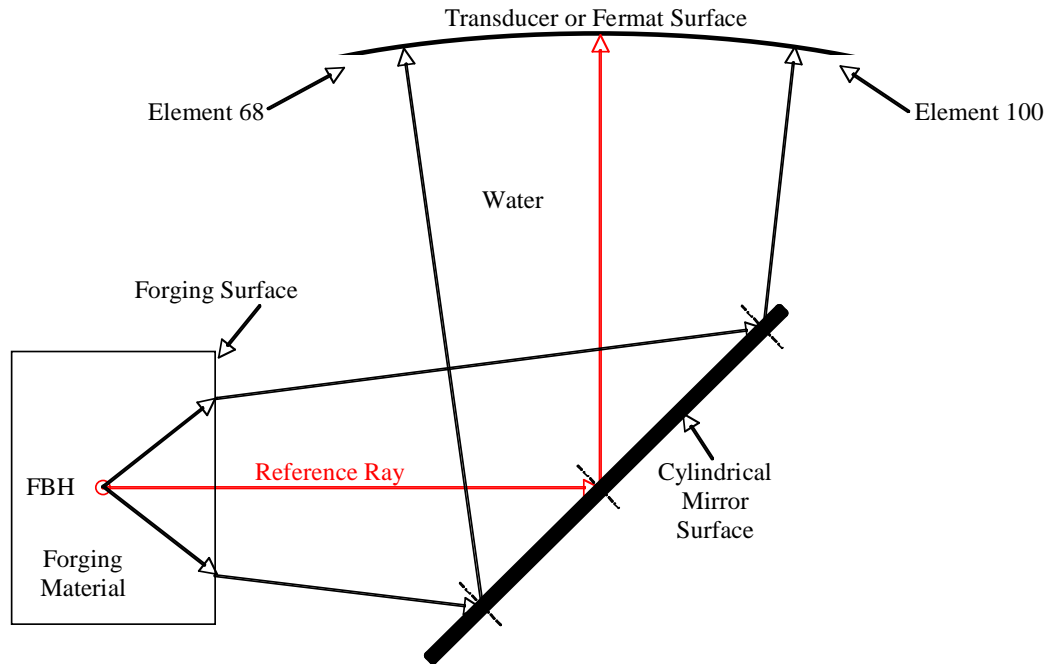
Figure 3.7: Configuration of the FBH and forging, mirror, transducer and Fermat surfaces including centerline reference ray for the 3D ray-tracing algorithm.

depth, are the previously referenced curved interface forging coupons. A cylindrical mirror with a 27.0-inch concave radius of curvature was used in these forging inspections.

A ray-tracing algorithm to determine a 3D Fermat surface for each FBH target depth will require input parameters such as transducer-to-mirror and mirror-to-surface water path lengths, depth of target focus, designed focus of cylindrical mirror, transducer array aperture based on depth of focus, and entry surface curvature. The transducer-to-mirror water path distance, d, was calculated to be 1.777 inches based on the measured distances shown in Figure 3.8. Given the selected total water path distance of 3.80 inches, the beam centerline mirror-to-surface distance in water, *water path - d* in Figure 3.8, becomes 2.023 inches.

With all necessary material and geometrical parameters determined or otherwise known, the delay time generation method using the 3D ray-tracing algorithm is described as follows:

1. Calculate the TOF reference value for the beam centerline using the curved interface calibration block values for FBH depth and forging-to-transducer water path distance.

2. Generate grid points on a portion of the forging surface sufficient to cover the area of the ultrasonic beam footprint, calculate lines normal to the forging surface at each grid point, and calculate lines from each forging surface grid point to the FBH location. Then, using these grid points and the lines passing through them, determine the direction of a ray from the FBH through each forging surface grid point after it refracts through the forging surface. (See Appendix B for details on these calculations.)

3. Calculate the refracted ray intersection point on the cylindrical mirror surface, then calculate the surface normal at this mirror intersection point using an exact method for determining the intersection point and surface normal of a ray with a cylindrical face [19].

4. Terminate each ray reflected from the mirror towards the transducer face at the TOF reference value for the beam centerline already calculated and record these Fermat surface coordinates. (See Appendix C for details on these calculations.)

5. Extract individual element delay times from the recorded Fermat surface data points. (See Appendix D for details on these calculations.)

The 3D ray-tracing algorithm was employed using the referenced parameters for FBHs in curved interface calibration specimens 2 through 13. Delay times were determined over half the circumference of each ring, from 0 to 180 degrees, as the left and right sides of the transducer face, the mirror surface, and the forging interface are symmetrical in shape. Sets of delay times over this half circumference, in 5 degree increments, are plotted in Figures 3.9 and 3.10 for even- and odd-numbered forging coupons, respectively.
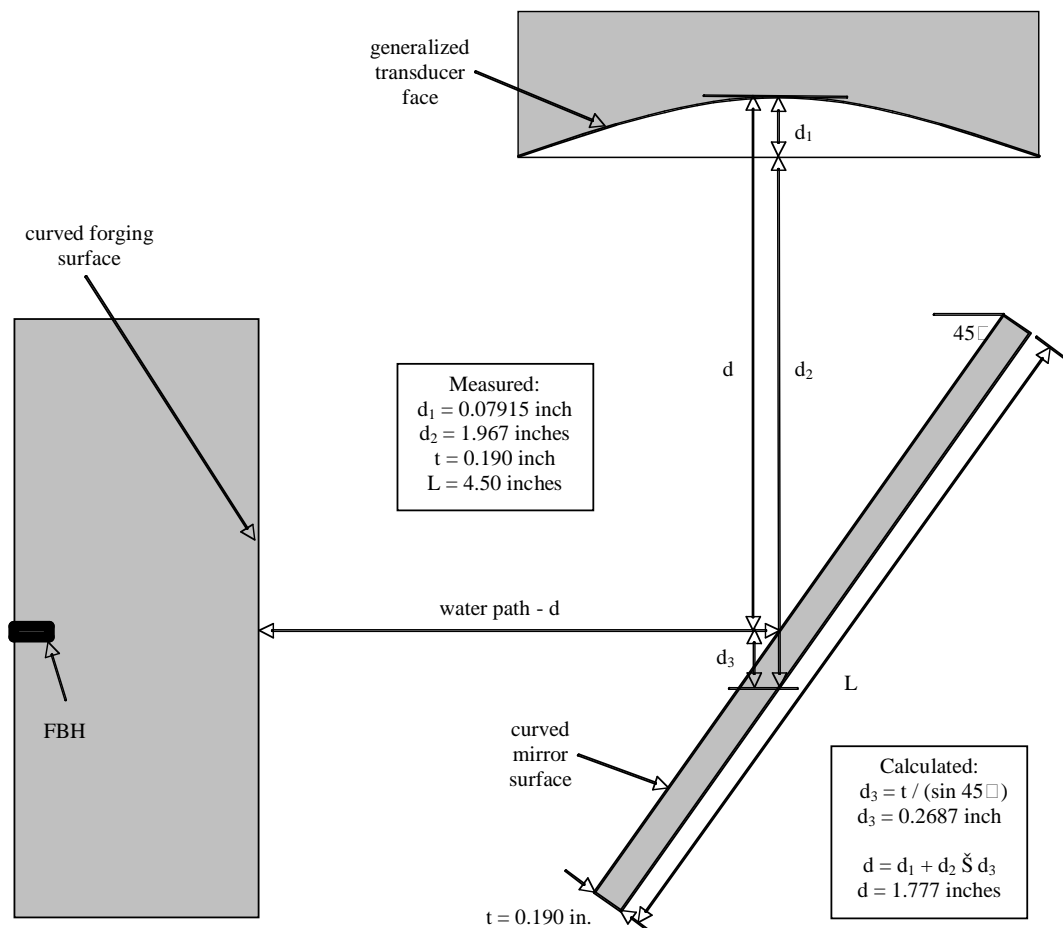
Figure 3.8: Schematic of array, mirror, and forging surface for the 3D ray-tracing algorithm.
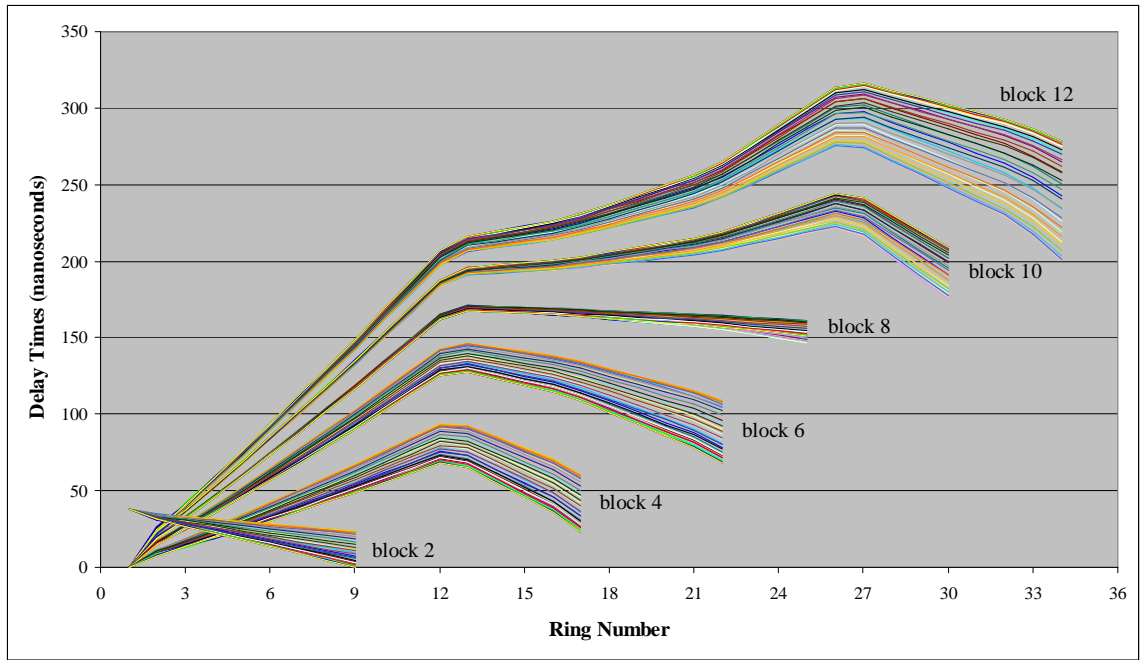
Figure 3.9: Circumferential delay times when focusing on FBHs in even-numbered curved interface forging coupons at a 3.8-inch water path distance when using the 3D ray-tracing algorithm.
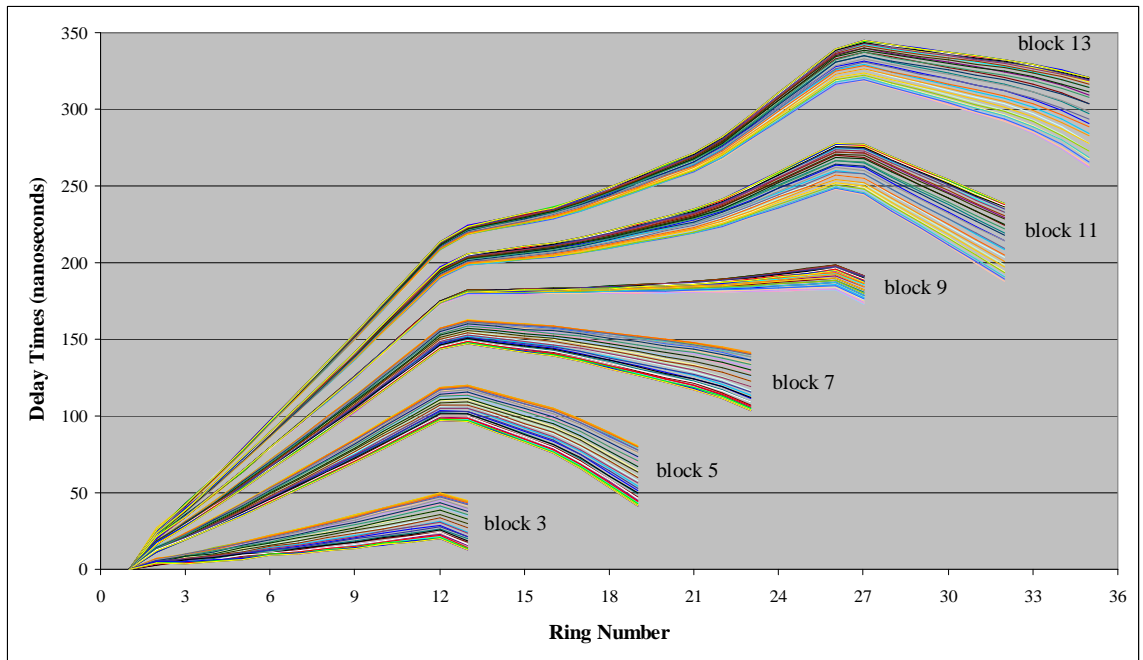
Figure 3.10: Circumferential delay times when focusing on FBHs in odd-numbered curved interface forging coupons at a 3.8-inch water path distance when using the 3D ray-tracing algorithm.

Figure 3.11 shows the circumferential delay times, averaged over each element of a specific ring whether or not that ring is segmented, as applied during an inspection. As described in Appendix A, rings 1-16 require one delay time per ring as each ring is a single element while segmented rings 17-21 require

two delay times per ring, rings 22-32 require four delay times per ring, rings 33 and 34 require eight delay times per ring, and rings 35-36 require twelve delay times per ring. Due to the aforementioned symmetry considerations, some of the delay times for elements of segmented rings 17-36 are identical. As a result of symmetry, rings 17-21 may use a maximum of two non-identical delay times per ring, rings 22-32 up to three non-identical delay times per ring, rings 33-34 up to five non-identical delay times per ring, and rings 35-36 up to seven non-identical delay times per ring. In effect, these delay times per ring is the upper limit on the amount of circumferential phasing that can be applied in this particular inspection technique.

In the following chapter, FBH signal response data acquired from the curved interface forging coupons when using delay time sets generated using the 3D ray-tracing algorithm will be presented and compared to FBH signal response data acquired from the curved interface calibration specimens when using time delay sets generated using the refined 2D ray-tracing algorithm. To reduce systematic errors, care was taken during data collection to minimize changes in the inspection setup. Specifically, scans were performed of the FBH in a forging coupon first with delay times from refined 2D method, immediately followed by data collection from the same FBH when using delay times from the 3D method, without making any other changes to the inspection setup. This acquired data will provide empirical evidence as to whether or not a significant focusing aberration has been reduced through the use of circumferential phasing of the transducer array. In addition, the 3D ray-tracing algorithm should be considered successful if the results presented in the next chapter show responses from the curved interface calibration specimens
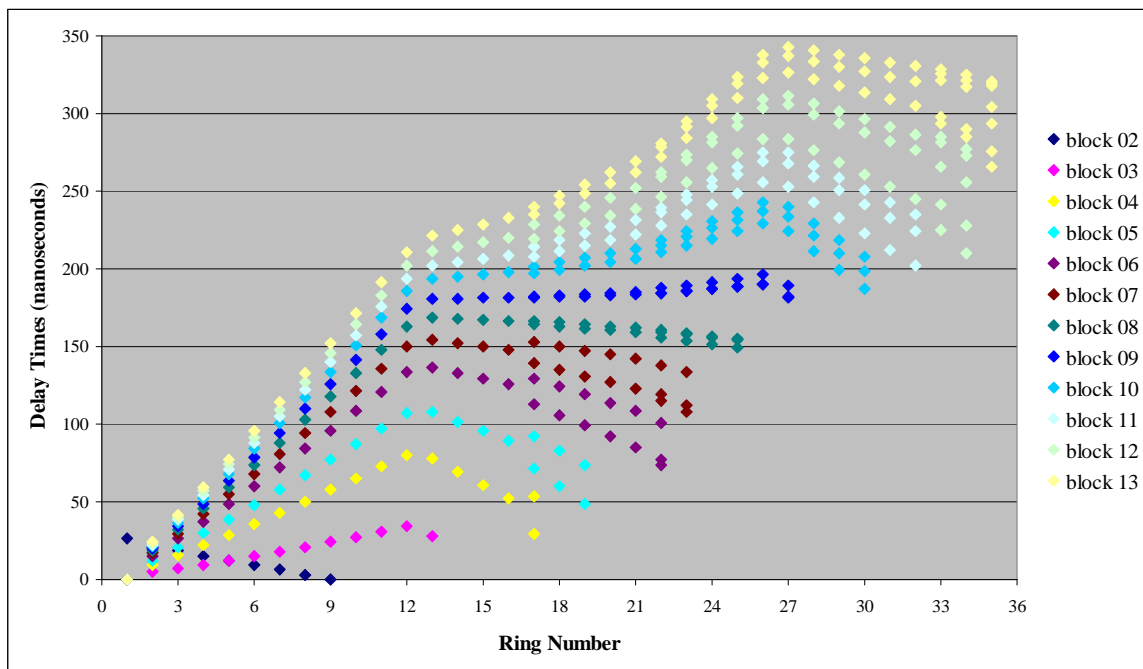
Figure 3.11: Circumferential delay times averaged over each element, to be applied during inspections, when focusing on FBHs in the curved interface forging coupons at a 3.8-inch water path distance when using the 3D ray-tracing algorithm.

when using compensating mirrors and circumferential phasing which approach the FBH signal responses from planar entry surface coupons when using neither compensating mirrors nor circumferential phasing, However, some signal loss is expected to occur due to partial transmission into, rather than complete reflection of the ultrasonic beam from, the surface compensating mirror .

Summary

In this chapter, three ray-tracing algorithms for delay time generation, of increasing sophistication for addressing anticipated focusing aberrations, were presented. These algorithms are referred to as the initial 2D, refined 2D, and 3D ray-tracing algorithms or delay time generation methods. The simplest ray-tracing algorithm, the initial 2D method, has several possible sources of focusing aberrations including use of the small angle approximation when accounting for refraction at the water-forging planar interface. The refined 2D method improves upon the initial 2D method by numerically accounting for refraction at the water-metal interface during inspection through planar interface forging coupons. Differences between sets of delay times generated using both of these methods were presented, and showed that a significant difference existed in terms of instrumentation limits for delay time resolutions.

Both the initial and refined 2D ray-tracing algorithms will provide delay time sets for inspection of FBHs in planar interface forging coupons. However, these same sets of delay times could also be used to inspect FBHs in curved interface forging coupons when surface compensating mirrors are employed. It was assumed that inspection data collected using delay time sets generated using the refined 2D method would be "better" than, or equivalent to, inspection data collected using delay time sets generated using the initial 2D methods. Hence, only delay time sets from the refined 2D method would be used when inspecting the curved interface forging coupons with surface compensating mirrors. This data will be compared to similar forging inspections performed on the curved interface forging coupons with the surface compensating mirror when using delay time sets generated using the 3D method, a method employing circumferential phasing of the transducer array, in an attempt to reduce additional focusing aberrations expected to exist in inspections employing the refined 2D method.

In the next chapter, inspection data will be presented for FBHs in planar interface forging coupons when using delay time sets generated using the initial 2D and refined 2D methods. Comparison of data collected with each of these methods will provide empirical evidence as to whether or not a more precise accounting of refraction at the water-metal interface significantly reduces focusing aberrations. Also, data will be presented on FBHs signal responses in curved interface forging coupons when using delay time sets provided using the refined 2D and 3D ray-tracing algorithms. Comparison of inspection data collected from FBHs in the curved interface calibration specimens will empirically determine whether or not the 3D ray-tracing algorithm significantly reduces focusing aberrations when compared to the refined 2D ray-tracing algorithms.

CHAPTER 4. RESULTS

Introduction

In the previous chapter of this dissertation, a description of three ray-tracing algorithms was presented along with delay time sets generated by each method for the phased array ultrasonic inspection of forging coupons containing FBH reference reflectors. These three algorithms were referred to as the initial 2D, refined 2D, and 3D methods. The initial 2D method employs an approximate small angle calculation of refraction at the water-forging interface of forging coupons while the refined 2D method attempts to improve upon this refraction calculation by exactly accounting for refraction at the interface. The 3D method also exactly accounts for refraction at the water-forging interface and, in addition, incorporates the geometry of a cylindrically shaped ultrasonic mirror designed to compensate for the conical surface of forging interfaces. Sets of delay times are generated that vary phasing circumferentially over segmented rings of the transducer array.

Time delay sets generated by both the initial and refined 2D ray-tracing algorithms were used to phase the transducer array during the acquisition of FBH response waveform data from planar interface forging coupons 2 through 13 at a 3.8-inch water path distance. The results of this data collection will be presented later in this chapter. Also to be presented are the FBH responses from curved interface forging coupons 2 through 13, inspected at a 3.8-inch water path distance when phasing the transducer array with time delays sets generated with both the refined 2D and 3D ray-tracing algorithms.

Before presentation of the results of these phased array inspections, the hardware limitations when applying delay time sets to phased array instrumentation will be discussed. During an inspection, the delay time sets generated by the ray-tracing algorithms at the required apertures may exceed the hardware limits of the phased array instrumentation. As an example, a generated delay time set may require 35 unique delay time values to phase the array, yet the available phased array hardware is limited to a total of 32 delay times with the additional restriction, as will be discussed shortly, that only a single delay time may be assigned to each electronic channel. Whether this phased array instrumentation limit is exceeded depends on the total number of delay times required for the inspection and, also, the specific array elements to be energized and phased. If the hardware limitation is exceeded within a focal law, several focal laws, each of which may not exceed the hardware limit, will be required to apply the complete delay time set in an inspection. Each focal law results in a single A-scan waveform at each scan location during the inspection. An effective grouping of delay times was developed to minimize the number of focal laws acquired when the hardware limitation is exceeded. A post-processing procedure was developed to sum the required waveforms at each scan location to form a single waveform. C-scan images of the complete scan area were then created using these summed waveforms.

C-scan images from each set of inspection data, captured over the course of an inspection scan, will be presented in this chapter as grayscale bitmap images plotted as a function of scan coordinates. An analysis of these C-scan images will include inspection gain settings, peak amplitude responses, beam width measurements, and signal-to-noise ratio (SNR) values. Each C-scan image presented has a peak 0.8 V or 80% Full-Screen-Height (%FSH) signal amplitude response on a scale with a maximum possible value of 1.0 V or 100%FSH. A gain setting was recorded for each of the C-scan images that resulted in this 80%FSH peak signal. In ultrasonic inspections, pressure waves received by transducers are converted to voltage signals, V_{in}, and output by the measurement system as an amplified voltage, V_{out}, after being subjected to an inspection gain setting, β, in units of decibels (dB) (See Equation 4.1) [20].

$$\text{Gain (in dB)} = \beta = \left(20dB\right)\log\left(\frac{V_{out}}{V_{in}}\right) \tag{4.1}$$

In ultrasonic inspections it is useful to compare a set of peak signal amplitude responses at a common gain setting. Equation 4.1 can be used to convert common peak amplitudes, V_{common}, achieved using recorded gains, $\beta_{recorded}$, to a set of peak amplitudes, V_{new}, which would have been produced at an arbitrarily chosen, common gain setting, β_{common} (See Equation 4.2).

$$V_{new} = V_{common}10^{\frac{\beta_{common} - \beta_{recorded}}{20dB}} \tag{4.2}$$

The width of the ultrasonic beam, as measured from C-scan images to be presented later in this chapter, will also form part of the evaluation of the ray-tracing methods presented in this dissertation. The beam width is a measurement of the focal spot size in the plane of the flaw being inspected. To allow for a direct comparison to the predicted 6-dB amplitude drop focal spot size presented in Equation 2.2, the focal spot size from the C-scan images will be measured along both the vertical and horizontal lines through the peak signal to a coordinate point in the C-scan where the amplitude is one-half of the peak amplitude. Since not all beam spots are symmetrically shaped in the C-scan images to be presented, both of the vertical and horizontal beam widths measurements will be individually presented.

The analysis of the C-scan images will conclude with SNR values to determine the inspection sensitivity of the FBH scans performed. SNR values will be calculated by measuring the peak amplitude in each C-scan images, i.e., 80%FSH, and dividing it by a noise amplitude averaged over ~400 pixels for each image (See Equation 4.3).

$$\text{Signal - to - Noise Ratio} = SNR = \frac{\text{Peak Signal Amplitude Response}}{\text{Average Noise Amplitude Response}} \tag{4.3}$$

Hardware Limitations of Delay Times

The phased array instrumentation used significant hardware limitations with regards to the application of delay time sets and the subsequent real-time summation of the responses from individual transducer array elements. The ultrasonic phased array instrumentation available for use in data collection performed for this dissertation was limited to a total of 32 delay times per focal law and a maximum of 128 transducers. A secondary limitation, to be described shortly, involves the specific method by which these 32 delay times are applied over 128 phased array transducer elements.

Each focal law generates a single A-scan waveform. The size of the beam aperture, i.e., the number of transducer array elements energized, is proportional to the number of delay time sets required for an inspection. The aperture is determined by maintaining a F6 beam focus at the FBH depth being inspected. As the aperture increases with increasing focal depth, the phased array instrumentation hardware limit of 32 delay times may be exceeded. If exceeded, the inspection must be performed with multiple focal laws wherein each focal itself does not exceed the hardware limitation. The hardware limit is especially likely to be exceeded if circumferential phasing is being employed, due to multiple delay times per segmented ring leading to a greater overall number of delay times within a set when compared to the initial and refined 2D methods. If multiple focal laws are required during data collection, the A-scan waveforms collected at each scan location by each focal law must be combined together in post-processing, rather than in real-time by the phased array instrumentation during an inspection, to provide a single waveform at each scan location before the results of the inspection can be presented as a single C-scan image.

The planar interface forging coupons were inspected using the initial and refined 2D methods, while the curved interface forging coupons were inspected using the refined 2D and 3D methods. Examination of the sets of delay times required for inspections of planar interface forging coupons 2 through 11 indicated that the hardware limit was not exceeded when using the initial and refined 2D methods. The limit was not exceeded for curved interface forging coupons 2 through 11 when using the refined 2D method. However, the hardware limits were exceeded when inspecting planar interface forging coupons 12 and 13 when using the initial and refined 2D methods, as well as when inspecting curved interface forging coupons 12 and 13 when using the refined 2D method. When inspecting forging coupons 12 and 13 from either set of forging coupons using either the initial or refined 2D method, 34 and 35 delay times, respectively, were required.

When performing inspections of the planar and curved interface forging coupons when using the initial and refined 2D delay time generation methods, only one delay time is applied to each ring of the transducer array. Tables 3.2 and 3.3 list the apertures required for the planar and curved interface forging coupons, respectively. Consideration of both hardware limitations results in the requirement of only one focal law during inspections of blocks 2 through 11 from both sets when using delay times from the initial and refined 2D methods. Blocks 12 and 13, however, require four focal laws during their inspections.

The secondary instrumentation hardware limitation influences the grouping of delay times when energizing and phasing transducer elements. In the available 32/128 model phased array instrument, 32

pulsers may phase transducer array elements at any given time over a total of 128 electronic channels. The available phased array instrumentation applies the 32 pulsers over 128 electronic channels by subdividing the 128 channels into four groups, where each group is allotted 32 delay times. Furthermore, these four groups of 32 electronic channels have, for each subgroup, the same delay time applied to the first channel of each subgroup. Similarly, the second channel of each subgroup must also have the same delay time. This trend continues for each proceeding channel in each subgroup, up to channel 32. For example, each of the channels 1, 33, 65, and 97 must have the same delay time applied to that channel. Similarly, elements hardwired to channels 2, 34, 66, and 98 must have identical delay times in a focal law. This secondary hardware limitation continues through to the final set of channels, i.e., 32, 64, 96, and 128 (See Table 4.1).

When performing inspections of the curved interface forging coupons when using the 3D method, blocks 2 through 4 require only a single focal law. While block 4 does require an aperture of 17 rings and ring 17 is segmented into two elements, both elements of ring 17 happen to have the same delay time and,

Table 4.1: Grouping 128 transducer elements to 32 delay time generators.

Delay Line	Group 1	Group 2	Group 3	Group 4
1	1	33	65	97
2	2	34	66	98
3	3	35	67	99
4	4	36	68	100
5	5	37	69	101
6	6	38	70	102
7	7	39	71	103
8	8	40	72	104
9	9	41	73	105
10	10	42	74	106
11	11	43	75	107
12	12	44	76	108
13	13	45	77	109
14	14	46	78	110
15	15	47	79	111
16	16	48	80	112
17	17	49	81	113
18	18	50	82	114
19	19	51	83	115
20	20	52	84	116
21	21	53	85	117
22	22	54	86	118
23	23	55	87	119
24	24	56	88	120
25	25	57	89	121
26	26	58	90	122
27	27	59	91	123
28	28	60	92	124
29	29	61	93	125
30	30	62	94	126
31	31	63	95	127
32	32	64	96	128

hence, curved interface forging coupon 4 may be inspected with a single focal law. More than one focal law will be required when inspecting the remainder of the curved interface forging coupons when using the 3D delay time generation method involving circumferential phasing. The total number of delay times generated by the 3D method for inspecting each curved interface forging coupon are tabulated in Table 4.2. Effectively grouping together delay times into focal laws sequentially applied during an inspection without violating either of the described hardware limitations is discussed in the next section of this chapter.

Due to the secondary hardware limitation, multiple focal law groups may be needed even when 32 or fewer non-identical delay times are being employed to phase elements of the transducer array. As an example of the implications of this limitation on the grouping of delay times within a focal law when using the 110-element array, consider the total number of focal laws required to inspect curved interface forging coupon #5 when using the 3D ray-tracing algorithm. For this forging coupon, 19 rings will be required in the transducer aperture (see Table 3.3). Rings 1 through 16 are not segmented and require only one delay time each, while rings 17 through 19 require two delay times each. For the element layout of this transducer array, a total of 22 delay times will be required to energize and phase an aperture of 19 rings. Because the necessary 22 delay times does not exceed the 32 available delay time pulsers, it would seem that only one focal law should be needed. However, subsequent consideration of the secondary hardware limitation shows the need for four focal laws, in which each focal law contains less than 32 delay times, to avoid using two delay times on the same electronic channel. Specifically, elements 17 and 49 are on the same electronic channel, as are elements 18 and 50 as well as elements 19 and 51. To operate within hardware limitations, four focal laws would need to be constructed for the inspection of curved interface forging coupon #5 when using delay times generated by the 3D method. One focal law will energize and phase, on both transmission and reception, elements 1 through 19. The second focal law will energize and phase, on transmission and reception, elements 49 through 51. A third focal law will energize and phase elements 1 through 19 on transmission and elements 49 through 51 on reception. The fourth focal law will energize and phase elements 49 through 51 on transmission and elements 1 through 19 on reception.

Table 4.2: Number of delay times required for each curved interface forging coupons when using the 3D ray-tracing algorithm.

Curved Interface Coupon	Aperture (Number of Rings)	Total Number of Delay Times
2	9	9
3	13	13
4	17	16 + 2 = 18
5	19	16 + 6 = 22
6	22	16 + 10 + 4 = 30
7	23	16 + 10 + 8 = 34
8	25	16 + 10 + 16 = 42
9	27	16 + 10 + 24 = 50
10	30	16 + 10 + 36 = 62
11	32	16 + 10 + 44 = 70
12	34	16 + 10 + 44 + 16 = 86
13	35	16 + 10 + 44 + 16 + 12 = 98

Effectively Grouping Delay Times into Sets of Focal Laws

For inspections of the curved interface calibration specimens, more than one delay time is necessary for each segmented ring to invoke circumferential phasing of the transducer array. Circumferential phasing often requires in excess of 32 delay times, even for relatively shallow FBH depths. Due to the hardware limitations discussed in the previous section, fewer than 32 delay times can lead to multiple focal laws per inspection. Each focal law applied during an inspection results in a saved waveform response. If multiple focal laws are required to apply a delay time set during an inspection, summation of multiple waveform responses must be performed after the inspection scan has been completed. Grouping delay times into focal laws to minimize the number of saved waveform responses becomes a critical issue in terms of finite inspection time, computer RAM, and hard drive space. Consider the extreme case of capturing a single A-scan waveform from each element within a required aperture during an inspection, which would then need to be summed together in a post-processing algorithm to produce the final inspection result. If delay time sets are not grouped together, the total number of waveforms can exceed several thousand waveforms, as a single waveform must be acquired and saved to the hard disk for each signal being individually received by each element from every other element in the aperture. Further, consider the transducer aperture required when inspecting curved interface forging coupon #13 when using the 3D method. As shown in Table 4.2, the 3D inspection method requires 98 delay times when inspecting this coupon. The maximum number of focal laws into which these delay times could be grouped would result in 98 x 98, or 9604, saved waveform responses, resulting in a prohibitively large amount of inspection time and computer resources.

Grouping delay times so that the phased array instrumentation sums, as much as possible, individual element waveforms in real-time during an inspection minimizes computational resources and overall inspection time. In this dissertation, an efficient grouping of delay times for maximize real-time summing during inspections was developed for data acquisition wherein each focal law did not exceed 32 delay times per focal law nor was more than one unique delay time applied per electronic channel.

The primary criteria for grouping together delay times with a minimum number of focal laws was to first create focal laws which would phase upon transmission and reception only those elements within each group of transducers (See Table 4.1), then phase upon transmission elements from one group while phasing upon reception elements from another group until a set of focal laws existed where all elements transmitted and received exactly once from all other elements in the aperture required in the forging coupon inspection to be performed. However, if the set of delay times being applied in an inspection involved the 3D method and circumferential phasing wherein segmented elements within a transducer ring requires different delay times, these focal laws would have to be further divided if more than one delay time was required for a single channel, e.g., if elements 17 and 48 from ring 17 were both being phased for transmission only or reception only within a focal law. Additionally, to further increase efficiency of grouping and minimize the

number of focal laws used in an inspection, one focal law may be combined with another if the second focal law assigns delay times to channels which are unused by the first focal law.

Delay times from the initial and refined 2D ray-tracing algorithms were grouped together into focal laws as tabulated in Table 4.3. Delay times from the 3D method were grouped together into focal laws as tabulated in Table 4.4. Additionally, graphical representations of the grouping of delay times into focal laws for the 3D inspection method are presented in Figures E.1 through E.12 in Appendix E of this dissertation.

In both Tables 4.3 and 4.4, each bracketed group of elements in the "Groups of Receiving Elements" column received signals from transmitted elements listed in the "Transmitting Elements" column. Each group of transmitting elements were matched to a group of receiving elements, which resulted in a single focal law that, upon data acquisition, will provide a saved A-scan waveform data set. Multiple focal laws from a single inspection resulted in an equal number of saved waveform responses, then summed together in a post-processing procedure to generate a single waveform for each scan location of the radial-rotational inspection.

Table 4.3: Effective grouping of delay time sets from the initial and refined 2D methods.

Block	Transmitting Elements	Groups of Receiving Elements
2	1-9	{1-9}
3	1-13	{1-13}
4	1-17, 49	{1-17, 49}
5	1-19, 49-51	{1-19, 49-51}
6	1-22, 49-54, 86, 118	{1-22, 86, 49-54, 118}
7	1-23, 49-55, 86-87, 118-119	{1-23, 49-55, 86-87,118-119}
8	1-25, 49-57, 86-89, 118-121	{1-25, 49-57, 86-87, 118-121}
9	1-27, 49-59, 86-91, 118-123	{1-27, 49-59, 86-91, 118-123}
10	1-30, 49-62, 86-94, 118-126	{1-30, 49-62, 86-94, 118-126}
11	1-32, 49-64, 86-96, 118-128	{1-32, 49-64, 86-96, 118-128}
12	1-32, 49-64, 86-96, 118-128	{1-32, 49-64, 86-96, 118-128} and {65-66, 69-70, 75-76, 79-80, 97-98, 101-102, 107-108, 111-112}
12	65-66, 69-70, 75-76, 79-80, 97-98, 101-102, 107-108, 111-112	{1-32, 49-64, 86-96, 118-128} and {65-66, 69-70, 75-76, 79-80, 97-98, 101-102, 107-108, 111-112}
13	1-32, 49-64, 86-96, 118-128	{1-32, 49-64, 86-96, 118-128} and {65-67, 69-71, 73, 75-77, 79-81, 83, 97-99, 101-103, 105, 107-109, 111-113, 115}
13	65-67, 69-71, 73, 75-77, 79-81, 83, 97-99, 101-103, 105, 107-109, 111-113, 115	{1-32, 49-64, 86-96, 118-128} and {65-67, 69-71, 73, 75-77, 79-81, 83, 97-99, 101-103, 105, 107-109, 111-113, 115}

Table 4.4: Effective grouping of delay time sets from the 3D method.

Block	Transmitting Elements	Groups of Receiving Elements
2	1-9	{1-9}
3	1-13	{1-13}
4	1-17, 49	{1-17, 49}
5	1-19	{1-19} & {49-51}
5	49-51	{1-19} & {49-51}
6	1-22, 86	{1-22, 86}, {49-54} & {118}
6	49-54	{1-22, 86}, {49-54} & {118}
6	118	{1-22, 86}, {49-54} & {118}
7	1-23, 86-87	{1-23, 86-87}, {49-55} & {118-119}
7	49-55	{1-23, 86-87}, {49-55} & {118-119}
7	118-119	{1-23, 86-87}, {49-55} & {118-119}
8	1-25, 86-89	{1-25, 86-87}, {49-57} & {118-121}
8	49-57	{1-25, 86-87}, {49-57} & {118-121}
8	118-121	{1-25, 86-87}, {49-57} & {118-121}
9	1-27, 86-91	{1-27, 86-91}, {49-59} & {118-123}
9	49-59	{1-27, 86-91}, {49-59} & {118-123}
9	118-123	{1-27, 86-91}, {49-59} & {118-123}
10	1-30, 86-94	{1-30, 86-94}, {49-62} & {118-126}
10	49-62	{1-30, 86-94}, {49-62} & {118-126}
10	118-126	{1-30, 86-94}, {49-62} & {118-126}
11	1-32, 86-96	{1-32, 86-96}, {49-64}, {86-96} and {118-128}
11	49-64	{1-32, 86-96}, {49-64}, {86-96} and {118-128}
11	118-128	{1-32, 86-96}, {49-64}, {86-96} and {118-128}
12	1-32	{49-64}, {65-66, 69-70, 75-76, 79-80} & {97-98, 101-102, 107-108, 111-112, 118-128}
12	1-32, 86-96	{1-32, 86-96}
12	49-64	{1-32, 86-96}, {65-66, 69-70, 75-76, 79-80} & {97-98, 101-102, 107-108, 111-112, 118-128}
12	49-66, 69-70, 75-76, 79-80	{49-66, 69-70, 75-76, 79-80}
12	65-66, 69-70, 75-76, 79-80	{49-64, 97-98, 101-102, 107-108, 111-112} & {118-128}
12	65-66, 69-70, 75-76, 79-80, 118-128	{1-32, 86-96}
12	86-96	{97-98, 101-102, 107-108, 111-112, 118-128}
12	86-98, 101-102, 107-108, 111-112	{49-64, 65-66, 69-70, 75-76, 79-80}
12	97-98, 101-102, 107-108, 111-112	{1-32, 86-96}
12	97-98, 101-102, 107-108, 111-112, 118-128	{97-98, 101-102, 107-108, 111-112, 118-128}
12	118-128	{49-64, 65-66, 69-70, 75-76, 79-80}
13	1-32	{49-64}, {65-67, 69-71, 73, 75-77, 79-81, 83} & {97-99, 101-103, 105, 107-109, 111-113, 115, 118-128}
13	1-32, 86-96	{1-32, 86-96}
13	49-64	{1-32, 86-96}, {49-64}, {65-67, 69-71, 73, 75-77, 79-81, 83} & {97-99, 101-103, 105, 107-109, 111-113, 115, 118-128}
13	65-67, 69-71, 73, 75-77, 79-81, 83	{49-64} & {65-67, 69-71, 73, 75-77, 79-81, 83}
13	65-67, 69-71, 73, 75-77, 79-81, 83, 86-96	{97-99, 101-103, 105, 107-109, 111-113, 115, 118-128}
13	65-67, 69-71, 73, 75-77, 79-81, 83, 118-128	{65-67, 69-71, 73, 75-77, 79-81, 83, 118-128}
13	86-99, 101-103, 105, 107-109, 111-113, 115	{49-64} & {65-67, 69-71, 73, 75-77, 79-81, 83}
13	97-99, 101-103, 105, 107-109, 111-113, 115	{1-32, 86-96}
13	97-99, 101-103, 105, 107-109, 111-113, 115, 118-128	{97-99, 101-103, 105, 107-109, 111-113, 115, 118-128}
13	118-128	{49-64} & {65-67, 69-71, 73, 75-77, 79-81, 83}

Acquisition of Data

One or more A-scan waveform responses were acquired and saved to the computer hard disk during inspections of blocks 2 through 13 in both sets of planar and curved interface forging coupons. Specifically, one A-scan waveform response was acquired and saved during inspections of each planar interface forging coupon 2 through 11, and four waveforms each for forging coupons 12 and 13, when using delay times from the initial 2D method. A similar set of A-scan waveforms were acquired from both sets of forging coupons using delay times generated using the refined 2D method. For both the initial and refined 2D delay time generation methods, the saved waveforms from specimens 12 and 13 from both forging coupon sets were individually summed together using a post-processing algorithm.

Table 4.5 tabulates the number of focal laws, and hence A-scan waveforms acquired during an inspection, for curved interface forging coupons 2 through 13 when using delay times from the 3D method.

Consistency was maintained during waveform acquisitions from individual FBH coupons by using common settings for all inspection parameters, excluding gain and sum gain settings. If the inspection of a forging coupon required multiple focal laws, each focal law was acquired during separate inspection runs as both the XY the radial-rotational motion control system appeared to consistently perform repeatable scans at the relatively slow rotational inspection speeds used.

Because individual focal laws were acquired during separate inspections, the full dynamic range of A-scan waveform amplitudes could be employed by adjusting the gain set for each focal law. An individual focal law could energize and phase either few or many elements for sending and receiving, so setting the gain higher when few elements were energized increased the signal-to-noise ratio and setting the gain lower prevented amplitude saturation from occurring when a relatively large number of elements were energized. The gains used during inspections of planar interface forging coupons employing initial 2D method delay time sets are tabulated in Table 4.6 and, similarly, Table 4.7 when employing the refined 2D method. Gain settings when inspecting the curved interface calibration specimens are provided in Table 4.8 when using delay times from the refined 2D method, and Table 4.9 when employing the 3D ray-tracing algorithm.

The phased array instrument used for the final data collection had been recently calibrated by the manufacturer, otherwise a lack of instrument calibration could have been a contribution to error in the acquired data. Potential sources of error due to a lack of instrument calibration include, but are not limited to, a relative reduction or complete loss of signal response along individual transmission and reception channels, a lack of signal amplitude linearity when adjusting gain settings, and excessive electronic noise.

Table 4.5: Number of focal laws required when using delay times from the 3D method.

Block #	Focal Laws	Block #	Focal Laws	Block #	Focal Laws
2	1	6	9	10	9
3	1	7	9	11	9
4	4	8	9	12	16
5	4	9	9	13	18

51

Table 4.6: Focal Law gains for planar interface forging coupons using the initial 2D method.

Focal Law \ Block	2	3	4	5	6	7	8	9	10	11	12	13
1	33.0	27.0	24.0	22.0	20.0	22.0	20.0	23.0	23.0	23.0	25.5	27.6
2											34.6	32.1
3											33.9	35.0
4											44.5	41.0

Table 4.7: Focal law gains for planar interface forging coupons using the refined 2D method.

Focal Law \ Block	2	3	4	5	6	7	8	9	10	11	12	13
1	33.0	27.0	24.0	22.0	20.0	22.0	20.0	21.0	20.0	20.0	22.7	23.4
2											33.2	30.9
3											32.0	32.7
4											44.0	39.5

Table 4.8: Focal Law gains for curved interface forging coupons using the refined 2D method.

Focal Law \ Block	2	3	4	5	6	7	8	9	10	11	12	13
1	33.5	31.5	28.0	28.0	26.0	28.0	26.0	24.0	26.0	28.0	30.2	30.9
2											47.1	44.0
3											45.6	42.0
4											57.8	53.3

Table 4.9: Focal Law gains for curved interface forging coupons using the 3D method.

Focal Law \ Block	2	3	4	5	6	7	8	9	10	11	12	13
1	35.0	31.5	29.7	28.7	28.1	30.2	27.2	27.2	28.0	27.7	31.6	32.5
2			54.5	46.7	38.8	41.0	39.5	39.5	43.9	44.6	47.3	48.5
3			49.6	41.9	56.4	52.8	43.9	43.9	42.2	40.8	60.2	52.7
4			75.7	57.8	38.2	40.9	37.9	37.9	40.1	41.4	40.2	41.3
5					48.5	49.7	42.4	42.4	40.8	41.2	44.8	45.7
6					65.0	52.0	48.3	48.3	51.9	52.6	41.5	42.8
7					52.0	62.7	52.8	52.8	50.4	52.2	49.4	45.0
8					62.5	59.2	52.0	52.0	52.6	52.8	54.1	58.6
9					63.0	71.6	51.6	51.6	51.7	54.2	59.6	63.5
10					80.1	59.8	55.0	55.0	50.6	52.3	49.8	63.5
11					76.7	67.7	54.0	54.0	51.6	50.8	63.1	63.1
12											61.4	52.3
13											51.1	49.7
14											44.1	52.6
15											50.5	58.1
16											52.1	58.1
17												61.1
18												41.1

Post-Processing of Inspection Data

After data acquisition, each saved data file from the phased array instrumentation control software was converted from a binary data file into an ASCII-formatted text document containing a 4-dimensional (4D) matrix of information, including scan location, index location, TOF, and amplitude. A post-processing computer program was developed to convert this 4D data matrix into a 2D C-scan bitmap image for each waveform data set collected for and presented in this dissertation, no matter which forging coupon was inspected or ray-tracing algorithm employed.

When multiple focal laws were required for an inspection, this post-processing program would also sum together all sets of A-scan waveform data from the inspection using a common gain setting, specifically the gain setting of the first focal law (see Tables 4.6 through 4.9), before generating a resultant 2D C-scan bitmap image. To allow for subsequent C-scan image analysis, these images were normalized by adjusting the common gain setting such that the peak amplitude response equaled 80%FSH on a 0%FSH to 100%FSH scale. Along with the final common gain, additional parameters associated with data collected for each specific specimen and ray-tracing algorithm were output for data analysis along with a grayscale C-scan bitmap image. C-scans of data from individual focal laws when multiple focal laws were required are presented in Appendix F.

Acquired Data – C-Scan Images

Grayscale C-scan bitmap images generated in post-processing for forging coupons 2 through 13 for each ray-tracing algorithm are shown arrayed in Figures 4.1 through 4.3. Each image consists of 60 by 60 pixels, corresponding to a 0.120-inch by 0.120-inch scan area at a resolution of 0.002 inch. The bitmaps are square images presented below with dimensions of 1.16-inch by 1.16-inch. In the grayscale bitmap images, white represents a 100%FSH amplitude signal and black represents a 0%FSH amplitude signal. The maximum flaw response in each image was normalized to an 80%FSH amplitude signal.

Block #	Planar Interface Forging Coupons and Initial 2D Method	Planar Interface Forging Coupons and Refined 2D Method	Curved Interface Forging Coupons and Refined 2D Method	Curved Interface Forging Coupons and 3D Method
2				
3				
4				
5				
6				
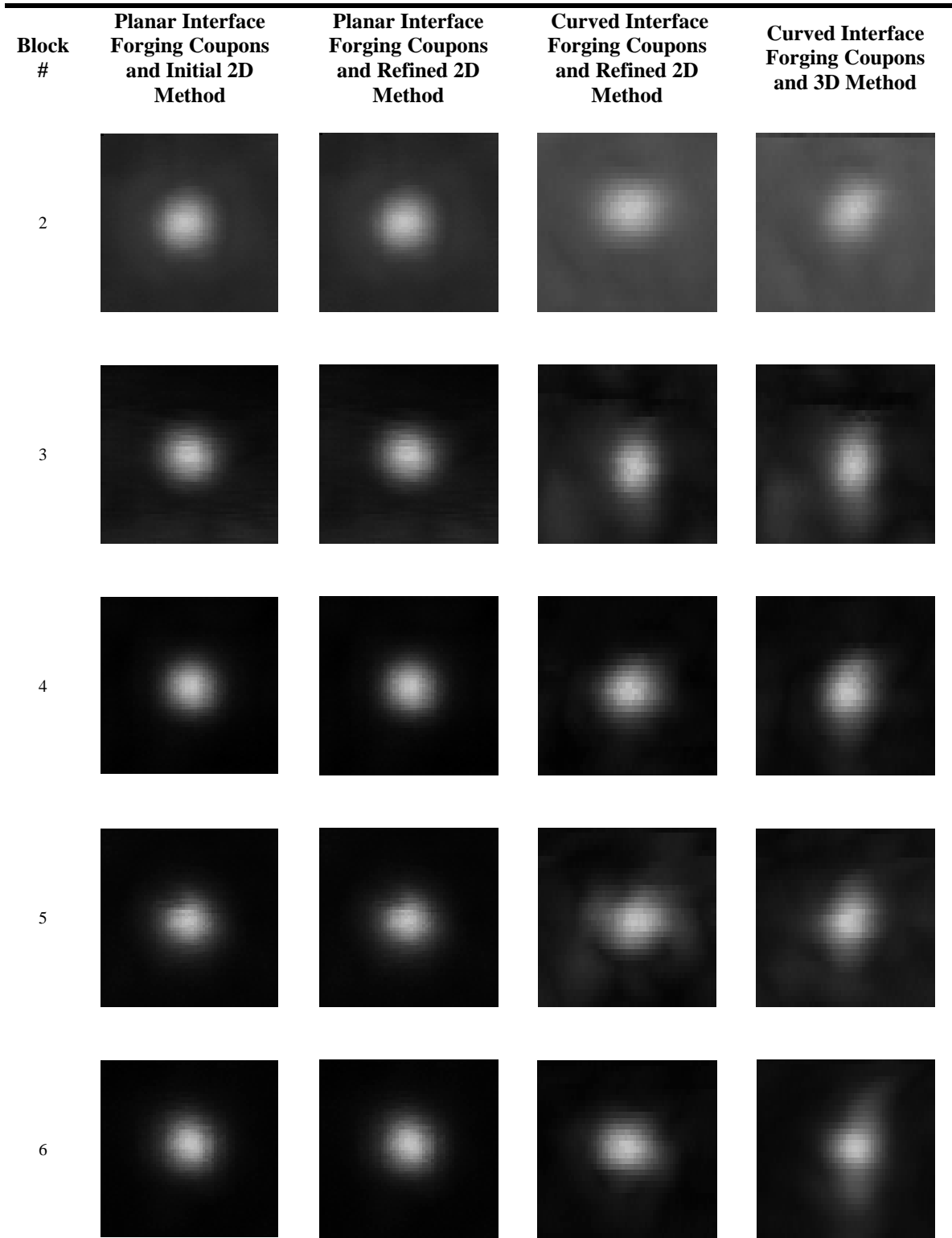
Figure 4.1: C-scan images of FBH inspections of blocks 2 through 6 from both forging coupon sets when using delay times generated by each of the three ray-tracing algorithms.
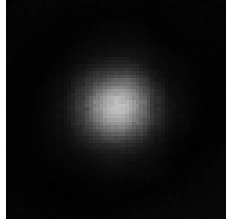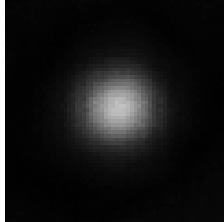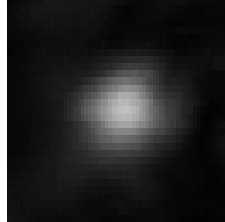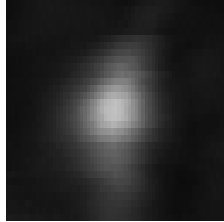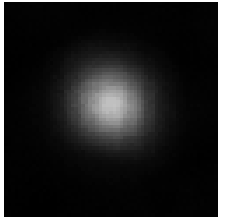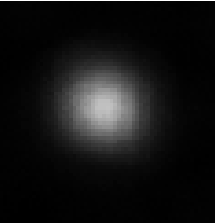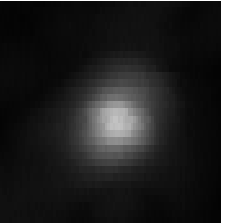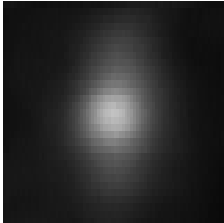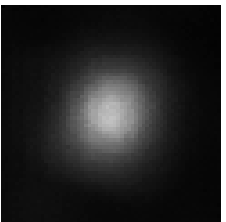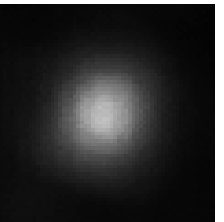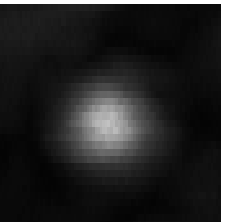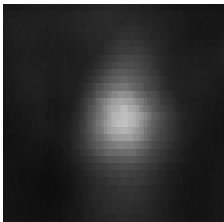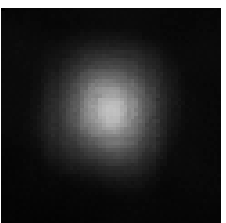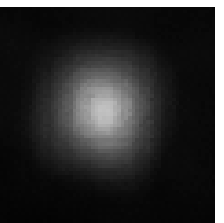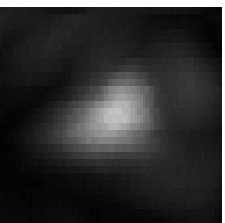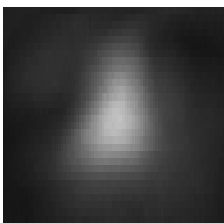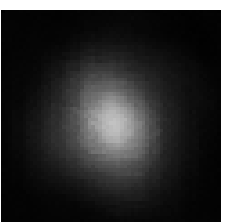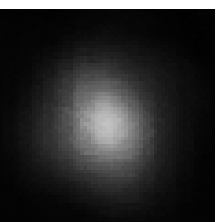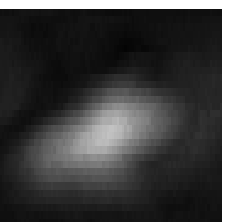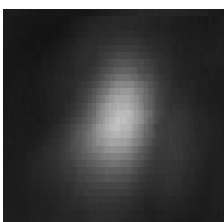
Block #	Planar Interface Forging Coupons and Initial 2D Method	Planar Interface Forging Coupons and Refined 2D Method	Curved Interface Forging Coupons and Refined 2D Method	Curved Interface Forging Coupons and 3D Method
7				
8				
9				
10				
11				

Figure 4.2: C-scan images of FBH inspections of blocks 7 through 11 from both forging coupon sets when using delay times generated by each of the three ray-tracing algorithms.
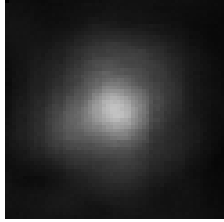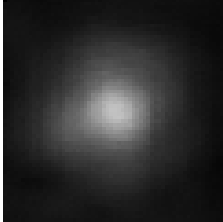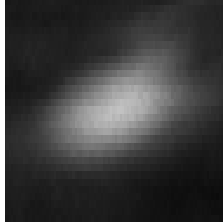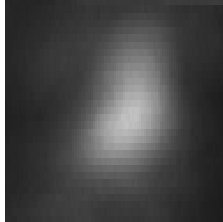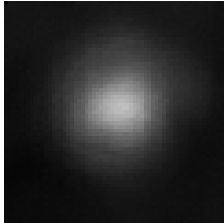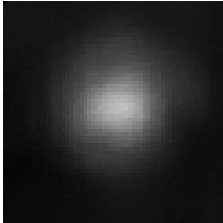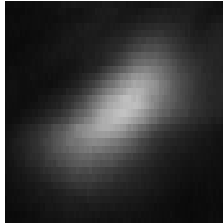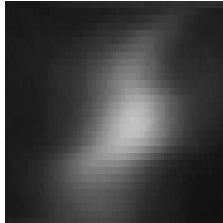
Block #	Planar Interface Forging Coupons and Initial 2D Method	Planar Interface Forging Coupons and Refined 2D Method	Curved Interface Forging Coupons and Refined 2D Method	Curved Interface Forging Coupons and 3D Method
12				
13				

Figure 4.3: C-scan images of FBH inspections of blocks 12 and 13 from both forging coupon sets when using delay times generated by each of the three ray-tracing algorithms.

Acquired Data – Analysis

Tabulated in Table 4.10 are the gain settings required to produce 80%FSH peak amplitude C-scan images for each specimen and ray-tracing algorithm, as output from post-processing of the acquired data. This data can alternatively be presented as peak amplitude responses relative to a common gain. The data presented in Table 4.10 has been converted to a set of peak amplitude signal responses produced at a single common gain setting of 59.0 dB for all four sets of data (see Table 4.11 and Figure 4.4).

For the data presented, the average half-maximum-amplitude width of the ultrasonic beam at the depth of a FBH was determined from horizontal and vertical line profiles passing directly through the peak amplitude coordinates in each C-scan image. The 6 dB drop in amplitude method, common in ultrasonic testing and previously discussed in Chapter 2, was used to determine the ultrasonic beam widths presented.

As the C-scan images presented in this chapter have peak amplitudes of 80%FSH, beam widths were measured at scan and index positions where the amplitude dropped to 40%FSH. Table 4.12 and Figure 4.5 show horizontal beam widths measured along the scan direction of the inspection, while Table 4.13 and Figure 4.6 show vertical beam widths measured along the index direction.

Evaluation of an ultrasonic technique generally includes measuring inspection sensitivity, where signal-to-noise ratio (SNR) is measured for a flaw of known type, size, and depth. For circular reflectors inspected at normal incidence and small in size relative to the ultrasonic beam, the surface area of the flaw divided by SNR remains constant. Hence, dividing a FBH diameter by the square root of its SNR predicts

the FBH diameter that would be detected with the same technique if SNR were equal to unity, assuming flaw type, depth and material properties remain unchanged.

Peak flaw amplitudes in the c-scans shown in Figures 4.1 through 4.3 were normalized to 80%FSH. Average noise amplitudes were measured for each C-scan presented in this dissertation are tabulated in Tables 4.14. The SNR values are tabulated in Table 4.15, and also plotted in Figure 4.7.

The measurement sensitivity, i.e., minimum FBH diameters, of each inspection performed in this dissertation are tabulated in Table 4.16 and plotted in Figure 4.8. In this dissertation, the SNR is the peak amplitudes of #1/2 (1/128-inch or ~0.0078-inch diameter) FBHs divided by average noise amplitude from the C-scan bitmap images presented in this chapter.

Table 4.10: Gain settings to achieve 80% FSH peak signal amplitudes in C-scan images.

Block #	FBH Depth (inches)	Planar Interface Forging Coupons and Initial 2D Method (dB)	Planar Interface Forging Coupons and Refined 2D Method (dB)	Curved Interface Forging Coupons and Refined 2D Method (dB)	Curved Interface Forging Coupons and 3D Method (dB)
2	0.20	31.9	32.2	32.2	33.9
3	0.45	26.7	27.0	31.0	31.6
4	0.70	23.5	24.0	28.3	28.9
5	0.90	22.8	23.4	27.5	26.0
6	1.15	20.3	19.9	24.7	23.0
7	1.35	21.9	21.0	27.0	24.6
8	1.60	20.3	19.2	25.1	23.0
9	1.80	23.0	21.1	23.6	21.2
10	2.05	22.8	20.0	26.0	25.1
11	2.25	22.6	19.6	28.2	21.6
12	2.50	20.4	18.0	27.9	22.9
13	2.70	19.7	17.9	27.4	23.4

Table 4.11: Peak signal amplitudes at a common gain of 59 dB from C-scan images.

Block #	FBH Depth (inches)	Planar Interface Forging Coupons and Initial 2D Method (%FSH)	Planar Interface Forging Coupons and Refined 2D Method (%FSH)	Curved Interface Forging Coupons and Refined 2D Method (%FSH)	Curved Interface Forging Coupons and 3D Method (%FSH)
2	0.20	18.1	17.5	17.5	14.4
3	0.45	33.0	31.8	20.1	18.8
4	0.70	47.7	45.0	27.4	25.6
5	0.90	51.7	48.2	30.1	35.7
6	1.15	68.9	72.1	41.5	50.5
7	1.35	57.3	63.5	31.8	42.0
8	1.60	68.9	78.2	39.6	50.5
9	1.80	50.5	62.8	47.1	62.1
10	2.05	51.7	71.3	35.7	39.6
11	2.25	52.9	74.7	27.7	59.3
12	2.50	68.1	89.8	28.7	51.1
13	2.70	73.8	90.8	30.4	48.2
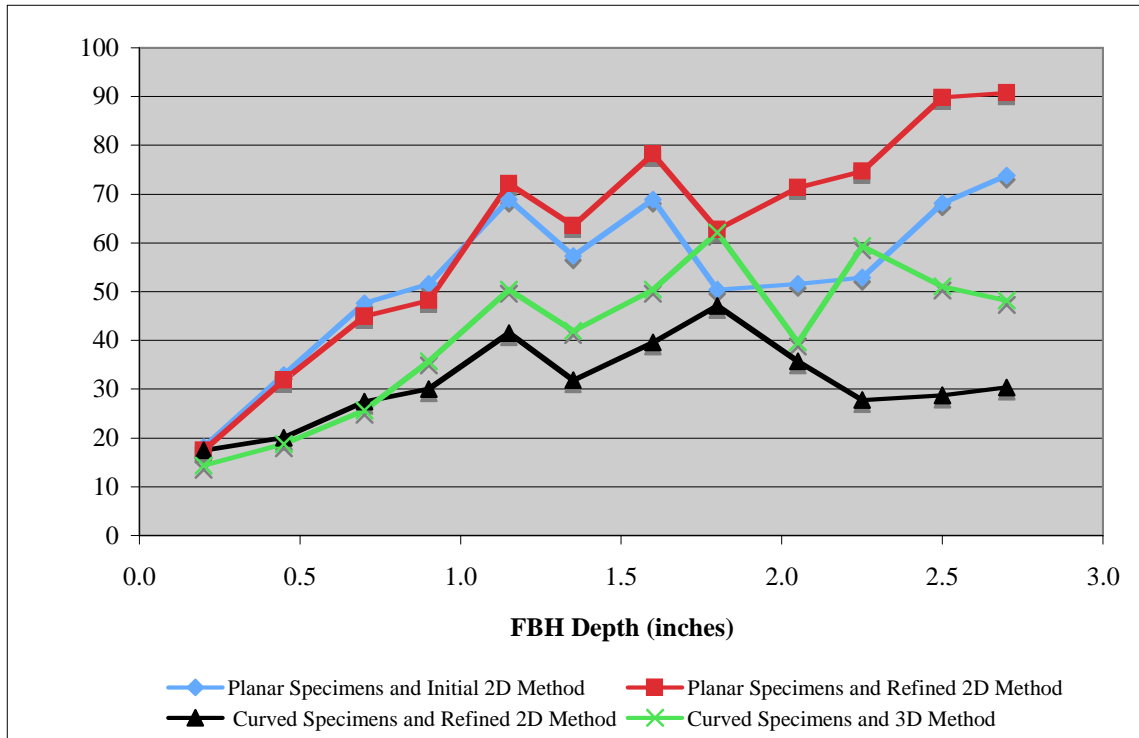
Figure 4.4: Peak FBH signal amplitudes at a common gain of 59 dB from C-scan images.

Table 4.12: Horizontal half-maximum-amplitude beam widths from C-scan images.

Block #	FBH Depth (inches)	Planar Interface Forging Coupons and Initial 2D Method (inches)	Planar Interface Forging Coupons and Refined 2D Method (inches)	Curved Interface Forging Coupons and Refined 2D Method (inches)	Curved Interface Forging Coupons and 3D Method (inches)
2	0.20	0.039	0.040	0.033	0.050
3	0.45	0.032	0.033	0.025	0.030
4	0.70	0.031	0.031	0.020	0.024
5	0.90	0.030	0.032	0.021	0.024
6	1.15	0.032	0.030	0.018	0.024
7	1.35	0.033	0.031	0.022	0.034
8	1.60	0.035	0.032	0.017	0.024
9	1.80	0.043	0.036	0.016	0.022
10	2.05	0.046	0.037	0.017	0.028
11	2.25	0.048	0.040	0.018	0.025
12	2.50	0.044	0.037	0.019	0.031
13	2.70	0.043	0.038	0.020	0.030
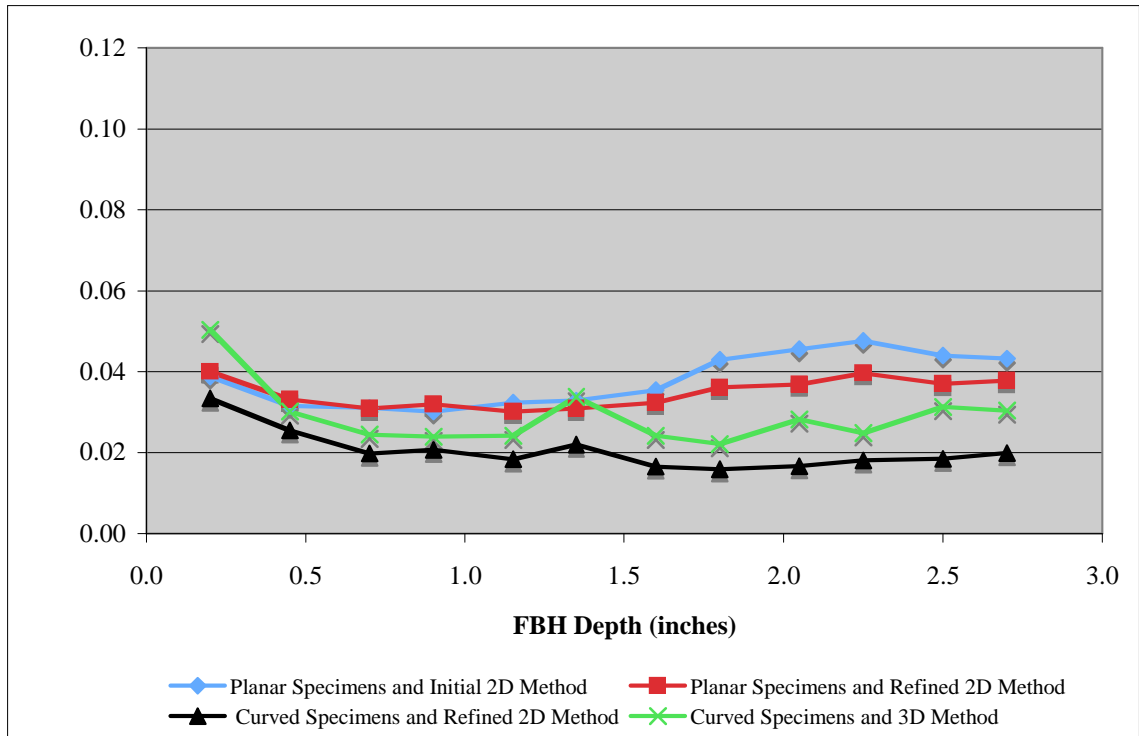
Figure 4.5: Horizontal half-maximum-amplitude beam widths from C-scan images.

Table 4.13: Vertical half-maximum-amplitude beam widths from C-scan images.

Block #	FBH Depth (inches)	Planar Interface Forging Coupons and Initial 2D Method (inches)	Planar Interface Forging Coupons and Refined 2D Method (inches)	Curved Interface Forging Coupons and Refined 2D Method (inches)	Curved Interface Forging Coupons and 3D Method (inches)
2	0.20	0.041	0.041	0.054	0.063
3	0.45	0.034	0.035	0.029	0.029
4	0.70	0.031	0.033	0.035	0.031
5	0.90	0.032	0.031	0.045	0.035
6	1.15	0.031	0.031	0.038	0.034
7	1.35	0.035	0.033	0.045	0.040
8	1.60	0.036	0.033	0.049	0.050
9	1.80	0.043	0.034	0.054	0.050
10	2.05	0.042	0.036	0.060	0.060
11	2.25	0.042	0.037	0.087	0.059
12	2.50	0.048	0.039	0.107	0.081
13	2.70	0.046	0.038	0.074	0.071
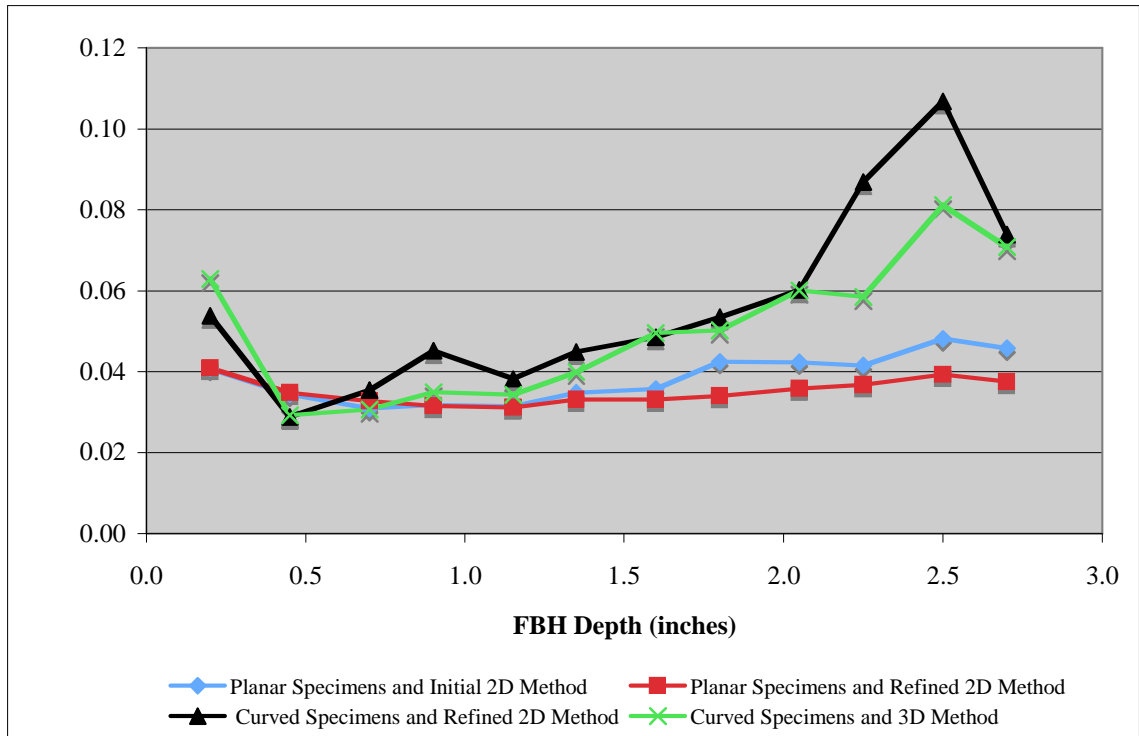
Figure 4.6: Vertical half-maximum-amplitude beam widths from C-scan images.

Table 4.14: Average noise amplitudes in C-scan images where peak amplitudes are 80%FSH.

Block #	FBH Depth (inches)	Planar Coupons and Initial 2D Method (%FSH)	Planar Coupons and Refined 2D Method (%FSH)	Curved Coupons and Refined 2D Method (%FSH)	Curved Forging and 3D Method (%FSH)
2	0.20	20.34	21.67	35.53	33.52
3	0.45	6.10	7.80	11.71	11.65
4	0.70	3.86	5.33	6.04	7.71
5	0.90	4.78	4.92	9.53	10.30
6	1.15	3.61	4.02	4.61	8.80
7	1.35	3.52	3.36	7.45	10.92
8	1.60	2.44	2.62	7.06	12.89
9	1.80	5.69	4.11	11.60	16.91
10	2.05	6.86	5.02	13.46	19.93
11	2.25	4.01	3.34	10.96	17.13
12	2.50	10.58	9.70	18.72	22.65
13	2.70	13.83	12.83	12.87	16.13

Table 4.15: Signal-to-noise ratios in C-scan images.

Block #	FBH Depth (inches)	Planar Coupons and Initial 2D Method (unitless)	Planar Coupons and Refined 2D Method (unitless)	Curved Coupons and Refined 2D Method (unitless)	Curved Coupons and 3D Method (unitless)
2	0.20	3.9	3.7	2.3	2.4
3	0.45	13.1	10.3	6.8	6.9
4	0.70	20.7	15.0	13.2	10.4
5	0.90	16.7	16.3	8.4	7.8
6	1.15	22.2	19.9	17.4	9.1
7	1.35	22.7	23.8	10.7	7.3
8	1.60	32.8	30.5	11.3	6.2
9	1.80	14.1	19.5	6.9	4.7
10	2.05	11.7	15.9	5.9	4.0
11	2.25	20.0	24.0	7.3	4.7
12	2.50	7.6	8.2	4.3	3.5
13	2.70	5.8	6.2	6.2	5.0

Table 4.16: FBH diameters producing SNR of unity as a method of measuring inspection sensitivity.

Block #	FBH Depth (inches)	Planar Coupons and Initial 2D Method (inches)	Planar Coupons and Refined 2D Method (inches)	Curved Coupons and Refined 2D Method (inches)	Curved Coupons and 3D Method (inches)
2	0.20	0.0039	0.0041	0.0052	0.0051
3	0.45	0.0022	0.0024	0.0030	0.0030
4	0.70	0.0017	0.0020	0.0021	0.0024
5	0.90	0.0019	0.0019	0.0027	0.0028
6	1.15	0.0017	0.0018	0.0019	0.0026
7	1.35	0.0016	0.0016	0.0024	0.0029
8	1.60	0.0014	0.0014	0.0023	0.0031
9	1.80	0.0021	0.0018	0.0030	0.0036
10	2.05	0.0023	0.0020	0.0032	0.0039
11	2.25	0.0017	0.0016	0.0029	0.0036
12	2.50	0.0028	0.0027	0.0038	0.0042
13	2.70	0.0032	0.0031	0.0031	0.0035
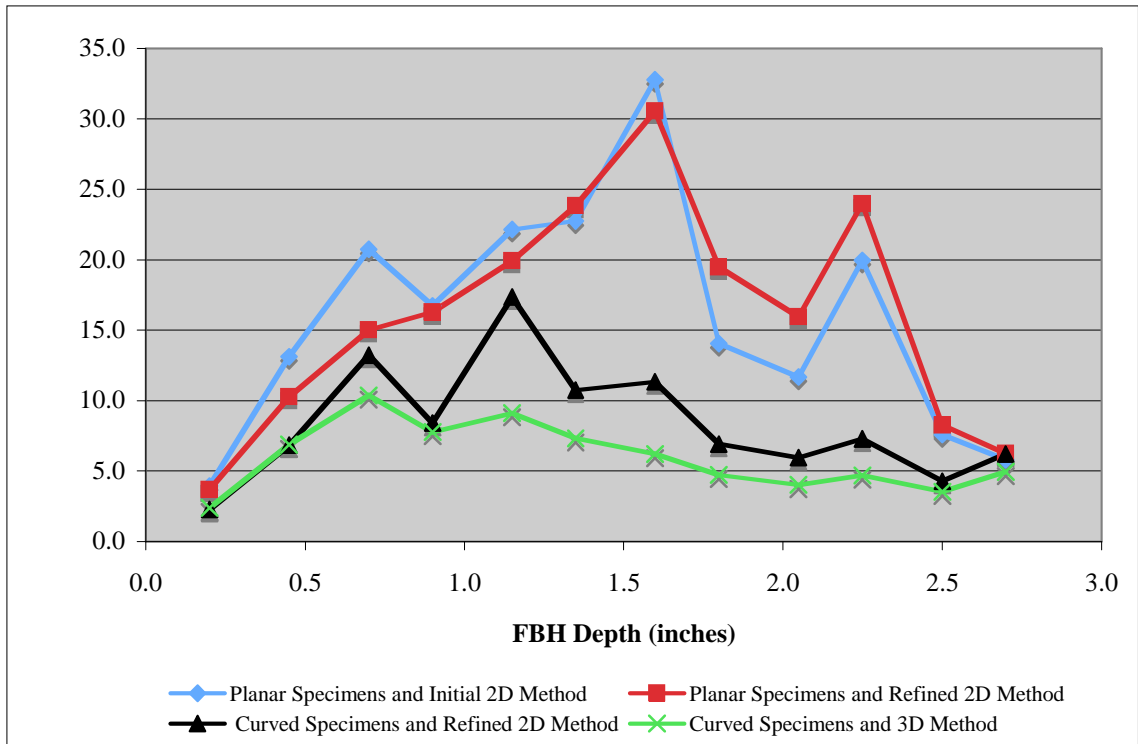
Figure 4.7: Signal-to-noise ratios in C-scan images.
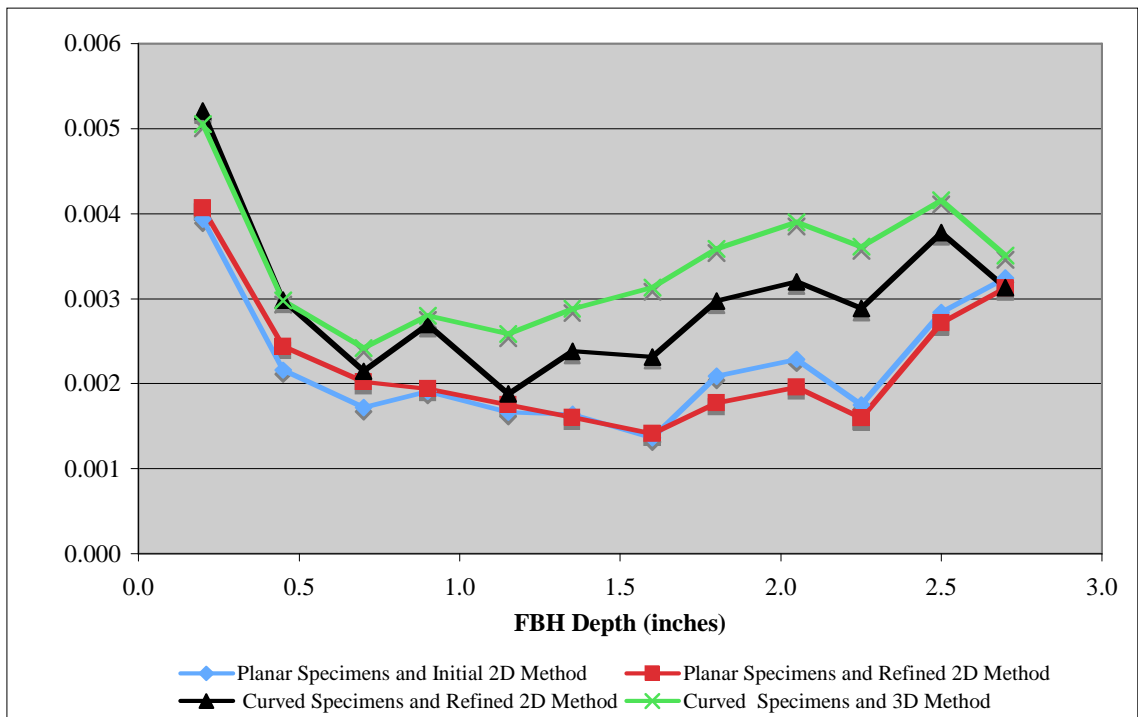
Figure 4.8: FBH diameters producing SNR of unity as a method of measuring inspection sensitivity.

Summary

Inspection data was acquired by the designed segmented, annular array from #1/2 FBHs located beneath planar interface forging coupons when phasing the transducer array with delay times generated by the initial and refined 2D ray-tracing algorithms. Data was also acquired by this array from #1/2 FBHs beneath curved interface forging coupons when phasing with delay times generated by the refined 2D and 3D ray-tracing algorithms in inspections which incorporated a cylindrically focused ultrasonic mirror designed to compensate for forging surface curvatures.

The phased array instrumentation hardware restrictions limited how delay times for phasing the transducer array elements were grouped together prior to data acquisition. Considerations of inspection factors such as finite acquisition time and computational resources led to the development of an effective grouping of delay time sets generated by each of the three ray-tracing algorithms presented in Chapter 3 of this dissertation. Post-processing of acquired A-scan waveform inspection data provided C-scan images of #1/2 FBH signal responses from the forging coupon sets. The C-scans bitmaps were subsequently analyzed to determine FBH peak signal amplitudes, average half-maximum-amplitude ultrasonic beam widths, average noise amplitudes, and signal-to-noise ratios. Also, the measurement sensitivity of each inspection technique was calculated using surface area of the FBH reflector and SNR.

The following chapter of this dissertation will evaluate the significance of the inspection data results presented in this chapter. An attempt will be made to determine the relative effectiveness of the initial and refined 2D delay time generation methods when inspecting the set of planar interface forging coupons. Also, the relative effectiveness of the refined 2D and 3D delay time generation methods when inspecting the set of curved interface forging coupons using compensating mirrors will be evaluated.

CHAPTER 5. CONCLUSIONS

Introduction

In this dissertation, three progressively more sophisticated ray-tracing algorithms are evaluated by analyzing results from multiple inspections of two forging material coupon sets containing #1/2 FBH reflectors at common depths. One set of forging coupons has a planar surface through which the ultrasonic inspection was performed. The second coupon set has a curved interface, a surface compensated for during ultrasonic inspections by the incorporation of a curved ultrasonic mirror. The three ray-tracing algorithms, called the initial 2D, refined 2D and 3D methods, provided sets of delay times for phasing the compound spherically focused, annular, segmented, ultrasonic transducer array operating at a center frequency of 10 MHz. This was specifically designed for ultrasonic nondestructive inspections of forging disks in the aerospace industry.

Each of the four inspection data sets presented in the previous chapter of this dissertation will be used to evaluate various aspects of the three different ray-tracing algorithms used to generate the three sets of delay times used in these inspections. These evaluations include:

- For the planar interface forging coupons, the initial and refined 2D inspections will be compared in order to evaluate whether or not focusing improvements had been achieved due to refining the method used for calculating refraction at the water-forging interface.
- For the refined 2D ray-tracing algorithm, inspections results of the planar and curved interface forging coupons will be compared in order to evaluate the performance of the surface ultrasonic mirror incorporated into inspections of the curved interface forging coupons to compensate for forging surface curvature.
- For the curved interface forging coupons, the refined 2D and 3D inspections will be compared in order to evaluate the circumferential phasing method used by the 3D ray-tracing algorithm.

Rectilinear scans of planar interface forging coupons were performed using the initial and refined 2D ray-tracing algorithms. Otherwise similar, these two algorithms employed different methods to calculate refraction at the planar forging-water interface, where the initial 2D ray-tracing algorithm used a small angle approximation while the refined 2D ray-tracing algorithm used a precise numerical method. Delay time sets generated by each algorithm were used to phase the transducer array elements during ultrasonic inspections performed on #1/2 FBH reflectors located within the planar interface forging coupons. Inspections of planar interface forging specimens will be evaluated to determine whether or not the refined 2D ray-tracing algorithm significantly reduces the effects of focusing aberrations, as compared

to similar inspections performed when using delay time sets generated by the initial 2D ray-tracing algorithm.

Rotational-radial scans of curved interface forging coupons were also performed using the delay time sets generated from the refined 2D method. All inspections of the convexly curved interface forging coupons incorporated a concave, cylindrically focused, ultrasonic mirror oriented between the transducer array and curved interface forging coupons to pre-distort the ultrasonic beam before refraction through the curved forging interface. The delay times generated by the refined 2D method for inspections of planar interface forging coupons were again used, now to phase the array when inspecting curved interface forging coupons with the surface compensating mirror. One purpose of inspecting curved interface forging coupons when using delay time sets from the refined 2D method was to evaluate the mirror as a source of focusing aberrations. This evaluation will be accomplished by comparing the results of inspections of the curved interface forging coupons to results of inspections of planar interface forging coupons when using a common set of delay times generated by the refined 2D method, whereby the inspections of the curved forging coupon use the surface compensating mirror and the planar forging coupon inspections do not.

Rotational-radial scans of curved interface forging coupons when using the surface compensating mirror were also performed when using delay time sets generated by the 3D ray-tracing algorithm. This 3D method is the only algorithm presented in this dissertation wherein the delay time values varied around the circumference of each segmented ring of the annular transducer, resulting in circumferential phasing of the array. Inspections of curved interface forging coupons when using the 3D method will evaluate whether or not focusing aberrations were significantly reduced as compared to similar curved interface forging coupon inspections performed using delay times generated by the refined 2D ray-tracing algorithm. If the results of the 3D method inspection do not compare favorably with the results of inspections when using the 2D methods, additional sources of focusing aberrations within the 3D method will be investigated.

A comparison between inspection methods will rely upon the results of measurements taken from the four sets of inspection data. The ray-tracing algorithms will be evaluated in terms of providing a significant reduction in the effects of focusing aberrations. Both the inspection data and the results of parameters inferred from the inspection data were previously presented in Chapter 4 of this dissertation. The data of each of the four inspections, including the initial and refined 2D inspections of planar interface coupons as well as the refined 2D and 3D inspections of curved interface coupons, were presented. Specific measurements of the inspection data included a purely qualitative examination of the C-scan bitmap images, inspection gain settings, peak amplitudes, horizontal and vertical beam widths, average noise amplitudes, signal-to-noise ratios, and inspection sensitivity.

To aid in making comparisons between data sets collected using the inspection methods, several descriptive statistics parameters were evaluated for the measurement results presented in Chapter 4 of this dissertation. As quantified in Eqns 5.1 through 5.4, these parameters included range, population mean, population standard deviation, and coefficient of variation [21]. Table 5.1 presents the values of these

parameters for each of the four data sets. Given the available number of forging coupons with FBHs at different material depths, there are $N = 12$ measurements in each data set.

$$\text{range} = X_{\text{maximum}} - X_{\text{minimum}} \tag{5.1}$$

$$\text{population mean} = \mu = \frac{1}{N}\sum_{i=1}^{N} X_i \tag{5.2}$$

$$\text{population standard deviation} = \sigma = \sqrt{\frac{1}{N}\sum_{i=1}^{N}\left(X_i - \mu\right)^2} \tag{5.3}$$

$$\text{coefficient of variation} = CV = \frac{\sigma}{\mu} \times 100\% \tag{5.4}$$

Table 5.1: Descriptive statistics for measured parameters.

Measured Variable	Statistic	Planar Interface Forging Coupons and Initial 2D Method	Planar Interface Forging Coupons and Refined 2D Method	Curved Interface Forging Coupons and Refined 2D Method	Curved Interface Forging Coupons and 3D Method
Gain Settings to Achieve 80%FSH (dB)	range	12.2	14.3	8.6	12.7
	μ	23.0	21.9	27.4	25.4
	σ	3.3	4.0	2.4	3.9
	CV	14%	18%	9%	15%
Peak Signal Amplitudes at a Fixed Gain (%FSH)	range	55.7	73.3	29.6	47.7
	μ	53.6	62.1	31.5	41.5
	σ	15.4	21.6	8.1	14.7
	CV	29%	35%	26%	35%
Horizontal Beam Widths (inches)	range	0.018	0.010	0.017	0.028
	μ	0.038	0.035	0.020	0.029
	σ	0.006	0.003	0.005	0.007
	CV	16%	10%	23%	25%
Vertical Beam Widths (inches)	range	0.017	0.010	0.078	0.052
	μ	0.038	0.035	0.056	0.050
	σ	0.006	0.003	0.022	0.016
	CV	15%	8%	38%	32%
Average Noise Amplitudes (%FSH)	range	17.9	19.05	30.92	25.81
	μ	7.1	7.1	12.5	15.7
	σ	5.1	5.3	7.9	6.9
	CV	71%	74%	63%	44%
Signal-to-Noise Ratio (unitless)	range	28.9	26.8	15.1	8.0
	μ	15.9	16.1	8.4	6.0
	σ	7.9	7.7	4.0	2.3
	CV	50%	48%	47%	38%
FBH Diameter Inspection Sensitivity (inches)	range	0.0026	0.0027	0.0033	0.0026
	μ	0.0022	0.0022	0.0030	0.0034
	σ	0.0007	0.0007	0.0008	0.0007
	CV	33%	34%	28%	21%

Wilcoxon Matched Pairs Signed Rank Hypothesis Test

In addition to making comparisons of the data sets based on descriptive statistics, statistical hypothesis testing will be performed in the form of the Wilcoxon matched pairs signed rank test. This test will be performed on the medians of six measured parameters, namely gain settings at fixed amplitude, horizontal and vertical beam widths, average noise amplitudes, SNR and FBH diameters for inspection sensitivity. Peak amplitudes will not be tested, as this parameter is simply a rescaling of gain settings at fixed amplitude. Each inspection data set was assigned a subscript designator as defined in Table 5.2 and illustrated in Figure 5.1. The Wilcoxon matched pair signed rank test is a non-parametric test that does not depend upon the data having a normal or Gaussian population distribution, and is relatively powerful compared to other non-parametric tests in that it takes into account both the signs of the difference and the magnitude of differences between pairs of observations. The measured parameters from the c-scan images presented in Chapter 4 are not assumed to have Gaussian, i.e., normal, distributions. This approach is based upon having a relatively low number of data points for each measured parameter, i.e., 12, as well as noting that the measured parameters presented in Figures 4.1 through 4.5 appear to be, in general, skewed rather than symmetric as found in normally distributed data. [21].

To compare two inspection methods with this test, matched pairs are constructed by taking the difference between measured values collected from FBHs located at common material depths when using two inspection methods. These matched pairs are then ranked by their magnitudes, with the sum of ranks from positive differences providing the test statistic for hypothesis testing. The Wilcoxon signed rank test for paired observations when not using large samples, i.e., when paired observations are not greater than 20, will be performed as follows [22, 23]:

1. For each matched pair (X_1, Y_1), …, (X_n, Y_n), record the differences $D_1 = X_1 - Y_1$, …, $D_n = X_n - Y_n$.
2. Rank these differences in order of magnitude, ignoring the signs of the differences. For differences that are tied, give each the average of the tied ranks.
3. Add the ranks for positive and negative differences separately. Check that they add together to give $(1/2) N (N+1)$.
4. The null hypothesis is H_0: $\mu_X = \mu_Y$.
5. The test statistic T is the sum of the ranks associated with the positive differences.
6. Using critical values c_1 and c obtained from Appendix A.9 of Reference 23, then for alternative hypotheses, H_a
    a. H_a: $\mu_X > \mu_Y$ and the rejection region for level α test is $T \geq c_1$.
    b. H_a: $\mu_X < \mu_Y$ and the rejection region for level α test is $T \leq c_2$, where $c_2 = N(N+1)/2 - c_1$.
    c. H_a: $\mu_X \neq \mu_Y$ and the rejection region for level α test is either $T \geq c_1$ or $T \leq c_2$.

Table 5.2: Designations for inspection data groups during statistical hypothesis testing.

Inspection Data Groups	Group Designator
Planar Interface Forging Coupons and Initial 2D Method	W
Planar Interface Forging Coupons and Refined 2D Method	X
Curved Interface Forging Coupons and Refined 2D Method	Y
Curved Interface Forging Coupons and 3D Method	Z
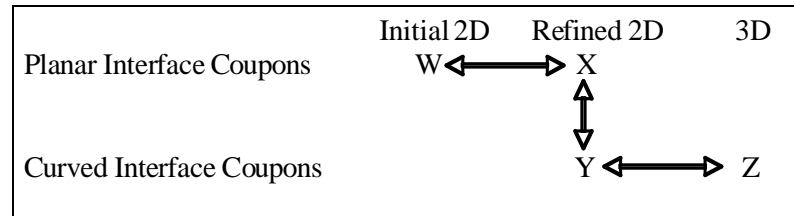
Figure 5.1: Pairs of inspection data groups to be evaluated using Wilcoxon Hypothesis Tests.

The hypothesis tests performed have a null hypothesis, H_0, which states that the difference in means for each parameter is zero. If H_0 is rejected, the alternative hypothesis, H_a, suggests that there is statistical evidence that the means are different, where the type of difference depends upon the alternative hypothesis used in the test. If H_0 is not rejected, no statistical evidence exists. Table 5.3 defines the null and three alternative hypotheses for each comparison being made when comparing inspection data groups.

A level of significance, α, of 0.10 was selected for each hypothesis test, i.e., the confidence level is 90% that the null hypothesis will not be rejected, prior to the hypothesis tests being performed. Each test has 12 data points, so the addition of the ranks for both positive and negative differences must be verified to equal $1/2\ n\ (n + 1) = 1/2\ (12)\ (12 + 1) = 78$.

The Wilcoxon signed rank test for 12 data points is used to define the rejection region for these alternative hypotheses. The critical values c_1 and c_2 equal 56 and 22, respectively, in one-sided significance level 0.10 tests and equal 61and 17, respectively, for two-sided significance level 0.10 tests [24].

The Wilcoxon matched pair signed rank test was performed for the paired inspection data groups for each of the measured parameters: gain setting at fixed amplitude, horizontal beam width, vertical beam width, average noise amplitude, signal-to-noise ratio, and FBH diameter inspection sensitivity. Tables 5.4 through 5.9 tabulate the differences between matched pairs along with the ranking of the signed differences for each of the paired inspection data groups being compared. The tabulated differences have the same units as the measured parameter, while ranking is based on the magnitudes of the differences.

Table 5.3: Null and alternative hypotheses for statistical comparison of the means of measured parameters.

Groups Compared	Null Hypothesis	Alternative Hypothesis #1	Alternative Hypothesis #2	Alternative Hypothesis #3
W and X	H_0: $\mu_W = \mu_X$	H_a: $\mu_W > \mu_X$	H_a: $\mu_W < \mu_X$	H_a: $\mu_W \neq \mu_X$
X and Y	H_0: $\mu_X = \mu_Y$	H_a: $\mu_X > \mu_Y$	H_a: $\mu_X < \mu_Y$	H_a: $\mu_X \neq \mu_Y$
Y and Z	H_0: $\mu_Y = \mu_Z$	H_a: $\mu_Y > \mu_Z$	H_a: $\mu_Y < \mu_Z$	H_a: $\mu_Y \neq \mu_Z$

Table 5.4: Gain setting Wilcoxon test for differences in mean values.

Block #	W – X Differences (dB)	W – X Ranking	X – Y Differences (dB)	X – Y Ranking	Y – Z Differences (dB)	Y – Z Ranking
2	-0.3	2	0.0	1	-1.7	2
3	-0.3	1	-4.0	5	-0.6	1
4	-0.5	4	-4.3	6	-0.6	3
5	-0.6	5	-4.1	2	1.5	4
6	0.4	3	-4.8	4	1.7	5
7	0.9	9	-6.0	9	2.4	6
8	1.1	11	-5.9	8	2.1	7
9	1.9	7	-2.5	3	2.4	9
10	2.8	10	-6.0	7	0.9	8
11	3.0	12	-8.6	11	6.6	12
12	2.4	6	-9.9	12	5.0	11
13	1.8	8	-9.5	10	4.0	10

Table 5.5: Horizontal beam width Wilcoxon test for differences in mean values.

Block #	W – X Differences (inches)	W – X Ranking	X – Y Differences (inches)	X – Y Ranking	Y – Z Differences (inches)	Y – Z Ranking
2	-0.0014	2	0.0068	1	-0.0171	12
3	-0.0016	3	0.0076	2	-0.0047	3
4	0.0001	1	0.0110	4	-0.0046	2
5	-0.0018	4	0.0112	5	-0.0031	1
6	0.0022	6	0.0118	6	-0.0058	4
7	0.0019	5	0.0090	3	-0.0118	10
8	0.0031	7	0.0157	7	-0.0076	7
9	0.0070	9	0.0201	10	-0.0062	5
10	0.0088	12	0.0203	11	-0.0115	9
11	0.0080	11	0.0215	12	-0.0066	6
12	0.0072	10	0.0184	9	-0.0128	11
13	0.0056	8	0.0178	8	-0.0105	8

Table 5.6: Vertical beam width Wilcoxon test for differences in mean values.

Block #	W – X Differences (inches)	W – X Ranking	X – Y Differences (inches)	X – Y Ranking	Y – Z Differences (inches)	Y – Z Ranking
2	-0.0001	1	-0.0129	5	-0.0090	9
3	-0.0004	4	0.0060	2	-0.0004	2
4	-0.0018	6	-0.0028	1	0.0048	7
5	0.0003	3	-0.0138	6	0.0103	10
6	0.0002	2	-0.0071	3	0.0041	6
7	0.0016	5	-0.0119	4	0.0052	8
8	0.0026	7	-0.0155	7	-0.0010	3
9	0.0085	11	-0.0195	8	0.0032	4.5
10	0.0065	9	-0.0244	9	0.0002	1
11	0.0050	8	-0.0502	11	0.0283	12
12	0.0089	12	-0.0675	12	0.0256	11
13	0.0084	10	-0.0365	10	0.0032	4.5

Table 5.7: Average noise amplitude Wilcoxon test for differences in mean values.

Block #	W – X Differences (%FSH)	W – X Ranking	X – Y Differences (%FSH)	X – Y Ranking	Y – Z Differences (%FSH)	Y – Z Ranking
2	-1.33	8	-13.86	12	2.01	4
3	-1.70	11	-3.91	4	0.06	1
4	-1.47	9	-0.71	3	-1.67	3
5	-0.14	1	-4.61	7	-0.77	2
6	-0.41	4	-0.59	2	-4.19	8
7	0.16	2	-4.09	5	-3.47	6
8	-0.18	3	-4.44	6	-5.83	10
9	1.58	10	-7.49	8	-5.31	9
10	1.84	12	-8.44	10	-6.47	12
11	0.67	5	-7.62	9	-6.17	11
12	0.88	6	-9.02	11	-3.93	7
13	1.00	7	-0.04	1	-3.26	5

Table 5.8: Signal-to-noise ratio Wilcoxon test for differences in mean values.

Block #	W – X Differences (unitless)	W – X Ranking	X – Y Differences (unitless)	X – Y Ranking	Y – Z Differences (unitless)	Y – Z Ranking
2	0.24	1	1.44	2	-0.14	2
3	2.86	8	3.42	5	-0.04	1
4	5.72	12	1.76	3	2.87	9
5	0.48	3	7.87	7	0.63	3
6	2.26	7	2.55	4	8.26	12
7	-1.08	5	13.07	10	3.41	10
8	2.25	6	19.20	12	5.13	11
9	-5.40	11	12.57	9	2.17	7
10	-4.27	10	9.99	8	1.93	6
11	-4.00	9	16.65	11	2.63	8
12	-0.69	4	3.97	6	0.74	4
13	-0.45	2	0.02	1	1.26	5

Table 5.9: FBH diameter inspection sensitivity Wilcoxon test for differences in mean values.

Block #	W – X Differences (inches)	W – X Ranking	X – Y Differences (inches)	X – Y Ranking	Y – Z Differences (inches)	Y – Z Ranking
2	-0.00013	7	-0.00114	9	0.00015	3
3	-0.00028	9	-0.00055	4	0.00001	1
4	-0.00030	10	-0.00013	3	-0.00028	4
5	-0.00003	1	-0.00076	5	-0.00011	2
6	-0.00009	4	-0.00012	2	-0.00072	10.5
7	0.00004	2	-0.00078	6	-0.00050	7
8	-0.00005	3	-0.00091	7	-0.00082	12
9	0.00031	11	-0.00120	10	-0.00062	8
10	0.00033	12	-0.00125	11	-0.00069	9
11	0.00015	8	-0.00130	12	-0.00072	10.5
12	0.00012	5.5	-0.00106	8	-0.00038	6
13	0.00012	5.5	0.00000	1	-0.00037	5

Comparison of Inspections – Planar Interface Forging Coupons

The purpose of inspections of the planar interface forging coupons was to evaluate whether or not the precise numerical method used by the refined 2D ray-tracing algorithm to take into account refraction at the water-forging interface reduced a source of focusing aberration thought to exist within the initial 2D ray-tracing algorithm due to its use of the small angle approximation when calculating for refraction.

Rectilinear scans of planar interface forging coupons 2 through 13 were performed using sets of delay times generated by the initial and refined 2D ray-tracing algorithms. Delay time sets from the initial and refined 2D methods used in inspections of the planar interface coupons were presented in Chapter 3 of this dissertation, where a direct comparison of the time delay sets showed that a significant delay time difference existed relative to the phasing, i.e., delay time, resolution hardware limit of available phased array instrumentation. This difference between the delay time sets suggests that, upon examination of the inspection data gathered using these two methods, a comparison can be made which will lead to one of these two ray-tracing algorithms being judged an improvement over the other.

A purely qualitative evaluation of the C-scan bitmap images previously presented for each planar interface forging coupon (see Tables 4.10 through 4.13) shows all 12 coupons to have a very similar beam size and shape when comparing the same planar interface forging coupon inspected using either the initial and refined 2D method.

A quantitative evaluation of the horizontal and vertical half-maximum-amplitude beam widths measured in the initial and refined 2D inspection images of the planar interface forging coupons supports these qualitative observations (see Table 5.1). However, each descriptive statistic for both beam width data sets is slightly smaller in the refined 2D method inspection relative to the initial 2D method inspection. The mean statistic of both beam width data sets is 8% smaller for the refined 2D inspections as compared to the initial 2D inspections. The beam width coefficients of variation between the two methods show a 36-47% smaller value for the refined 2D inspections.

Individual values of the horizontal and vertical beam width data are similar for FBHs less than 1-inch in depth in the planar interface forging coupons. At greater FBH depths, the refined 2D inspections provided slightly smaller beam widths relative than those found in the initial 2D inspection results.

Relatively low gain settings required to reach chosen target peak signal amplitude are desirable in ultrasonic inspections, as these lead to an improved signal-to-noise ratio. Examination of the signal amplifier gain settings required to achieve a fixed peak signal amplitude of 80% Full-Screen-Height (%FSH), previously presented in Table 4.14, shows a maximum difference of 2.8 dB between initial and refined 2D inspections of the same planar interface forging coupon. For FBHs less than 1-inch in depth, the initial 2D method inspections had slightly smaller gain settings. At greater FBH depths, the refined 2D method inspections had slightly smaller gain settings.

Given the logarithmic scale of decibels, the units of signal amplitude gain, it can be helpful when evaluating inspection data to convert from logarithmically-scaled gains settings recorded for a fixed peak signal amplitude to a set of linearly-scaled peak amplitudes at a fixed gain setting. Fixed gain peak signal amplitude data (see Table 4.15 and Figure 4.1) shows that coupons 2 thru 5, with FBHs less than 1-inch-deep, of the planar interface forging coupons have relatively higher peak signal amplitude responses in the initial 2D method inspections when compared to the refined 2D method inspections. However, coupons 6 and 13, with FBHs greater than 1-inch-deep, have peak signal amplitudes slightly higher in the refined 2D method inspections relative to the initial 2D method inspections.

Statistically, the mean gain setting at fixed amplitude is 1.1 dB lower for the refined 2D method inspections as compared to the initial 2D method inspections while, given the inverse relationship between gains at fixed amplitude and amplitudes at fixed gain, the means peak signal amplitude at fixed gain is 8.5 %FSH higher for the refined 2D inspections as compared to the mean of the initial 2D inspections. The three descriptive statistics range, standard deviation, and coefficient of variation each show relatively lower values in the gain and amplitude data for the refined 2D method inspections of planar interface forging coupons than that recorded for the initial 2D method inspections.

Average noise amplitudes from the C-scan images (see Table 4.18) are lower in 50% of the 12 refined 2D method inspections of planar interface forging coupons, including inspections of those coupons with the 5 deepest FBHs, as compared to the same coupons being inspected with the initial 2D method.

Signal-to-noise ratios (SNR), defined in this dissertation to be the peak signal amplitude divided by the average noise amplitude from each C-scan image (see Equation 4.3), were presented previously in Table 4.19 and plotted in Figure 4.4. Of the 12 planar interface forging coupons inspected with the refined 2D method, 50% provided a greater SNR, including inspections of those coupons with the 5 deepest FBHs, as compared to the initial 2D method inspections.

The Wilcoxon matched pair signed rank test was performed, with the signed differences and rankings previously tabulated in Tables 5.4 through 5.9. Table 5.10 provides the sum of rankings and test statistic T for each test when comparing groups W and X, i.e., the initial and refined 2D methods.

Table 5.11 summarizes the Wilcoxon hypothesis test results for the six measured parameters presented in Tables 5.4 through 5.9, tabulating whether or not the null hypothesis, H_0, was rejected based on the rejection region for each of three alternative hypotheses.

Table 5.10: Summary of sum of ranks and test statistic, *T*, for comparing groups W and X.

Measured Parameter	Sum of Ranks	Test statistic, *T*
Gain to achieve fixed peak amplitude	78	66
Horizontal beam width	78	69
Vertical beam width	78	67
Average noise amplitude	78	42
Signal-to-noise ratio	78	18.5
FBH diameter for inspection sensitivity	78	44

Table 5.11: Wilcoxon matched pair signed rank hypothesis tests for comparing groups W and X.

Measured Parameter	H_0: $\mu_W = \mu_X$ 1st H_a: $\mu_W > \mu_X$ with Rejection Region $T \geq 56$	H_0: $\mu_W = \mu_X$ 2nd H_a: $\mu_W < \mu_X$ with Rejection Region $T \leq 22$	H_0: $\mu_W = \mu_X$ 3rd H_a: $\mu_W \neq \mu_X$ with Rejection Region $T \geq 61$ or $T \leq 17$
Gain setting	Reject H_0	Do Not Reject H_0	Reject H_0
Horizontal beam width	Reject H_0	Do Not Reject H_0	Reject H_0
Vertical beam width	Reject H_0	Do Not Reject H_0	Reject H_0
Average noise amplitude	Do Not Reject H_0	Do Not Reject H_0	Do Not Reject H_0
Signal-to-noise ratio	Do Not Reject H_0	Reject H_0	Do Not Reject H_0
Inspection sensitivity	Do Not Reject H_0	Do Not Reject H_0	Do Not Reject H_0

These Wilcoxon matched pair signed rank test results provide evidence at a level of significance of 0.10 that the measured parameters gain setting and both beam widths have dissimilar means when comparing group W and group X, due to the null hypothesis always being rejected for the third alternative hypothesis. Additionally, for these three parameters, the null hypothesis was rejected for the first alternative hypothesis but not the second alternative hypothesis. Therefore, statistical evidence suggests that group W has larger mean values for gain setting, horizontal beam width, and vertical beam width.

For the parameter SNR, the null hypothesis was rejected for the second alternative hypothesis, thereby providing statistical evidence that group W has a smaller mean value when compared to group X.

Table 5.12 summarizes the statistical evidence provided by these hypothesis tests between groups W and X. For an inspection method to show improvement over another, gain setting should decrease, vertical and/or horizontal beam widths should decrease, average noise amplitude should decrease, SNR should increase, or FBH diameters for inspection sensitivity should decrease or meet targeted inspection requirements. The evidence suggests that, relative to group X, group W has mean values that are larger for gain setting, larger for horizontal beam width, larger for vertical beam widths, and smaller for SNR.

Therefore, this dissertation concludes that the refined 2D ray-tracing algorithm reduces a source of focusing aberration significantly as compared to the initial 2D ray-tracing algorithm by more accurately calculating the refraction effect at the water-forging interface during inspections of planar interface forging coupons containing #1/2 FBHs at material depths ranging from 0.2 to 2.7 inches when using the 10 MHz, compound spherical, segmented, annular phased array described in Appendix A.

Table 5.12: Summary of statistical evidence from hypothesis tests when comparing groups W and X.

Measured Parameter	Evidence that $\mu_W > \mu_X$?	Evidence that $\mu_W < \mu_X$?	Evidence that $\mu_W \neq \mu_X$?
Gain setting	Yes	No evidence available	Yes
Horizontal beam width	Yes	No evidence available	Yes
Vertical beam width	Yes	No evidence available	Yes
Average noise amplitude	No evidence available	No evidence available	No evidence available
Signal-to-noise ratio	No evidence available	Yes	No evidence available
Inspection sensitivity	No evidence available	No evidence available	No evidence available

Comparison of Inspections – Refined 2D Ray-tracing Algorithm

By comparing the inspection results of the planar interface forging coupons with the inspection results of the curved interface forging coupons, when the refined 2D method is used during both sets of inspections, an evaluation was performed on the cylindrically curved ultrasonic mirror designed for surface curvature compensation during inspections of curved interface forging coupons. The comparison of group X inspections with group Y inspections will be used to determine whether or not this mirror is a source of focusing aberrations.

A single set of delay times generated by the refined 2D method was used during inspections of planar interface forging coupons without using a mirror and during inspections of curved interface forging coupons when using a mirror for surface compensation. The delay times sets generated by the refined 2D ray-tracing algorithm for rectilinear inspections of the planar interface forging coupons 2 through 13 were also used during rotational-radial scans of the curved interface forging coupons 2 through 13 along with the surface compensating mirror. The measured longitudinal sound velocities of both sets of planar and curved interface forging coupons (see Tables 2.2 and 3.1, respectively) show minor differences between forging coupons with FBHs at similar depths. Two sets of delay times were generated by the refined 2D method (see Tables 3.5 and 3.6, respectively) when using the two different sets of measured sound velocities. The refined 2D algorithm delay time sets for both the planar and curved interface forging coupons have values with a maximum difference of 3 nanoseconds when focusing at similar material depths (see Figure 3.5). This delay time difference is very near the phased array instrumentation delay time resolution limit of 2 nanoseconds. However, in addition to evaluating the performance of the surface compensating mirror, empirical evidence was needed to determine if the difference in delay time sets is, or is not, a minor influence during inspections of the two coupon sets when using the refined 2D inspection method.

A qualitative evaluation of the C-scan bitmap images previously presented for each set of refined 2D method inspections, one set taken from inspections of the planar interface forging coupons and another set from the curved interface forging coupons (see Tables 4.10 through 4.13), shows most images to have dissimilar beam size or shape when comparing coupons having FBH reflectors at a common material depth. Only the C-scan images from coupons 2 and 9 from both coupon sets show relatively circular beam shapes when using the refined 2D method. It is also observed that, while the beam spots for the planar interface forging coupons are generally circular in shape, the beam spots for the curved interface forging coupons 10 thru 13 are generally elliptical in shape with their major axis in the diagonal, or radial-rotational, direction.

Examination of the statistics presented in Table 5.1 shows the average value of the vertical half-maximum-amplitude beam widths to be 60% smaller in the planar coupon inspections than in the curved coupon inspections when using the refined 2D method. However, the average value of horizontal beam widths is 56% smaller for the curved coupon inspections. The three descriptive statistics range, standard

deviation, and coefficient of variation for both horizontal and vertical beam widths show more variability for the curved coupon inspections than that recorded for the planar coupon inspections.

When examining individual values, the horizontal beam width measurements show all refined 2D inspections of both planar and curved forging coupon sets provided smaller beam widths for the curved coupon inspections than those found in the planar coupon inspection results. The vertical beam width data are nearly as consistent, but reversed, as all but one of the 12 planar coupon inspections had a smaller beam width than that measured in the curved coupon inspections when using the refined 2D method.

Examination of the signal amplifier gain settings required to achieve a fixed peak signal amplitude of 80%FSH, previously presented in Table 4.14, indicates that a relatively lower, sometimes significantly lower, gain setting was required for planar coupons 3 thru 13 when compared to the curved coupon set when using the refined 2D method. Curved coupon 2 required the same gain setting as its planar coupon counterpart. A maximum gain setting difference of 9.9 dB was recorded between planar and curved coupons with FBHs having similar depths.

Fixed gain peak signal amplitude data (see Table 4.15 and Figure 4.1) shows that all of the planar coupons, excluding coupon 2, have relatively higher peak amplitudes when compared to the curved coupons when using the refined 2D method. The mean peak amplitude at fixed gain is 30.6 %FSH greater for planar coupons relative to curved coupons. The three descriptive statistics range, standard deviation, and coefficient of variation each show that relatively more variability exists in the gain and amplitude data for the planar coupon inspections than that recorded for the curved coupon inspections when using the refined 2D method.

Average noise amplitudes from the C-scan images (see Table 4.18) are lower for all 12 planar coupons as compared to average noise amplitudes from inspections of the curved coupons when using the refined 2D method.

Similarly, SNR values (see Table 4.19 and Figure 4.4) are higher for all 12 planar coupons, as compared to the SNR from the curved interface forging coupons, in the refined 2D method inspections.

The Wilcoxon matched pair signed rank test was performed, with the signed differences and rankings previously tabulated in Tables 5.4 through 5.9. Table 5.13 provides the sum of rankings and test statistic T for each test when comparing groups X and Y.

Table 5.14 summarizes the Wilcoxon hypothesis test results for the six measured parameters presented in Tables 5.4 through 5.9, tabulating whether or not the null hypothesis, H_0, was rejected based on the rejection region for each of three alternative hypotheses.

These Wilcoxon matched pair signed rank test results provide evidence at a level of significance of 0.10 that all measured parameters, excluding SNR, are statistically dissimilar when comparing groups X and Y, due to the null hypothesis being rejected for the third alternative hypothesis.

Table 5.13: Summary of sum of ranks and test statistic, *T*, for comparing groups X and Y.

Measured Parameter	Sum of Ranks	Test statistic, *T*
Gain to achieve fixed peak amplitude	78	1
Horizontal beam width	78	78
Vertical beam width	78	2
Average noise amplitude	78	0
Signal-to-noise ratio	78	18.5
FBH diameter for inspection sensitivity	78	1

Table 5.14: Wilcoxon matched pair signed rank hypothesis tests for comparing groups X and Y.

Measured Parameter	H_0: $\mu_X = \mu_Y$ *1st* H_a: $\mu_X > \mu_Y$ with Rejection Region $T \geq 56$	H_0: $\mu_X = \mu_Y$ *2nd* H_a: $\mu_X < \mu_Y$ with Rejection Region $T \leq 22$	H_0: $\mu_X = \mu_Y$ *3rd* H_a: $\mu_X \neq \mu_Y$ with Rejection Region $T \geq 61$ or $T \leq 17$
Gain setting	Do Not Reject H_0	Reject H_0	Reject H_0
Horizontal beam width	Reject H_0	Do Not Reject H_0	Reject H_0
Vertical beam width	Do Not Reject H_0	Reject H_0	Reject H_0
Average noise amplitude	Do Not Reject H_0	Reject H_0	Reject H_0
Signal-to-noise ratio	Do Not Reject H_0	Reject H_0	Do Not Reject H_0
Inspection sensitivity	Do Not Reject H_0	Reject H_0	Reject H_0

For the parameters gain setting, vertical beam width, average noise amplitude, SNR and FBH diameters for inspection sensitivity, the null hypothesis was rejected for the second alternative hypothesis. Therefore, statistical evidence exists that group X has lower mean values for these measured parameters.

For the parameter horizontal beam width, the null hypothesis was rejected for the first alternative hypothesis. Therefore, statistical evidence exists that group X has a larger mean value for horizontal beam width than group Y.

The performance of the surface curvature compensating mirror as a source of focusing aberration is statistically evident in 4 of the 6 measured parameters, specifically improved mean values of gain setting, vertical beam width, average noise amplitude, and FBH diameter for inspection sensitivity for planar coupon inspections when compared to curved coupon inspections using a surface compensating mirror. In contrast, statistical evidence provided for horizontal beam width inspection data suggests this parameter is, on average, larger for planar coupon inspections.

Table 5.15 summarizes the statistical evidence provided by these hypothesis tests between groups X and Y. For a method to show improvement over another, gain setting should decrease, vertical and/or horizontal beam widths should decrease, average noise amplitude should decrease, SNR should increase, or FBH diameters for inspection sensitivity should decrease or meet targeted inspection requirements.

The statistical evidence suggests that, relative to group Y, group X has mean values that are smaller for gain setting, larger for horizontal beam width, smaller for vertical beam widths, smaller for average noise amplitude, smaller for SNR, and smaller for FBH diameters for inspection sensitivity.

Therefore, it is the conclusion of this dissertation that the surface curvature compensating mirror is a source of focusing aberration, albeit likely a minor source given the limited statistical evidence found.

Table 5.15: Summary of statistical evidence from hypothesis tests when comparing groups X and Y.

Measured Parameter	Evidence that $\mu_X > \mu_Y$?	Evidence that $\mu_X < \mu_Y$?	Evidence that $\mu_X \neq \mu_Y$?
Gain setting	No evidence available	Yes	Yes
Horizontal beam width	Yes	No evidence available	Yes
Vertical beam width	No evidence available	Yes	Yes
Average noise amplitude	No evidence available	Yes	Yes
Signal-to-noise ratio	No evidence available	Yes	No evidence available
Inspection sensitivity	No evidence available	Yes	Yes

Comparison of Inspections – Curved Interface Forging Coupons

The purpose of inspections of the curved interface forging coupons is to evaluate whether or not delay time sets generated from the 3D algorithm, a method using circumferential phasing of the transducer array, would significantly reduce sources of focusing aberrations when compared to inspections performed upon the curved interface forging coupons when using delay times generated by the refined 2D algorithm.

Rotational-radial scans of curved interface forging coupons 2 through 13 were performed using sets of delay times generated by the refined 2D and 3D ray-tracing algorithms. In this dissertation, delay time sets used in inspections of the curved interface forging coupons were previously presented in Table 3.6 for the refined 2D method as well as Tables D.2 and D.3 from Appendix D for the 3D method.

The results of inspections of curved interface forging coupons 2 through 13, containing #1/2 FBH reflectors ranging in depth from 0.2 inches to 2.7 inches were presented in Chapter 4 of this dissertation, with C-scan bitmap images of these inspections presented in Tables 4.10 through 4.13.

A purely qualitative evaluation of the two C-scan bitmap images for each curved coupon inspected using the refined 2D and 3D methods may be performed, where examination of the C-scans from both inspections shows a generally similar beam size and shape for all coupons if relatively low amplitudes are ignored in the 3D method inspections. While similar in overall appearance, a somewhat dispersed beam spot shape of relatively low amplitude signals for curved coupons 6 thru 13 can be easily seen.

Using the descriptive statistics found in Table 5.1, a quantitative evaluation of the horizontal and vertical half-maximum-amplitude beam widths measured in refined 2D and 3D inspection method images of curved coupons shows mean horizontal beam widths to be 45% larger for 3D method inspections than for refined 2D method inspections. However, the mean values for vertical beam widths are 12% larger for refined 2D method inspections than for 3D method inspections,

Examination of the signal amplifier gain settings required to achieve a fixed peak signal amplitude of 80%FSH, previously presented in Table 4.14, indicates that a relatively lower gain setting was required for coupons 5 thru 13 for 3D method inspections as compared to refined 2D method inspections. A maximum gain setting difference of 6.6 dB was recorded between refined 2D and 3D method inspections of curved coupon #11.

Fixed gain peak signal amplitude data (see Table 4.15 and Figure 4.1) shows that nearly all of the 3D method inspections, excluding coupons 2 thru 4, have relatively greater peak amplitudes when compared to the refined 2D method when inspecting the curved coupon set. The mean peak amplitude at fixed gain is 10.0 %FSH greater for 3D method inspections relative to refined 3D method inspections.

Average noise amplitudes from the C-scan images (see Table 4.18) are relatively lower for refined 2D method inspections of curved coupons 4 thru 13 when compared to 3D method inspections.

Similarly, SNR values (see Table 4.19 and Figure 4.4) are higher for 10 out of 12 curved coupons, excluding coupons 2 and 3, for the refined 2D method inspections relative to 3D method inspections.

The Wilcoxon matched pair signed rank test was performed, with the signed differences and rankings previously tabulated in Tables 5.4 through 5.9. Table 5.16 provides a sum of rankings and test statistic T for each test when comparing groups Y and Z.

Table 5.17 summarizes the Wilcoxon hypothesis test results for the six measured parameters presented in Tables 5.4 through 5.9, tabulating whether or not the null hypothesis, H_0, was rejected based on the rejection region for each of three alternative hypotheses.

These Wilcoxon matched pair signed rank test results provide evidence at a level of significance of 0.10 that the measured parameters gain setting, horizontal and vertical beam widths, average noise amplitude and FBH diameters for inspection sensitivity have dissimilar mean values when comparing groups Y and Z, due to the null hypothesis being rejected for the third alternative hypothesis.

For the parameters horizontal beam width, average noise amplitude, SNR, and FBH diameters for inspection sensitivity, the null hypothesis was rejected for the second alternative hypothesis, thereby providing statistical evidence that group Y has smaller mean values for these parameters than group Z.

For the parameters gain setting and vertical beam width, the null hypothesis was rejected for the first alternative hypothesis, thereby providing statistical evidence that group Y has larger mean values for these parameters than group Z.

Table 5.18 summarizes the statistical evidence provided by these hypothesis tests between groups Y and Z. For an inspection method to show improvement over another, gain setting must decrease, vertical and/or horizontal beam widths must decrease, average noise amplitude must decrease, SNR must increase, or FBH diameters for inspection sensitivity must decrease or meet targeted inspection requirements.

The statistical evidence suggests that, relative to group Z, group Y has mean values that are larger for gain setting, smaller for horizontal beam width, larger for vertical beam widths, smaller for average noise amplitude, smaller for SNR, and smaller for FBH diameters for inspection sensitivity.

Therefore, this dissertation concludes that the 3D ray-tracing algorithm reduces a source of focusing aberration as compared to the refined 2D ray-tracing algorithm by incorporating circumferential phasing during inspections of curved interface forging coupons containing #1/2 FBH reflectors at material depths ranging from 0.2 to 2.7 inches when using a surface curvature compensating mirror phasing of the 10 MHz, compound spherical, segmented, annular phased array described in Appendix A.

Table 5.16: Summary of sum of ranks and test statistic, *T*, for comparing groups Y and Z.

Measured Parameter	Sum of Ranks	Test statistic, *T*
Gain to achieve fixed peak amplitude	78	72
Horizontal beam width	78	0
Vertical beam width	78	64
Average noise amplitude	78	5
Signal-to-noise ratio	78	18.5
FBH diameter for inspection sensitivity	78	4

Table 5.17: Wilcoxon matched pair signed rank hypothesis tests for comparing groups Y and Z.

Measured Parameter	H_0: $\mu_Y = \mu_Z$ 1st H_a: $\mu_Y > \mu_Z$ with Rejection Region $T \geq 56$	H_0: $\mu_Y = \mu_Z$ 2nd H_a: $\mu_Y < \mu_Z$ with Rejection Region $T \leq 22$	H_0: $\mu_Y = \mu_Z$ 3rd H_a: $\mu_Y \neq \mu_Z$ with Rejection Region $T \geq 61$ or $T \leq 17$
Gain setting	Reject H_0	Do Not Reject H_0	Reject H_0
Horizontal beam width	Do Not Reject H_0	Reject H_0	Reject H_0
Vertical beam width	Reject H_0	Do Not Reject H_0	Reject H_0
Average noise amplitude	Do Not Reject H_0	Reject H_0	Reject H_0
Signal-to-noise ratio	Do Not Reject H_0	Reject H_0	Do Not Reject H_0
Inspection sensitivity	Do Not Reject H_0	Reject H_0	Reject H_0

Table 5.18: Summary of statistical evidence from hypothesis tests when comparing groups Y and Z.

Measured Parameter	Evidence that $\mu_Y > \mu_Z$?	Evidence that $\mu_Y < \mu_Z$?	Evidence that $\mu_Y \neq \mu_Z$?
Gain setting	Yes	No evidence available	Yes
Horizontal beam width	No evidence available	Yes	Yes
Vertical beam width	Yes	No evidence available	Yes
Average noise amplitude	No evidence available	Yes	Yes
Signal-to-noise ratio	No evidence available	Yes	No evidence available
Inspection sensitivity	No evidence available	Yes	Yes

Summary

Four sets of inspection data described and presented in previous chapters of this dissertation were used to perform 3 evaluations, including the statistical comparison of inspections of planar interface forging coupons when using the initial and refined 2D methods, inspections when using the refined 2D method upon both the planar and curved interface forging coupons with and without a surface compensating mirror, respectively, and inspections when using the refined 2D and 3D methods upon the curved interface forging coupons with a surface compensating mirror.

No direct evaluations were made between the 3D method inspections of curved forging coupons and either inspection of the planar forging coupons due to relative differences between these inspections, including disk forgings materials from which the coupon sets were cut, planar versus curved coupon interface conditions, use of the surface compensating mirror, and the ray-tracing algorithm employed, resulting in an inability to isolate dominant focusing aberrations during subsequent data analysis.

To aid in evaluating between inspection data sets, the parameters range, mean, standard deviation, and coefficient of variation were used to provide descriptive statistics for the measurement results given in the previous chapter. The Wilcoxon matched pairs signed rank test, a non-parametric, statistical hypothesis test useful for evaluating non-normally distributed data, was used to evaluate inspection methods via means of paired measurement parameters presented in Chapter 4 of this dissertation.

The measurement parameters evaluated to compare inspection data include signal amplifier gain setting, horizontal and vertical half-maximum-amplitude beam widths, average noise amplitude, SNR, and FBH diameters for inspection sensitivity.

This chapter concluded that the refined 2D method inspections significantly reduced a source of focusing aberration primarily due to statistical evidence being found that the means of gain setting, vertical beam width, and horizontal beam width were larger, and SNR smaller, for the initial 2D method when compared to the refined 2D method.

This chapter also concluded that the surface curvature compensating mirror is a minor source of focusing aberration primarily due to limited statistical evidence being found, including the means of gain setting, vertical beam width, average noise amplitude being statistically smaller during planar coupon inspections as compared to curved coupon inspections when using the refined 2D inspection method.

Finally, this chapter concluded that the 3D method inspections reduced a source of focusing aberration primarily due to statistical evidence being found that the mean of gain setting was larger, and the mean of SNR was smaller, for the refined 2D method when compared to the 3D method during inspections of curved coupons.

Ideas for Future Research

This dissertation studies an improved method for detecting flaws in critical rotating components of gas engine turbines, seeking to increase flaw sensitivity in aerospace titanium alloys to improve flight safety. The expectation of the performance of this improved method, the circumferential phasing of a segmented, annular phased array transducer, was greater than that actually realized in this dissertation. Specifically stated, the circumferential phasing method when used with a surface compensating mirror on the curved interface forging coupons was expected to rival the performance of the refined 2D method when inspecting the planar interface forging coupons without using a mirror. Instead, this dissertation presented results showing 1) a minor source of focusing aberration for curved coupon inspections when using a mirror as compared to planar coupon inspections without a mirror, and 2) only three out of six measured parameters provided statistical evidence that the 3D method exceeded the performance of the 2D refined method when inspecting curved coupons while both inspection methods used a surface compensating mirror.

In the interests of comparing the 3D method against its expected performance relative to the refined 2D inspections of planar interface coupons, Tables 5.19 through 5.21 summarize the Wilcoxon hypothesis test results for the six measured parameters when comparing groups X and Z.

Statistical evidence suggests that, relative to group Z, group X has mean values that are larger for horizontal beam width and smaller mean values for gain setting, vertical beam width, average noise amplitude, SNR, and FBH diameters for inspection sensitivity. This comparison between groups X and Z has statistical evidence similar to the previously presented comparison between groups Y and Z, with the exception that group X is now shown to have a smaller mean value for gain setting than group Z.

In terms of expected performance, the 3D inspections of curved coupons rival the 2D refined inspections of planar coupons only in terms of the measured parameters horizontal beam width and SNR. Possible reasons for this lack of expected performance of the 3D method include: incorrect registration of scan indices when multiple focal laws are used, issues associated with the fact that the forging coupon

Table 5.19: Summary of sum of ranks and test statistic, T, for comparing groups X and Z.

Measured Parameter	Sum of Ranks	Test statistic, T
Gain to achieve fixed peak amplitude	78	0
Horizontal beam width	78	56
Vertical beam width	78	9
Average noise amplitude	78	0
Signal-to-noise ratio	78	18.5
FBH diameter for inspection sensitivity	78	0

Table 5.20: Wilcoxon matched pair signed rank hypothesis tests for comparing groups X and Z.

Measured Parameter	H_0: $\mu_X = \mu_Z$ 1st H_a: $\mu_X > \mu_Z$ with Rejection Region $T \geq 56$	H_0: $\mu_X = \mu_Z$ 2nd H_a: $\mu_X < \mu_Z$ with Rejection Region $T \leq 22$	H_0: $\mu_X = \mu_Z$ 3rd H_a: $\mu_X \neq \mu_Z$ with Rejection Region $T \geq 61$ or $T \leq 17$
Gain setting	Do Not Reject H_0	Reject H_0	Do Not Reject H_0
Horizontal beam width	Reject H_0	Do Not Reject H_0	Reject H_0
Vertical beam width	Do Not Reject H_0	Reject H_0	Do Not Reject H_0
Average noise amplitude	Do Not Reject H_0	Reject H_0	Do Not Reject H_0
Signal-to-noise ratio	Do Not Reject H_0	Reject H_0	Reject H_0
Inspection sensitivity	Do Not Reject H_0	Reject H_0	Do Not Reject H_0

Table 5.21: Summary of statistical evidence from hypothesis tests when comparing groups X and Z.

Measured Parameter	Evidence that $\mu_X > \mu_Z$?	Evidence that $\mu_X < \mu_Z$?	Evidence that $\mu_X \neq \mu_Z$?
Gain setting	No evidence available	Yes	No evidence available
Horizontal beam width	Yes	No evidence available	Yes
Vertical beam width	No evidence available	Yes	No evidence available
Average noise amplitude	No evidence available	Yes	No evidence available
Signal-to-noise ratio	No evidence available	Yes	Yes
Inspection sensitivity	No evidence available	Yes	No evidence available

material is not isotropic and homogeneous as assumed when deriving focal law delay times in the ray-tracing algorithms, and questions of whether adding multiple C-scans for different focal laws would increase the vulnerability to electronic noise.

The inspections presented in this dissertation were either XY raster or radial-rotational scans. When multiple focal laws were required to inspect a specific forging coupon, A-scan waveforms were acquired separately, one after another, until the full data set was collected. In post-processing, these individual data sets were summed together to provide a final C-scan bitmap image. If the mechanical positioning of the transducer relative to the coupon under inspection is not sufficiently repeatable in terms of individual A-scan waveform collection points during these multiple acquisitions, the resultant post-processed data could be compromised and provide less-than-ideal inspection results.

A proposed alternative inspection setup may reduce or eliminate this potential source of focusing aberrations. The inspection data collected for this dissertation was from #1/2 FBH reflectors located at various depths within sets of forging coupons beneath planar or curved interfaces. Significant time, effort, and funds were required to fabricate these FBH coupon sets. An alternate setup for capturing measurement data on the performance of the ray-tracing algorithms presented in this dissertation would be to forego the use of FBHs altogether, instead preparing planar and curved interface coupons where the base of each coupon is cut along the plane of the flat tip of the FBH. In this proposed experimental setup, the transducer array would be oriented in position relative to a coupon's interface surface, and acquisition data collected via the pitch-catch ultrasonic method where the transmitting probe is the transducer array and the receiving probe would be a single element, large aperture, short focal length transducer focused on and mechanically scanning the base of the coupon being inspected. In this way, FBH fabricating costs and variability in their manufacture would be removed from the experiment, as well as significantly reducing the complexity of the original experimental setup.

The ray-tracing algorithms presented in this dissertation use longitudinal forging material velocities measured and averaged over a small volume from each of the forging coupons inspected. The forging material volume chosen for these velocity measurements is not fully identical to the ultrasonic beam path used during the forging coupon inspections, resulting in a potential source of focusing aberrations perhaps not fully addressed in this dissertation. Further study on gathering coupon and beam path specific material velocities can be used in the ray-tracing algorithms to calculate more realistic individual element delay time sets for inspection focal laws. Potential studies include measuring or calculating detailed velocity maps for each forging coupons as input into the ray-tracing algorithms, obtained by pre-scanning the forging coupon under inspection using single element transducers or by determining beam path velocity using the phased array transducer when oriented relative to the forging coupon just prior to inspection. Or, incorporating a form of model-based velocity maps into the ray-tracing algorithm may also be helpful.

Another potential source of focusing aberrations not explicitly investigated in this dissertation is the influence of electronic noise in the measurements, particularly when data from multiple focal laws was

acquired and summed for specific coupon inspections. The phased array instrumentation and transducer used to collect the inspection data in this dissertation appeared to have a relatively low level of electronic noise, relative to the other phased array instrumentation used by the author. However, the electronic noise level of the inspection system was not quantified nor was an analysis performed when summing A-scan waveforms in multiple focal law forging coupon inspections.

As the state of the art continues to evolve and, hopefully, generally advance, further work likely to require attention involves exploring and understanding the hardware limitations in ultrasonic phased array technology, especially with regards to the maximum number of delay times and total number of transducer elements available to be energized. It is suggested that the individual interested in the development of phased array technology follow changes in hardware from a technology-driven but also a customer-driven point-of-view. Current examples of technology-driven advancement are phased array instrumentation electronics becoming fully digitally based. While there are several functional benefits to this advancement, it has resulted is some losses of connectivity, specifically the loss of an RF signal output sometimes used to interface, i.e., slave, phased array instrumentation with other ultrasonic acquisition systems. Also, a current example of a customer-driven development is the small, lightweight, portable, user-friendly phased array inspection units with a built-in acquisition software interface being released to meet the current inspection market. Because these smaller units have a larger potential market than research-level phased array units, awareness that suppliers of phased array instrumentation and transducers appear to be focusing a significant portion of their internal resources on supporting these application efforts could prove helpful when trying to anticipate the further development of phased array technology.

APPENDIX A. PHASED ARRAY TRANSDUCER ELEMENT LAYOUT

This appendix contains the manufacturing specifications and individual element layout of the transducer array used for data collection in this dissertation. Three 10 MHz, 110-element, piezo-composite phased array transducers were fabricated by Imasonic SA of France (P/N CDC3446B-1 du 16/10/2003), S/Ns 3446-A101, 3446-B101, and 3446-B102. The transducer with S/N 3446-B101 was used in the acquisition of data in this dissertation. Figure A.1 shows the overall layout of the 36-ring transducer.

Each element of the transducer array is hardwired to an electronic channel leading to the phased array instrumentation. The technical specifications of a phased array transducer array necessarily include a schematic of this wiring to allow for the correct energizing and phasing of selected array elements. Each of the elements in the array has been uniquely identified with an element number corresponding to a hardware channel as shown in the numbering scheme provided in the following array element illustrations. The array has a total of thirty-six rings, numbered radially outwards from the innermost center element.
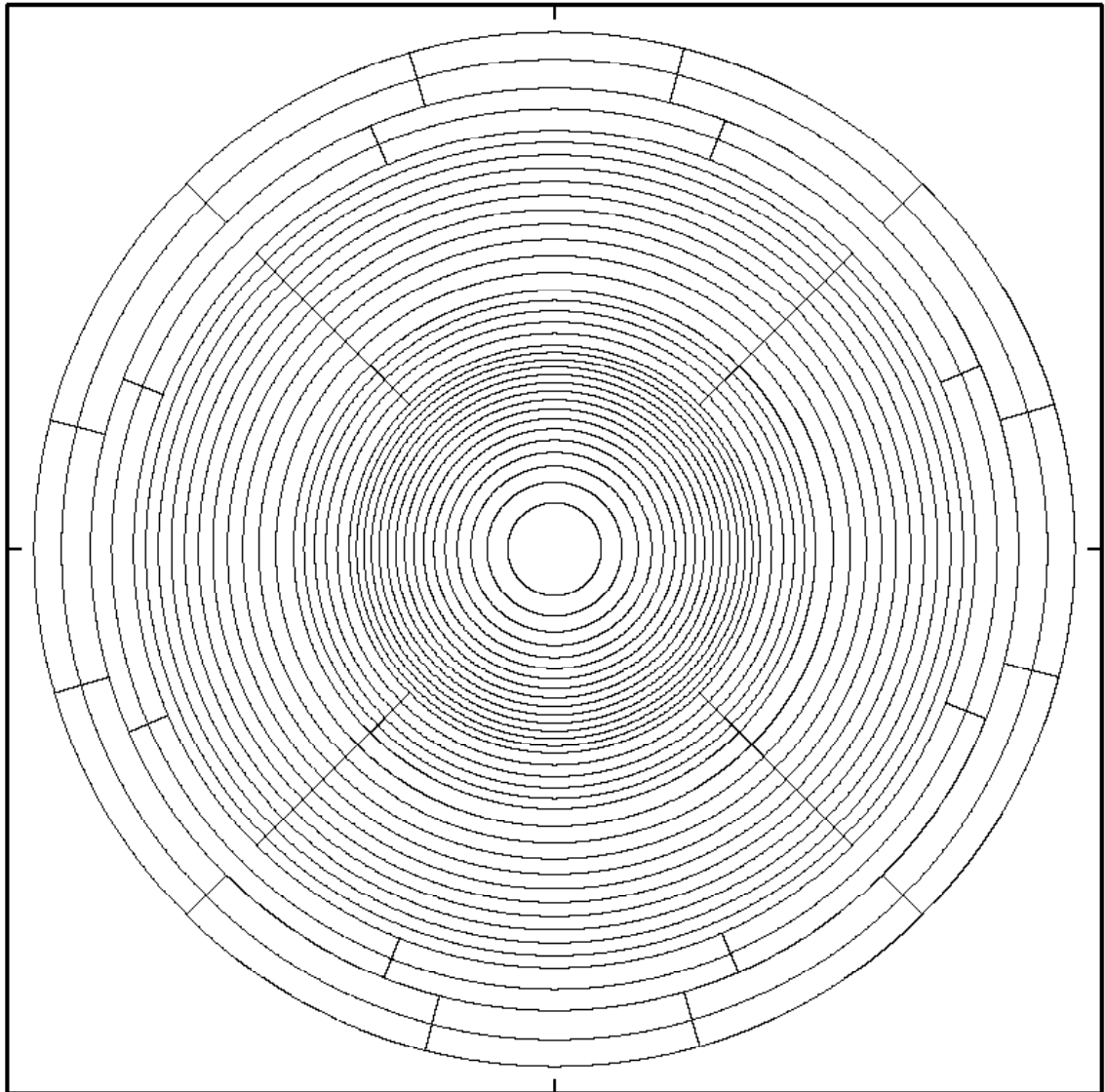
Figure A.1: Overall transducer element layout of the 36-ring segmented annular phased array.

The sixteen innermost rings of the transducer array consist of the single elements 1 through 16. These sixteen rings are not segmented. Note that the innermost element is considered to be the first ring (See Figure A.2).

Beginning with ring 17, each ring in the array is segmented equally by area into individual elements, although the amount of segmentation may vary. Rings 17 through 21 have each been segmented into four equal-area elements. Although these rings have four segments, each ring consists of only two numbered elements as symmetrically opposing array elements have been hardwired together. The five rings 17 through 21 of the transducer array consist of the ten elements 17-21 and 49-53 (See Figure A.3).

Similar to the element layout of rings 17 through 21, rings 22 through 32 have been segmented into four elements per ring. Unlike the elements in rings 17 through 21, each segment of rings 22 through 32 is individually hardwired to a unique electronic channel. Rings 22 through 32 consist of elements 22-32, 54-64, 86-96, and 118-128 (See Figure A.4).

The outer four rings of the transducer array, rings 33 through 36, are further segmented into a greater number of individual elements. Each element in rings 33 through 36 is directly associated with a
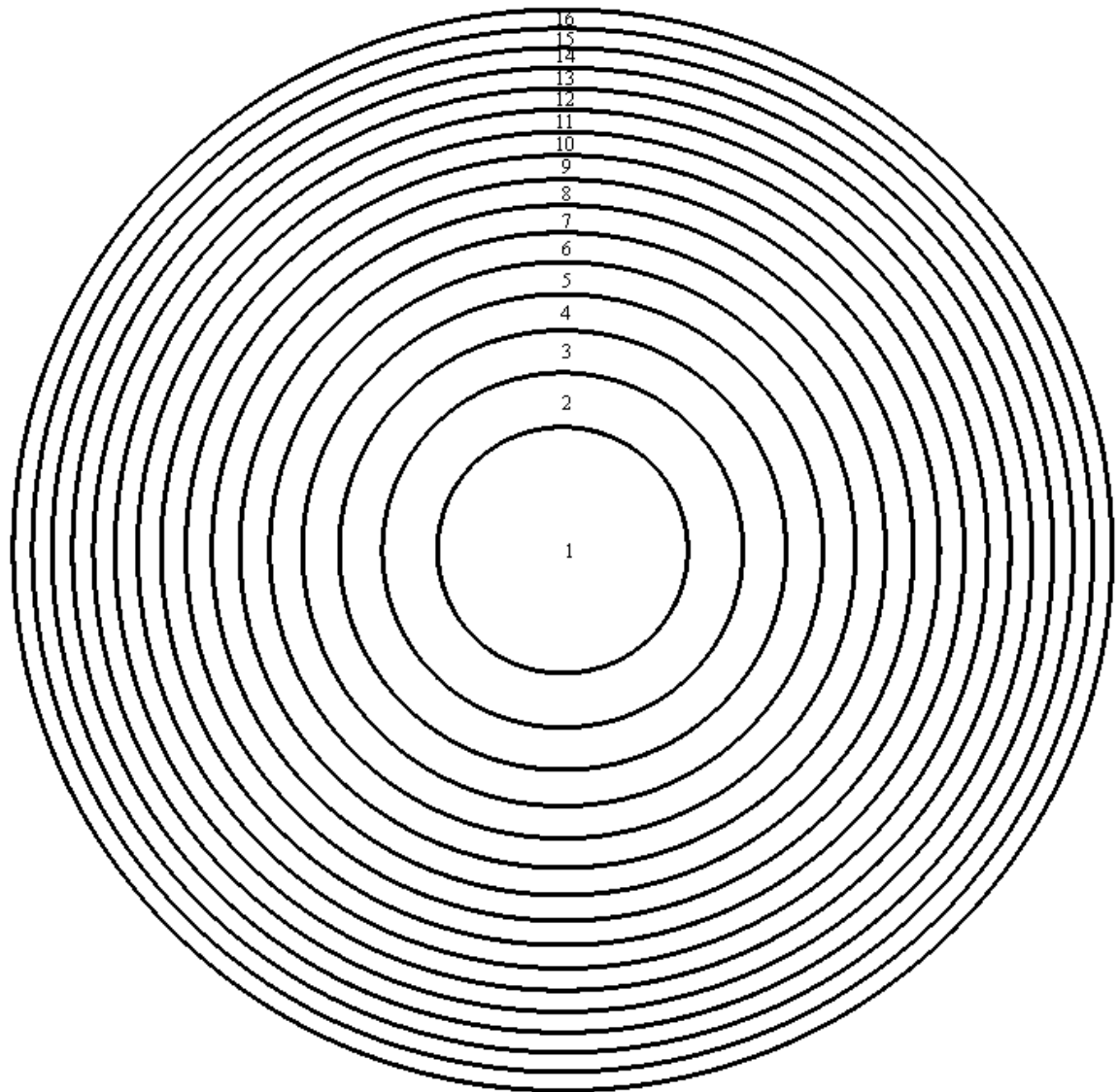
Figure A.2: Element layout of the inner 16 rings in the transducer array.

unique electronic channel. Rings 33 and 34 have been segmented equally into eight elements, whilst rings 35 and 36 have been segmented into twelve equal area elements. Overall, rings 33 through 36 consist of elements 65-84 and 97-116 (See Figure A.5).

Tabulated in Table A.1 are the dimensions of the rings in the transducer array, including radius, height, and width. Height is recorded at the outer radius of each annular ring. Height is recorded at the outer edge of each ring. Width is the annular element width, excluding an inter-element gap specified to be 0.12 mm.

The array includes the design feature of a compound spherical transducer face with three different radii of curvature (See Figure 2.11). The radius of curvature for the inner region consisting of rings 1 through 12 is 136.88 mm, while 283.73 mm is the radius of curvature for the middle region consisting of rings 13 through 26, and 418.62 mm is the radius of curvature for the inner region consisting of rings 27 through 36.

Figure A.3: Element layout of rings 17 through 21 in the transducer array.

Figure A.4: Element layout of rings 22 through 32 in the transducer array.
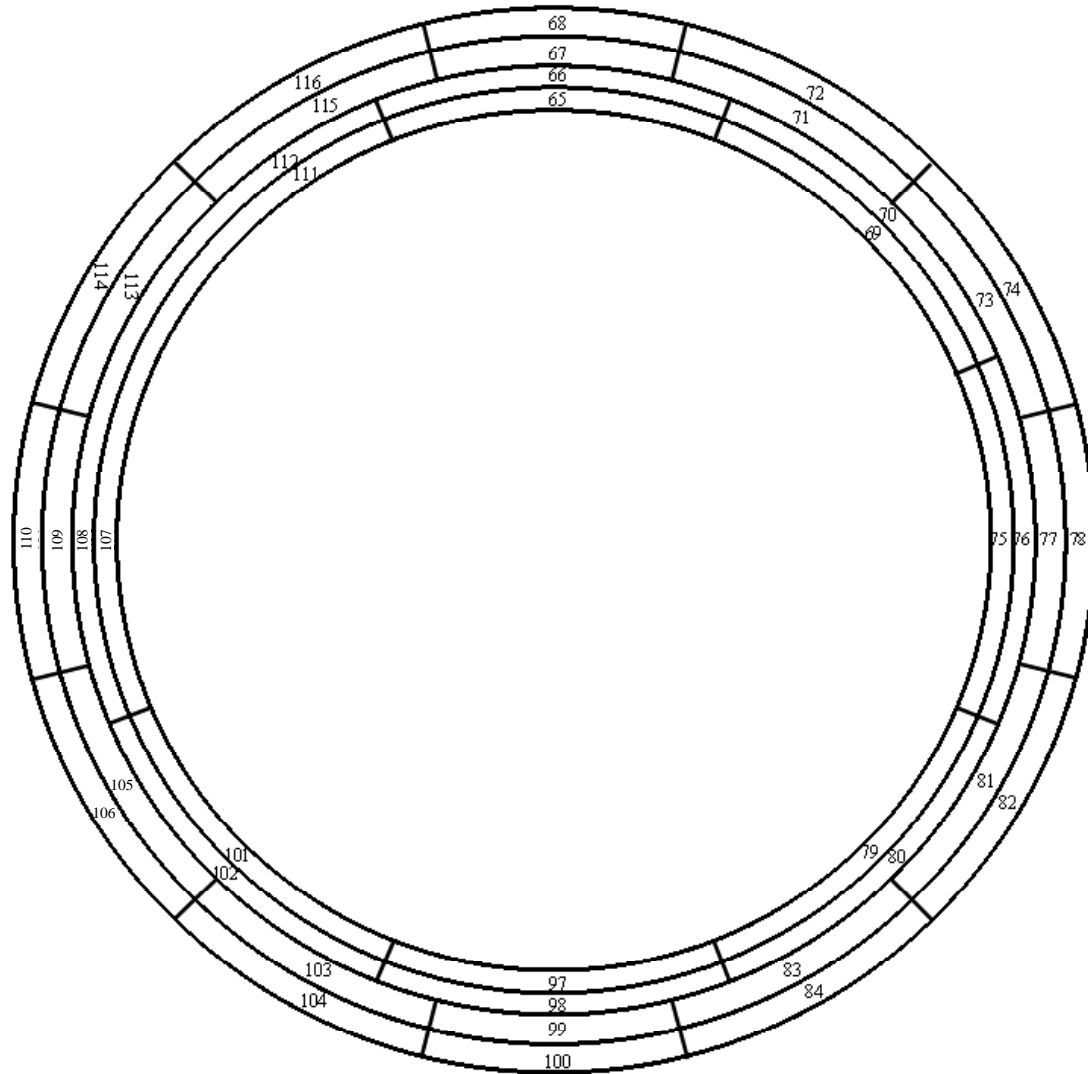
Figure A.5: Element layout of the 4 outermost rings in the transducer array.

Table A.1: Layout specifications for all rings in the transducer array.

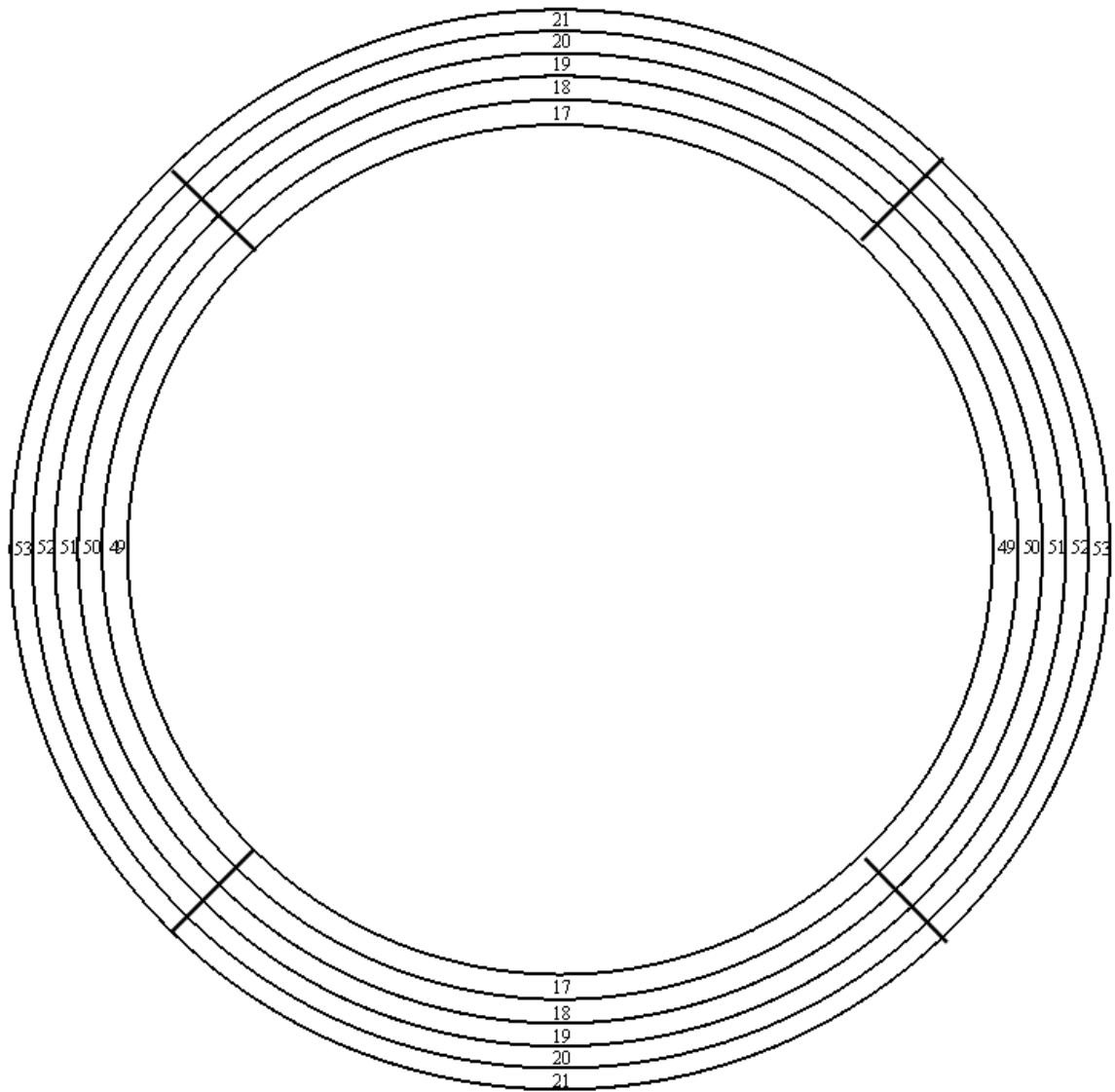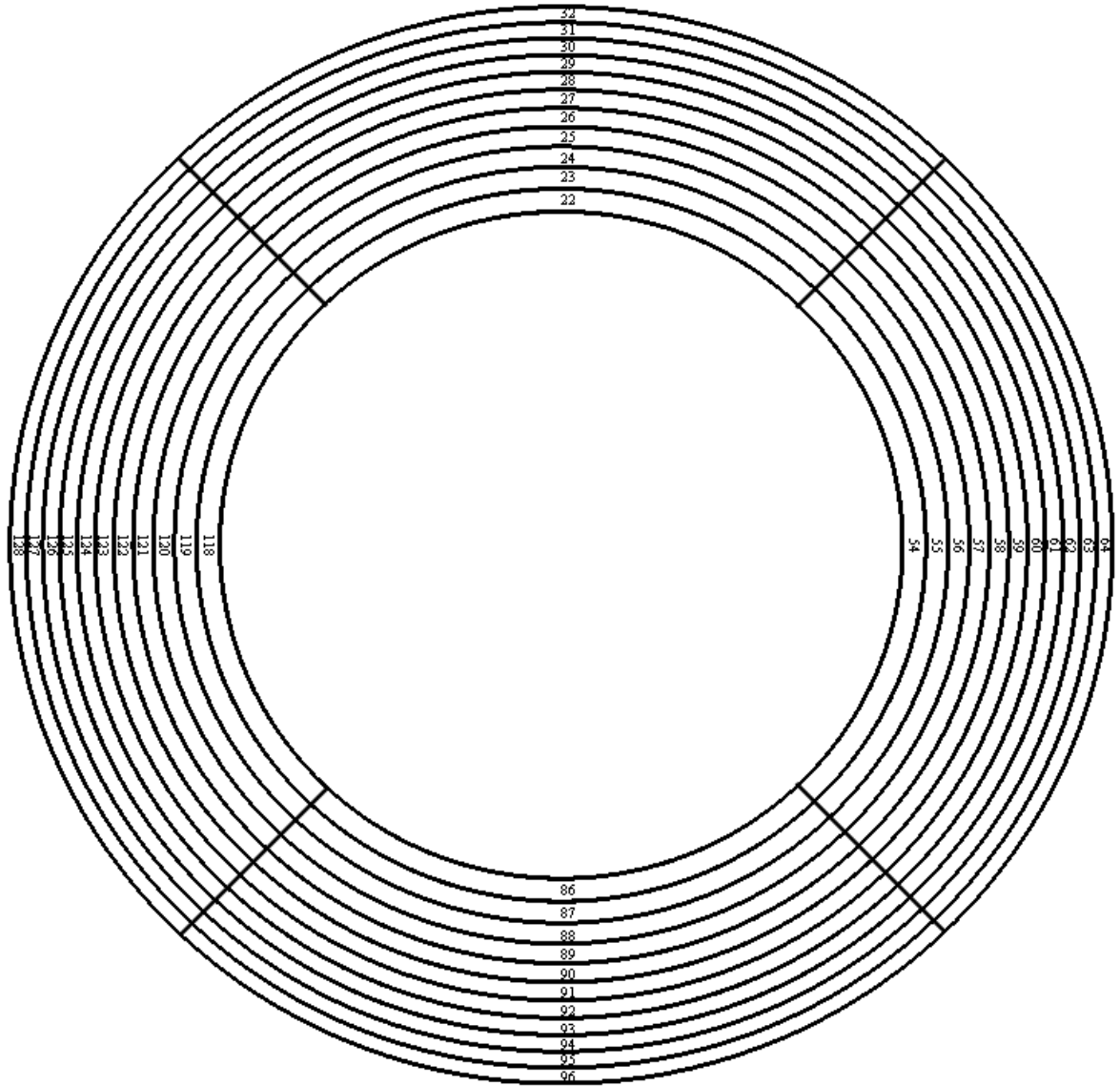| Ring Number	Radius (mm)	Radius (inches)	Height (mm)	Height (inches)	Width (mm)	Width (inches)	Number of Segments	Curvature Radius (mm)	Curvature Radius (inches)
1	3.1564	0.1243	0.0364	0.0014	3.0364	0.1195	1	136.88	5.3890
2	4.5492	0.1791	0.0756	0.0030	1.2728	0.0501	1	136.88	5.3890
3	5.6353	0.2219	0.1161	0.0046	0.9661	0.0380	1	136.88	5.3890
4	6.5633	0.2584	0.1574	0.0062	0.8079	0.0318	1	136.88	5.3890
5	7.3903	0.2910	0.1996	0.0079	0.7070	0.0278	1	136.88	5.3890
6	8.1454	0.3207	0.2426	0.0096	0.6352	0.0250	1	136.88	5.3890
7	8.8464	0.3483	0.2862	0.0113	0.5810	0.0229	1	136.88	5.3890
8	9.5044	0.3742	0.3304	0.0130	0.5380	0.0212	1	136.88	5.3890
9	10.1273	0.3987	0.3752	0.0148	0.5029	0.0198	1	136.88	5.3890
10	10.7208	0.4221	0.4205	0.0166	0.4735	0.0186	1	136.88	5.3890
11	11.2892	0.4445	0.4663	0.0184	0.4484	0.0177	1	136.88	5.3890
12	11.8358	0.4660	0.5127	0.0202	0.4267	0.0168	1	136.88	5.3890
13	12.3649	0.4868	0.5352	0.0211	0.4090	0.0161	1	283.83	11.174
14	12.8772	0.5070	0.5581	0.0220	0.3924	0.0154	1	283.83	11.174
15	13.3746	0.5266	0.5811	0.0229	0.3774	0.0149	1	283.83	11.174
16	13.8582	0.5456	0.6043	0.0238	0.3636	0.0143	1	283.83	11.174
17	14.6725	0.5777	0.6453	0.0254	0.6943	0.0273	2	283.83	11.174
18	15.4501	0.6083	0.6867	0.0270	0.6575	0.0259	2	283.83	11.174
19	16.1961	0.6376	0.7283	0.0287	0.6260	0.0246	2	283.83	11.174
20	16.9143	0.6659	0.7703	0.0303	0.5982	0.0236	2	283.83	11.174
21	17.6079	0.6932	0.8126	0.0320	0.5737	0.0226	2	283.83	11.174
22	18.8158	0.7408	0.8903	0.0351	1.0879	0.0428	4	283.83	11.174
23	19.9576	0.7857	0.9685	0.0381	1.0218	0.0402	4	283.83	11.174
24	21.0439	0.8285	1.0472	0.0412	0.9662	0.0380	4	283.83	11.174
25	22.0823	0.8694	1.1263	0.0443	0.9184	0.0362	4	283.83	11.174
26	23.0791	0.9086	1.2059	0.0475	0.8768	0.0345	4	283.83	11.174
27	24.0415	0.9465	1.2602	0.0496	0.8424	0.0332	4	418.62	16.481
28	24.9712	0.9831	1.3147	0.0518	0.8097	0.0319	4	418.62	16.481
29	25.8718	1.0186	1.3695	0.0539	0.7806	0.0307	4	418.62	16.481
30	26.7459	1.0530	1.4245	0.0561	0.7541	0.0297	4	418.62	16.481
31	27.5960	1.0865	1.4798	0.0583	0.7301	0.0287	4	418.62	16.481
32	28.4242	1.1191	1.5353	0.0604	0.7082	0.0279	4	418.62	16.481
33	29.9044	1.1773	1.6387	0.0645	1.3602	0.0536	8	418.62	16.481
34	31.3200	1.2331	1.7425	0.0686	1.2956	0.0510	8	418.62	16.481
35	33.2815	1.3103	1.8943	0.0746	1.8415	0.0725	12	418.62	16.481
36	35.1398	1.3835	2.0467	0.0806	1.7383	0.0684	12	418.62	16.481

APPENDIX B. REFRACTION AT FORGING-WATER INTERFACE

Introduction

This appendix provides details on the calculations performed at the forging-mirror interface for the 3D ray-tracing algorithm described in Chapter 3 of this dissertation. The generation of grid points on the forging surface, the determination of lines normal to the forging surface at each of these grid points, and the calculation of lines from each grid point to the FBH within the forging will be described. The 2000 by 2000 point forging surface grid increases surface area on the forging with increasing FBH depth, always being slightly larger than the expected ultrasonic beam footprint on the forging surface. The direction of a ray passing through each grid point and refracted at the forging-water interface is then determined.

The step-by-step algorithm for determining the direction of the ray passing though each grid point on the forging surface and refracted through the forging-water interface is as follows. Each of the 6 points outlined in the algorithm will be discussed in detail in the following sections.

1. Using a cylindrical coordinate system with the coordinate origin located on the forging axis, generate a grid of points on the conically shaped forging surface with an area slightly larger than the estimated beam footprint on the forging surface.
2. Determine the location of the FBH in the defined cylindrical coordinate system.
3. In the defined cylindrical coordinate system, at each grid point determine the second of two points defining a line normal to the forging surface, when this second point is located on the axis of the conical forging.
4. Convert all (r, θ, z) points generated using the defined cylindrical coordinate system to (x, y, z) points in a rectilinear coordinate system with a coordinate origin located on the forging surface directly above the location of the FBH (See Point B in Figure B.1).
5. Calculate the distance from the FBH to each grid point and save as a TOF value by using the longitudinal material velocity of the curved interface calibration block containing the FBH.
6. Use Snell's Law of Refraction at each forging surface grid point to determine the direction of the ray refracted from the forging material into the water medium.

Forging Surface Grid

A grid of points on the conical surface of a forging will be generated in a cylindrical coordinate system using the global labeling system $(r_{N1}, \theta_{N1}, z_{N1})$, where $N1$ is an index ranging from 0 to 1999. The generation of grid points begins at the center of the grid at coordinate $(r_{999}, \theta_0, z_{999}) = (r_{999}, 0, 0)$, where r_{999} is the forging radius at the elevation of the coordinate origin, such that a line normal to the forging surface at this grid point passes through the FBH coordinate (r_f, θ_f, z_f) (See Figure B.1).

The forging radius at the elevation of the defined coordinate origin, i.e., the curvature of the calibration block along the circumference of the forging directly "above" the FBH, is a known parameter recorded during the fabrication of the curved interface calibration blocks. Specifically, 7.8663 inches is the radius of curvature for curved interface coupons 2 through 7, while 6.7419 inches is the radius of curvature for curved interface coupons 8 through 12 and 7.3591 inches is the radius of curvature for curved interface coupon 13. Another known parameter is 60.02°, the apex angle of the conically shaped forging disk holder. Before (r, z) grid point coordinates can be generated, values for z_0 and z_{1999} must be determined based on the ultrasonic beam footprint size on the forging surface. Note that z_0 and z_{1999} are equal in magnitude, but opposite in sign. Therefore, the distances AB and BC are also equal, and these distances should be slightly greater than the radius of the ultrasonic beam when intersecting the forging surface. Values of H and R, the geometric focal length in water and the aperture radius, respectively, from Table 3.3 are used to estimate the initial beam radius, L_F, on the forging surface by equating the tangent functions of θ (See Figure B.2 and Equations B.1 and B.2).

$$\tan \theta = \frac{H}{R} = \frac{H - wp}{L_F} \qquad (B.1)$$

$$L_F = R\left(1 - \frac{H}{wp}\right) \tag{B.2}$$

Figure B.1: Schematic for curved forging surface grid point generation.

Figure B.2: Schematic for estimating beam footprint radius on forging-water interface.

The grid point coordinate θ must also be defined in terms of the beam radius. A symmetry condition exists which reduces the number of forging surface grid points by half. Specifically, symmetry exists between the positive and negative values of θ, so only positive values will be used for the grid point coordinate θ_{N1}. Figure B.3 shows the azimuthal labeling scheme of θ as well as illustrating the described symmetry condition.

Upon executing the algorithm using the estimated ultrasonic beam footprint radii, L_F, it was observed from the generated Fermat surfaces that the beam footprint on the forging surface was slightly underestimated, i.e., the apertures generated were slightly smaller than those required for maintaining an F/6 beam focus (See Equation 2.1). Consequently, L_F was adjusted for each curved interface coupon to generate Fermat surfaces that met the transducer aperture requirements for an F/6 beam focus.

Estimated and adjusted values for the ultrasonic beam footprint radius at the forging surface for the curved interface calibration blocks are tabulated in Table B.1. Also tabulated in Table B.1, using adjusted L_F values, are the point-to-point grid separation distances Δr, Δz, and $\Delta \theta$ along the radial, elevation, and circumferential directions, respectively.

The forging surface grid of points were generated in the algorithm by using two nested loops. The first nested loop has an inner loop that indexes from θ_0 to θ_{1999}, incrementing by $\theta_{1999}/N1$. The outer loop indexes from r_{999} to r_{1999}, incrementing by positive $2*AB/N1$. The second nested loop has the same inner loop as above, but an outer loop that indexes from r_{999} to r_{1999}, incrementing by negative $2*AB/N1$. As previously mentioned, the forging radius r_{999} equals 7.8663 inches for curved interface forging coupons 2 through 7, 6.7419 inches for curved interface forging coupons 8 through 12, and 7.3591 inches for curved interface forging coupon 13.
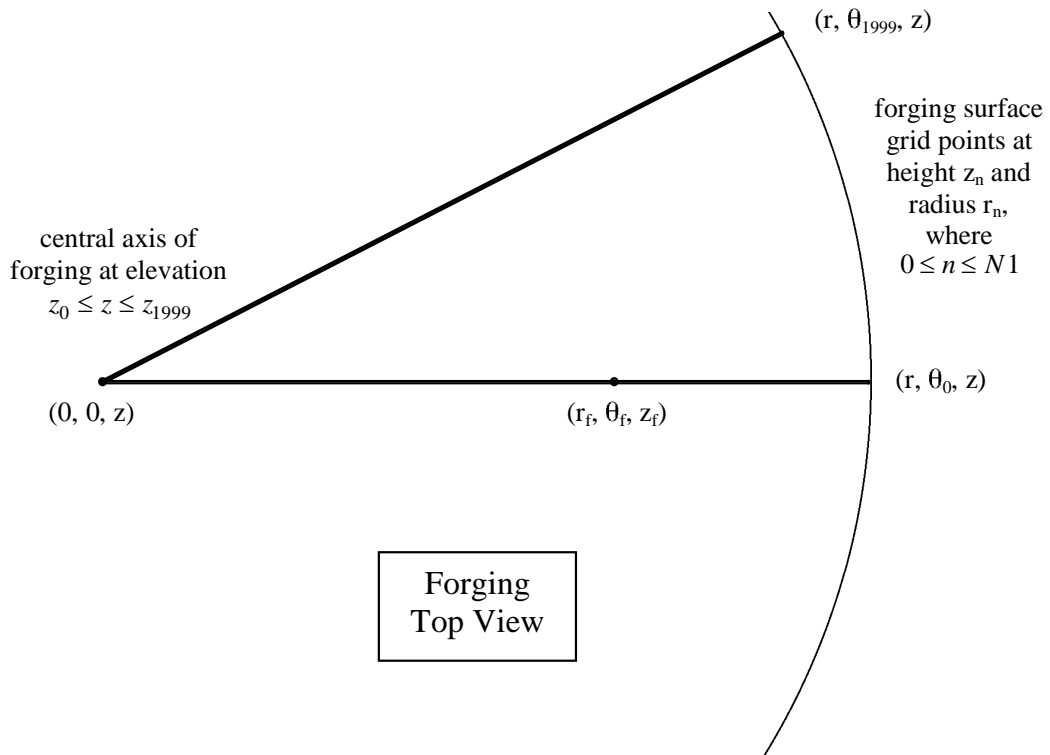

Figure B.3: Azimuthal labeling scheme for grid point generation on the forging-water interface of the curved interface calibration specimens.

Table B.1: Estimated and adjusted beam footprint values on the curved interface forging coupons at a 3.80-inch water path, F/6 beam focus, and sound velocity in water of 1489.7 m/s.

Block #	H (mm)	R (mm)	L_F (estimated) (mm)	L_F (adjusted) (mm)	Δr (mm)	Δz (mm)	$\Delta \theta$ (radians)
2	117.7	9.8	1.8	2.3	1.1244E-3	1.9489E-3	5.1187E-6
3	144.2	12.0	4.0	5.0	2.4736E-3	4.2876E-3	1.1261E-5
4	170.8	14.2	6.2	7.2	3.5980E-3	6.2366E-3	1.6380E-5
5	191.9	16.0	7.9	9.0	4.4975E-3	7.7957E-3	2.0475E-5
6	218.4	18.2	10.2	11.7	5.8467E-3	1.0134E-2	2.6617E-5
7	239.3	19.9	11.9	13.5	6.7462E-3	1.1694E-2	2.8153E-5
8	266.1	22.2	14.1	15.3	7.6457E-3	1.3253E-2	3.7228E-5
9	286.9	23.9	15.9	16.6	9.4447E-3	1.6371E-2	4.2449E-5
10	313.6	26.1	18.1	21.6	1.0794E-2	1.8710E-2	4.8514E-5
11	334.9	27.9	19.9	24.3	1.2143E-2	2.1048E-2	5.4578E-5
12	360.9	30.1	22.0	26.1	1.3043E-2	2.2608E-2	6.3506E-5
13	382.3	31.9	23.8	27.0	1.3492E-2	2.3387E-2	6.0186E-5

Flat Bottom Hole

The depth of the FBH, d_{FBH}, in each calibration blocks is known (See Table 3.2). The forging radius at the elevation of the defined coordinate origin, r_{999}, is also known. Based on the geometry shown in Figure B.1, the radial and axial FBH coordinates, r_f and z_f, may be calculated using Equations B.3 and B.4, respectively. The azimuthal FBH coordinate, θ_f, is always equal to zero due to the definition of the origin of the cylindrical coordinate system. The FBH coordinate (r_f, θ_f, z_f) is tabulated in Table B.2 for each curved interface calibration block.

$$r_f = r_{999} - d_{FBH} \sin(60.02°) \tag{B.3}$$

$$z_f = -d_{FBH} \cos(60.02°) \tag{B.4}$$

Table B.2: FBH coordinates in cylindrical coordinates with origin on axis of forging disk.

Block #	r_{49} (inches)	d_{FBH} (inches)	r_f (inches)	θ_f (degrees)	z_f (inches)
2	7.8663	0.200	7.6931	0.00	-0.1000
3	7.8663	0.450	7.4766	0.00	-0.2250
4	7.8663	0.700	7.2601	0.00	-0.3500
5	7.8663	0.900	7.0869	0.00	-0.4500
6	7.8663	1.15	6.8704	0.00	-0.5750
7	7.8663	1.35	6.6972	0.00	-0.6750
8	6.7419	1.60	5.3563	0.00	-0.8000
9	6.7419	1.80	5.1831	0.00	-0.9000
10	6.7419	2.05	4.9665	0.00	-1.0250
11	6.7419	2.25	4.7933	0.00	-1.1250
12	6.7419	2.50	4.5768	0.00	-1.2500
13	7.3591	2.70	5.0208	0.00	-1.3500

Forging Surface Normal Line

Two coordinate points can be used to define a line. Using a specific grid point on the forging surface as one such point, a second point on the central axis of the forging disk can be used to define a line normal to the forging surface at the grid point. Given that the location of this coordinate origin is also on the central axis of the forging disk, both the radial and azimuthal components of this second coordinate point are equal to zero. Elevation, the nontrivial coordinate component of this second point, defines the line

normal to the forging surface at a given forging grid point. Using the geometry illustrated in Figure B.4, the elevation component can be determined with a tangent function (See Equations B.5 and B.6). Note that all grid points on a given elevation, i.e., having identical azimuthal components, share the same coordinate point on the forging disk central axis.

After grid point and normal line generation in the defined cylindrical coordinate system is completed, it becomes more convenient to continue the algorithm in a rotated rectilinear (x, y, z) coordinate system with a new origin located directly above the FBH at grid point $(r_{999}, \theta_0, z_{999})$. It is also convenient if the (x, y, z) coordinate system were rotated such that the x-axis is tangent to the forging surface at grid point $(r_{999}, \theta_0, z_{999})$ in the circumferential direction, the y-axis is directed normal to the forging surface at grid point $(r_{999}, \theta_0, z_{999})$, and the z-axis is placed tangent to the forging surface.

$$\tan\left(60.02°\right) = \frac{r_n}{z_n - z_n^{normal}} \tag{B.5}$$

$$z_n^{normal} = z_n - \frac{r_n}{\tan\left(60.02°\right)} \tag{B.6}$$
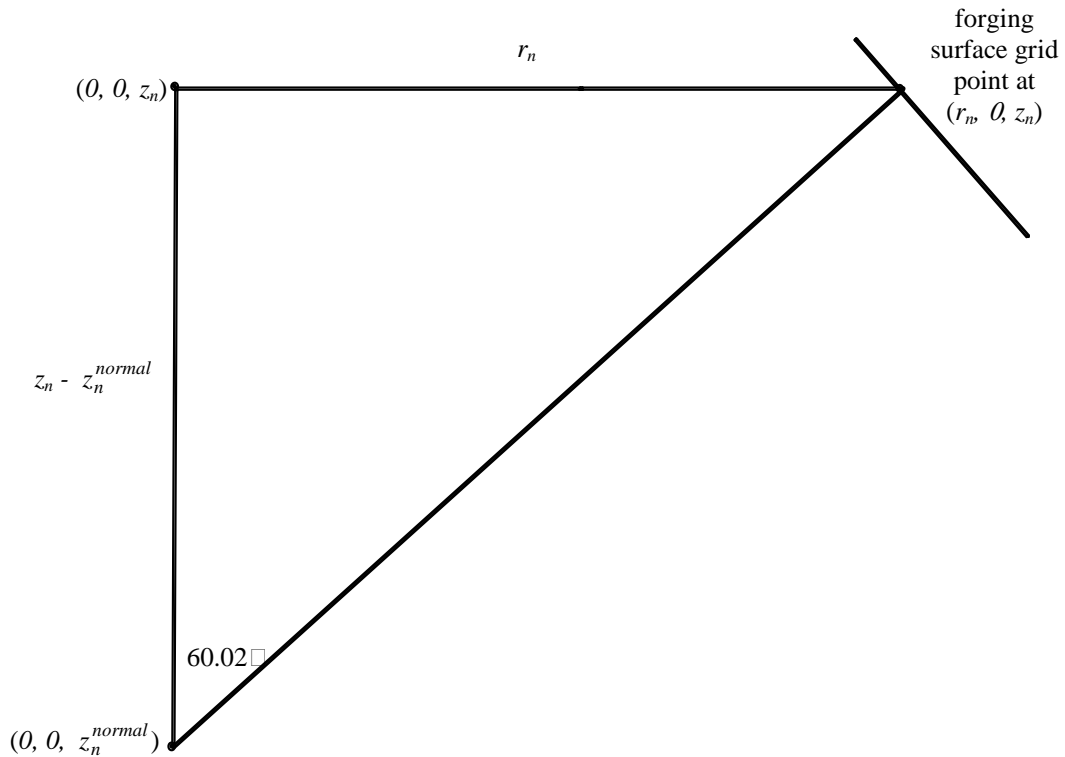
Figure B.4: Schematic of forging surface normal line starting point on central axis.

Rectilinear Coordinate System

The following operations were performed on each (r, θ, z) coordinate point, including forging surface grid points, points defining the forging surface normal line, and the location of the FBH, to convert all points from cylindrical to rectilinear coordinates with the specified origin and axis directions.

1. Convert each cylindrical coordinate point (r_n, θ_n, z_n) to rectilinear coordinate points (x^0_n, y^0_n, z^0_n) without translation or rotation (See Equation B.7) [25].
2. Translate the rectilinear coordinate system (x^0, y^0, z^0) from its origin on the central axis of the forging disk to a new rectilinear coordinate system (x', y', z') with its origin located on the forging surface directly above the FBH, i.e., grid point $(r_{999}, \theta_0, z_{999})$ (See Equation B.8).

3. Perform a 29.98° right-hand rotation about the y-axis of the rectilinear coordinate system (x', y', z') origin to create the final rectilinear coordinate system (x, y, z) such that the x-axis is normal to, and the z-axis is tangent to, the forging surface at the (r_{999}, θ_0, z_{999}) grid point (See Equations B.9 through B.11.

After converting from the original cylindrical coordinate system and performing the translation and rotation operations, the resultant (x, y, z) rectilinear coordinate system is shown in Figure B.5.

$$x_n^0 = r_n \cos \theta_n; \qquad y_n^0 = r_n \sin \theta_n; \qquad z_n^0 = z_n \tag{B.7}$$

$$x_n' = x_n^0 - r_{49}; \qquad y_n' = y_n^0; \qquad z_n' = z_n^0 \tag{B.8}$$

$$x_n = x_n' \cos(29.98°) + y_n'(0) + z_n' \sin(29.98°) \tag{B.9}$$

$$y_n = x_n'(0) + y_n'(1) + z_n'(0) \tag{B.10}$$

$$z_n = -x_n' \sin(29.98°) + y_n'(0) + z_n' \cos(29.98°) \tag{B.11}$$
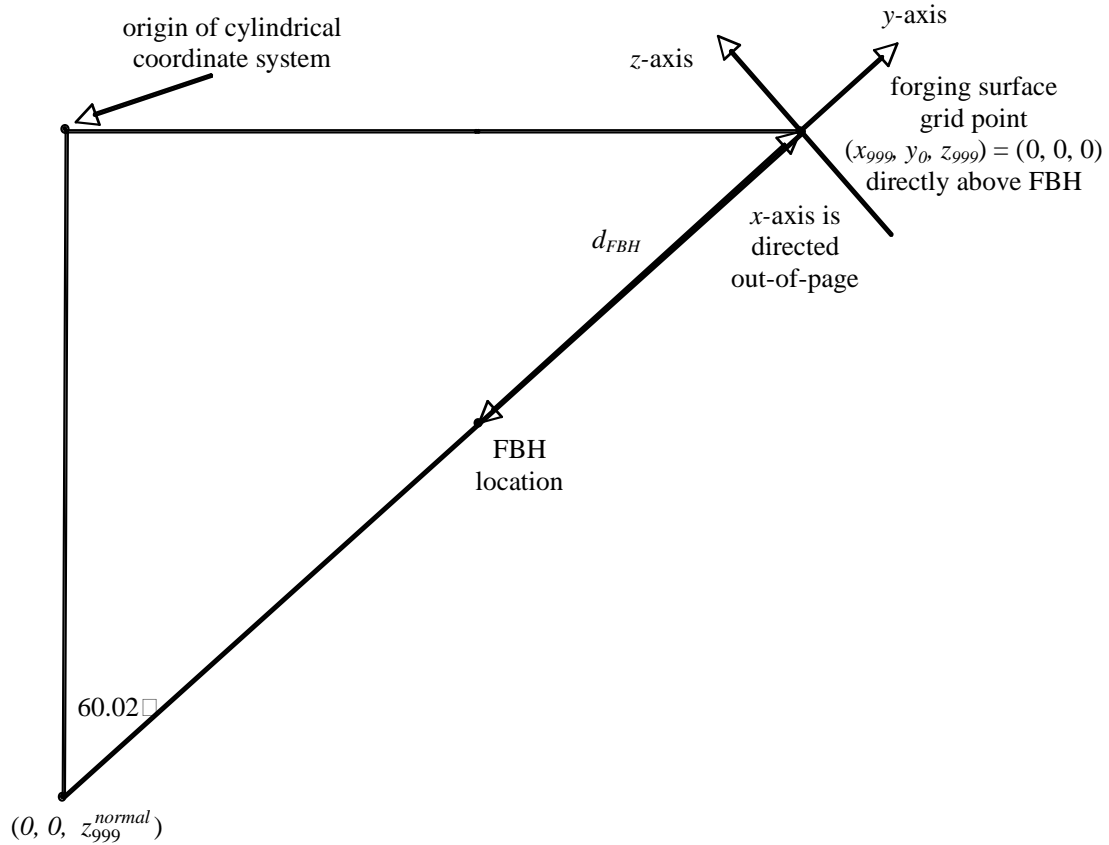
Figure B.5: Schematic of rectilinear coordinate system after translation and rotation.

Time-Of-Flight

The final goal of the ray-tracing algorithm is to generate element delay times for phasing the transducer array elements, which in part requires the time-of-flight (TOF) between forging grid points (x_n, y_n, z_n) and the FBH coordinate (x_f, y_f, z_f). This TOF can be calculated if the longitudinal material sound velocity is known. The longitudinal sound velocity for each curved interface calibration block is tabulated in Table 3.1. The distance, d_f, between each forging grid point (x_n, y_n, z_n) and the FBH coordinate (x_f, y_f, z_f) is expressed in Equation B.12 [26].

$$d_f = \sqrt{\left(x_n - x_f\right)^2 + \left(y_n - y_f\right)^2 + \left(z_n - z_f\right)^2} \tag{B.12}$$

Snell's Law of Refraction

Three coordinate points were determined in the (*x*, *y*, *z*) global coordinate system: the forging surface grid point, a point on the forging's central axis used to determine a surface normal at the forging surface grid point, and the position of the FBH. These three coordinate points were used to generate two vectors, a vector from the FBH to the forging surface grid point and a surface normal at the forging surface grid point. After being divided by their lengths, these two unit vectors were used to define a local coordinate system (*t*, *n*, *s*) at each individual grid point. Using these two unit vectors, an outward surface normal and incident ray from the FBH, Snell's Law was applied to determine the direction of the ray refracted through the forging surface into water at each forging surface grid point.

A ray traveling from the FBH in the forging each grid point on the forging surface will be refracted at that forging-water interface before projected into the surrounding water medium. Here, Snell's Law of Refraction requires the longitudinal material velocities of water and the curved interface forging coupons and one of two angles (see Figure B.6 and Equation B.13). At each forging surface grid point, the angle, θ_1, between the inner surface normal and the incident ray defined by a specific forging grid point and the FBH location in the forging medium is known. Unknown is the second angle, θ_2, between the outer surface normal vector and the refracted ray in the water medium.

$$\frac{\sin\theta_1}{v_1} = \frac{\sin\theta_2}{v_2} \quad \Rightarrow \quad \theta_2 = \arcsin\left(\frac{v_2}{v_1}\sin\theta_1\right) \tag{B.13}$$

As Snell's Law of Refraction is a two-dimensional expression for calculating the angle of a ray refracted through an interface of two materials, and the described ray-tracing algorithm is a 3D construct, then a local coordinate system (*t, n, s*) for each forging grid point must be determined before Snell's Law can be applied (See Figure B.7). In this local coordinate system (*t, n, s*), the incident angle, θ_1, is the dot product (See Equation B.14) of the inner normal unit vector, *n*, based on the line normal to the forging surface (See Equation B.15) and the incident ray unit vector, *f*, based on the ray from the FBH to the forging surface grid point (See Equation B.16).

$$\cos\theta_1 = n \cdot f \tag{B.14}$$

$$\text{unit vector } n = \frac{\left(g_1 - n_1\right)x + \left(g_2 - n_2\right)y + \left(g_3 - n_3\right)z}{\sqrt{\left(g_1 - n_1\right)^2 + \left(g_2 - n_2\right)^2 + \left(g_3 - n_3\right)^2}} = n_x x + n_y y + n_z z \tag{B.15}$$

$$\text{unit vector } f = \frac{\left(g_1 - f_1\right)x + \left(g_2 - f_2\right)y + \left(g_3 - f_3\right)z}{\sqrt{\left(g_1 - f_1\right)^2 + \left(g_2 - f_2\right)^2 + \left(g_3 - f_3\right)^2}} = f_x x + f_y y + f_z z \tag{B.16}$$
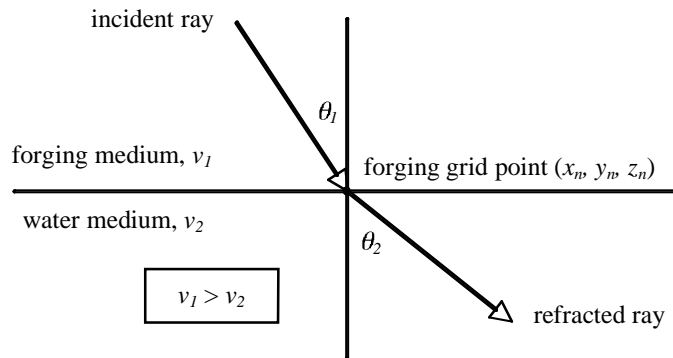

Figure B.6: Schematic of 2D Snell's Law of Refraction at the forging-water interface.

In the equations located in this section of Appendix B, (g_1, g_2, g_3) refers to the forging surface grid point coordinate, (f_1, f_2, f_3) refers to the coordinate location of the FBH, and (n_1, n_2, n_3) refers to the point on the central axis of the forging disk which defines the normal surface line for each forging grid point. Unit vectors n and f have components (n_x, n_y, n_z) and (f_x, f_y, f_z), respectively.

For the components of the local coordinate system (t, n, s), the t-axis is orthogonal to both unit vectors n and f as defined by the cross product of n and f (See Equation B.17). As $\vec{t}$ is not of unit length, it must be converted to unit vector t by dividing $\vec{t}$ by its length (See Equation B.18). Similarly, the s-axis is orthogonal to both unit vectors t and n as defined by the cross product of t and n (See Equation B.19). The unit vector s is similarly determined from the vector $\vec{s}$ (See Equation B.20).

$$\vec{t} = n \times f = \begin{vmatrix} x & y & z \\ n_x & n_y & n_z \\ f_x & f_y & f_z \end{vmatrix} = \left(n_y f_z - n_z f_y \right)x - \left(n_x f_z - n_z f_x \right)y + \left(n_x f_y - n_y f_x \right)z \qquad (B.17)$$

$$t = \frac{\vec{t}}{\left| t \right|} = t_x x + t_y y + t_z z \qquad (B.18)$$

$$\vec{s} = t \times n = \begin{vmatrix} x & y & z \\ t_x & t_y & t_z \\ n_x & n_y & n_z \end{vmatrix} = \left(t_y n_z - t_z n_y \right)x - \left(t_x n_z - t_z n_x \right)y + \left(t_x n_y - t_y n_x \right)z \qquad (B.19)$$

$$s = \frac{\vec{s}}{\left| \vec{s} \right|} = s_x x + s_y y + s_z z \qquad (B.20)$$

In the (t, n, s) local coordinate system shown in Figure B.7, the refracted ray, u, can be expressed in this coordinate system as a function of the refracted angle, θ_2, using sine and cosine terms from a simple vector analysis (See Equation B.21). Note that the unit vector u will always have a zero component in the out-of-plane t-axis direction. Substitution into Equation B.21 of unit vectors n and s from Equations B.15 and B.20, respectively, and angle θ_2 from Equation B.13 will result in unit vector u known in terms of the forging surface grid point (g_1, g_2, g_3), the FBH location (f_1, f_2, f_3), and point (n_1, n_2, n_3) used to define a normal to the forging surface. By using Equation B.13, the refracted angle θ_2 can be substituted by incident angle θ_1, defined in Equation B. 14.

$$u = \left(0 \right)t + \left(\cos\theta_2 \right)n + \left(\sin\theta_2 \right)s = \left(\cos\theta_2 \right)n + \left(\sin\theta_2 \right)s \qquad (B.21)$$
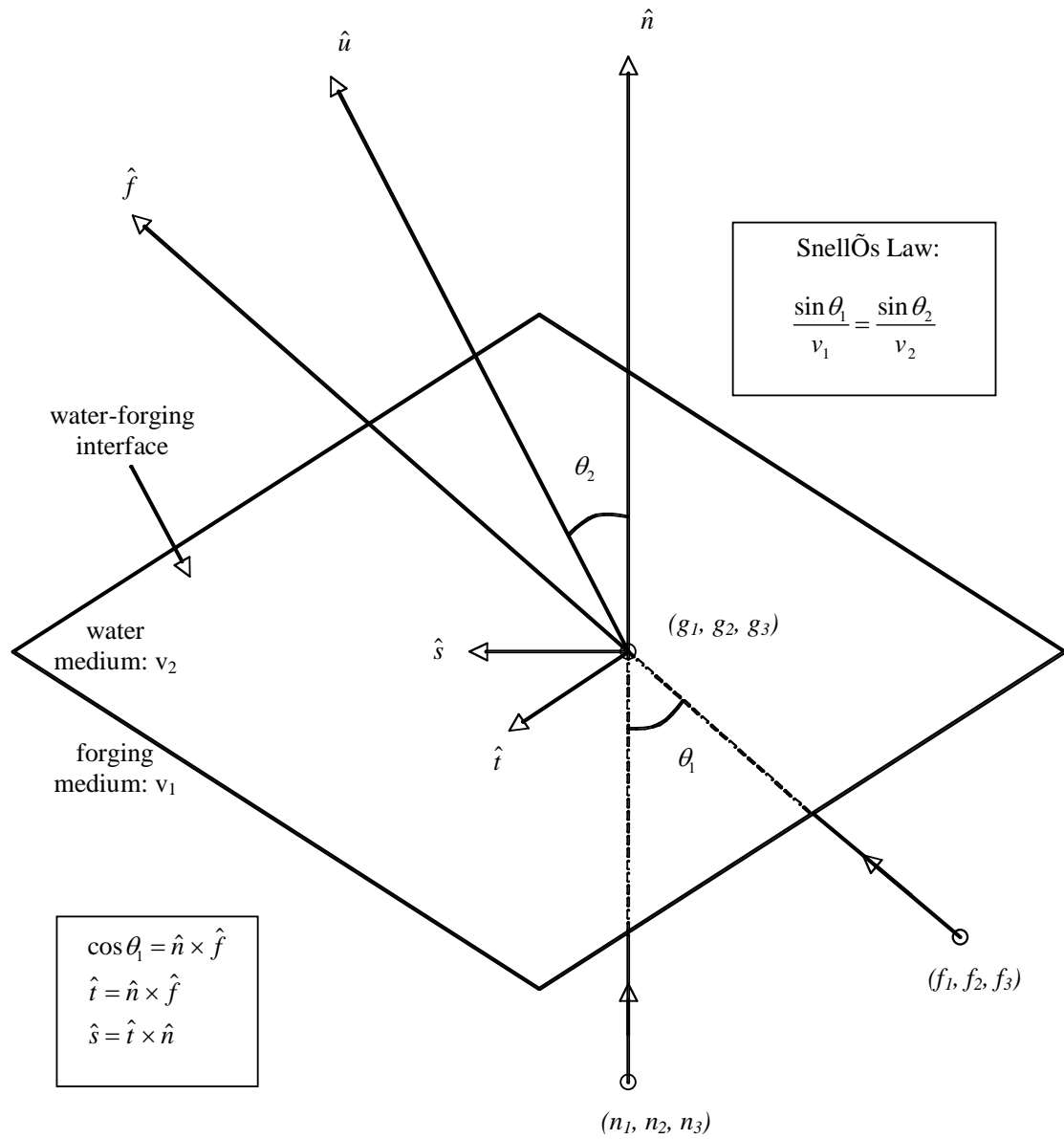
Figure B.7: Schematic illustrating the application of Snell's Law of Refraction at the forging-water interface using local coordinates.

The figure contains the following labels:

$\hat{u}$, $\hat{n}$, $\hat{f}$

Snell's Law:

$$\frac{\sin \theta_1}{v_1} = \frac{\sin \theta_2}{v_2}$$

water-forging interface

θ_2

(g_1, g_2, g_3)

water medium: v_2

$\hat{s}$

$\hat{t}$

θ_1

forging medium: v_1

$$\cos \theta_1 = \hat{n} \times \hat{f}$$
$$\hat{t} = \hat{n} \times \hat{f}$$
$$\hat{s} = \hat{t} \times \hat{n}$$

(f_1, f_2, f_3)

(n_1, n_2, n_3)

APPENDIX C – FERMAT SURFACES

This appendix provides details on the Fermat surfaces generated upon execution of the 3D ray-tracing algorithm described in Chapter 3 of this dissertation. A single Fermat surface was generated for each curved interface forging coupon 2 through 13. In the following appendix, Appendix D, the group of (*x, y, z*) coordinates comprising each Fermat surface will be analyzed to determine the delay time sets necessary to phase each element in the transducer array's aperture energized for a given forging coupon.

Each of the Fermat surfaces generated is a grid of 2000 by 2000 points located very near the face of the transducer array. These 4 million grid points are the termination points of an equal number of rays beginning at the FBH in a curved interface forging coupon that were refracted through the curved forging-water interface and reflected from a 27.0-inch radius, concave, cylindrical mirror oriented at 45 degrees to the ultrasonic beam centerline. Each ray is terminated at a total travel time identical to the time-of-flight (TOF) of the beam centerline reference ray passing in a normal direction through the curved forging-water interface and ultimately traveling a total distance of 3.80 inches in water, a water path along which it was reflected at the symmetry axis of the cylindrical mirror. In chapter 3, Figure 3.8 provides a 2-D schematic of the locations of the FBH and forging, mirror, and transducer/Fermat surfaces, and illustrates the paths of several representative rays including the beam centerline reference ray.

For each curved interface forging coupon 2 through 13, a figure will be presented containing 2-D and 3-D plots of the FBH location (represented by a "+" sign) along with grid points for the curved forging-water interface (identified in green), cylindrically focused mirror (identified in red), and the Fermat surface (identified in blue). Additionally, each plot contains a grid of points representing the location of the center of transducer elements (identified in purple) within the aperture required to maintain an F6 focus for each curved interface forging coupon. With regards to the grid of points representing transducer elements, the location of the center array element was located at the termination point of the beam centerline reference ray. Figures C.1 through C.12 provide representations of these surfaces for the curved interface forging coupons 2 through 13, respectively. In these figures, the scales of the x-, y-, and z-axis are identical. Note that, due to symmetry considerations, only one half of the forging surface, mirror surface, Fermat surface, and transducer elements are shown in the plots.
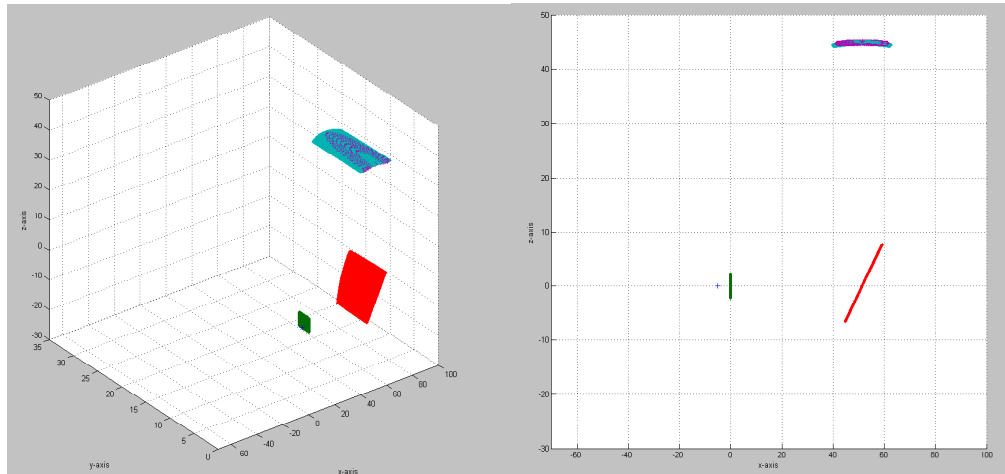

Figure C.1: 3D (left) and 2D (right) plots of the FBH (+) and forging (green), mirror (red), Fermat (blue), and transducer (purple) surfaces for the curved interface forging coupon #2.

Figure C.2: 3D (left) and 2D (right) plots of the FBH (+) and forging (green), mirror (red), Fermat (blue), and transducer (purple) surfaces for the curved interface forging coupon #3.
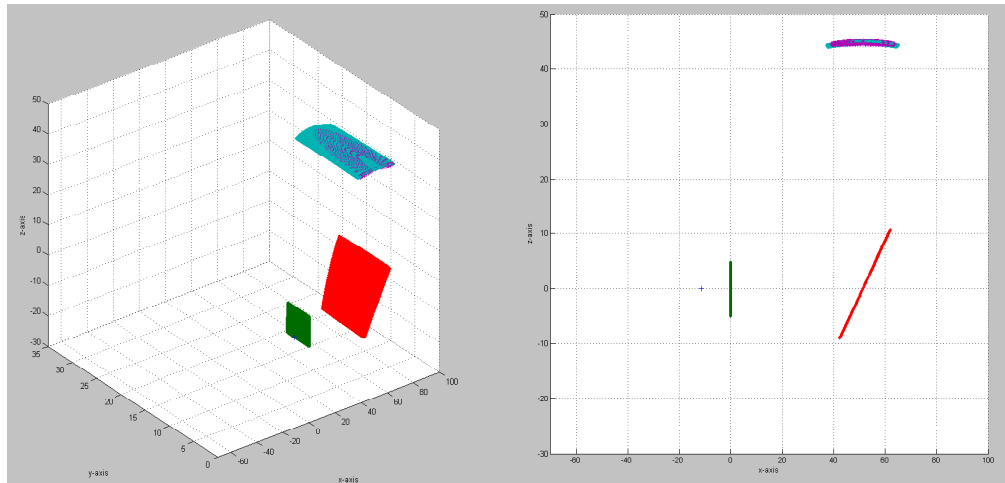

Figure C.3: 3D (left) and 2D (right) plots of the FBH (+) and forging (green), mirror (red), Fermat (blue), and transducer (purple) surfaces for the curved interface forging coupon #4.

Figure C.4: 3D (left) and 2D (right) plots of the FBH (+) and forging (green), mirror (red), Fermat (blue), and transducer (purple) surfaces for the curved interface forging coupon #5.

Figure C.5: 3D (left) and 2D (right) plots of the FBH (+) and forging (green), mirror (red), Fermat (blue), and transducer (purple) surfaces for the curved interface forging coupon #6.
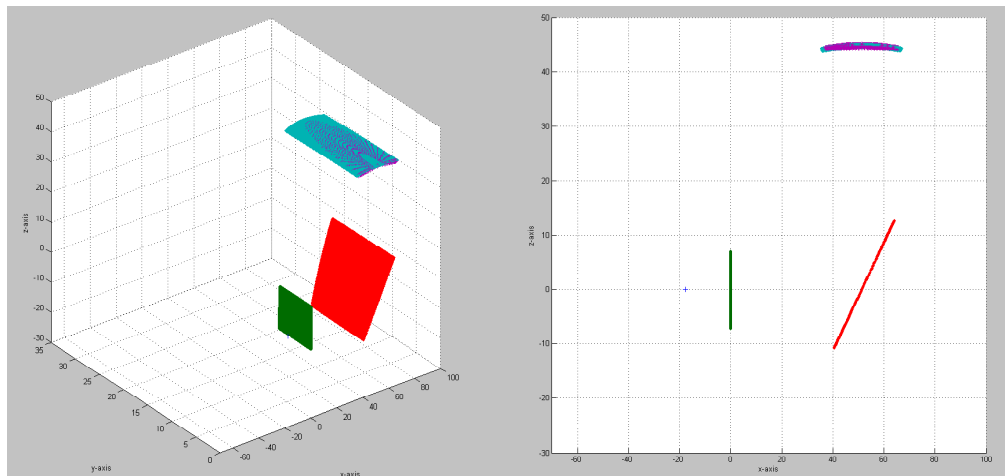

Figure C.6: 3D (left) and 2D (right) plots of the FBH (+) and forging (green), mirror (red), Fermat (blue), and transducer (purple) surfaces for the curved interface forging coupon #7.
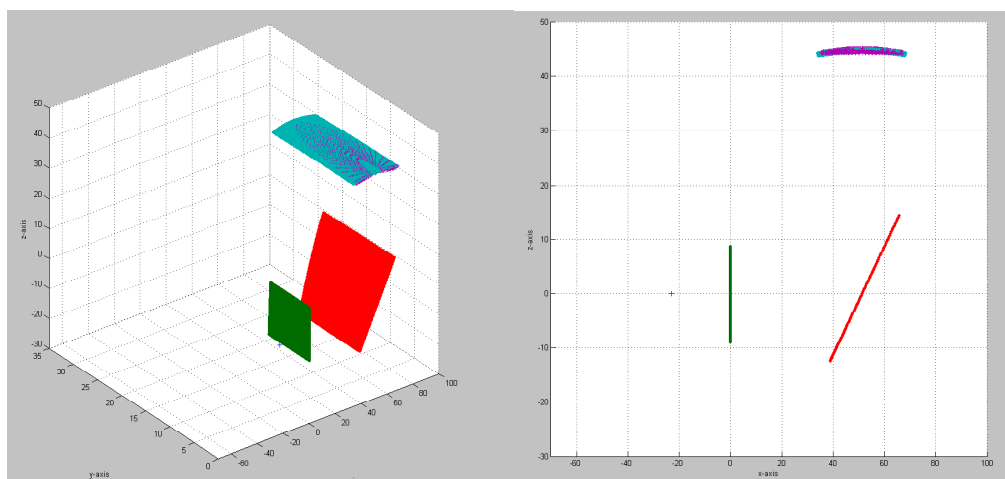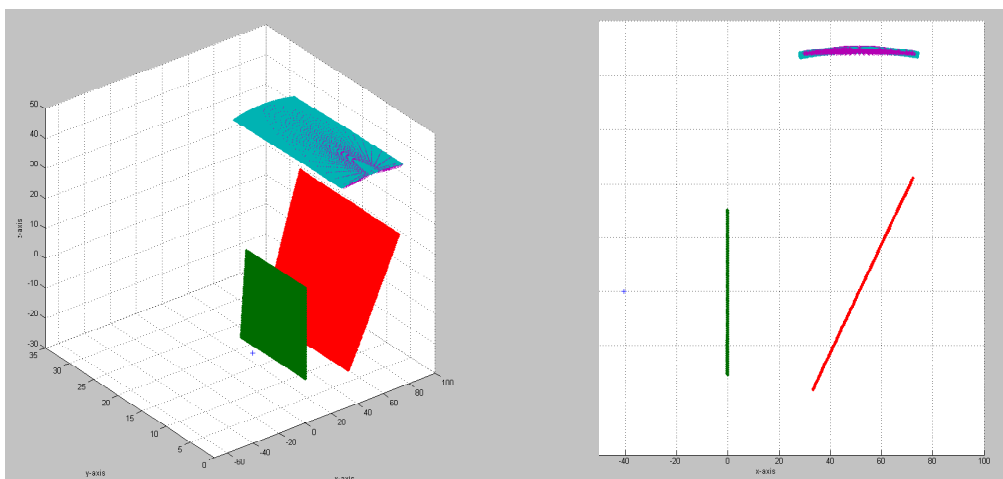

Figure C.7: 3D (left) and 2D (right) plots of the FBH (+) and forging (green), mirror (red), Fermat (blue), and transducer (purple) surfaces for the curved interface forging coupon #8.
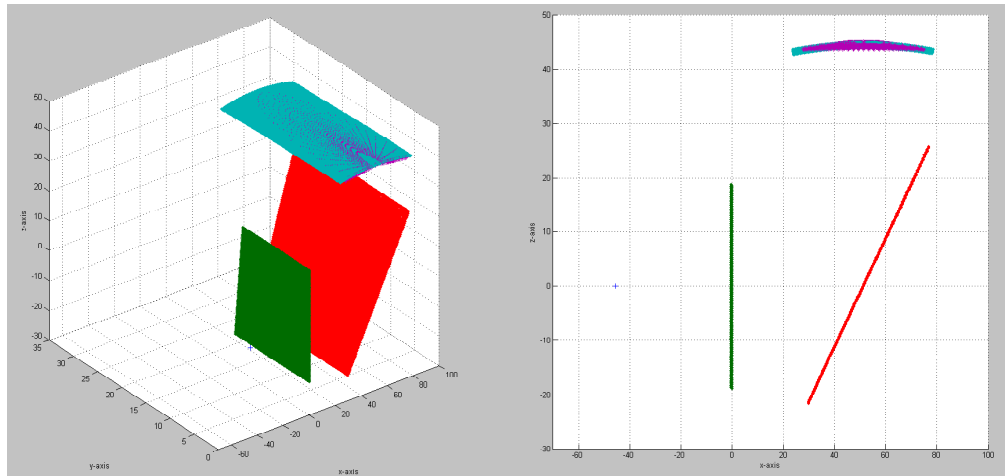
Figure C.8: 3D (left) and 2D (right) plots of the FBH (+) and forging (green), mirror (red), Fermat (blue), and transducer (purple) surfaces for the curved interface forging coupon #9.
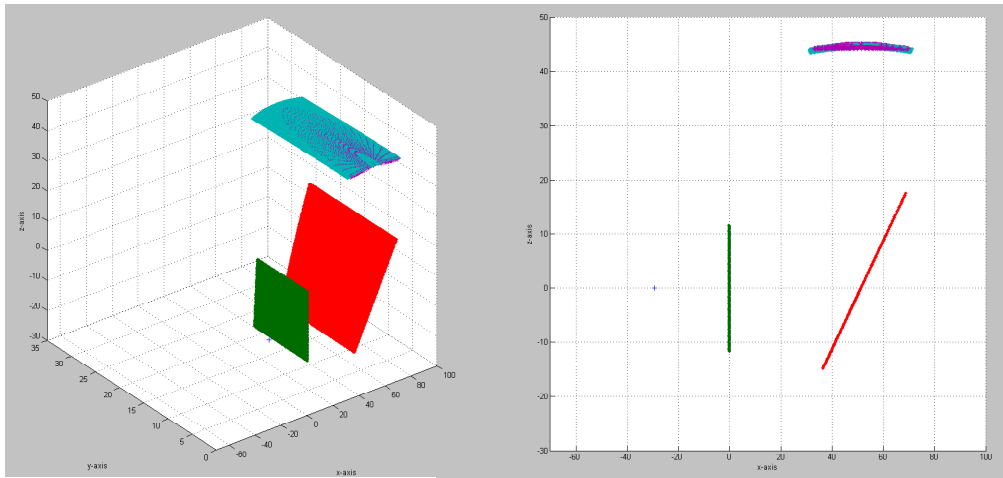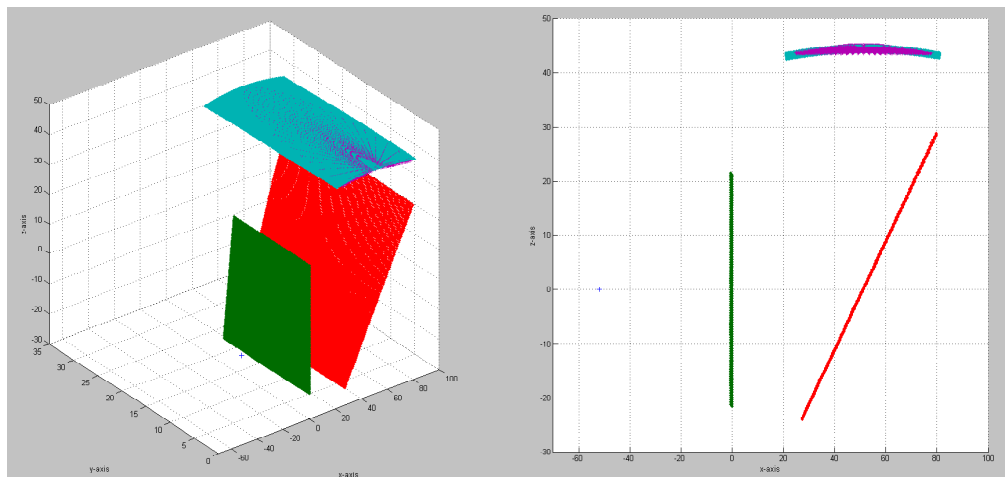

Figure C.9: 3D (left) and 2D (right) plots of the FBH (+) and forging (green), mirror (red), Fermat (blue), and transducer (purple) surfaces for the curved interface forging coupon #10.

Figure C.10: 3D (left) and 2D (right) plots of the FBH (+) and forging (green), mirror (red), Fermat (blue), and transducer (purple) surfaces for the curved interface forging coupon #11.
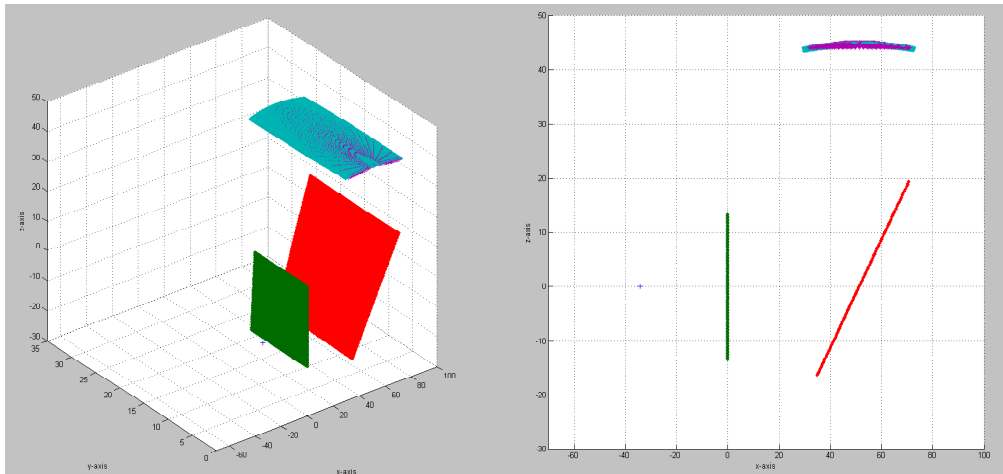
Figure C.11: 3D (left) and 2D (right) plots of the FBH (+) and forging (green), mirror (red), Fermat (blue), and transducer (purple) surfaces for the curved interface calibration specimen #12.

Figure C.12: 3D (left) and 2D (right) plots of the FBH (+) and forging (green), mirror (red), Fermat (blue), and transducer (purple) surfaces for the curved interface forging coupon #13.
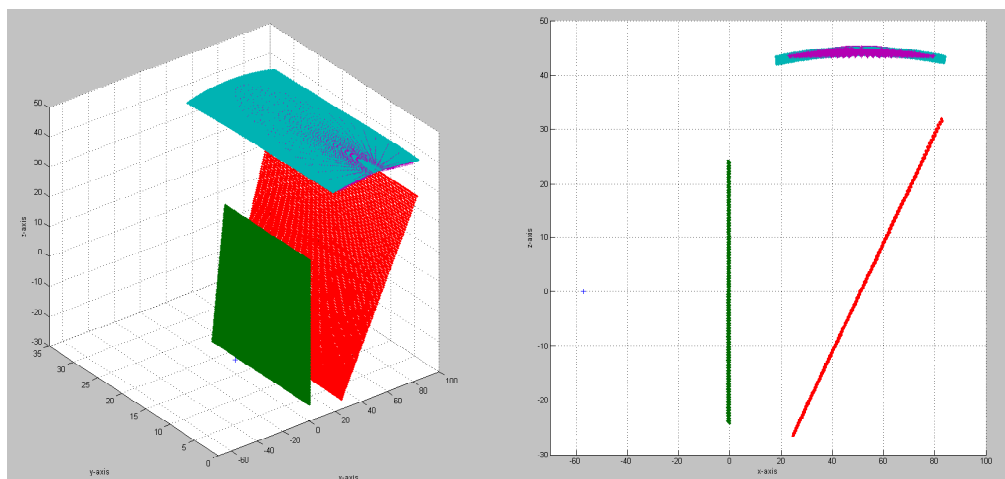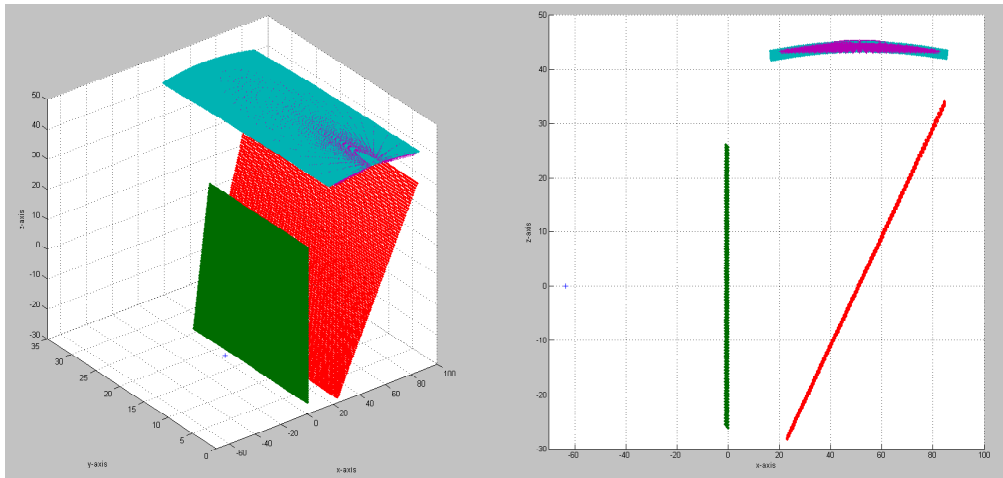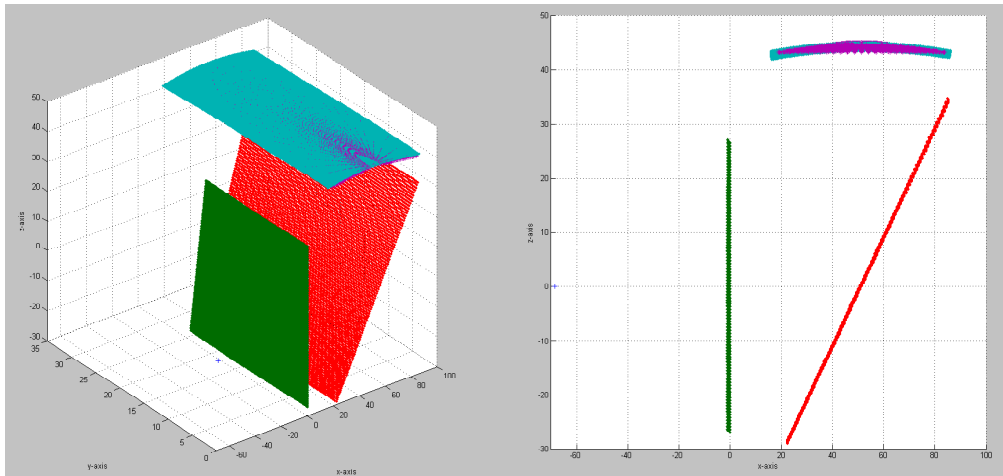
APPENDIX D. DELAY TIMES

This appendix provides details on extracting circumferential delay times from the Fermat surfaces generated upon execution of the 3D ray-tracing algorithm described in Chapter 3 of this dissertation.

A grid of points representing the transducer face was generated using the transducer specifications data sheet (see Table A.1). For rings 2 through 36 of the transducer array, thirty-seven grid points were defined for each ring located midway between each ring's inner and outer radii, arranged circumferentially every 5 degrees from 0 to 180 degrees. See Figures D.1, D.2, and D.3 for plots of these transducer face grid points in the XY-, XZ-, and YZ-planes, respectively.

The transducer face grid points presented have the same coordinate origin and axes orientations as the Fermat surface grid points presented in Appendix C. A single grid point was created for the innermost element, i.e., ring #1 or element 1, of the transducer array, identifying the location of the termination point of the beam centerline reference ray for each Fermat surface.

For a given Fermat surface, each of the transducer face grid points within the required aperture were matched to a delay time value. This matching process was accomplished by searching the Fermat surface grid points to locate the ray termination grid point nearest to each transducer array grid point. Then, the distance in water between these two grid coordinates was calculated and converted into units of time, resulting in the delay time needed for phasing at that grid point on the transducer face. For each Fermat surface grid point matched point to a transducer face grid point, a single delay time was extracted.

Each of the thirty-seven grid points located within a ring included in the aperture of the transducer has an associated delay time value. For non-segmented rings 1 through 16, these delay times were averaged over the entire ring as only one delay time could be applied when energizing these elements. Delay times of segmented rings were averaged over individual elements within each segmented ring.

Figures D.4 through D.15 plot the delay time values for each ring of the array, whether segmented or not, within the required aperture for curved interface forging coupons 2 through 13, respectively. The range of delay time values for each element in the aperture is provided in the legend of each plot.

The range of values over which delay times are averaged within a single element is the source of a defocusing aberration. Current phased array instrumentation hardware has a delay time resolution limit of 2 nanoseconds. If the range of delay time values for an individual element is approximately one-half the period of the sound wave, destructive wave interference can occur due to this phase variation. This defocusing aberration condition can be resolved by the design and manufacture of a transducer array with a further segmentation of elements until the range of delay times for each individual element does not exceed a given phase variation constraint.

The phase variation constraint is often taken to be 60°, i.e., one-sixth of the period of a wave. This constraint can be applied over individual elements of the transducer array during the calculation of delay times to determine if a defocusing aberration condition exists. At a frequency of 10 MHz, the period of a sound wave is $T = 1/f = 100$ nanoseconds. Maximum destructive interference occurs when two waves arrive at a transducer grid point with the same amplitude and frequency, but 180° out of phase with one another. In other words, one wave lags the other by half a period. At a 10 MHz frequency, this have period equals 50 nanoseconds. A 60° phase variation constraint is exceeded when the range of delay time values for grid points spread across a single transducer element exceeds one-sixth of the period, or 16.7 ns.

Excessive phase variation over an element results in a reduction in the intensity level of the ultrasonic beam being received due to destructive wave interference. The theoretical loss in intensity level of the entire ultrasonic beam can be determined for each forging coupon inspection using the principle of superposition of sinusoidal waves [28]. This theoretical loss of intensity can then be converted into a loss of signal strength in units of decibels [29]. First, the range of delay times over each element is converted into a phase difference (See Equation D.1). Second, the physics principle of superposition of sinusoidal waves, when assuming both waves have the same frequency, can be used to determine an intensity level from the phase difference (See Equations D.2 and D.3). For each time delay set, the intensity level of each element is summed together equally, i.e., with the same relative weight, as the area of each transducer element is approximately equal. Finally, a ratio of the summed intensity level over the maximum intensity level during complete constructive wave interference, i.e., four times the initial intensity (See Equation D.4), is converted into a sound intensity level in units of decibels (See Equation D.5).
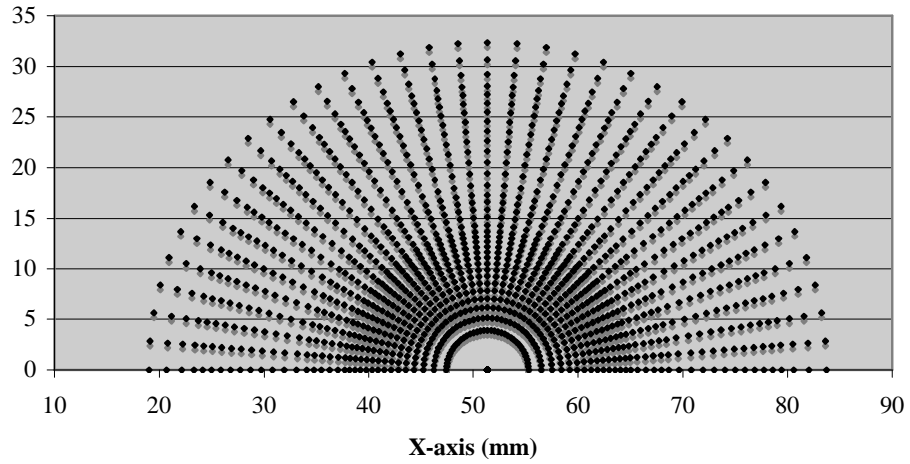
Figure D.1: Transducer array grid points for 36 rings as seen from the XY-plane.
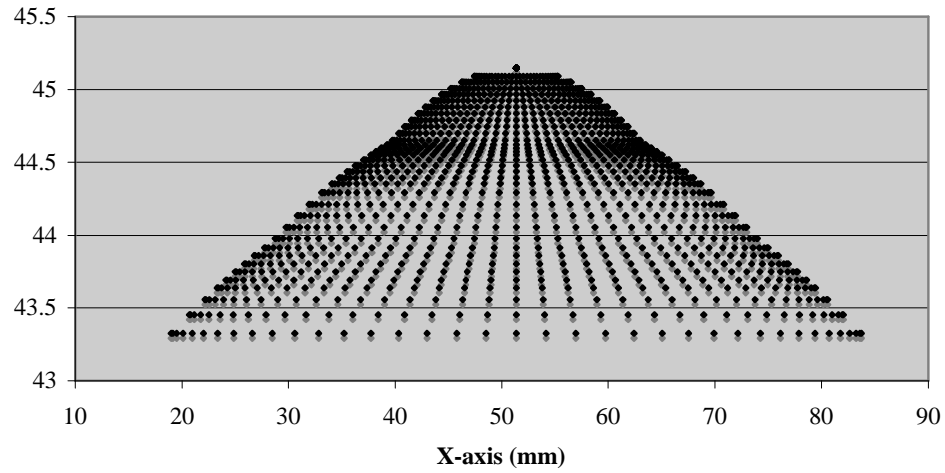
Figure D.2: Transducer array grid points for 36 rings as seen from the XZ-plane.
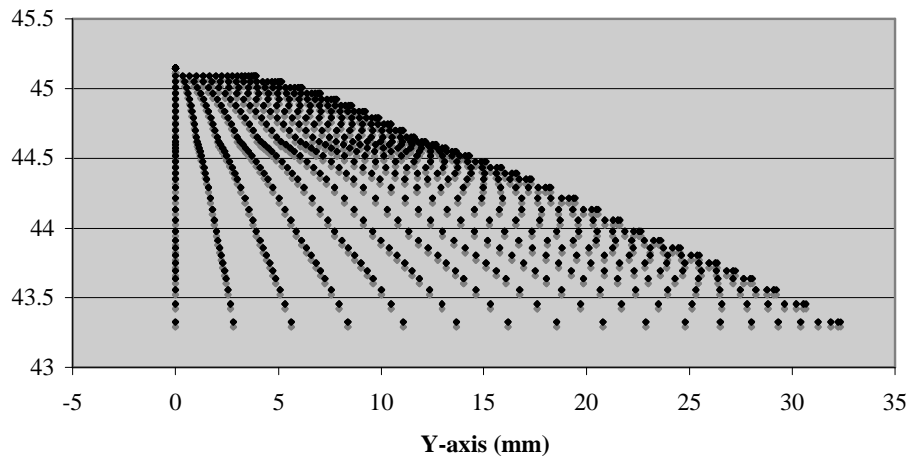
Figure D.3: Transducer array grid points for 36 rings as seen from the YZ-plane.
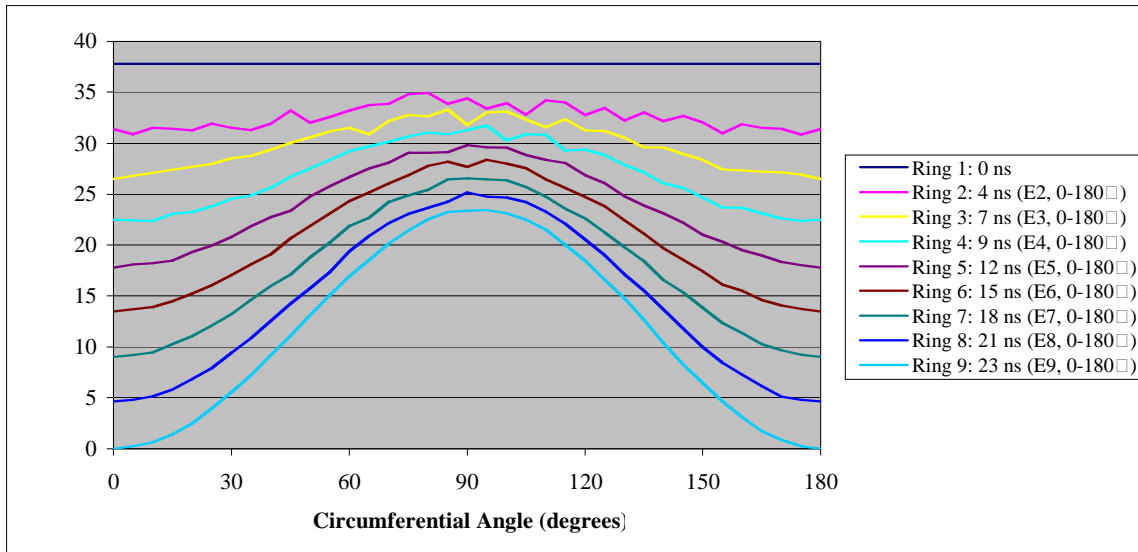
Figure D.4: Delay times and ranges for rings 1 through 9 when inspecting curved interface forging coupon #2.
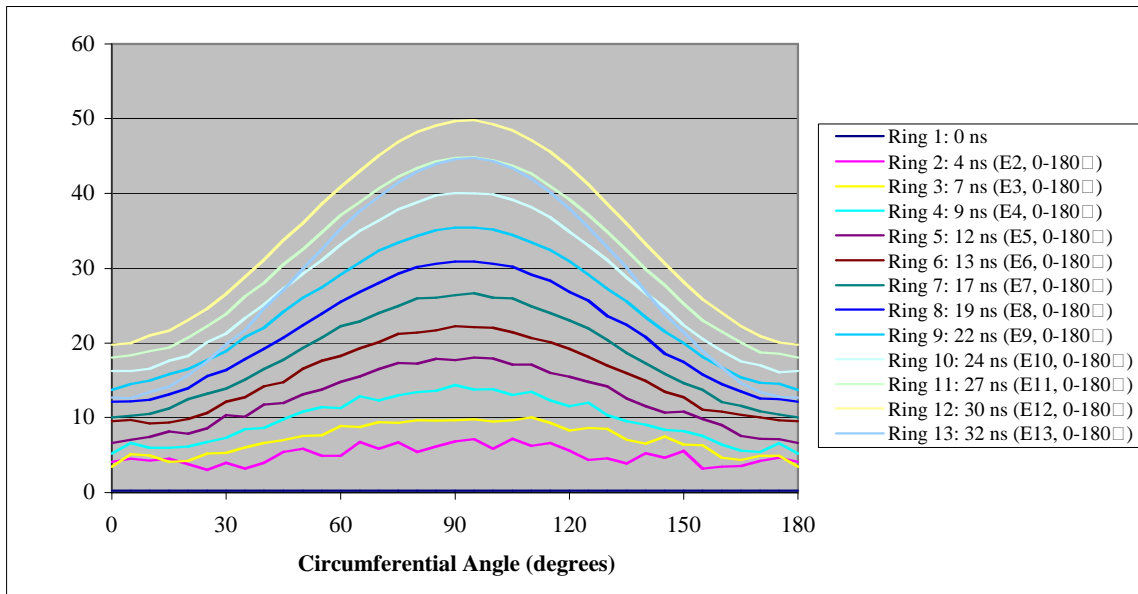
Figure D.5: Delay times and ranges for rings 1 through 13 when inspecting curved interface forging coupon #3.
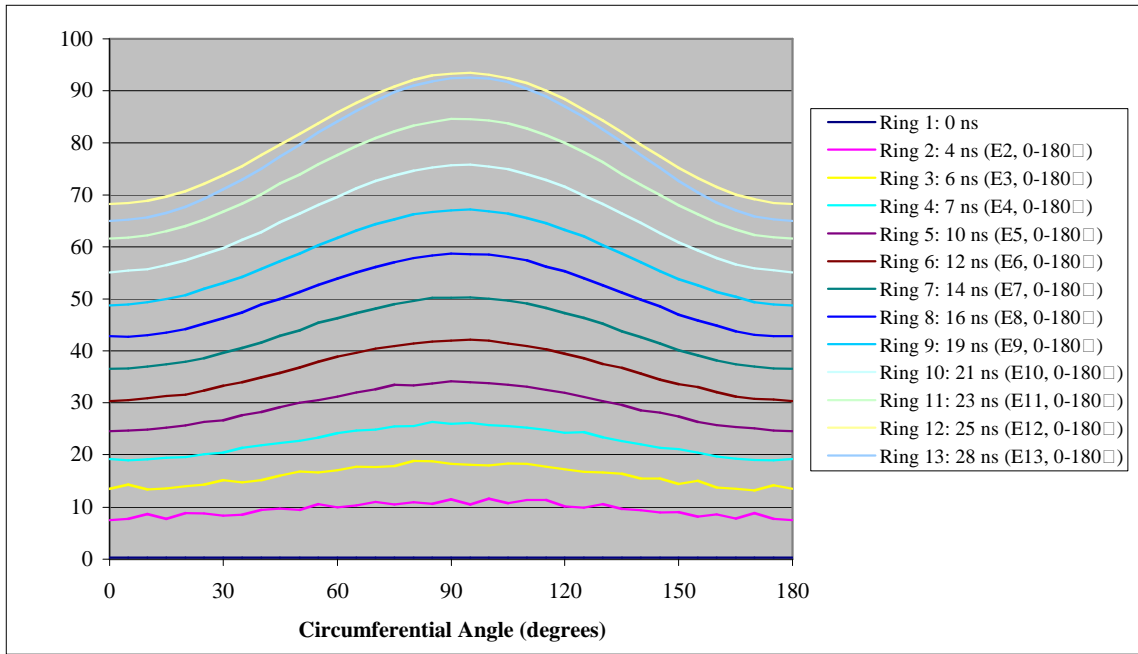
(a)
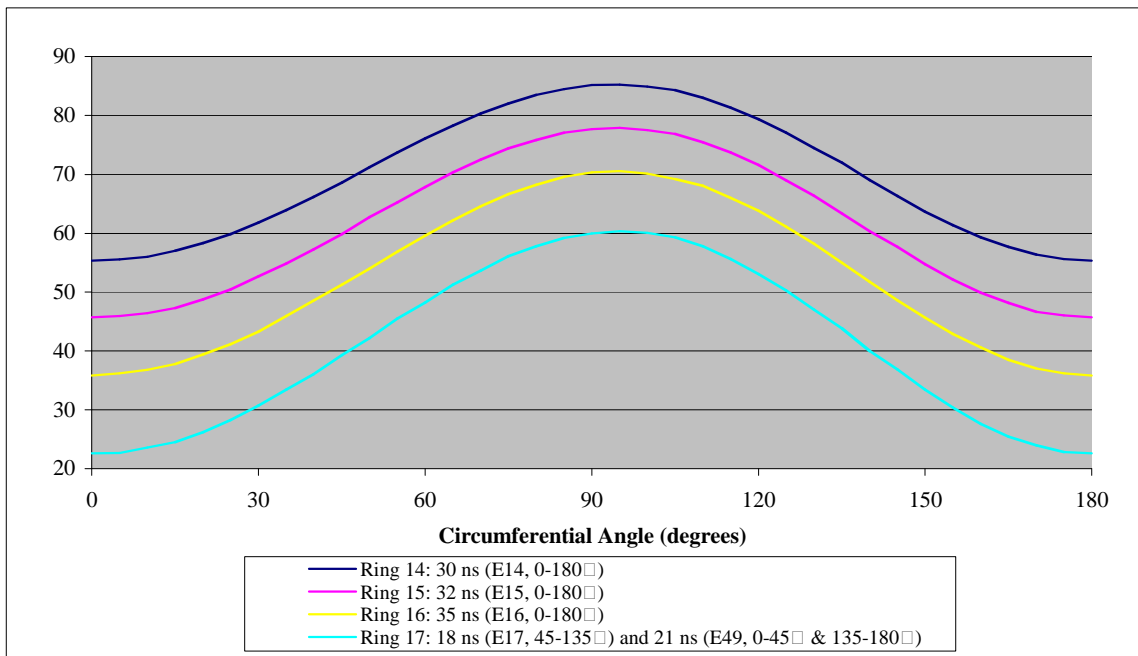
(b)

Figure D.6: Delay times and ranges for rings (a) 1 through 13 and (b) 14 through 17 when inspecting curved interface forging coupon #4.
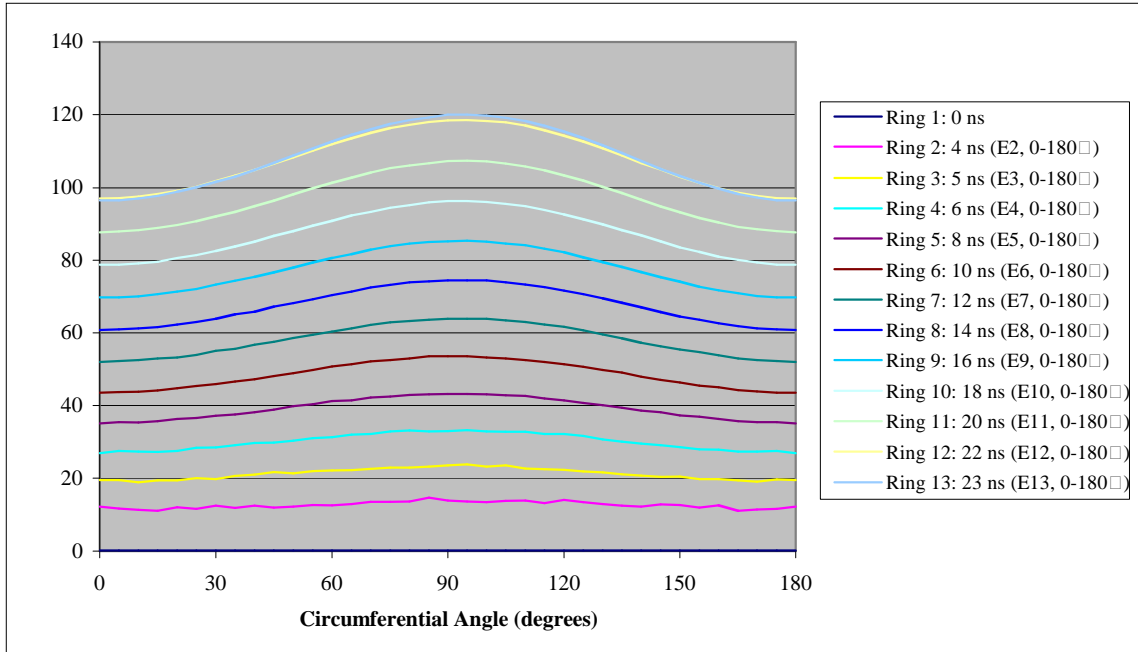
(a)
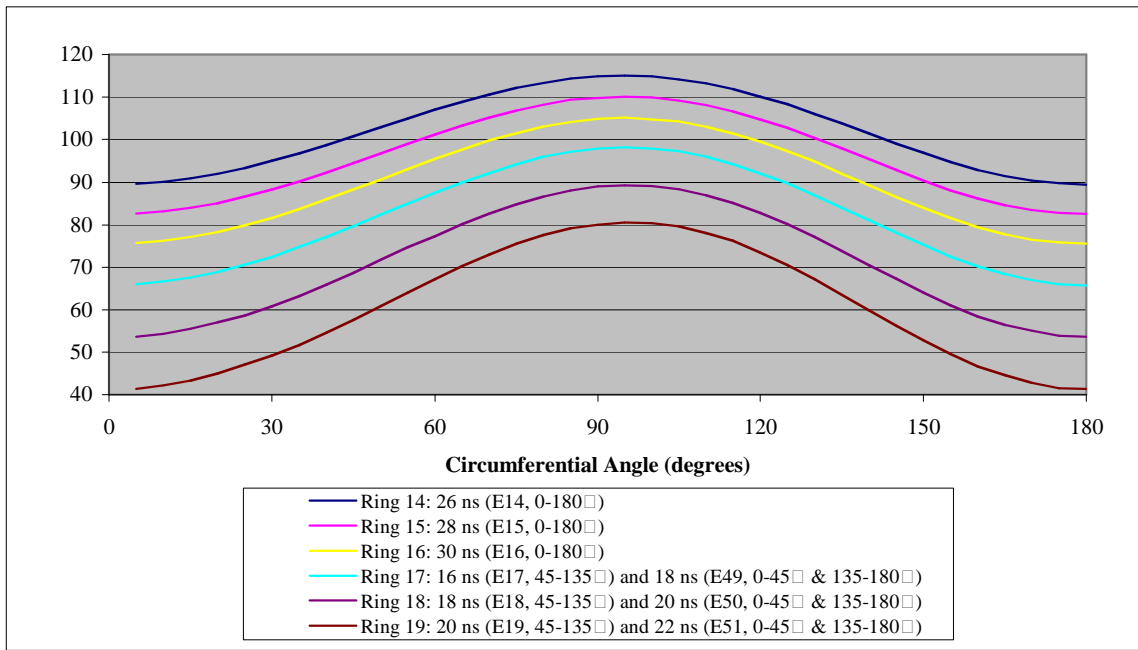
(b)

Figure D.7: Delay times and ranges for rings (a) 1 through 13 and (b) 14 through 19 when inspecting curved interface forging coupon #5.
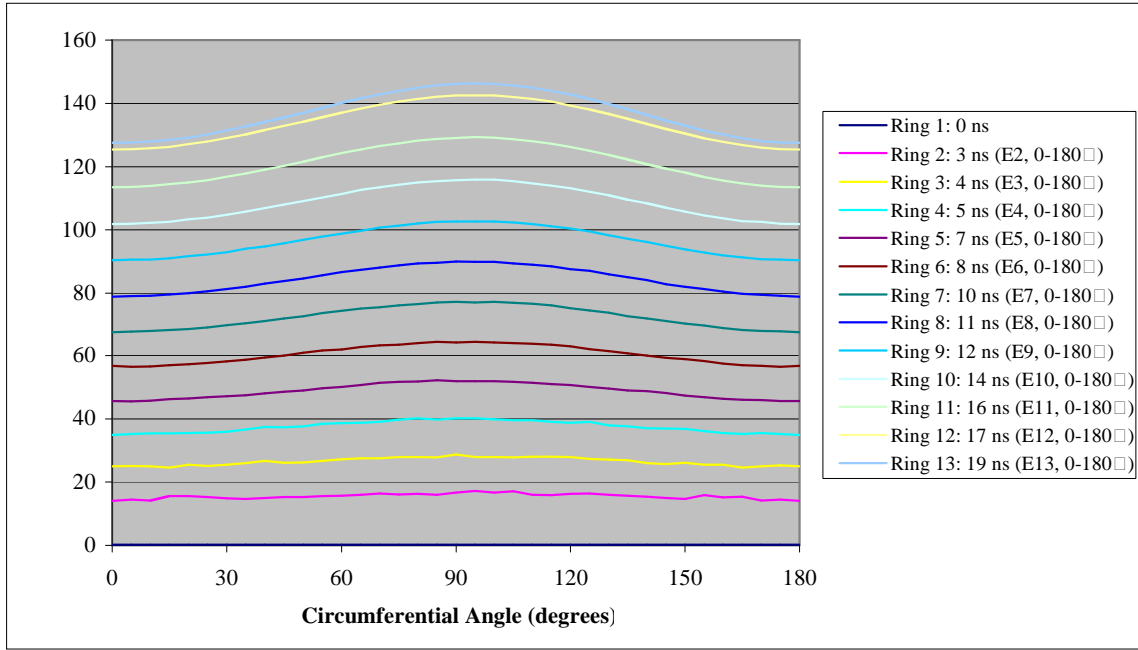
(a)
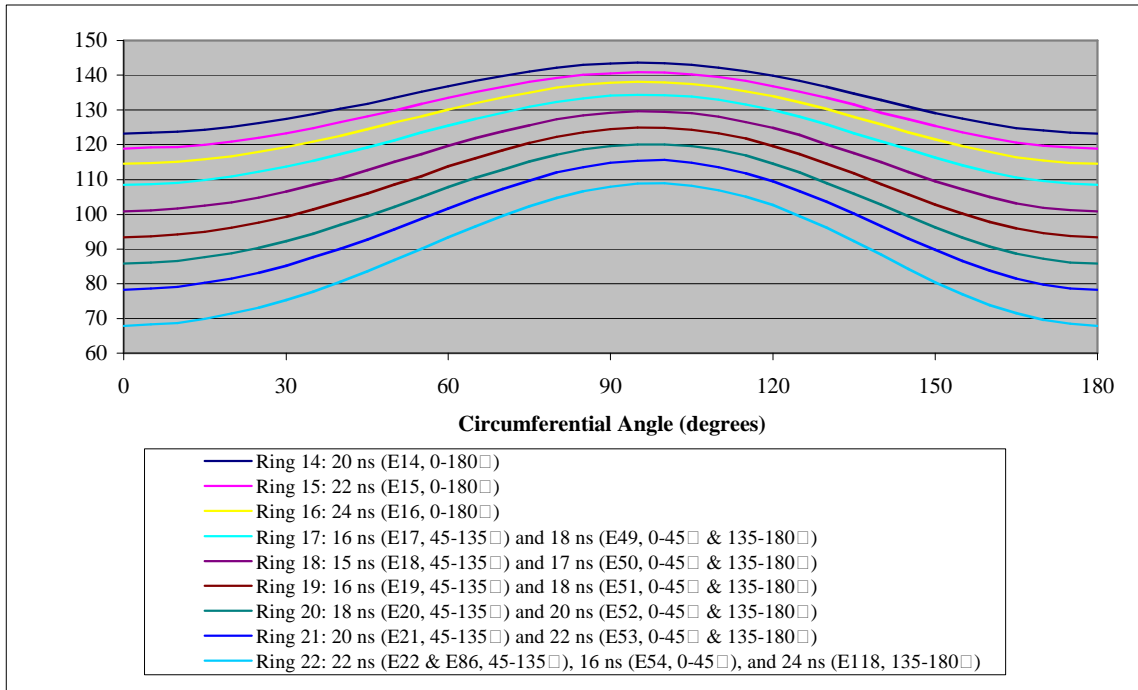
(b)

Figure D.8: Delay times and ranges for rings (a) 1 through 13 and (b) 14 through 22 when inspecting curved interface forging coupon #6.
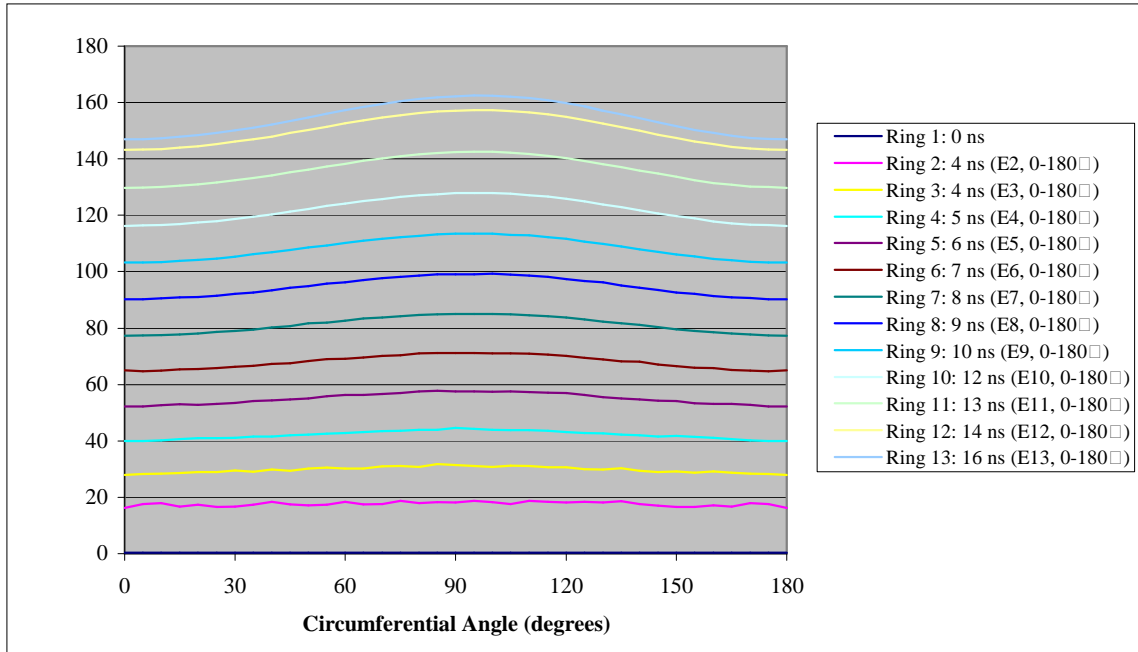
(a)
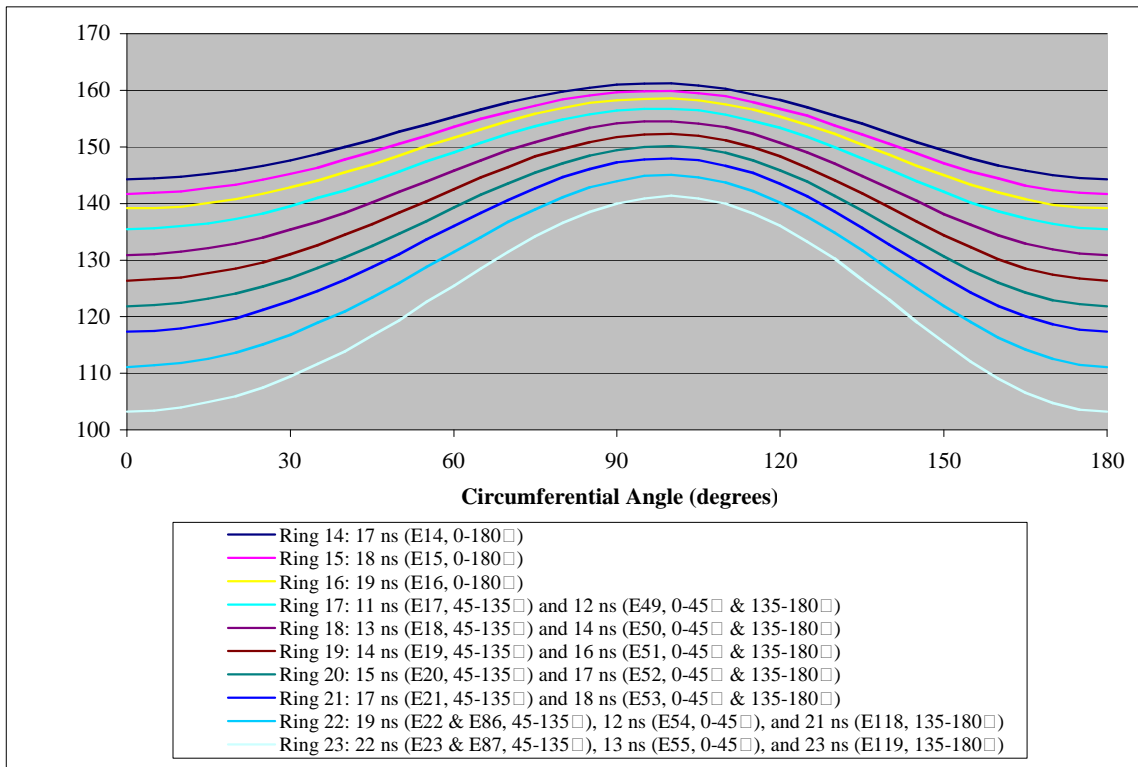
(b)

Figure D.9: Delay times and ranges for rings (a) 1 through 13 and (b) 14 through 23 when inspecting curved interface forging coupon #7.

110
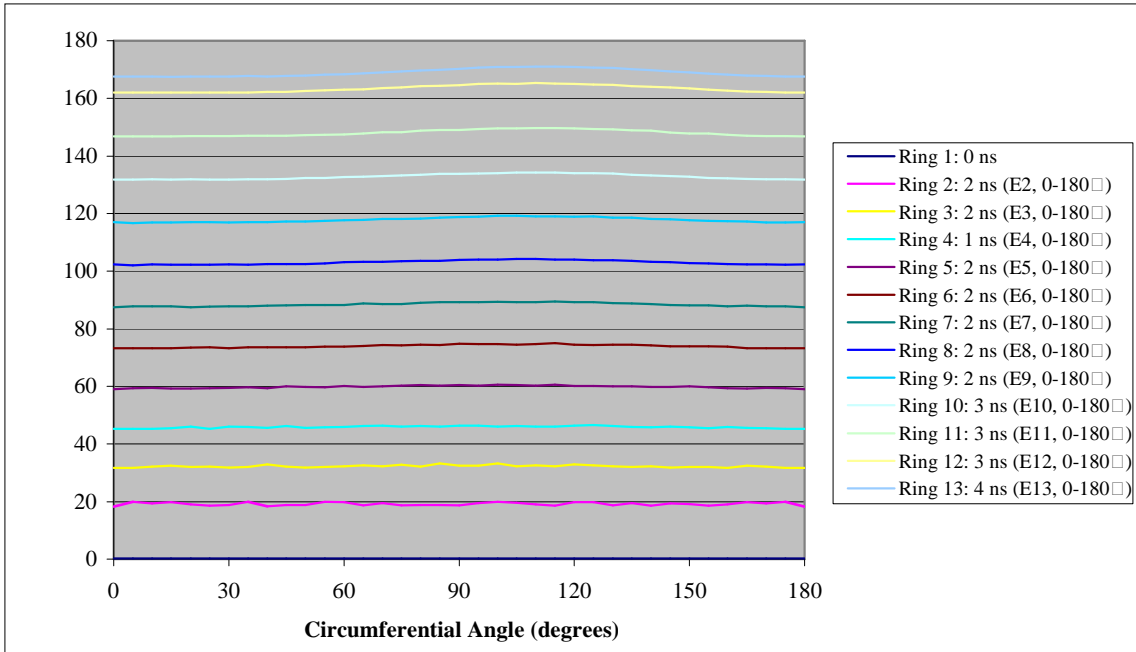
(a)
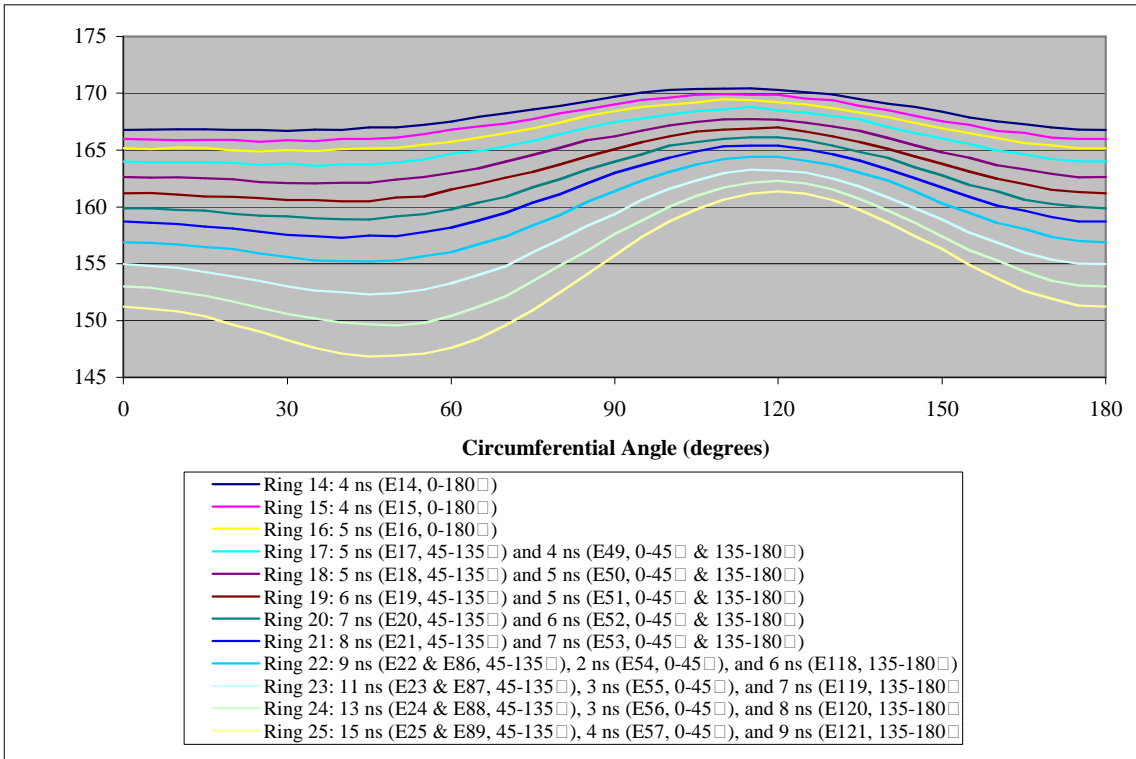
(b)

Figure D.10: Delay times and ranges for rings (a) 1 through 13 and (b) 14 through 25 when inspecting curved interface forging coupon #8.
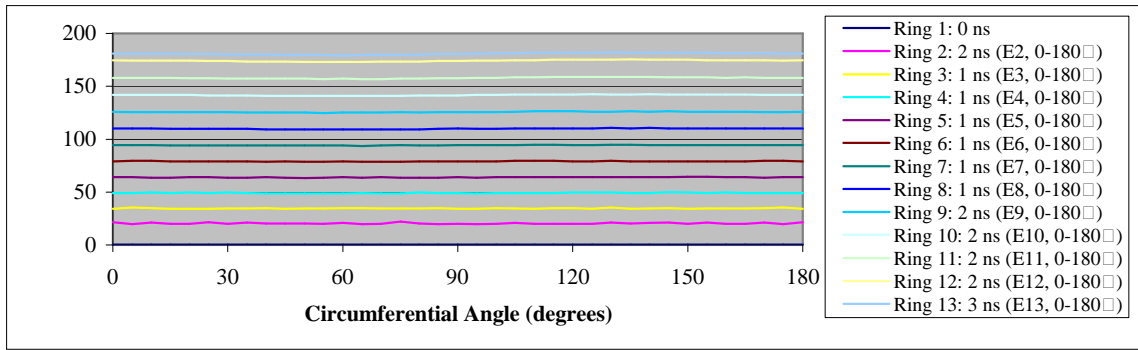
(a)
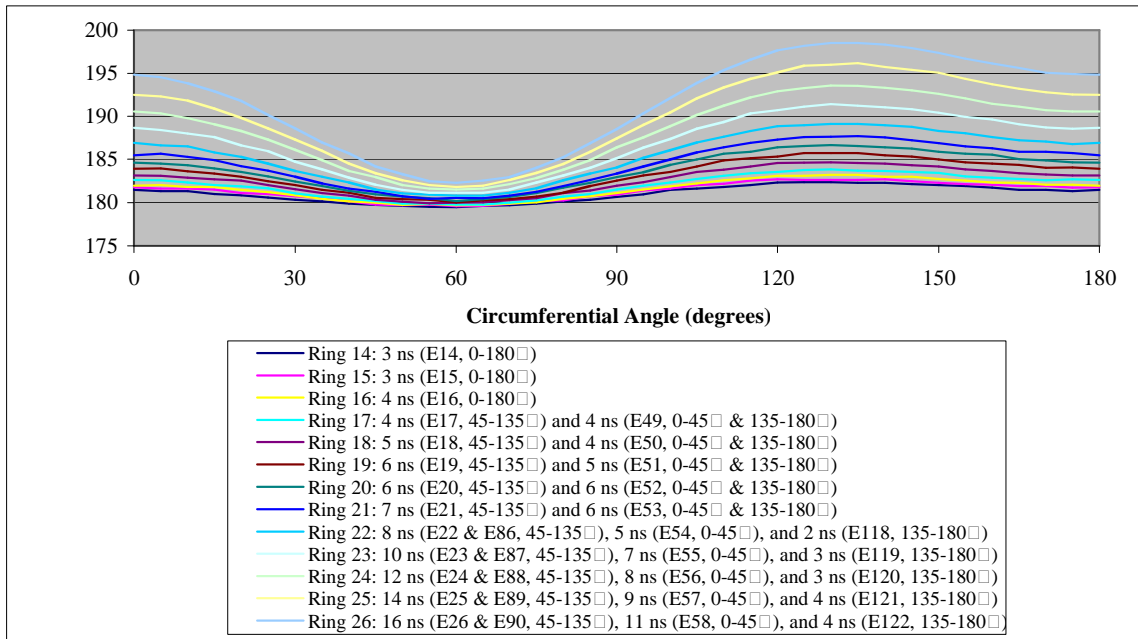
(b)
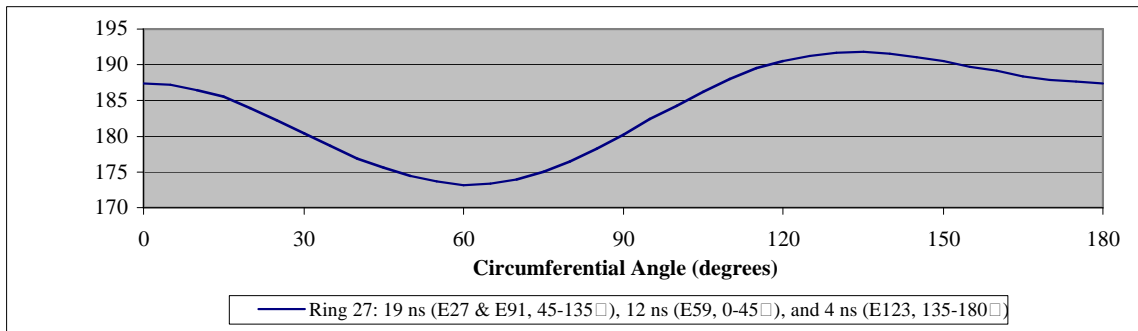
(c)

Figure D.11: Delay times and ranges for rings (a) 1 through 13, (b) 14 through 26, and (c) 27 when inspecting curved interface forging coupon #9.
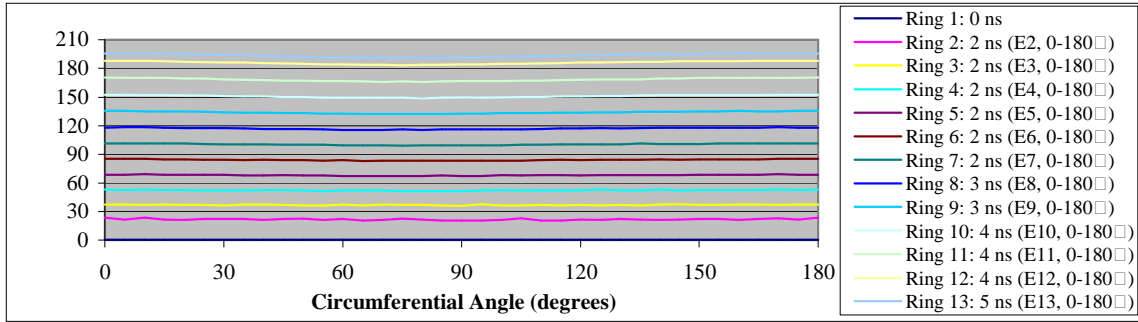
(a)
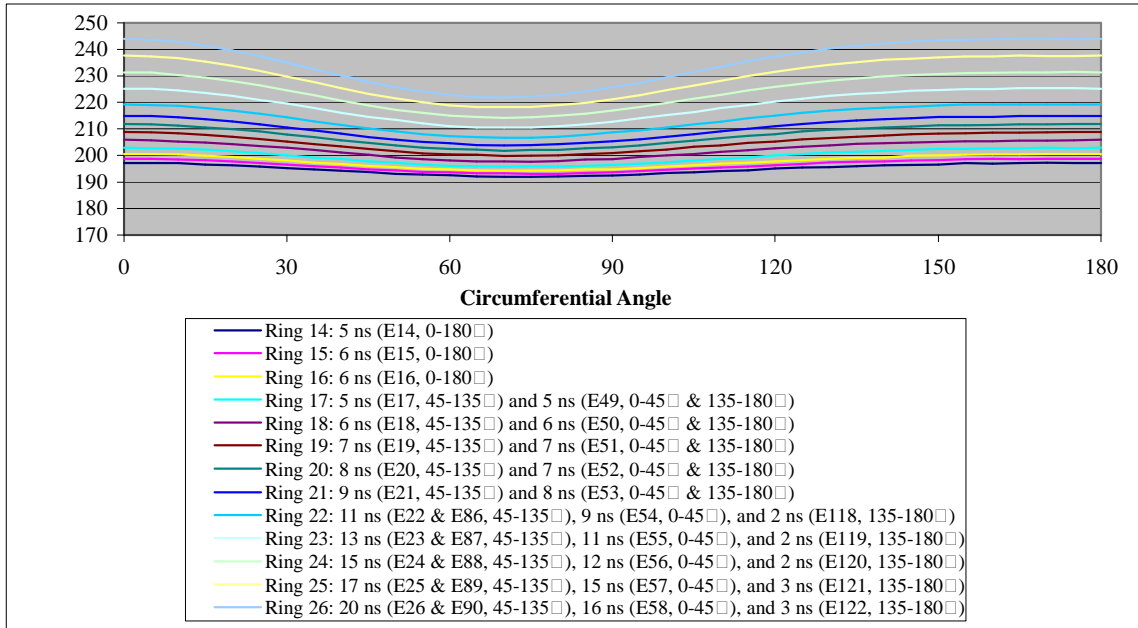
(b)
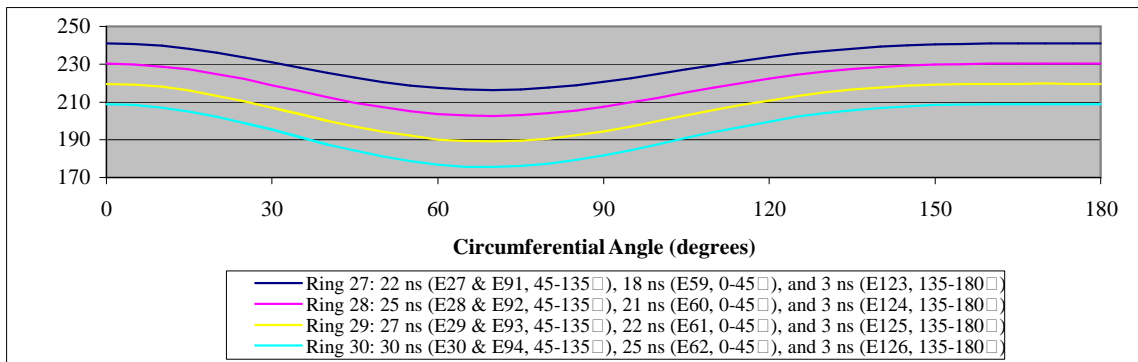
(c)

Figure D.12: Delay times and ranges for rings (a) 1 through 13, (b) 14 through 26, and (c) 27 through 30 when inspecting curved interface forging coupon #10.
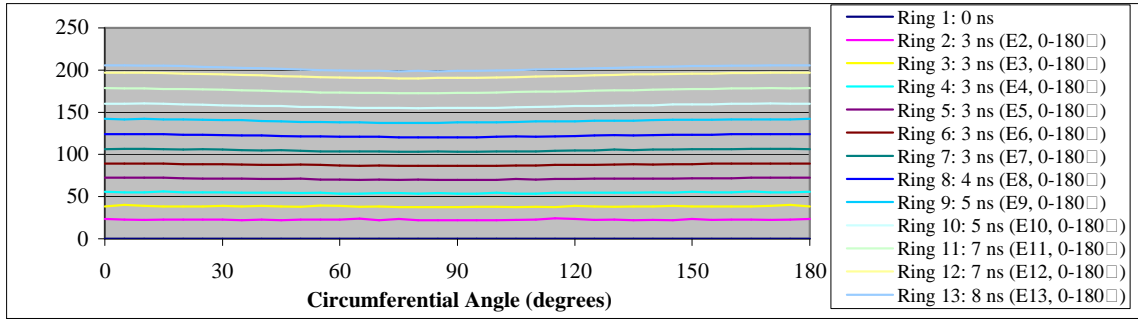
(a)
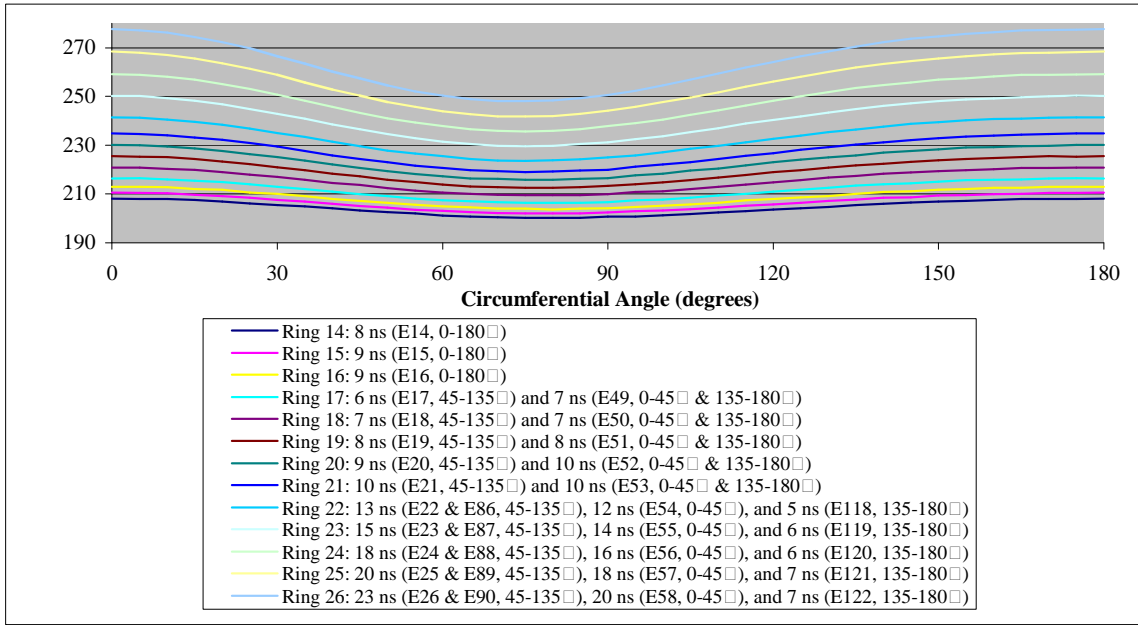
(b)
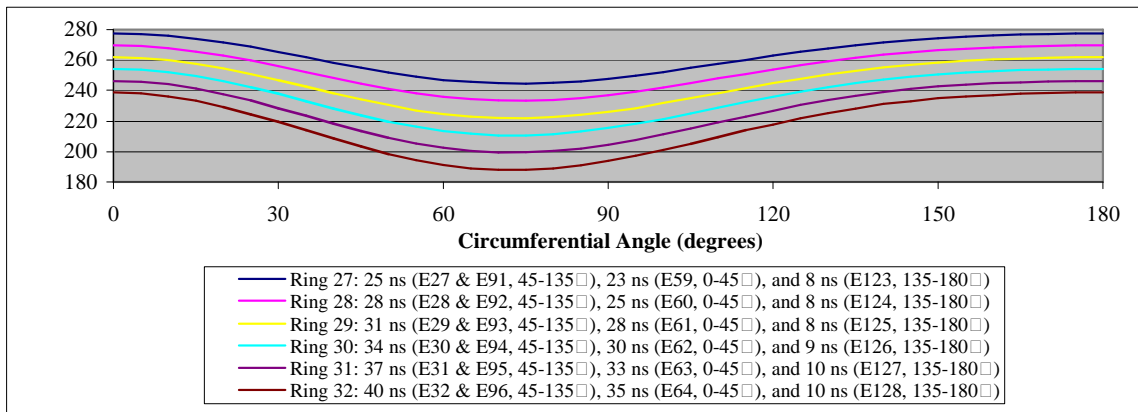
(c)

Figure D.13: Delay times and ranges for rings (a) 1 through 13, (b) 14 through 26, and (c) 27 through 32 when inspecting curved interface forging coupon #11.
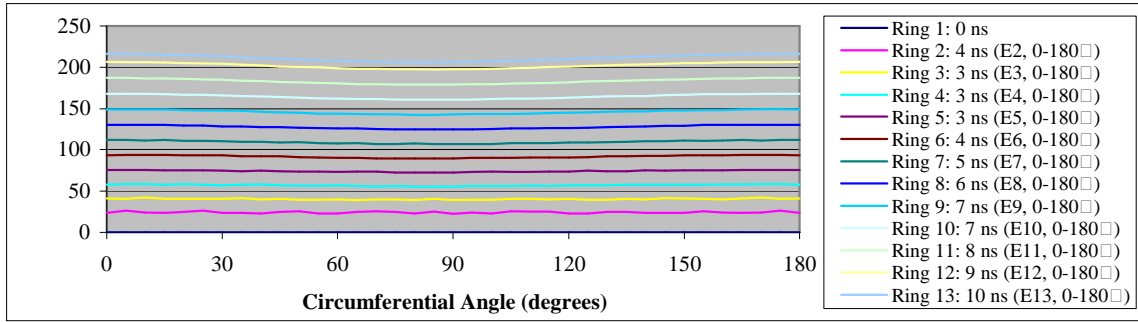
(a)
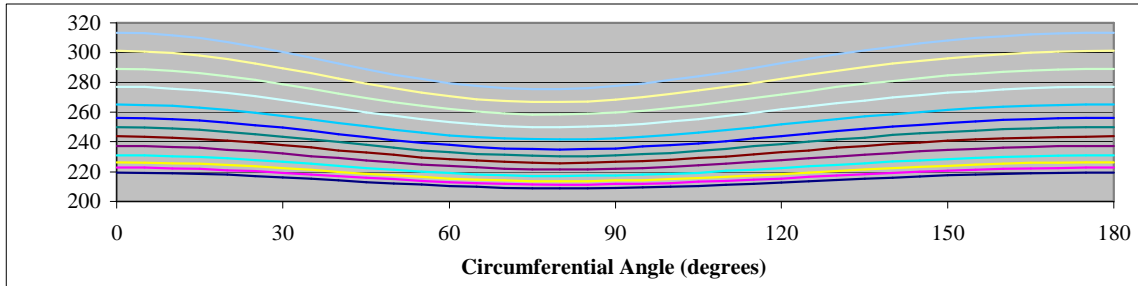
(b)
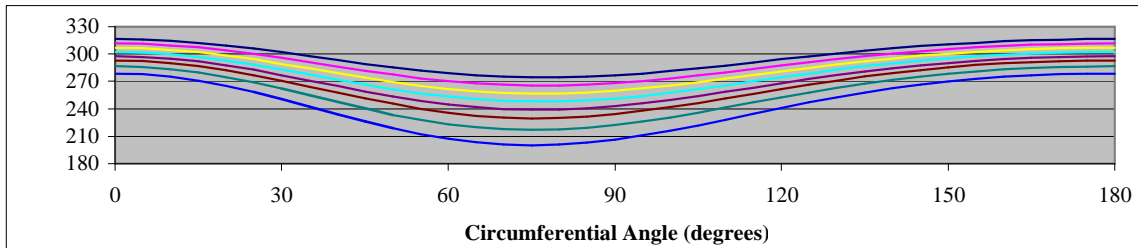
(c)

Figure D.14: Delay times and ranges for rings (a) 1 through 13, (b) 14 through 26, and (c) 27 through 34 when inspecting curved interface forging coupon #12.
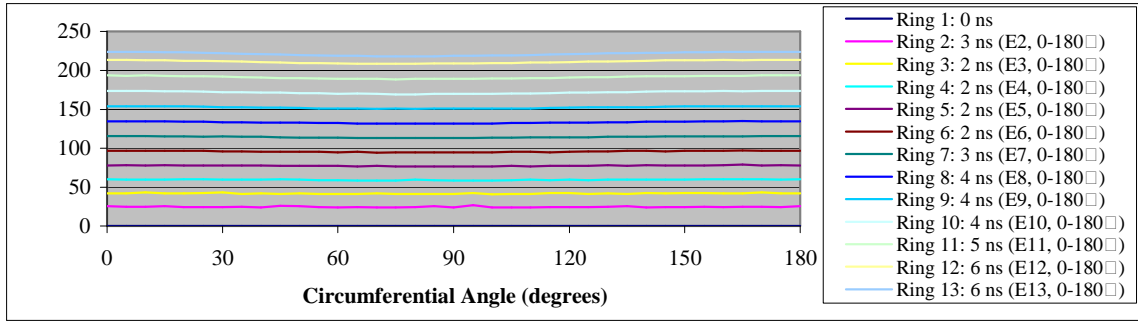
(a)
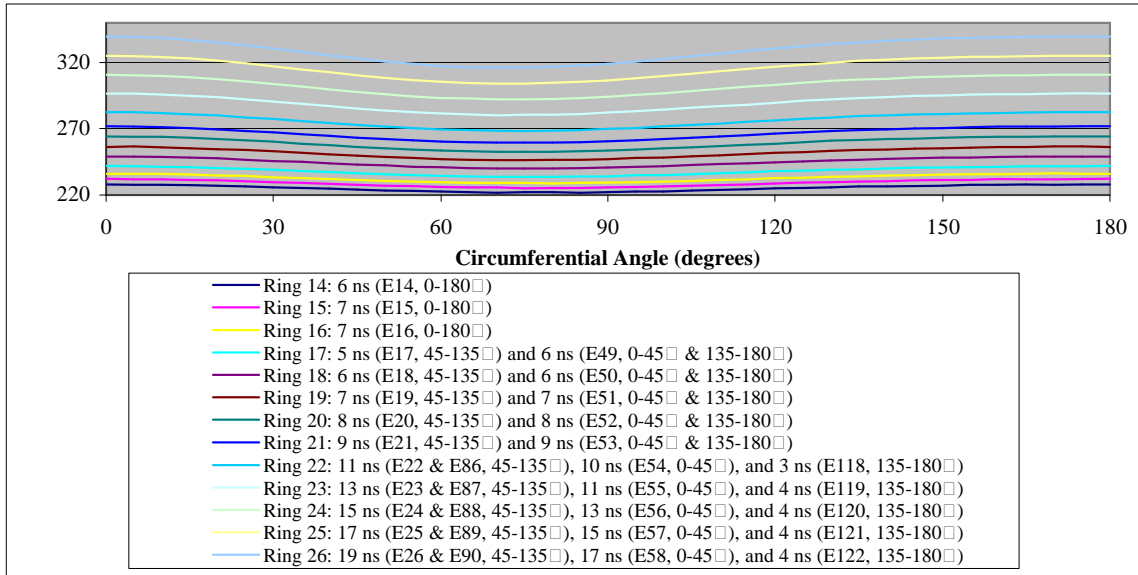
(b)
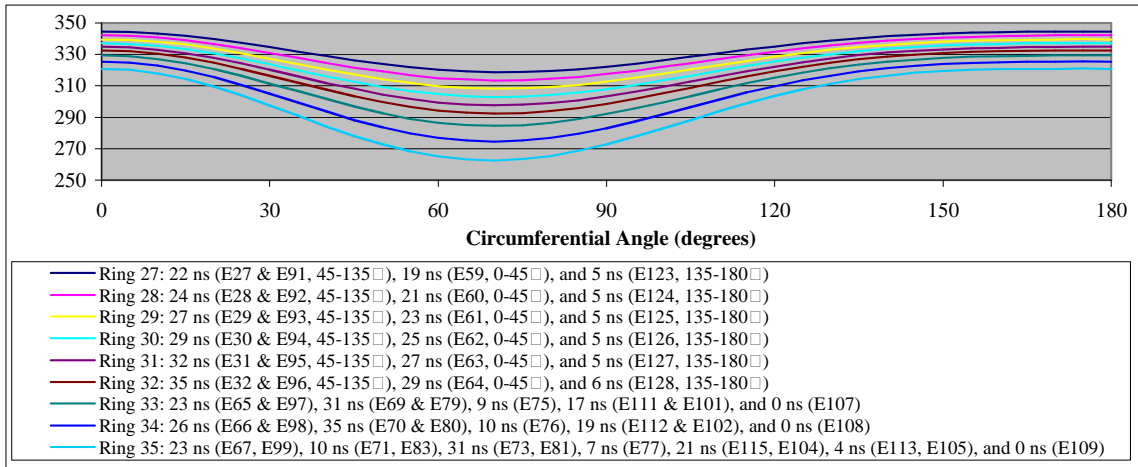
(c)

Figure D.15: Delay times and ranges for rings (a) 1 through 13, (b) 14 through 26, and (c) 27 through 35 when inspecting curved interface forging coupon #13.

$$\text{phase difference} = \Delta\phi = \left(\frac{\text{Range in Delay Times Over an Element (ns)}}{\text{Period (ns)}}\right) \times 360° \qquad (D.1)$$

$$\text{sound intensity} = I = 2I_0\left[1 + \cos\Delta\phi\right], \text{ where } I_0 \text{ is the initial sound intensity} \qquad (D.2)$$

$$I_n = c_nI_0, \text{ where } c_n = 2\left[1 + \cos\Delta\phi_n\right] \text{ and } n \text{ is the number of elements in the aperture} \qquad (D.3)$$

$$\text{maximum sound intensity per element} = I_{max} = 2I_0\left[1 + \cos(0°)\right] = 4I_0 \qquad (D.4)$$

$$\text{intensity level change (decibels)} = 10\log\frac{\sum_{i=1}^{n} I_n}{nI_{max}} = 10\log\frac{I_0\sum_{i=1}^{n} c_n}{4nI_0} = 10\log\left[\frac{1}{4n}\sum_{i=1}^{n} c_n\right] \qquad (D.5)$$

Tabulated in Table D.1 are the intensity level changes due to destructive interference occurring when waves arrive at different times at an element for ultrasonic beams generated during the inspection of curved interface calibration specimens 2 through 13 with the 3D ray-tracing algorithm.

Plotted in Figure D.16 and tabulated in Tables D.2 and D.3 are the delay times, averaged over each element in the aperture necessary for achieving an F/6 beam focus, for phasing individual elements of the transducer array based on Fermat surfaces generated for each curved interface calibration specimens 2 through 13 when using the 3D ray-tracing algorithm. These sets of delay time values were entered into text files in the format required by the phased array instrumentation. Using these formatted files containing the delay times, laboratory data was acquired and used to produce the C-scan images when using the 3D ray-tracing algorithm presented in Chapter 4 of this dissertation.

Table D.1: Intensity level changes due to destructive sound wave interference during the inspection of curved interface forging coupons 2 through 13 when using the 3D ray-tracing algorithm.

Block #	$\frac{1}{4}\sum_{i=1}^{n} c_n$	Number of Elements in Aperture, n	$\frac{1}{n}\left[\frac{1}{4}\sum_{i=1}^{n} c_n\right]$	Intensity Level Change (dB)
2	7.42	9	0.824	-0.84
3	9.19	13	0.707	-1.51
4	12.21	18	0.678	-1.69
5	16.06	22	0.730	-1.37
6	22.89	30	0.763	-1.18
7	27.49	34	0.809	-0.92
8	40.16	42	0.956	-0.19
9	47.06	50	0.941	-0.26
10	52.52	62	0.847	-0.72
11	51.84	70	0.741	-1.30
12	52.37	86	0.609	-2.15
13	73.09	98	0.746	-1.27

Figure D.16: Circumferential delay times averaged over each element when focusing on FBHs in the curved interface forging coupons when using the 3D ray-tracing algorithm.

Table D.2: Circumferential delay times averaged over each element when focusing on FBHs in the curved interface forging coupons when using the 3D ray-tracing algorithm (elements 1-25 only).

Ele. #	Ring #	Block 02	Block 03	Block 04	Block 05	Block 06	Block 07	Block 08	Block 09	Block 10	Block 11	Block 12	Block 13
1	1	26	0	0	0	0	0	0	0	0	0	0	0
2	2	21	5	9	12	15	17	19	20	22	22	24	25
3	3	18	7	16	21	26	29	32	34	37	38	40	42
4	4	15	9	22	30	37	42	46	49	52	55	57	59
5	5	12	12	29	39	49	55	60	64	68	71	74	77
6	6	9	15	36	48	60	68	74	79	84	88	92	96
7	7	6	18	43	58	72	81	88	94	100	105	109	114
8	8	3	21	50	67	84	94	103	110	117	122	127	133
9	9	0	24	58	77	96	108	118	125	134	140	146	152
10	10		27	65	87	108	122	133	141	151	157	164	172
11	11		31	73	97	121	136	148	158	168	175	183	191
12	12		34	80	107	133	150	163	174	186	194	202	211
13	13		28	78	108	136	154	169	181	193	202	211	221
14	14			70	102	133	152	168	181	195	204	214	225
15	15			61	96	129	150	167	181	196	206	217	229
16	16			52	90	126	148	166	181	198	209	220	233
17	17			54	92	130	153	167	181	197	208	219	235
18	18				83	124	150	165	182	200	212	224	242
19	19				74	119	147	164	182	202	215	229	248
20	20					114	145	163	183	204	219	234	255
21	21					109	142	162	183	207	222	239	262
49	17			29	72	113	139	164	182	201	214	228	240
50	18				60	106	135	163	183	204	219	234	247
51	19				48	99	131	162	183	207	223	240	255
52	20					92	127	160	184	210	227	246	262
53	21					85	123	159	185	213	232	252	269
22	22					101	138	161	185	210	228	246	272
23	23						133	159	186	215	235	256	284
24	24							157	187	220	242	265	297
25	25							155	188	224	249	274	310

Table D.3: Circumferential delay times averaged over each element when focusing on FBHs in the curved interface forging coupons when using the 3D ray-tracing algorithm (elements 26-115 only).

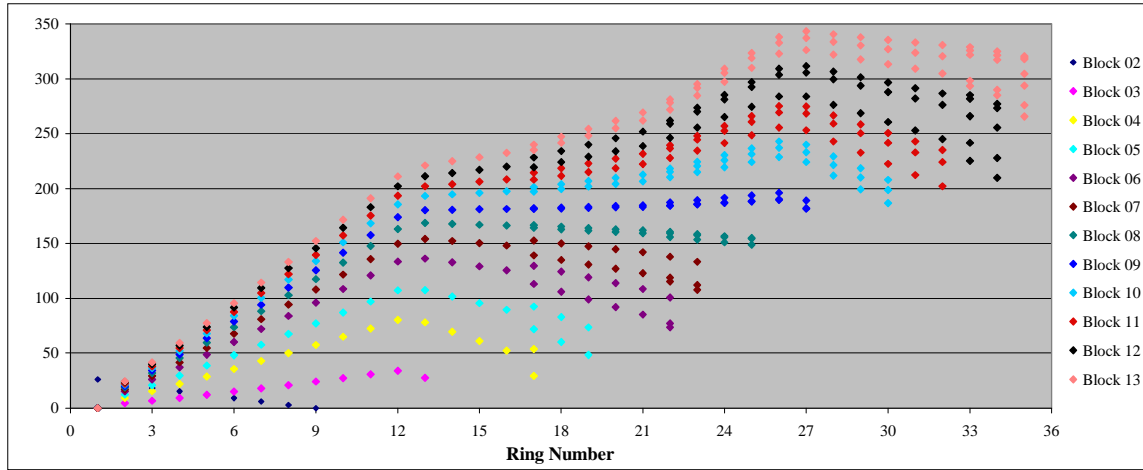| Ele. #	Ring #	Block 02	Block 03	Block 04	Block 05	Block 06	Block 07	Block 08	Block 09	Block 10	Block 11	Block 12	Block 13
26	26								190	229	256	284	323
27	27								182	224	253	284	326
28	28									212	243	276	322
29	29									199	233	268	318
30	30									187	223	261	313
31	31										212	253	309
32	32										202	245	305
54	22					73	115	156	184	215	237	259	278
55	23						108	153	186	221	245	270	292
56	24							151	187	226	253	281	305
57	25							149	188	232	261	292	319
58	26								190	237	269	304	333
59	27								182	233	268	305	337
60	28									222	259	299	334
61	29									210	250	294	330
62	30									199	242	288	327
63	31										233	282	324
64	32										224	276	320
65	33											225	293
66	34											210	285
67	35												276
68	36												
69	33											242	298
70	34											228	290
71	35												266
72	36												
73	35												294
74	36												
75	33											282	326
76	34											273	321
77	35												318
78	36												
107	33											285	329
108	34											277	325
109	35												321
110	36												
111	33											266	322
112	34											256	317
113	35												319
114	36												
115	35												305

Table D.4: Circumferential delay times averaged over each element when focusing on FBHs in the curved interface forging coupons when using the 3D ray-tracing algorithm (elements 118-128 only).

Ele. #	Ring #	Block 02	Block 03	Block 04	Block 05	Block 06	Block 07	Block 08	Block 09	Block 10	Block 11	Block 12	Block 13
118	22					77	119	159	188	219	240	262	281
119	23						112	158	190	224	248	274	295
120	24							156	192	230	257	285	309
121	25							155	194	237	266	297	324
122	26								196	243	275	309	338
123	27								189	240	275	312	343
124	28									229	267	306	341
125	29									219	259	301	338
126	30									208	251	296	335
127	31										243	291	333
128	32										235	287	331

APPENDIX E. GROUPING DELAY TIMES FOR 3D METHOD

The following tables graphically present the grouping of delay times generated by the 3D ray-tracing algorithm, i.e., when using circumferential phasing of the transducer array, when inspecting curved interface forging coupons 2 through 13 as previously tabulated in Table 4.4 in chapter 4 of this dissertation.

Figure E.1: Grouping delay times into 1 focal law for curved interface forging coupon #2.

Figure E.2: Grouping delay times into 1 focal law for curved interface forging coupon #3.

Figure E.3: Grouping delay times into 4 focal laws for curved interface forging coupon #4.

Receiving Elements		
	#1 - 19	#49 - 51
Transmitting Elements #1 - 19	1	2
#49 - 51	3	4

Figure E.4: Grouping delay times into 4 focal laws for curved interface forging coupon #5.

Receiving Elements			
#1 - 22	#49 - 54	#86	#118
1	2	1	3
4	5	4	6
1	8	1	10
7	9	7	11

(Transmitting Elements: #1 - 22, #49 - 54, #86, #118)

Figure E.5: Grouping delay times into 5 focal laws for curved interface forging coupon #6.

		Receiving Elements			
		#1 - 23	#49 - 55	#86 - 87	#118 - 119
Transmitting Elements	#1 - 23	1	2	1	3
	#49 - 55	4	5	4	6
	#86 - 87	1	8	1	10
	#118 - 119	7	9	7	11

Figure E.6: Grouping delay times into 9 focal laws for curved interface forging coupon #7.

		Receiving Elements			
		#1 - 25	#49 - 57	#86 - 89	#118 - 121
Transmitting Elements	#1 - 25	1	2	1	3
	#49 - 57	4	5	4	6
	#86 - 89	1	8	1	10
	#118 - 121	7	9	7	11

Figure E.7: Grouping delay times into 9 focal laws for curved interface forging coupon #8.

		Receiving Elements			
		#1 - 27	#49 - 59	#86 - 91	#118 - 123
Transmitting Elements	#1 - 27	1	2	1	3
	#49 - 59	4	5	4	6
	#86 - 91	1	8	1	10
	#118 - 123	7	9	7	11

Figure E.8: Grouping delay times into 9 focal laws for curved interface forging coupon #9.

		Receiving Elements			
		#1 - 30	#49 - 62	#86 - 94	#118 - 126
Transmitting Elements	#1 - 30	1	2	1	3
	#49 - 62	4	5	4	6
	#86 - 94	1	8	1	10
	#118 - 126	7	9	7	11

Figure E.9: Grouping delay times into 9 focal laws for curved interface forging coupon #10.

Transmitting Elements	Receiving Elements			
	#1 - 32	#49 - 64	#86 - 96	#118 - 128
#1 - 32	1	2	1	3
#49 - 64	4	5	4	6
#86 - 96	1	8	1	10
#118 - 128	7	9	7	11

Figure E.10: Grouping delay times into 9 focal laws for curved interface forging coupon #11.

		Receiving Elements
		#1 - 32	#49 - 64	#65 - 80	#86 - 96	#97 - 112	#118 - 128
\multirow{10}{*}{**Transmitting Elements**}	#1 - 32	1	2	3	1	4
	#49 - 64	5	\multicolumn{2}{c}{8}	5	\multicolumn{2}{c}{10}
	#65 - 80	6			6	9	12
	#86 - 96	1	\multicolumn{2}{c}{13}	1	\multicolumn{2}{c}{15}
	#97 - 112	7			7	14
	#118 - 128	6	\multicolumn{2}{c}{16}	6		

Figure E.11: Grouping delay times into 16 focal laws for curved interface forging coupon #12.

		Receiving Elements				
		#1 - 32	#49 - 64	#65 - 81, 83	#86 - 96	#97 - 113, 115	#118 - 128
Transmitting Elements	#1 - 32	1	2	3	1	4	
	#49 - 64	5	8	10	5	12	
	#65 - 81, 83	6	9	11	6	13	
	#86 - 96	1	14	15	1	13	
	#97 - 113, 115	7			7	18	
	#118 - 128	6	16	17	6		

Figure E.12: Grouping delay times into 18 focal laws for curved interface forging coupon #13.

APPENDIX F. INDIVIDUAL FOCAL LAW C-SCANS PRIOR TO SUMMING

This appendix provides individual focal law C-scans when multiple focal laws were required to inspect FBHs due to phased array hardware limitations, where multiple focal law data was post-processed to generate summed C-scan images. Also included are the gain settings required to achieve peak amplitudes of 80%FSH for this individual focal law data. Of the C-scan images previously presented, the following inspections required multiple focal laws and resulted in summed C-scan images: initial 2D inspections of planar coupons 12 and 13 (See Table F.1 and Figure F.1), refined 2D inspections of planar coupons 12 and 13 (See Table F.2 and Figure F.2), refined 2D inspections of curved coupons 12 and 13 (See Table F.3 and Figure F.3), and 3D inspections of curved coupons 4 thru 13 (See Table F.4 and Figures F.4 thru F.13).

Table F.1: Gain settings to achieve 80%FSH in initial 2D inspections of planar coupons 12 and 13.

Focal Law Block	1	2	3	4	Summed
12	25.5	34.6	33.9	44.5	20.4
13	27.6	32.1	35.0	41.0	19.7

Table F.2: Gain settings to achieve 80%FSH in refined 2D inspections of planar coupons 12 and 13.

Focal Law Block	1	2	3	4	Summed
12	22.7	33.2	32.0	44.0	18.0
13	23.4	30.9	32.7	39.5	17.9

Table F.3: Gain settings to achieve 80%FSH in refined 2D inspections of curved coupons 12 and 13.

Focal Law Block	1	2	3	4	Summed
12	30.2	47.1	45.6	57.8	27.9
13	30.9	44.0	42.0	53.3	27.4

Table F.4: Gain settings to achieve 80%FSH in 3D inspections of curved coupons 4 thru 13.

Block Focal Law	4	5	6	7	8	9	10	11	12	13
1	29.7	28.7	28.1	30.2	27.2	27.2	28.0	27.7	31.6	32.5
2	54.5	46.7	38.8	41.0	39.5	39.5	43.9	44.6	47.3	48.5
3	49.6	41.9	56.4	52.8	43.9	43.9	42.2	40.8	60.2	52.7
4	75.7	57.8	38.2	40.9	37.9	37.9	40.1	41.4	40.2	41.3
5			48.5	49.7	42.4	42.4	40.8	41.2	44.8	45.7
6			65.0	52.0	48.3	48.3	51.9	52.6	41.5	42.8
7			52.0	62.7	52.8	52.8	50.4	52.2	49.4	45.0
8			62.5	59.2	52.0	52.0	52.6	52.8	54.1	58.6
9			63.0	71.6	51.6	51.6	51.7	54.2	59.6	63.5
10			80.1	59.8	55.0	55.0	50.6	52.3	49.8	63.5
11			76.7	67.7	54.0	54.0	51.6	50.8	63.1	63.1
12									61.4	52.3
13									51.1	49.7
14									44.1	52.6
15									50.5	58.1
16									52.1	58.1
17										61.1
18										41.1
summed c-scan	28.9	26.0	23.0	24.6	23.0	21.2	25.1	21.6	22.9	23.4

Block 12 Focal Law 01	Block 12 Focal Law 02	Block 12 Focal Law 03	Block 12 Focal Law 04	Block 12 Summed
Block 13 Focal Law 01	Block 13 Focal Law 02	Block 13 Focal Law 03	Block 13 Focal Law 04	Block 13 Summed
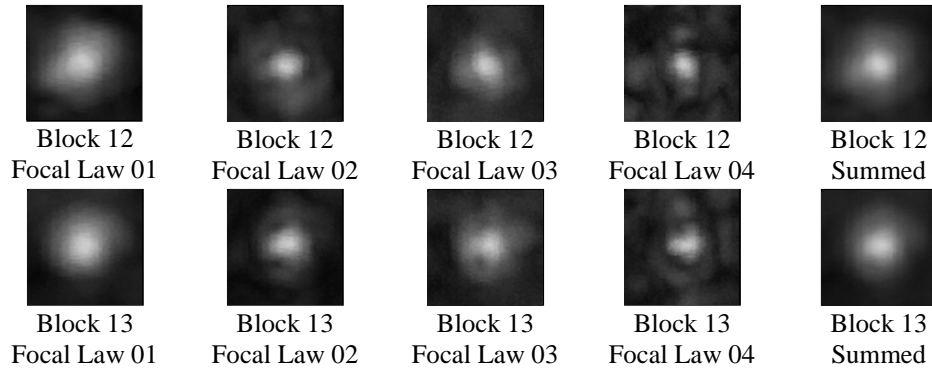
Figure F.1: Initial 2D method inspection C-scans of planar interface forging coupons #12 and #13.
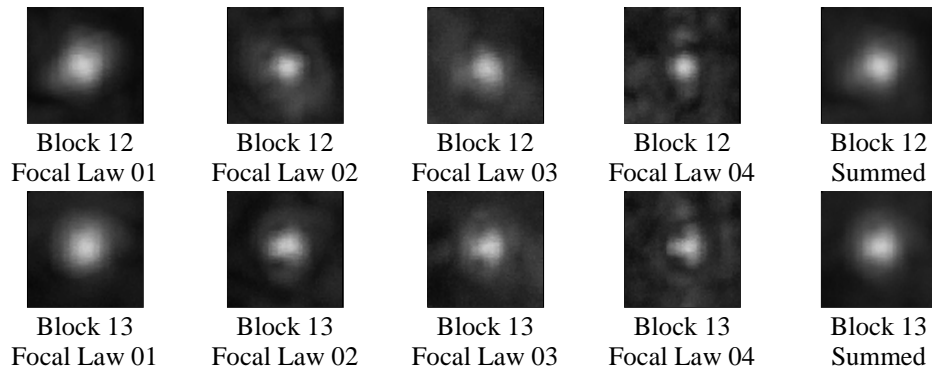
Block 12 Focal Law 01	Block 12 Focal Law 02	Block 12 Focal Law 03	Block 12 Focal Law 04	Block 12 Summed
Block 13 Focal Law 01	Block 13 Focal Law 02	Block 13 Focal Law 03	Block 13 Focal Law 04	Block 13 Summed

Figure F.2: Refined 2D method inspection C-scans of planar interface forging coupons 12 and 13.

Block 12 Focal Law 01	Block 12 Focal Law 02	Block 12 Focal Law 03	Block 12 Focal Law 04	Block 12 Summed
Block 13 Focal Law 01	Block 13 Focal Law 02	Block 13 Focal Law 03	Block 13 Focal Law 04	Block 13 Summed
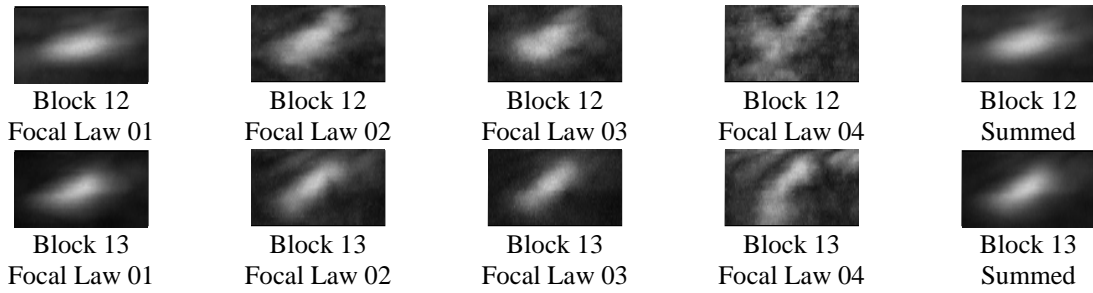
Figure F.3: Refined 2D method inspection C-scans of curved interface forging coupons 12 and 13.

Focal Law 01	Focal Law 02	Focal Law 03	Focal Law 04	Summed

Figure F.4: 3D method inspection C-scans of curved interface forging coupon #4.

Focal Law 01	Focal Law 02	Focal Law 03	Focal Law 04	Summed
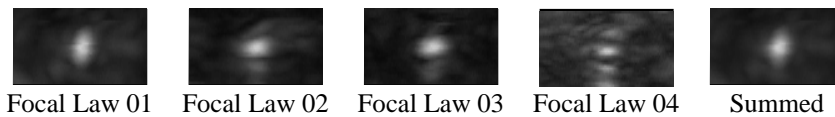
Figure F.5: 3D method inspection C-scans of curved interface forging coupon #5.

Focal Law 01   Focal Law 02   Focal Law 03   Focal Law 04   Focal Law 05

Focal Law 06   Focal Law 07   Focal Law 08   Focal Law 09   Focal Law 10

Focal Law 11   Summed
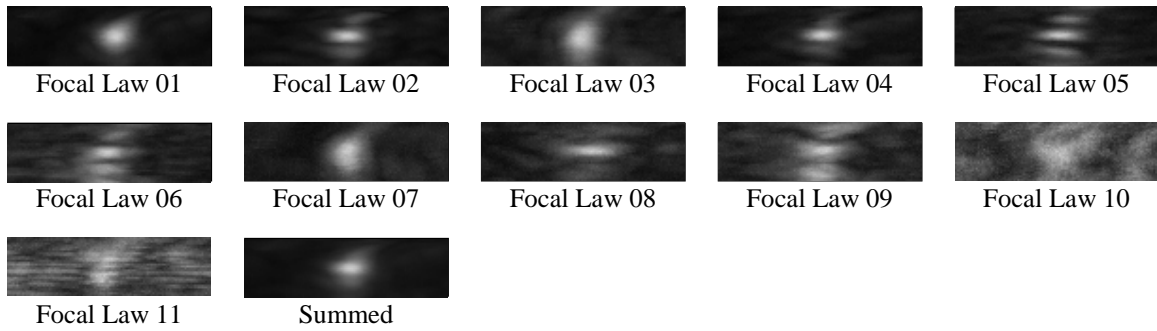
Figure F.6: 3D method inspection C-scans of curved interface forging coupon #6.

Focal Law 01   Focal Law 02   Focal Law 03   Focal Law 04   Focal Law 05

Focal Law 06   Focal Law 07   Focal Law 08   Focal Law 09   Focal Law 10

Focal Law 11   Summed
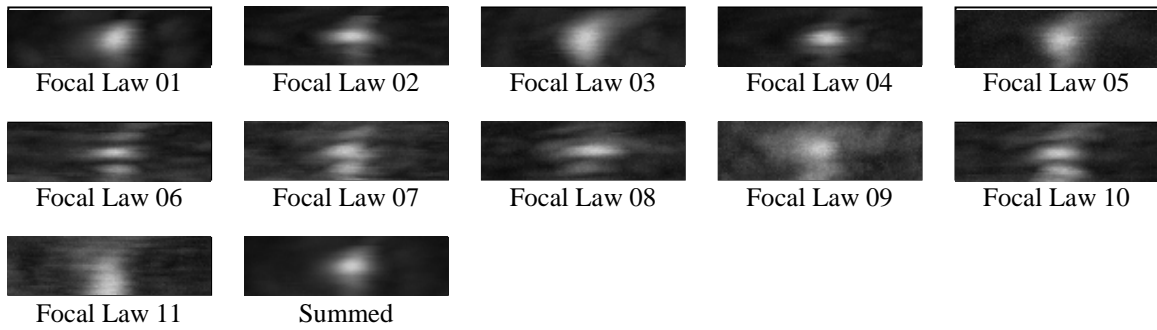
Figure F.7: 3D method inspection C-scans of curved interface forging coupon #7.

Focal Law 01   Focal Law 02   Focal Law 03   Focal Law 04   Focal Law 05

Focal Law 06   Focal Law 07   Focal Law 08   Focal Law 09   Focal Law 10

Focal Law 11   Summed
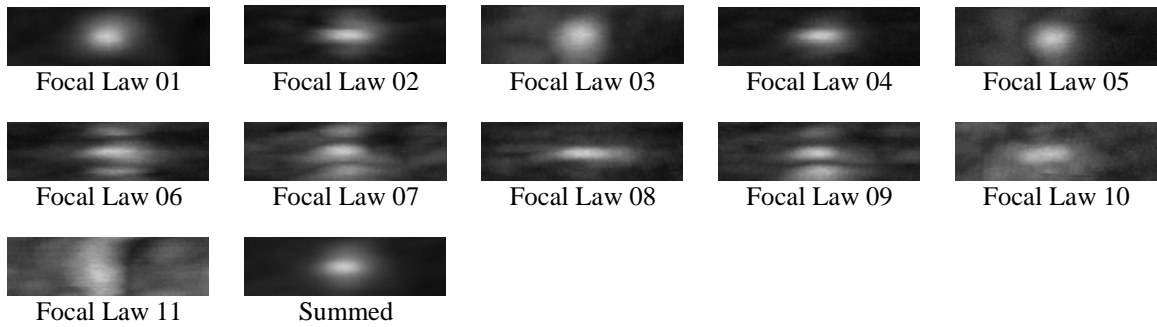
Figure F.8: 3D method inspection C-scans of curved interface forging coupon #8.

Focal Law 01   Focal Law 02   Focal Law 03   Focal Law 04   Focal Law 05

Focal Law 06   Focal Law 07   Focal Law 08   Focal Law 09   Focal Law 10

Focal Law 11   Summed
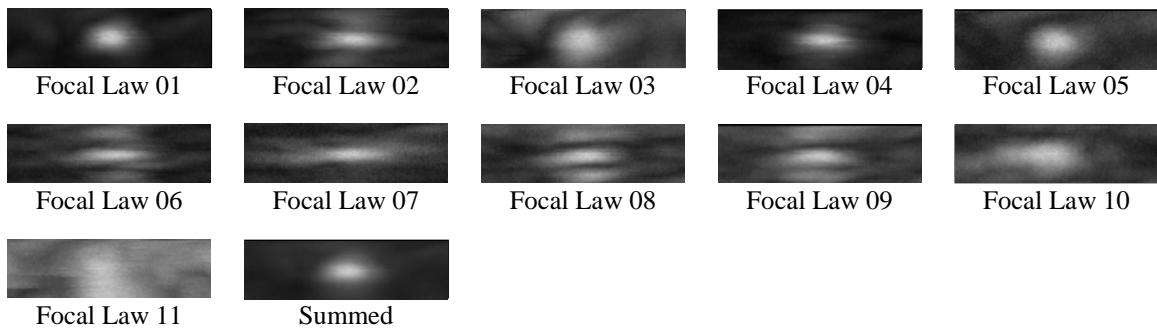
Figure F.9: 3D method inspection C-scans of curved interface forging coupon #9.

Focal Law 01   Focal Law 02   Focal Law 03   Focal Law 04   Focal Law 05

Focal Law 06   Focal Law 07   Focal Law 08   Focal Law 09   Focal Law 10

Focal Law 11   Summed
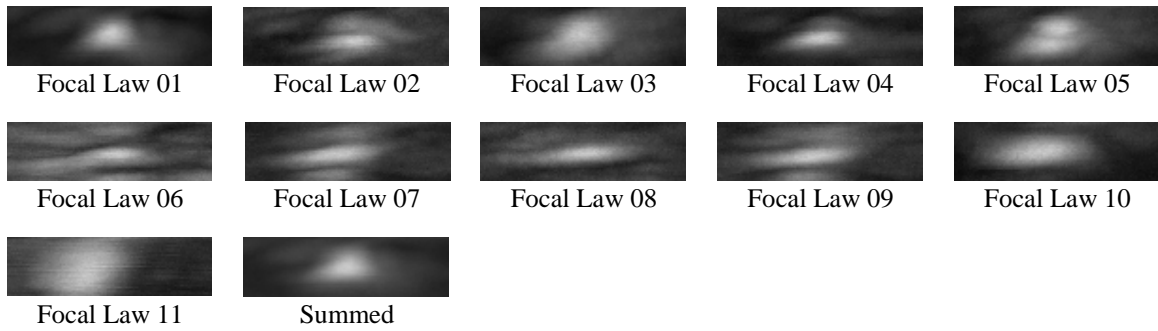
Figure F.10: 3D method inspection C-scans of curved interface forging coupon #10.

Focal Law 01   Focal Law 02   Focal Law 03   Focal Law 04   Focal Law 05

Focal Law 06   Focal Law 07   Focal Law 08   Focal Law 09   Focal Law 10

Focal Law 11   Summed
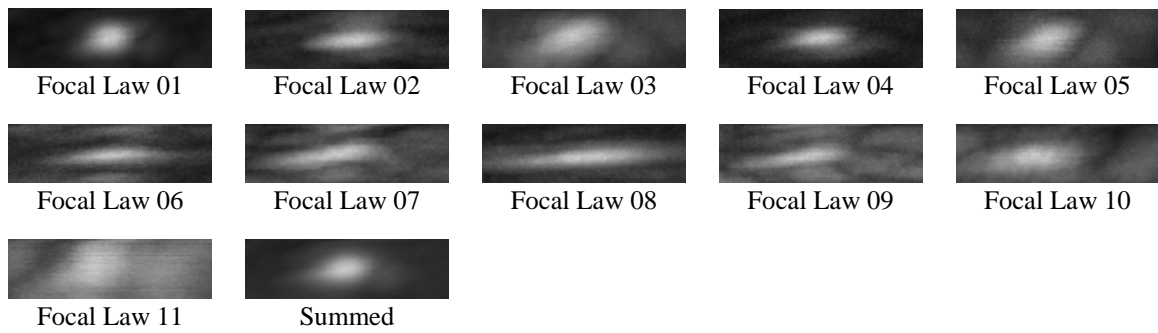
Figure F.11: 3D method inspection C-scans of curved interface forging coupon #11.

Focal Law 01   Focal Law 02   Focal Law 03   Focal Law 04   Focal Law 05

Focal Law 06   Focal Law 07   Focal Law 08   Focal Law 09   Focal Law 10

Focal Law 11   Focal Law 12   Focal Law 13   Focal Law 14   Focal Law 15

Focal Law 16   Summed
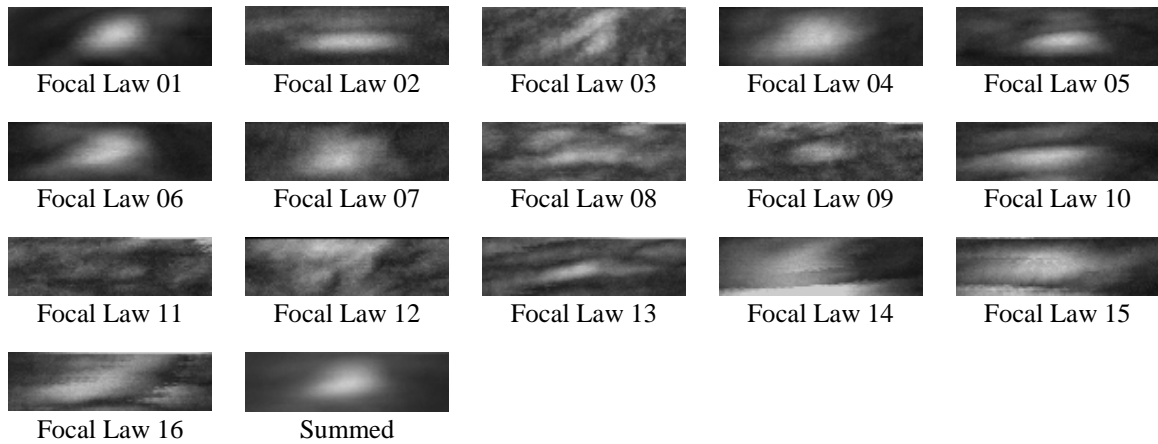
Figure F.12: 3D method inspection C-scans of curved interface forging coupon #12.

Focal Law 01   Focal Law 02   Focal Law 03   Focal Law 04   Focal Law 05

Focal Law 06   Focal Law 07   Focal Law 08   Focal Law 09   Focal Law 10

Focal Law 11   Focal Law 12   Focal Law 13   Focal Law 14   Focal Law 15

Focal Law 16   Focal Law 17   Focal Law 18   Summed

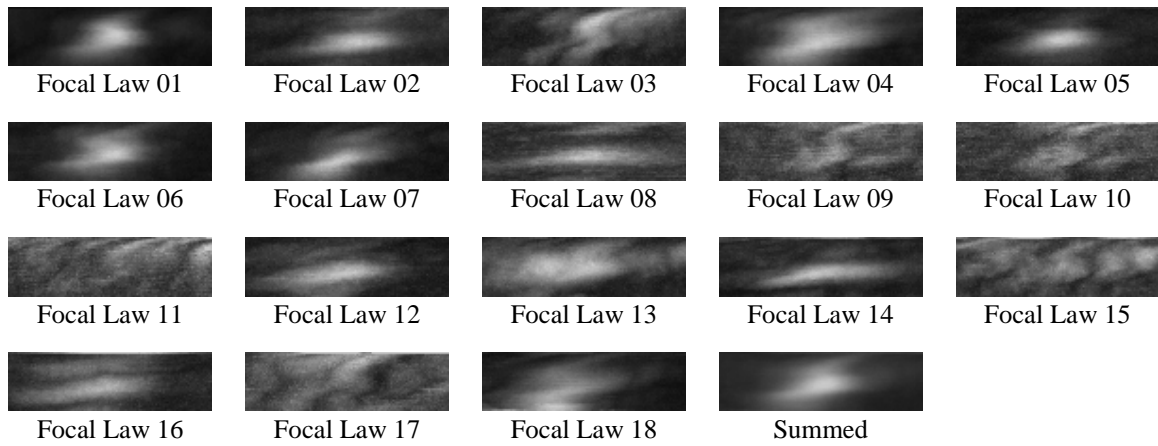**Figure F.13: 3D method inspection C-scans of curved interface forging coupon #13.**

BIBLIOGRAPHY

1. Howard, P. J. and Gilmore, R. S., "Ultrasonic noise and the volume of the ultrasonic pulse" in *Review in the Progress in Quantitative Nondestructive Evaluation*, Vol. 24, eds. D. O. Thompson and D. E. Chimenti, Plenum Press, New York, NY, 2005, p. 922.

2. Margetan, F. J., Yalda, I., Thompson, R. B., Umbach, J., Suh, U., Howard, P. J., Copley, D. C., and Gilmore, R., "Ultrasonic grain noise modeling: recent applications to engine titanium inspections" in *Review in the Progress in Quantitative Nondestructive Evaluation*, Vol. 16, eds. D. O. Thompson and D. E. Chimenti, Plenum Press, New York, NY, 1997, p. 1555.

3. Roberts, R. A. and Friedl, J., "Phased array inspection of titanium disk forgings targeting #1/2 FBH sensitivity" in *Review in the Progress in Quantitative Nondestructive Evaluation*, Vol. 24, eds. D. O. Thompson and D. E. Chimenti, Plenum Press, New York, NY, 2005, p. 922.

4. Wooh, S.-C. and Shi, Y., "A simulation study of the beam steering characteristics for linear phased arrays", *Journal of Nondestructive Evaluation* **18**(2), p. 39-57 (1999).

5. Clay, A. C., Wooh, S.-C., Azar, L., and Wang, J.-Y., "Experimental study of phased array beam steering characteristics", *Journal of Nondestructive Evaluation*, **18**(2), p. 59-71 (1999).

6. Margetan, F. J., Umbach, J., Roberts, R., Friedl, J., Degtyar, A., Keller, M., Hassan, W., Brasche, L., Klassen, A., Wasan, H., and Kinney, A., "Inspection development for titanium forgings", *FAA Report DOT/FAA/AR-xx/xx*, filed November 15, 2004, p. 34-36.

7. Smith, F. G. and Thomson, J. H., *Optics*, 2nd Ed., John Wiley & Sons, Ltd., New York, NY, 1988, p. 122.

8. Schmerr, L. W., *Fundamentals of Ultrasonic Nondestructive Evaluation: A Modeling Approach*, Plenum Press, New York, NY, 1998, p. 279.

9. Arfken, G. B, Griffing, D. F., Kelley, D., Priest, J., *University Physics*, Academic Press, New York, NY, 1984, p. 756-7.

10. Rose, Joseph L., *Ultrasonic Waves in Solid Media*, Cambridge University Press, New York, NY, 1999, p. 46-7.

11. Allmeasures.com, http://www.allmeasures.com/formulae/static/materials/58/speedofsound.htm, "Calculating the velocity of sound in distilled water given water bath temperature in degrees Celsius, degrees Fahrenheit, or Kelvin", 1999-2004, accessed June 13, 2005.

12. Smith, F. G. and Thomson, J. H., *Optics*, 2nd Ed., John Wiley & Sons, Ltd., New York, NY, 1988, p. 91.

13. Schmerr, L. W., Fundamentals of Ultrasonic Nondestructive Evaluation: A Modeling Approach, Plenum Press, New York, NY, 1998, p. 197.

14. Longhurst, R. S., *Geometrical and Physical Optics*, Longmans, Green and Co., London, 1957, p. 320-1.

15. Wikipedia - the free encyclopedia, http://en.wikipedia.org/wiki/Aberration_in_optical_systems, "Aberration in optical systems", containing text incorporated from the Encyclopœdia Britannica, 11th Ed., a publication now in the public domain, accessed August 23, 2006.

16. Friedl, J. H., Gray, T. A., Khandelwal, P., and Dunhill, T., "Ultrasonic Phased Array Inspection of Seeded Titanium Billet" in *Review in the Progress of Quantitative Nondestructive Evaluation*, Vol. 23, eds. D. O. Thompson and D. E. Chimenti, Plenum Press, New York, p. 809.

17. Friedl, J., Roberts, R., Margetan, F., Degtyar, A., Hassan, W., Umbach, J., Brasche, L., and Keller, M., "Transducer variability study", *FAA Supplemental Report DOT/FAA/AR-xx/xx*, filed May 4, 2005.

18. Abramowitz, Milton and Stegun, Irene A., Eds, Handbook of Mathematical Functions with Formulas, Graphs, and Mathematical Functions, Dover Publications, New York, 1972, p. 20.

19. Cychosz, Joseph M. and Waggenspack, Warren N., Jr., "Intersecting a Ray with a Cylinder" in *Graphic Gems IV IGM*, Ed. Paul Heckbert, p. 356-359.

20. Faissler, William L., *An Introduction to Modern Electronics*, John Wiley & Sons, Inc., New York, 1991, p. 445.

21. Levine, David M., Stephan, David F., Krehbiel, Timothy C., and Berenson, Mark L., *Statistics for Managers Using Microsoft® Excel*, 5th Ed., Pearson Prentice Hall, New Jersey, 2008, p. 134-5.

22. Levine, David M., Stephan, David F., Krehbiel, Timothy C. and Berenson, Mark L., *Statistics for Managers*, 5th Ed., Prentice Hall, New Jersey, 2008, p. 236.

23. Barlow, Roger J., *Statistics: A Guide to the Use of Statistical Methods in the Physical Sciences*, John Wiley & Sons, Inc., New York, 1989, p. 176-7.

24. Devore, Jay L., *Probability and Statistics for Engineering and the Sciences*, 4th Ed., Duxbury Press, California, 1995, p. 628-34.

25. Devore, Jay L., *Probability and Statistics for Engineering and the Sciences*, 4th Ed., Duxbury Press, California, 1995, p. 713.

26. Spiegel, Murray R., *Schaum's Outline Series: Mathematical Handbook of Formulas and Tables*, McGraw-Hill, Inc., 1995, p. 49.

27. Spiegel, Murray R., *Schaum's Outline Series: Mathematical Handbook of Formulas and Tables*, McGraw-Hill, Inc., 1995, p. 34.

28. Arfken, George B., Griffing, David F., Kelly, Donald C., and Priest, Joseph, *University Physics*, Academic Press, 1984, p. 786-7.

29. Arfken, George B., Griffing, David F., Kelly, Donald C., and Priest, Joseph, *University Physics*, Academic Press, 1984, p. 353-4.